

Design and measurement of superconducting microwave kinetic inductance detectors

Inaugural-Dissertation

zur

Erlangung des Doktorgrades
der Mathematisch-Naturwissenschaftlichen Fakultät
der Universität zu Köln



Vorgelegt von
Florian Blauth
aus Köln

Druck und Bindung: PRESSEL Digitaler Produktionsdruck

Köln, 2019

Berichterstatter: Prof. Dr. Jürgen Stutzki
(Gutachter) Prof. Dr. Joachim Hemberger
Tag der Abschlussprüfung: 15.1.2019

Abstract

Microwave kinetic inductance detectors (MKID) are superconducting broadband direct detectors. If a superconducting thin film patterned into a resonator is illuminated with photons, Cooper pairs break up and the kinetic inductance of the film changes. This shifts the resonance frequency downwards and the dissipation of the resonator increases, which can be detected in the phase and amplitude of a transmitted signal.

In this thesis, a waveguide coupled MKID is designed and simulated. 350 GHz radiation is coupled into a copper waveguide via a horn antenna. A waveguide probe leads the signal onto a 9 μm silicon membrane where it is absorbed in a 40 nm superconducting aluminum film which is the inductive part of a superconducting resonator. The capacitor of the resonator is made of niobium. Two versions of the device are developed, a transmission line resonator and a lumped element resonator design. The new design will enable an accurate understanding of the optical sensitivity of MKIDs and allow comparison of different resonator materials. Since two different resonator types are used, the direct comparison of transmission line and lumped resonators will also be possible.

A measurement setup is developed including an ADR cryostat to cool MKID devices down to below 100 mK. An analog readout system using either a vector network analyzer or an IQ mixer is designed and built. The necessary software to control the ADR, the temperature monitoring, the readout signal generation and detection and the signal acquisition of the setup is also developed.

The waveguide coupled MKID design is fabricated in our in-house microfabrication laboratory and measured in the new setup. In my measurements, the devices do not show a resonance feature. The VNA and DC measurements are analyzed to determine a plausible hypothesis of the failure. The devices are diagnosed for critical issues during fabrication which will be addressed in a future iteration.

To verify the measurement setup, a test device of the IRAM NIKA 2 MKID camera is measured and the complete analysis pipeline is exercised. The quasi-particle lifetime in the aluminum thin films is measured and a dark and optical noise equivalent power are determined. The results are within the uncertainty comparable to measurements of IRAM themselves.

A test chip designed in my master thesis that contains eight NbTiN resonators is measured in the new setup and non-linear effects under strong readout power are studied. Parametric amplification and oscillation of a resonator are shown qualitatively.

Zusammenfassung

Microwave Kinetic Inductance Detectors (MKID) sind breitbandige, supraleitende Leistungsdetektoren. Diese bestehen aus einem supraleitenden Dünnschicht in Form eines Resonators.

Beleuchtet man diesen mit Photonen, ändert sich dessen kinetische Induktivität. Dadurch verringert sich die Resonanzfrequenz und die Verluste im Resonator steigen an, was in einer Änderung der transmittierten Amplitude und Phase gemessen werden kann.

Diese Arbeit beschreibt die Entwicklung eines MKID, welches an einen Hohlleiter gekoppelt ist. Strahlung im Frequenzbereich um 350 GHz wird mit einer Hornantenne in den Hohlleiter gekoppelt. Eine Antenne im Hohlleiter leitet das Signal auf eine 9 μm dicke Siliziummembran, wo es in einer 40 nm dicken, supraleitenden Aluminiumleitung absorbiert wird. Die Aluminiumleitung ist die Induktivität eines supraleitenden Resonators. Der Kondensator des Resonators besteht aus Niob.

Zwei Varianten des hohlleitergekoppelten MKID werden vorgestellt. Die erste Variante verwendet einen Resonator bestehend aus einem planaren Wellenleiter und die zweite Variante einen Resonator, welcher aus diskreten Elementen aufgebaut ist. Mit diesem neuen MKID soll die Empfindlichkeit unter optischer Bestrahlung genauer untersucht werden. Zudem soll es die Erforschung von alternativen Materialien für den Absorber der MKID ermöglichen. Zusätzlich können mit den Varianten des Designs die beiden Resonatortypen direkt miteinander verglichen werden.

Ein neuer Messaufbau mit einem ADR Kryostaten ermöglicht es, MKID auf eine Temperatur unter 100 mK herunter zu kühlen. Eine analoge Ausleseelektronik, die entweder einen Netzwerkanalysator oder einen IQ Mischer zur Messung verwendet, wurde entwickelt und aufgebaut. Dazu wurde die nötige Software programmiert, die das Temperaturmanagement, die Fernsteuerung des Messequipments und die eigentliche Datenaufnahme übernimmt.

Die hohlleitergekoppelten MKID wurden in unserem Mikrostrukturlabor gefertigt und in dem neuen Messaufbau gemessen. Die Transmissionsmessung mit dem Netzwerkanalysator zeigt jedoch keine Resonanzfrequenz. Die Messungen der Teststrukturen und die Messungen mit dem Netzwerkanalysator wurden analysiert um eine plausible Diagnose für die Fehlfunktion zu erstellen. Die Ursache liegt in einem Kontaktproblem, welches nur mit einem veränderten Fabrikationsprozess verhindert werden kann.

Um den neuen Messaufbau zu testen wurde ein MKID Testdetektor, welcher für die NIKA 2 Kamera von IRAM hergestellt wurde, gemessen. Mit diesem Detektor wurden alle Messprozeduren und Analysewerkzeuge getestet und verbessert. Die Quasipartikel-Lebensdauer der Aluminiumfilme konnte gemessen werden und das NEP (äquivalente

Rauschleistung) konnte unter minimaler optischer Bestrahlung und mit realistischer Bestrahlung gemessen werden. Die Messergebnisse sind vergleichbar mit publizierten Werten von Messungen am IRAM.

Ein Testdetektor mit 8 Resonatoren, welcher in meiner Masterarbeit entwickelt wurde, wurde noch einmal in dem neuen Messaufbau gemessen. Nichtlineare Effekte, welche bei starkem Auslesesignal, auftreten wurden beobachtet. Es konnten parametrische Verstärkung und parametrische Oszillation nachgewiesen werden.

Contents

1	Introduction	1
1.1	Organization of this thesis	1
1.2	The long way to modern astronomy	2
1.2.1	From the antiques till the medieval	3
1.2.2	Understanding the nature of light	4
1.2.3	Towards sub-mm astronomy	4
1.2.4	Today's situation	5
1.3	Detectors for the CCAT-prime telescope	5
1.3.1	Scientific aims of the CCAT-prime telescope	6
1.3.2	Why direct detectors	9
2	Microwave kinetic inductance detectors	11
2.1	The working principle of kinetic inductance detectors	11
2.1.1	Superconductivity	11
2.1.2	The microwave kinetic inductance detector	12
2.1.3	A pair breaking detector	13
2.1.4	Kinetic inductance	16
2.1.5	Radiation absorption in a superconductor	17
2.2	Properties of the superconducting resonator	17
2.2.1	Resonance frequency and quality factor of the superconducting resonator	17
2.2.2	Transmission of the ideal resonator	19
2.2.3	Resonator model including mismatch	20
2.2.4	Multiplexing	20
2.2.5	Calculating the complex conductivity	21
2.2.6	Surface impedance	22
2.2.7	Fitting material parameters	23
2.2.8	The effect of high readout power	24
2.3	Noise sources in a kinetic inductance detector	24
2.3.1	Power spectral density	26

2.3.2	Noise Equivalent Power (NEP)	26
2.3.3	Generation-recombination noise	27
2.3.4	Photon noise	28
2.3.5	Two-level systems	30
2.3.6	Kondo effect	30
2.3.7	Readout system noise	31
2.3.8	A full MKID sensitivity model	33
2.4	Overview of MKID based instruments	34
2.4.1	NIKA 2	34
2.4.2	A-MKID	34
2.4.3	MKID based multi color detectors and spectrometers	35
2.4.4	The ARCONS near infrared camera	35
3	Measurement Setup	37
3.1	ADR cryostat	37
3.1.1	ADR principle	37
3.1.2	The HPD Rainier model 103 cryostat	40
3.1.3	Increasing and decreasing the magnet current	41
3.1.4	Operation and monitoring software	42
3.1.5	Temperature control and stabilization	43
3.1.6	ADR security precautions	44
3.2	General cold measurement setup	44
3.2.1	Heated black body load	45
3.2.2	LED pulse setup	46
3.2.3	R/T setup	46
3.3	MKID readout system	47
3.3.1	Vector network analyzer readout	48
3.3.2	IQ mixer readout mode	48
3.3.3	Cold readout system	49
3.3.4	Room temperature switchable readout processor	51
3.3.5	Analog to digital converters and low pass filters	53
3.3.6	Measurement and control software	54
3.3.7	Estimation of readout system noise	56
3.4	Measurement procedures	57
3.4.1	VNA transmission measurement and temperature sweep	57
3.4.2	Measurement of IQ mixer frequency sweeps	58
3.4.3	Measurement of time domain data for noise analysis	59

3.4.4	LED pulse	60
3.4.5	Search for Cosmic ray events	61
3.5	Measurement setup for different devices	61
3.5.1	Cold setup for waveguide coupled devices	61
3.5.2	Cold NIKA chip measurement setup	64
3.5.3	NbTiN test chip setup	66
4	Design and simulation of a waveguide coupled MKID	67
4.1	A waveguide coupled MKID Detector	67
4.1.1	Design decisions and constraints	68
4.1.2	Simulation software	69
4.2	Transmission lines	70
4.2.1	Rectangular waveguide	70
4.2.2	Coplanar waveguide transmission line	71
4.3	The waveguide coupled lumped element MKID (WGKID)	71
4.3.1	Horn antenna and waveguide	72
4.3.2	Waveguide probe and substrate	74
4.3.3	Symmetric 3 dB power splitter	74
4.3.4	Absorber lines	76
4.3.5	Lumped element resonator	77
4.3.6	Connection to the readout system	78
4.3.7	Inductively coupled design	79
4.4	The waveguide coupled transmission line resonator design (TMKID)	79
4.4.1	Waveguide and antenna	80
4.4.2	readout ground stubs	80
4.4.3	Absorber line	81
4.4.4	Resonator and Coupler	81
4.5	Preparing fabrication	83
4.5.1	Selection of variations	83
4.5.2	Layer order and thicknesses	83
4.5.3	Tolerance analysis	84
4.5.4	Wafer layout and test structures	85
5	Measurement and diagnosis of waveguide coupled MKID devices	89
5.1	Fabrication of devices	89
5.1.1	Lift-off process	89
5.1.2	Silicon On Insulator (SOI) technology	90

5.1.3	Description of the micro-fabrication process	91
5.2	DC measurement of test structures	95
5.2.1	Measurement of transition temperature and resistivity	95
5.2.2	Measurement of current-voltage characteristics	96
5.2.3	Experiment to reduce contact resistance	98
5.3	VNA transmission measurements	98
5.3.1	Measurement of WGKID devices	99
5.3.2	Measurement of TMKID devices	101
5.4	Hypotheses for possible failures of the devices	101
5.4.1	Interpretation of DC measurements	103
5.4.2	Interpretation of VNA measurements	104
5.5	Conclusion and suggestion for improvements	105
6	Measurement and analysis of NIKA 2 MKID test arrays	107
6.1	Description of the NIKA 2 test devices	108
6.2	Measurement of resonance frequency and quality factors using the VNA . .	109
6.2.1	Transmission of the chip	109
6.2.2	Fitting procedure	111
6.2.3	Reduction of quality factor over time	112
6.2.4	Qualitative investigation of the influence of external magnetic field .	112
6.2.5	Measurement of temperature dependence of resonance frequency and quality factor	115
6.3	Determination of the complex gap parameter	116
6.3.1	Simulation of the kinetic inductance fraction	117
6.3.2	Correction for non-monotonical frequency shift	118
6.3.3	Fitting resonator parameters	119
6.4	Measurement of the quasiparticle lifetime using excitation pulses	121
6.4.1	Measurement of LED pulse response	121
6.4.2	Processing of LED pulse measurements	122
6.4.3	Dependence on LED power and readout system power	123
6.4.4	Temperature dependence of quasiparticle lifetime from LED pulses	124
6.4.5	Quasiparticle lifetime from cosmic ray events	125
6.5	Noise measurements using the IQ mixer	125
6.5.1	Measurement of time domain data for noise analysis	125
6.5.2	Analysis of the measured IQ mixer frequency sweep	126
6.5.3	Calculation of the power spectral density	128
6.5.4	Calculation of amplitude and phase noise spectral density	130

6.5.5	Logarithmic averaging	132
6.5.6	Quasiparticle lifetime from noise spectra	132
6.6	Calculation of dark NEP	133
6.6.1	Calculating the phase responsivity from the frequency shift data . .	135
6.6.2	Dark NEP	136
6.7	Determination of optical NEP	137
6.7.1	Calculation of optical power	137
6.7.2	Measurement of the optical phase response	140
6.7.3	Calculation of optical NEP	140
7	Summary and outlook	143
7.1	Evaluation of the measurements of NIKA 2 test devices	143
7.1.1	Evidence for aging of the devices	144
7.1.2	Influence of external magnetic field on the quality factors	145
7.1.3	Determination of complex gap parameter	147
7.1.4	Comparison and discussion of quasiparticle lifetime measurements .	148
7.1.5	Discussion of the measured dark and optical NEP	152
7.2	Concluding evaluation of the measurement setup	153
7.2.1	Remaining issues of the measurement setup	153
7.2.2	Suggested improvement of the measurement setup	154
7.3	Evaluation of the waveguide coupled MKID	155
7.3.1	Design and simulation results	156
7.3.2	Measurement	156
7.3.3	Analysis of the failure	157
7.3.4	Discussion of the waveguide coupled devices	157
7.4	Outlook: Towards a sub-mm MKID camera	158
8	Appendix A: Non-linear effects in NbTiN resonators	161
8.1	Description of the NbTiN test chip	161
8.2	The two-tone readout setup	162
8.3	Measurement	163
8.3.1	Measurement with strong VNA signal only	163
8.3.2	Two-tone power sweep with pump tone frequency on the resonance	163
8.3.3	Two-tone power sweep with pump tone frequency below the resonance	164
8.3.4	Measurement with pump tone using the spectrum analyzer	165
8.3.5	Measurement with very high pump tone power	166

8.4	Analysis	167
8.4.1	Resonance frequency and quality factor in dependence of pump tone power	167
8.4.2	The hysteretic state	167
8.4.3	Parametric amplification	168
8.4.4	Overdriven resonator	169
8.5	Summary and discussion	169
	Bibliography	182

1 Introduction

1.1 Organization of this thesis

This thesis reports about the development of a superconducting power detector for application in radioastronomy in the sub-millimeter wavelength range and the implementation and verification of a measurement setup to determine the sensitivity of such a detector.

The upcoming new CCAT-prime radio telescope will require cameras in the frequency range below 1.5 THz with pixel numbers exceeding ten thousand at least. A promising and relatively new technology to achieve these pixel numbers are microwave kinetic inductance detectors (MKID) [24]. These detectors sense power through the change of the kinetic inductance in a strip of superconducting material when quasiparticles are generated by incident photons.

Our work group started the development of MKID from scratch with the work in my master thesis [16], where already a very basic measurement setup with a ^3He adsorption cryostat was implemented. This cryostat reached a minimum temperature of 300 mK. Also, a test chip containing eight NbTiN resonators was designed and fabricated. Starting from that, a new measurement setup with an ADR cryostat with a minimum temperature below 100 mK became necessary, because the previous cryostat could not achieve sufficiently low temperatures for operating aluminum MKID.

At the time when this thesis work was started, there was no immediate plan for an specific MKID instrument. Therefore it was decided to design an experimental MKID which will be a waveguide coupled detector. This device is developed to investigate the optical sensitivity of MKID and will enable research on new materials for the kinetic inductance part of the detector.

The two main tasks of this thesis can be summarized as follows:

1. For measurement of future MKID, a measurement setup using a new ADR cryostat has to be planned, implemented and tested. This includes building and testing the readout electronics.
2. An MKID using aluminum as sensitive material has to be designed, fabricated and

measured to investigate the optical sensitivity of MKID and to verify my measurement setup.

In the last year of this thesis, the construction of the CCAT-prime observatory became certainty, changing the focus of this thesis a little bit towards the development of MKID cameras, which however could not be thoroughly implemented any more.

The first two chapters of this thesis give a brief introduction in the science case and describe the theoretical basics of the methods used within this thesis. Chapter 2 in detail describes the working principle of MKID. In chapter 3, the measurement setup is described, together with the measurement procedures used later. Chapters 4 and 5 deal with the design and the measurement of the waveguide coupled MKID. As it will turn out, the detectors are not ready yet and need further refined fabrication processes. Therefore, in chapter 6, the measurement of an MKID test device from the NIKA 2 camera that was kindly supplied from IRAM is described. With this device, the full evaluation of the measurement setup is carried out. Finally, in chapter 7, the results of this thesis are summarized and discussed.

Some additional measurements using the MKID device with NbTiN resonators from my master thesis under high readout power are summarized in appendix A. The results of this measurements might trigger future experiments, as effects like parametric amplification and oscillation are observed in resonators driven in their non-linear regime by high readout power.

Despite the larges amount of technological development described in this thesis and that generally is necessary for astronomical instrumentation today, astronomy started as a very basic science with people using nothing than their bare eyes to examine their universe. A small historical overview including the rise of high frequency technology will be given in the next section.

1.2 The long way to modern astronomy

Astronomy is a quite a peculiar branch of science. There are indeed a few applications of observing the position of stars, as the north polar star was guiding ships and travelers since the ancient times. The motion of the sun brings us day and night and the inclined earth axis determines our seasons, whose explanation however does not require detailed understanding of our cosmos.

So why did an ancient civilization around 1600 B.C. spend about 2 kilograms of precious bronze to forge something like the sky disk of Nebra, which is the oldest documented map of the stars? And why do we still today send satellites into space which observe phenomena

which will never ever affect our (physical) daily life and cost billions of Euros doing so?

There surely is no unique answer to that question. The human curiosity makes us ask question regarding our origin and the meaning of our existence, which triggered the development of religion and science alike and often blended with each other. Today, our understanding of the universe is already so advanced, that we claim to know about the early beginning of the universe and can let whole galaxies live their lives in big computer simulations. The big picture seems to be fairly clear to us, but it can be the details which lead to astonishingly new insights, therefore we should keep questioning and keep doing our research.

1.2.1 From the antiques till the medieval

The early observational astronomy was mainly astrometry, dedicated to the measurement of the position of stars and planets. The first astronomers did not use any optical instruments but merely mechanical quadrants or similar instruments to measure the angular position of objects on the sky. They had to rely on their eyes only. The first partition of the sky was done by the assignment of the zodiacal signs. Hipparchos (190-120 B.C.) put together the first catalog of stars. Around 100 A.D., Ptolemy developed a his geocentric model of the universe stating that the sun and the planets move around the earth, guided by a complex mechanical system. This model could already describe the observations up to the available accuracy. Jumping from ancient Greece to medieval Europe, the catholic church adopted the geocentric view of the universe as it suited the believed predominant role of mankind in the universe, created by God. However, Nikolaus Copernicus devised in 1543, that the complicated calculations would become much easier if a different model was used, where the sun is in the center of the solar system and everything revolved around it in circular orbits. Copernicus himself had excellent contacts to the church and the pope, therefore his model could be published as long as it was considered as a hypothetical mathematical simplification.

Tycho Brahe (1546-1601) did the last significant observations using only his eyes and a mechanical quadrant. He could push the accuracy to below one arc minute, which enabled his scholar, Johannes Kepler, to recognize an $8'$ deviation of the orbit of Mars from the perfect circular shape and led to the formulation of Keplers laws. This however was published in 1609, after the death of Tycho Brahe, who himself did not believe in the heliocentric model.

Galileo Galilei, who was in contact with Kepler, was one of the first to use an optical lens telescope to observe astronomical objects. His discovery of the five largest moons of Jupiter in 1610 led to a large dispute with the catholic church, because it was an observation

which significantly supported the heliocentric model of the solar system. From then on, the optical telescope became indispensable as an astronomical instrument. Newtons law of gravity published around 1687 then delivered the full explanation of Keplers laws.

1.2.2 Understanding the nature of light

The visible wavelength range between 300 and 700 nm was the only wavelength range understood as 'light' for a long time. With the final phases of the age of Enlightenment in Europe, also a wealth of new scientific findings were made. After it became clear that light can be split up into different colors, black lines were discovered in the spectrum of sunlight by Wollaston in 1802 and then by Fraunhofer in 1814 [39], after whom these lines are named. Fraunhofer also developed an advanced optical spectrograph.

After Gilbert, Volta, Coulomb, Ohm, and others paved the way for electronics and magnetism experimentally, James Clerk Maxwell presented the first unified theory for electrodynamics in 1865 [65]. His theory predicted electromagnetic waves, which were first experimentally verified by Heinrich Hertz in 1886 [46], shortly before Oliver Lodge could show these waves, too. These findings are the basis for the advance of radio communication, which would trigger the development towards higher frequencies and more sensitive equipment. It then also became clear that visible light and radio waves are described by the same theory, as both are electromagnetic waves.

On the high energy end of the spectrum, Conrad Röntgen discovered the X-rays in 1895 [85]. From then on, it was clear, that the electromagnetic spectrum is much broader than just the visible wavelength range.

1.2.3 Towards sub-mm astronomy

The commercial application of the electromagnetic waves as a way to communicate over a distance emerged quite rapidly, resulting in a complicated mess of concurring companies, patents and technologies. The first systems had spark-gap transmitters which use up a wide portion of the frequency spectrum and only pulses can be transmitted. On the receiver end, the rectification is the most critical part of the system. For a brief historical overview of these developments, the introduction in [61] is recommended.

The practical demonstration of the waveguide by Southworth and Hargreaves in 1932 showed a way to transport high frequency signals with exceptional low loss. In 1937, the first British radar system was operational and upgraded to 200 MHz till 1941. The second world war augmented the interest on radar technology and boosted the development of high power radiation sources for higher and higher frequencies, but also triggered the

development of antennas and rectifiers. With the invention of the cyclotron and the later the magnetron, extremely powerful radar systems up to 10 GHz were operational at the end of the war.

The birth hour of radio astronomy was actually shortly before the war, as Karl G. Jansky examined excess noise in an antenna designed for transatlantic communication at 20 MHz [51]. He could prove, that the origin of the received noise signal is not in our solar system and triggered the interest of exploring the sky at radio frequencies. His work was continued by Grote Reber at shorter wavelengths afterwards to narrow down the nature of the signal [83].

1.2.4 Today's situation

Modern astronomy gets information about stars, external galaxies, interstellar gas and dust by observation of the whole electromagnetic spectrum ranging from radio waves up to x-ray. Other sources of information are high energy particles from interstellar origin or from the sun like protons or neutrinos or, very recently, gravitational waves [1]. All information sources, except for the part of the electromagnetic spectrum we can see with our eyes, need specific detectors which convert the invisible photons, particles or gravitational waves to something that can be analyzed and processed.

In modern sub-mm/Terahertz radio astronomy the development of detectors which are extremely sensitive and have many detecting elements (pixels) is ongoing. Because background limited performance (or quantum limited sensitivity in heterodyne systems) is already achieved for an individual detector, further sensitivity can only be gained by increasing the number of pixels.

The research within my thesis is on Microwave Kinetic Inductance Detectors (MKIDs) whose working principle is discussed in chapter 2. They will, once brought to full maturity, unite the demands of sensitivity, pixel number and simplicity, also in the sense of cost efficiency. The focus of my work is on the aspect of sensitivity of MKIDs.

1.3 Detectors for the CCAT-prime telescope

CCAT-prime [77] is a new sub-mm telescope that will be finished in 2021 (see fig. 1.1). It will be located on the Cerro-Chajnantor in Chile, 5600 m above the sea level offering even better atmospheric conditions for THz frequencies than the ALMA site at 5000 m. Its unique optical Cross-Dragnone design (fig. 1.1, right) will enable a minimal blocking of the aperture and will make it an exceptional instrument for large scale mapping [73, 78]. Its 6 m primary and secondary mirrors will have a surface accuracy better than 10.7 μm

RMS and will enable observations at wavelengths between $200\ \mu\text{m}$ (1.5 THz) and 3 mm (100 GHz). The optical design results in a large field of view of 7.8° at 3 mm and 4° at 1 mm.

One of CCAT-primes planned first light scientific instruments is prime-Cam, a camera designed for several wavelength ranges between 3 mm and $350\ \mu\text{m}$. It consists of initially three up to 7 sub-cameras which can be exchanged separately and matched to a science case. The sensitive elements will be either Microwave Kinetic Induction Detectors (MKID) or Transition Edge Sensors (TES). Not all sub cameras need to use the same technology. The detectors are operated at a temperature around 100 mK. The the planned sub cameras will consist of 4320 TES detectors for the longest wavelength and 18216 MKID for 860 GHz. The total size of the instrument including its cryostat and pulse tube coolers is comparable to that of a small car. The results of my thesis will be of interest for the design of a MKID sub-camera and the scientific motivation for a large format camera discussed in sec. 1.3.1 also motivates my work. Prime-Cam will address questions in cosmology, regarding the epoch of reionization, the cosmic microwave background and the formation of early galaxies.

The second first light instrument for CCAT-prime will be CHAI, the CCAT Heterodyne Array Instrument. It will be a two color, dual polarization heterodyne array with 2×64 mixers at 460 GHz and 2×64 mixers at 800 GHz and will be able to do high resolution spectroscopy maps at an unprecedented speed. The main task for CHAI is the investigation of the local interstellar medium and especially its dynamic properties. Its dual polarization detection will also enable the detailed investigation of galactic magnetic fields. The CHAI instrument will be developed at the I. Physikalisches Institut at the University of Cologne.

1.3.1 Scientific aims of the CCAT-prime telescope

The very stable weather conditions and the optical Cross-Dragone design together with the 6 m primary mirror make CCAT-prime an instrument especially suited for cosmological investigations requiring large-scale surveys. Therefore four of the scientific goals are questions concerning the early universe and the formation of the first galaxies. The following science cases are specifically for prime-Cam and will be discussed as examples for the power of direct detector cameras at multiple simultaneously observable wavelengths.

The nature of our universe as we experience it is determined in the first billion years. With an estimated age of 13.7 billion years, it has been in quite a constant state for most of its lifetime (see fig. 1.2). To our present knowledge, the universe started from a singularity with the "big bang", which is today visible as the cosmic microwave background

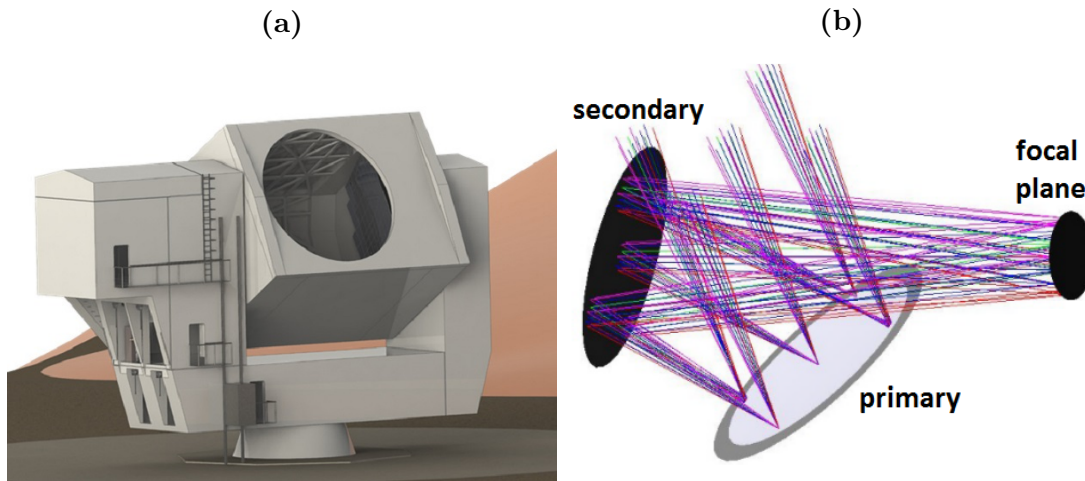


Figure 1.1: (a) Artist impression of the CCAT-prime telescope (image: VERTEX Antennentechnik). (b) The optical design of the Cross-Dragone system. The secondary mirror is as big as the primary mirror and produces an obstruction-free and very flat focal plane.

(CMB), radiating a thermal spectrum at a temperature of 2.7 K. It was discovered by Wilson and Penzias in 1964 by accident as an isotropic radiation that can be received from every direction. Today's accurate measurements using the COBE, WMAP [13, 48] and the Planck [80] satellites show slight deviations from a blackbody at a constant temperature. The statistics of that deviation can be used to test cosmological models of the universe.

The speed of light is a universal constant in all reference systems. The light we observe from astronomical objects has always already traveled the distance between the observed object and the observer. Because of that, we are only able to look at the past of the specific object. The farther away an object is, the farther in the past we look by observing these objects.

The universe has expanded since its creation, meaning that wavelength of all the radiation that traveled through the universe is stretched. The amount of wavelength shift caused by the expanding universe is called cosmological red shift and is defined as $z = \frac{\lambda - \lambda_0}{\lambda_0}$ where λ is the observed frequency and λ_0 the rest-frame frequency. Because the time the radiation traveled determines the amount of red shift, high red shift implies (cosmologically) old objects and far distances. As examples, galactic objects have cosmological red shift close to 0 (but are red- or blue-shifted due to their relative velocities) and the oldest galaxies observed have a red shift of 6 to 11 for objects measured during the epoch of reionization. The redshift of the CMB is approximately 1100, with the assumption of the temperature of the universe being 3000 K when the CMB was created [94].

The epoch of reionization which is around 400 million ($6 < z < 20$) years after the big bang and marks the formation of the first, massive and short living stars. Besides the

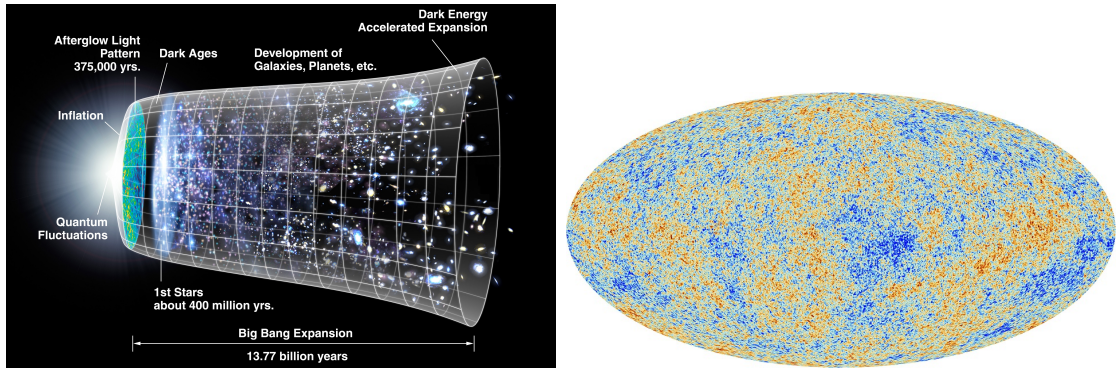


Figure 1.2: Left: The evolution of the universe from the big bang till today. Image: NASA. Right: The temperature fluctuation of the cosmic microwave background as measured from the Planck satellite. Image: ESA

cosmological microwave background, the first signals are received from that era. Three of the five CCAT-prime science goals targeting on the CMB and the epoch of reionization are described briefly in the following paragraphs.

Investigation of galaxy cluster velocity utilizing the kinetic Sunyaev-Zel'dovich effect

The Sunyaev-Zel'dovich effect (SZ) describes the observable deformation of the cosmic microwave background (CMB) spectrum by free electrons in foreground galaxy clusters [93]. Photons of the CMB undergo inverse Compton scattering with high energy electrons in the halo of these galaxy clusters and are up-converted to higher frequencies.

In the thermal SZ, the electrons have high energy due to their temperature. The weaker kinetic SZ, which is of main interest in this application, originates in the kinematics of the galaxy clusters, where the wavelength of CMB photons is then shifted according to the bulk motion of the cluster. This velocity information can be used as a probe for investigation of the nature of dark energy, to test gravity on large scales and to apply constraints on the neutrino mass [22].

Intensity mapping of ionized carbon from the epoch of reionization The early universe went through a dark age between 100 and 270 million years after the big bang where only the photons of the microwave background were present. This age ended with the epoch of reionization. When and how the first star-forming galaxies occurred will be investigated by observing ionized carbon [CII]. [23].

In the early universe, carbon can only be created in the second generation of stars, because initially only hydrogen and helium is supposed to be present. The carbon has to be created in the first generation of stars by nucleosynthesis. As soon as the carbon is released, ionized carbon will be an immediate tracer of star formation, because the radiation

of young stars will ionize the carbon atoms. Observing the red-shift of the ionized carbon line can also be used to determine the onset of second generation star formation in time.

Intensity mapping is the predominant way observing the cosmic microwave background but can also be used for these observations. The individual radiation sources are explicitly not resolved but add up in these observations. This lowers the requirements in sensitivity. Ionized carbon is in this case used as a tracer for star formation. Atomic Hydrogen can be directly observed by its 21 cm hyperfine structure transition. This requires much larger observatories like the Square Kilometer Array (SKA) for the weak hyperfine structure line, which are observations complementary to those of [CII]. The bright ionized carbon line at $158\mu\text{m}$ in its rest frame reaches into the CCAT band at the high redshift ($z = 6 - 9$). Many detectors with a medium resolution ($R=300-500$) are required for these observations, which could be fulfilled by a camera behind an interferometric spectrometer of the required resolution.

Precise mapping of the cosmic microwave background The 6 m primary mirror and the high transmittivity of the optics make CCAT-prime an outstanding platform for CMB mapping. The flat focal plane can hold second generation instruments up to millions of detectors leading to an mapping speed beyond the capabilities of any current instrument. The coverage of the sub-mm frequency bands provides better foreground removal than e.g. the Planck data can provide. These observations will also resolve the polarization components of the CMB, if they can be observed. Especially foreground radiation by dust can disturb the measurement of possible polarization components in the CMB, where the high frequency bands of CCAT-prime can help to remove these disturbances.

Large format cameras are generally workhorses of astronomy. They are efficient for all applications where low spectral resolution is sufficient ($R < 300$). For medium resolution, an imaging spectograph might be used which can also profit from a sensitive direct detector like the MKID. For the highest resolution requirement ($R > 1 \times 10^6$) a heterodyne receiver is necessary which can clearly resolve the detailed shape of molecular lines. For these tasks, CCAT-prime will be equipped with the CHAI instrument.

1.3.2 Why direct detectors

Direct detectors only detect the power of the incoming signal and can not retrieve any information of the phase. Heterodyne systems usually consist of a mixing element and a local oscillator, which converts the incoming signal down in frequency. This makes analysis with high resolution digital spectrometers possible and enables an enormous spectral resolution

above 1×10^6 . Modern heterodyne receivers are available for a frequency range from the low radio up to the Terahertz range. The ability to resolve spectral lines and determine the velocity profile of the observed objects gives detailed insight into the dynamics of the interstellar medium. In the field of spectral resolution, direct detectors can not compete with heterodyne instruments. Still, direct detectors have distinct advantages:

- Direct detectors do not require a local oscillator signal. This makes the construction of large arrays much simpler and leads to the fact that direct detectors do not suffer from the quantum limit and can be fundamentally more sensitive.
- They have more spacial detecting elements than any heterodyne instrument. The NIKA 2 [2] camera already has 616 pixels on the low frequency band and existing bolometer cameras like SCUBA 2 [14] reach 10000 pixels. Supercam [44], the largest existing heterodyne array above 300 GHz currently contains 64 detectors. Therefore if low spectral resolution is sufficient, direct detectors have much higher mapping speed.
- Direct detectors are more flexible than heterodyne instruments, as a camera can be turned into a spectrometer by inserting a dispersing element in the beam in front of the detector.
- At high frequencies, the realization of direct detectors becomes more easy, as powerful semiconductor technology is available. The construction of sensitive high frequency heterodyne systems becomes however more and more challenging. At low frequencies, this situation is somewhat reversed, but MKID are a promising candidate to build cameras for the frequency range around 100 GHz as well.

The science cases mentioned in sec. 1.3.1 all benefit from the mapping speed of a many pixel camera. This is the main advantage of direct detector cameras and makes the development of new systems a promising task.

2 Microwave kinetic inductance detectors

Microwave kinetic inductance detectors (MKID) are broadband photon detectors which exploit the superconducting effect of kinetic inductance [24]. In this chapter the basic operation is explained starting with the necessary superconducting principles and how to build a detector out of them. Then the superconducting resonator is explained and analyzed. Finally, the noise sources in MKID are listed and the noise equivalent power (NEP) is explained.

2.1 The working principle of kinetic inductance detectors

2.1.1 Superconductivity

Superconductors exhibit zero DC resistance below a transition temperature T_c and completely expel magnetic fields up to a critical field density H_C . The first description of the electrodynamics in the superconducting state was given around 1935 with the London-equations [62]

$$\mathbf{E} = \frac{\partial}{\partial t} (\Lambda \mathbf{J}_s) \quad (2.1)$$

$$\mathbf{h} = -c \nabla \times (\Lambda \mathbf{J}_s) \quad (2.2)$$

$$\text{where } \Lambda = \frac{4\pi\lambda^2}{c^2} = \frac{m}{n_s e^2} \quad (2.3)$$

where \mathbf{E} is the electric field, \mathbf{h} is the magnetic flux density and c is the speed of light. Λ is a phenomenological parameter containing the London penetration depth λ . This is the depth, measured from the surface of the superconductor, at which the magnetic field in a superconductor decays to $1/e$ times its flux density. n_s is the number density of superconducting electrons [97]. These equations explain e.g. the Meissner effect, but do not attempt to understand the underlying microscopic mechanism of superconductivity.

The first microscopic quantum mechanical theory of superconductivity was developed

by Bardeen, Cooper and Schrieffer [4]. According to this theory, the electrons in the superconductor below T_c deform the positively charged crystal lattice of the material to create an effective attractive interaction. The electrons pair up into Cooper pairs which are now bosons and can therefore condense into one single quantum state, the superconducting ground state. The Cooper pairs are the charge carriers for lossless supercurrent. The binding energy of a Cooper pair is 2Δ and can be approximated for many superconductors as

$$2\Delta \approx 3.52k_B T_c = 73 \frac{\text{GHz}}{1 \text{ K}} T_c \quad (2.4)$$

where T_c is the transition temperature and $k_B \approx 1.381 \times 10^{-23} \text{ J K}^{-1}$ is the Boltzmann constant. The gap energy 2Δ is the minimum energy needed to excite (break) cooper pairs. These excitations are always in pairs and are called quasi-particles, as they are a combination of electron and hole excitation in the density of states.

The density of states in the superconductor is given by the BCS theory at zero temperature as [97]

$$\frac{N_s}{N_0} = \begin{cases} \frac{E}{\sqrt{E^2 - \Delta^2}} & (E > \Delta) \\ 0 & (E < \Delta) \end{cases} \quad (2.5)$$

The density of states for zero temperature is shown in fig. 2.1.

2.1.2 The microwave kinetic inductance detector

A microwave kinetic inductance detector (MKID) is basically an LC resonator, whose inductive section is made of a superconducting material. Generally, the whole resonator is patterned in a superconducting thin film. If photons above the pair breaking energy ($h\nu > 2\Delta$) are absorbed in the inductive section, Cooper pairs break up and generate quasi-particles. The kinetic inductance and the loss in the inductor increase and the resonance frequency $\omega_0 = 1/\sqrt{LC}$ decreases.

If the resonator is coupled to a readout line, the shift in resonance frequency and amplitude can be determined by a transmission measurement, which is used to detect the absorbed photons. A circuit diagram is shown in fig. 2.1. An MKID is read out using one readout tone tuned to the resonance frequency of the "dark" resonator, which is not receiving any signal. The readout tone frequency is far below the pair breaking energy, therefore it does not excite the resonator except for the mechanisms described in sec. 2.2.8. The amplitude or the phase transmission of the read out tone is measured at the output of the detector in comparison to the input tone. An example of the resonator response to radiation is shown in fig. 2.2. The resonance frequency shift generates a large shift in phase and the generation of quasiparticles increases the loss which causes a change in

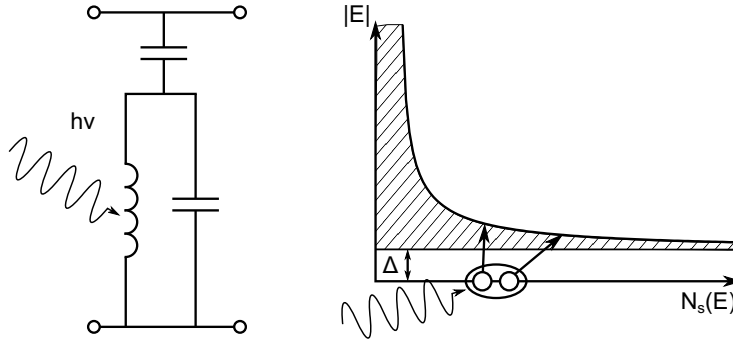


Figure 2.1: Left: The principle schematic of an MKID detector. The superconducting inductor is sensitive to radiation. **Right:** If the superconductor is excited by photons with energy above the gap energy, Cooper pairs break up and create quasi-particles. The kinetic inductance increases. [106]

the depth of the resonance (or amplitude). The signal is split up in real and imaginary parts of the transmission which is done by an IQ mixer (see sec. 3.3.2) that makes it possible to measure both responses at once. The phase readout tracks the actual kinetic inductance, but both readout modes can be used for detecting photons. The details of kinetic inductance, radiation absorption and about the resonator response are discussed in the following sections.

2.1.3 A pair breaking detector

The most simple model for a pair breaking detector like a MKID is a two-state system as illustrated in fig. 2.3 a). The low energy state consists of Cooper pairs, which can be excited by energy input into a higher energetic state. Both states are separated by a gap caused by the minimum energy required to break a cooper pair. This energy is given by the superconductors gap parameter 2Δ which in BCS superconductors is related to the critical temperature T_c , as shown in (2.4). Consider a two level system where the Cooper pair bath is illuminated by a steady stream of photons with photon energy $h\nu > 2\Delta$. This is a suitable assumption for sub-mm astronomy where many photons with low energy are usually received. Quasiparticles are generated at a constant rate

$$R_{\text{gen}} = \eta \frac{P_{\text{ph}}}{2\Delta} \quad (2.6)$$

where P_{ph} is the power of incoming photons and η is the generation efficiency. Quasiparticles recombine after a statistical $1/e$ lifetime τ_{qp} releasing their energy into the phonon bath. The recombination rate depends on the number of existing quasiparticles and the

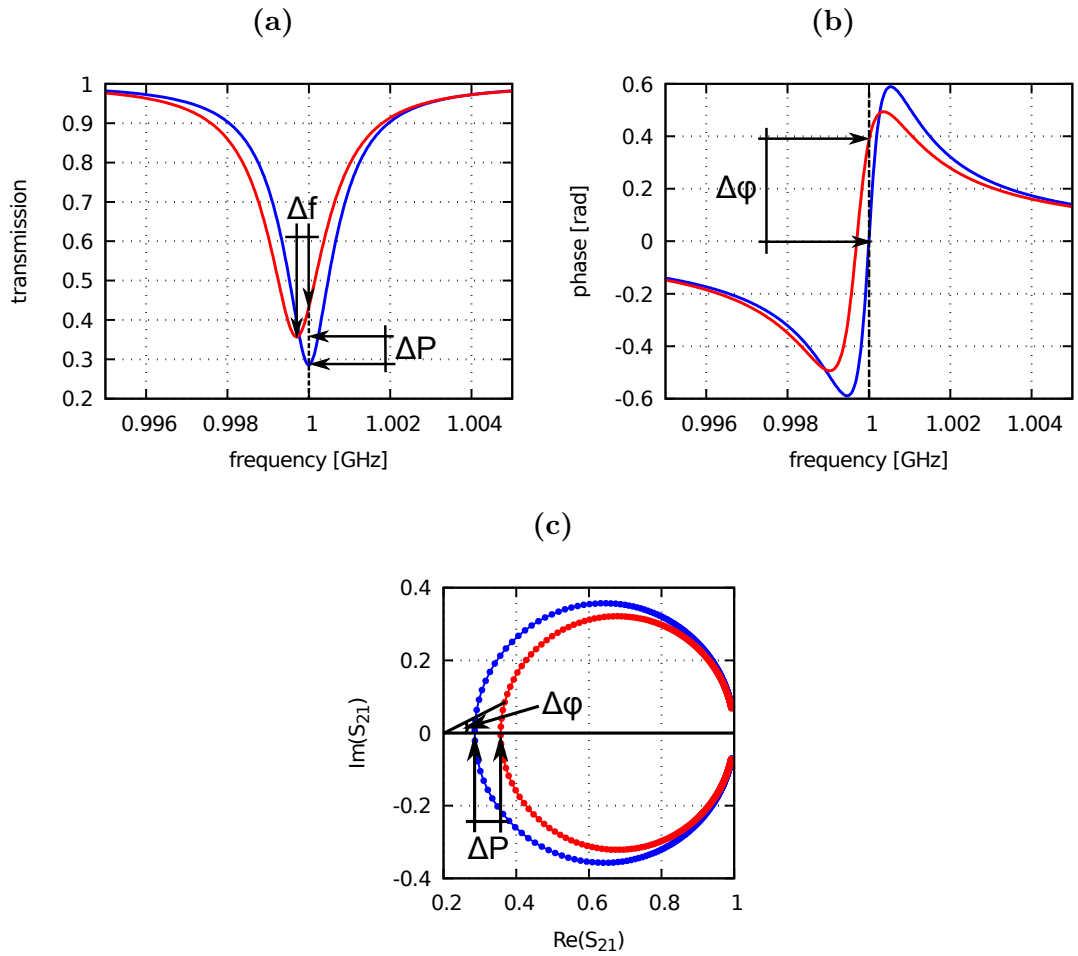


Figure 2.2: The response of an ideal resonator as calculated with (2.18). The blue curves show a hypothetical "dark" resonator and the red curves an excited resonator under radiation. The amount of excitation is exaggerated here for visibility. **(a)** The absolute transmission S_{21} shows that resonance frequency of the excited resonator goes down and the depth of the resonator decreases showing increased loss. **(b)** The phase is the most sensitive readout mechanism as a low shift in resonance frequency results in a large shift in phase when the resonator readout tone stays constant. **(c)** The real and imaginary parts of $|S_{21}|^2$ plotted against each other show the circular shape of the resonances. Here the amplitude and phase readout modes can be differentiated. The phase change results from the change in the angle at the resonance frequency and the amplitude response from the radius change. For small excitations, the phase is proportional to the change in y-direction and the amplitude is proportional to the change in x-direction.

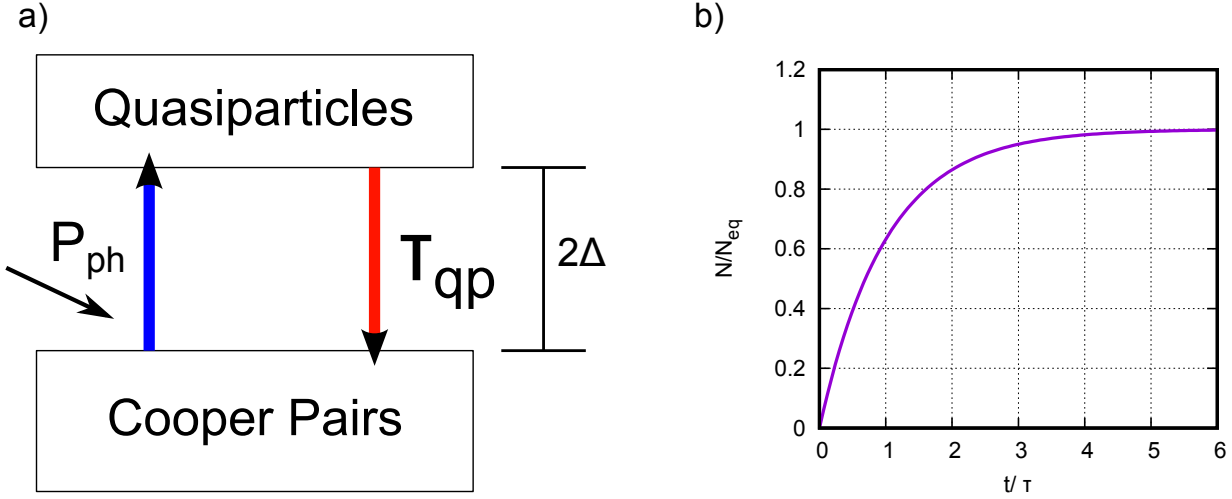


Figure 2.3: (a) Illustration of a pair breaking detector as two-level system. The incoming photons with an energy $h\nu > 2\Delta$ with the power P_{ph} generates quasi-particles. They recombine after a recombination-time τ_{qp} . (b) Dynamic evolution of the quasiparticle number normalized to the equilibrium value plotted against time in quasiparticle lifetimes.

lifetime:

$$R_{\text{rec}} = \frac{N_{\text{qp}}}{\tau_{\text{qp}}} \quad (2.7)$$

After a while an approximate equilibrium state will set in where the amount of generated and recombined quasiparticles is equal. In this state the number of quasiparticles can be determined as:

$$N_{\text{qp}} = \frac{\eta P_{\text{ph}} \tau_{\text{qp}}}{2\Delta} \quad (2.8)$$

The number of quasiparticles is thus directly proportional to the incoming power which is to be detected. The response of the detector is also determined by the quasiparticle lifetime because it shifts the equilibrium distribution towards more quasiparticles and thus a larger change of kinetic inductance.

dynamic behavior The argumentation above considers equilibrium of generation and recombination. Since the generation is linear and the recombination exponential, the dynamic behavior after switching on the photon stream might be of interest to estimate a response time of the detector. For doing that, equations (2.6) and (2.7) can be subtracted to get a differential equation for the time dependent quasiparticle number

$$\frac{dN(t)}{dt} = R_{\text{gen}} - R_{\text{rec}} = \eta \frac{P_{\text{ph}}}{2\Delta_0} - \frac{N_{\text{qp}}}{\tau_{\text{qp}}} \quad (2.9)$$

This equation can be solved easily for the homogeneous case ignoring R_{rec} and then doing a variational approach for the inhomogeneous case. The boundary condition is that $N(t = 0) = 0$. The result is then

$$N(t) = \eta \frac{P_{\text{ph}} \tau_{\text{qp}}}{2\Delta_0} \left(1 - e^{-\frac{t}{\tau_{\text{qp}}}} \right) \quad (2.10)$$

which has the form of limited exponential growth and is shown in fig. 2.3 as normalized plot. The important timescale here is again the quasiparticle lifetime τ_{qp} . After $3\tau_{\text{qp}}$, 95% of the equilibrium value of N is reached, which should be a limit when operating a detector in chopped mode. For aluminum the quasiparticle lifetime is in the range of 1 ms [6] which is one of the longest lifetimes known for MKID application.

2.1.4 Kinetic inductance

To measure the change in quasiparticle density of a superconductor, a macroscopic physical quantity has to be used. In an MKID, the kinetic inductance is that quantity.

Cooper pairs in a superconductor can move collision free over a long distance compared to electrons in normal conductors. When an electric field is applied, they are accelerated in the direction of the field. When the polarity of the external field is changed, the Cooper pairs first need to decelerate before they reverse their velocity and cause a current in the other direction. Macroscopically, there is a phase delay between the applied voltage and the current. In this case, the current comes later than the electric field, which causes the effect of additional inductance by the stored kinetic energy of the cooper pairs. Therefore this effect is called kinetic inductance.

A phenomenological approach to the kinetic inductance can be made by relating the kinetic energy of the cooper pairs to an energy stored in an inductor

$$\frac{1}{2} m_{\text{cp}} v^2 \cdot N_{\text{cp}} = \frac{1}{2} L_k I^2 \quad (2.11)$$

where I is the current, L_k the kinetic inductance, $m_{\text{cp}} = 2m_e$ the mass of a Cooper pair and v the velocity of the charge carriers and N_{cp} the number of charge carriers. The current can be expressed as $I = 2evn_{\text{cp}}A$ with the cooper pair density n_{cp} and the conductor cross sectional area A . The number of charge carriers can also be expressed by the density as $N_{\text{cp}} = n_{\text{cp}}V = n_{\text{cp}}Al$, where l is the length of the hypothetical wire. Equation (2.11) can then be solved for L_k which yields

$$L_k = \frac{m_{\text{cp}} v^2 N}{I^2} = \frac{2m_e v^2 n_{\text{cp}} A l}{4e^2 n_{\text{cp}}^2 A^2} = \frac{m_e l}{2Ae^2 n_c} \quad (2.12)$$

The kinetic inductance is inverse proportional to the density of Cooper pairs. By measuring changes in kinetic inductance, changes in the quasiparticle density can be detected. When the Cooper pair density decreases, less charge carriers have to transport more current and thus have to increase their velocity in order to do so. This increases the kinetic inductance decreases the resonance frequency of the resonator.

2.1.5 Radiation absorption in a superconductor

The process of radiation absorption in a superconductor resulting in generation of quasiparticles was analyzed in [59] for the case of a photon with high energy in the range of keV. This photon creates a primary photoelectron which deposits its energy via secondary electrons and phonons which then at the end of the cascade create quasiparticle excitations. The conversion efficiency of photon energy to number of quasiparticles is determined as $\eta \approx 0.57$, which is a value widely used for MKID detector analysis. However, in most MKID usage cases the energy is not deposited by one high energy photon but by a stream of photons with energy of a few times the gap energy 2Δ . This case has been investigated experimentally by de Visser et al. in [28] with a wideband tantalum MKID. At low photon energies just above the gap energy 2Δ , one photon can exactly create two quasiparticles. As the energy increases the efficiency decreases as quasiparticles with higher excitation energy are created. That the mechanics are not simple is shown by the fact that at a photon energy of 4Δ the generation efficiency has a minimum. Slightly above the gap energy the efficiency goes up to nearly 1 before it stabilizes at about 60 % at a few gap energies. This value will also be suitable for our detector which operates around 350 GHz and uses aluminum as absorber, because 350 GHz is around 5 times the aluminum gap energy.

2.2 Properties of the superconducting resonator

MKIDs are superconducting resonators patterned into a planar thin film and coupled to some sort of readout line. In the following, the transmission of the resonator is discussed in the impedance picture.

2.2.1 Resonance frequency and quality factor of the superconducting resonator

The schematic used to analyze the transmission of a MKID resonator is shown in fig. 2.4. A loaded parallel LC resonator is coupled to the readout line with a small capacitor C_c . The readout line is terminated with its characteristic impedance Z_0 . The inductor $L =$

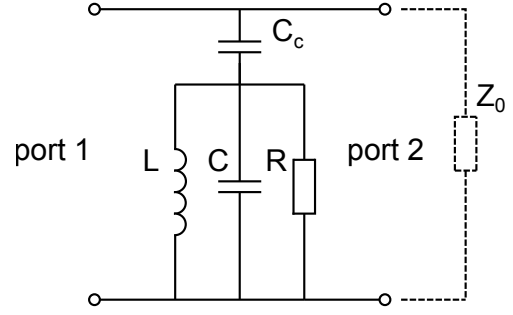


Figure 2.4: The schematic of an MKID resonator coupled to the readout line using a capacitor C_c .

$L_k + L_g$ is (partly) made of superconducting material which reacts to incoming radiation by generating quasiparticles and changing L_k . L_g is the fixed part of the inductance caused by its geometry. The kinetic inductance fraction α is introduced to specify the part of the kinetic inductance in the total inductance as

$$\alpha = \frac{L_k}{L_g + L_k} \quad (2.13)$$

For the LC resonator, the derivation of the standard damped harmonic oscillator is used. This yields the results for the unloaded resonance frequency $\omega_0 = \sqrt{\frac{1}{LC}}$. The resistance R and the connection to the readout line, which are basically in parallel as seen from the resonator, dampen the oscillations (see fig. 2.4). This damping is combined in the damping constant δ which is defined in the derivation as $\delta = \frac{1}{2R_{\text{eff}}C}$ where $R_{\text{eff}} = R + |Z_c|$ and $Z_c = Z_0 - i/(\omega C_c)$ is the impedance of the coupling capacity and the readout line in series. The loaded resonance frequency is given as $\omega_L = \sqrt{\omega_0^2 - 2\delta^2}$. The damping constant δ is roughly half the full width of the resonance at half maximum, thus $\text{FWHM} \approx 2\delta$. The quality factor of the resonator can be defined as

$$Q = \frac{\omega_0}{\text{FWHM}} \approx \frac{\omega_0}{2\delta} = R\sqrt{\frac{C}{L}} \quad (2.14)$$

The determination of Q using the full width at half maximum can be easily done graphically, but is only possible for symmetric resonances, as will be explained in sec. 2.2.3. As mentioned above, the damping constant δ has contributions from the internal loss of the resonator and from the coupling to the readout line which can be changed by design. Because of the different nature of the loss mechanisms, it is useful to differentiate between them by assigning different quality factors. The internal quality factor Q_i accounts for losses caused by the resonator only and the coupling quality factor Q_c for external losses. Because the quality factors are proportional to the resistances as shown in (2.14) and the

resistances are connected in parallel to the resonator, the quality factors add up as

$$\frac{1}{Q} = \frac{1}{Q_c} + \frac{1}{Q_i} \quad (2.15)$$

where Q is the measured effective quality factor of the resonator.

2.2.2 Transmission of the ideal resonator

The resonator circuit shown in fig. 2.4 represents one single resonator as it is measured in the MKID setup. To measure its transmission, a probe signal is sent into port 1 and the response is measured at port 2. The impedance seen from port 1 of the resonator is

$$Z_{\text{coup}} = \left(\frac{1}{i\omega L} + i\omega C + \frac{1}{R} \right)^{-1} + \frac{1}{i\omega C_c} \quad (2.16)$$

This impedance can be used to calculate the scattering matrix parameter S_{21} which states the voltage measured at port 2 when port 1 is excited, while all other ports are terminated with their characteristic impedance (which is automatically given in a two-port network). S_{21} is calculated using an ABCD matrix approach which gives for this case [81]

$$S_{21}(\omega) = \frac{1}{1 + \frac{Z_0}{2Z_{\text{coup}}(\omega)}} \quad (2.17)$$

inserting (2.16) and following the approximations given in [106], the transmission for the ideal superconducting resonator is

$$S_{21}(\omega) = 1 - \frac{Q}{Q_e} \frac{1}{1 + 2iQ \frac{\delta\omega}{\omega_0}} \quad (2.18)$$

where $\frac{\delta\omega}{\omega_0} = \frac{\omega - \omega_0}{\omega_0}$ is the fractional frequency shift, Q the absolute quality factor of the resonance and Q_e the external quality factor. S_{21} is a complex transmission which contains amplitude and phase information. The amplitude and phase are determined as

$$|S_{21}| = \sqrt{S_{21} \cdot S_{21}^*} \quad (2.19a)$$

$$\phi = \arctan \left(\frac{\Re S_{21}}{\Im S_{21}} \right) \quad (2.19b)$$

where S_{21}^* denotes the complex conjugate and \Re and \Im the real and imaginary part of S_{21} . Plots of (2.18) are shown in fig. 2.2.

2.2.3 Resonator model including mismatch

Since the superconducting resonator always has to be connected to an external circuit to be measured, there is a good chance that there is impedance mismatch somewhere in the system. This usually shows during measurement as an asymmetric transmission $|S_{21}|^2$ of the resonance which can not be fitted with the simple model (2.18). The model by Khalil et al. [55] includes a mismatch on the readout circuitry by introducing a complex coupling quality factor

$$\hat{Q}_e^{-1} = \left| \hat{Q}_e^{-1} \right| e^{i\phi} \quad (2.20)$$

where the phase part ϕ accounts for the mismatch. The complex transmission S_{21} of the resonator with mismatch is then given as:

$$S_{21} = (1 + \hat{\epsilon}) \left(1 - \frac{Q \hat{Q}_e^{-1}}{1 + 2iQ \frac{\delta\omega}{\omega_0}} \right) \quad (2.21)$$

where $\hat{\epsilon}$ is a small complex parameter from the derivation which will be neglected in the following, Q is the total quality factor of the resonance, Q_e is the coupling quality factor (sticking to Khalil's notation) and $\delta\omega/\omega_0$ is the fractional frequency shift.

An additional problem is, that those asymmetric resonances give an incorrect result for the internal quality factor, if it is determined by the normal resonator model or geometrically. The internal quality factor respecting the mismatch in form of the complex coupling quality factor Q_e can then be calculated from

$$\frac{1}{Q_e} = \Re \left(\left| \hat{Q}_e^{-1} \right| e^{i\phi} \right) \quad (2.22a)$$

$$\frac{1}{Q_i} = \frac{1}{Q} - \frac{1}{Q_e} \quad (2.22b)$$

The resonator model introduced in this section will be used to fit all resonance features measured in chapters 5, 6 and Appendix A. The extracted resonance frequencies and quality factors are the basis for all further analysis.

2.2.4 Multiplexing

One significant advantage of MKID in comparison to other direct detectors is their intrinsic possibility of multiplexing a number of detectors in the readout frequency domain. Since these detectors have to be cooled down to temperatures of around 100 mK, the thermal loading on the detector and the cooling system has to be minimal. Without any scheme of multiplexing, it would be necessary to have a single wire for each detector. A large array

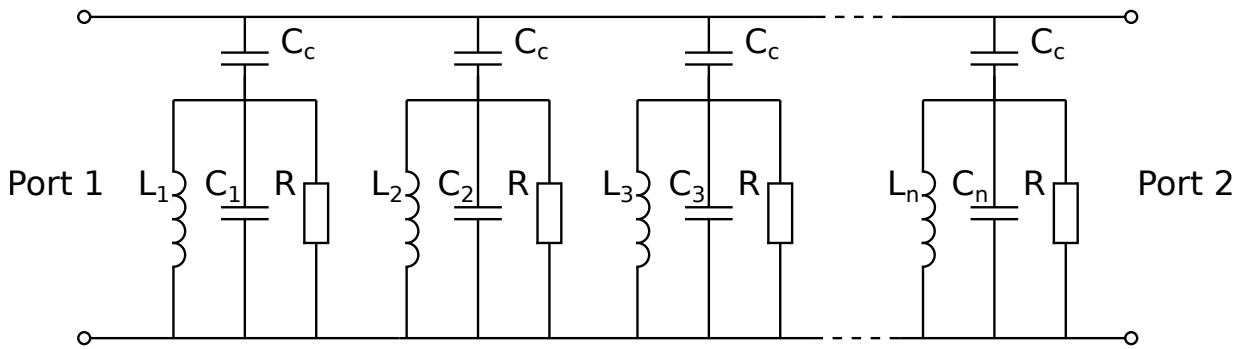


Figure 2.5: The schematic of a multiplexed MKID. Each resonator attached to the readout line is tuned to a different resonance frequency. If pixel n is excited, the n -th resonance feature in the spectrum responds.

of thousands of pixels would require thousands of wires connected to the low temperature stage of a cooling machine, which would conduct heat and limit the cryogenic hold time or even make achieving the necessary temperatures impossible. Besides, the pure mechanical complications of managing so many connections would be a challenge. A MKID is a superconducting resonator tuned to a certain resonance frequency. It is read out using two coax cables, one for the input signal and one for the return signal. For an MKID array, many resonators, each tuned to a slightly different resonance frequency can be connected to the same readout line. The readout signal comb is then generated and analyzed by a digital system based on fast analog to digital and digital to analog converters and the amplitude and phase responses are calculated in a FPGA [18, 69]. That way, hundreds of resonators can be connected to a single readout line, as indicated in the schematic in fig. 2.5. The practical concept of multiplexing is shown in chapter 6, where a 25 pixel detector is measured. The NIKA 2 instrument uses 6 readout lines for 1140 pixels [2]. Limitations are the available digital bandwidth and the quality factor of the resonators, determining how close they can be packed in frequency. This directly relates to the fabrication tolerances and repeatability which determine the random scatter in resonance frequency. Taking these factors into account, the separation in frequency space has to be designed such, that the probability of colliding resonances due to random effects is limited.

2.2.5 Calculating the complex conductivity

The resonance frequency and the quality factor of a superconducting resonator change with temperature, because thermal energy creates quasiparticles which have the same effect on the complex conductivity as quasiparticles created by photons [40]. The electrodynamics of a superconductor were first derived by Mattis and Bardeen [64]. Their theory makes

it possible to calculate the complex conductivity $\sigma = \sigma_1 + i\sigma_2$ as a function of temperature and frequency. Input parameters are the superconducting gap parameter Δ and the normal state conductivity σ_n which can all be determined at DC. σ_1 represents the Ohmic conductance limiting the quality factor and σ_2 the reactive part of the conductivity which represents the change in resonance frequency or phase. A problem with the Mattis-Bardeen theory is that it postulates a divergence of the quality factor as the device temperature approaches zero. This is contradictory to observations, as even in the probably best shielded setups like [9], always a saturation in quality factor below a certain temperature is measured. To accommodate for that, the extended Mattis-Bardeen theory introduces a complex gap parameter $\Delta = \Delta_1 + i\Delta_2$ [74, 75]. The complex part effectively limits the quality factor. The approximate expression used to calculate the complex conductivity assumes that $T \ll T_c$ and $\hbar\omega \ll 2\Delta_1$ for a thermal quasiparticle distribution. It gives

$$\frac{\sigma_1(T)}{\sigma_n} \cong \frac{4\Delta_1}{\hbar\omega} e^{\frac{-\Delta_1}{k_B T}} \sinh\left(\frac{\hbar\omega}{2k_B T}\right) K_0\left(\frac{\hbar\omega}{2k_B T}\right) + \frac{\pi\Delta_2}{\hbar\omega} \left[1 + \frac{2\Delta_1}{k_B T} e^{\frac{-\Delta_1}{k_B T}} e^{\frac{-\hbar\omega}{k_B T}} I_0\left(\frac{\hbar\omega}{2k_B T}\right)\right] \quad (2.23a)$$

$$\frac{\sigma_2(T)}{\sigma_n} \cong \frac{\pi\Delta_1}{\hbar\omega} \left[1 - 2e^{-\frac{\Delta_1}{k_B T}} e^{-\frac{\hbar\omega}{2k_B T}} I_0\left(\frac{\hbar\omega}{2k_B T}\right)\right] \quad (2.23b)$$

where I_0 and K_0 are the zeroth order modified Bessel functions of the first and second type. ω is the frequency at which the conductivities are calculated and T the corresponding temperature.

From the complex conductivities, the change in resonance frequency and internal quality factor Q_i with temperature can be calculated as

$$\frac{f - f_0}{f_0} = \frac{\delta f}{f_0} = -\frac{1}{2}\alpha \frac{\sigma_2(T) - \sigma_2(0)}{\sigma_2(0)} \quad (2.24)$$

$$Q_i = \frac{1}{\alpha} \frac{\sigma_2(T)}{\sigma_1(T)} \quad (2.25)$$

The kinetic inductance fraction α introduced in (2.13) scales both parameters.

2.2.6 Surface impedance

The surface impedance determines the influence of the material layer on the high-frequency electrodynamics. Following the argumentation in [106], the analytical calculation of the surface impedance from the conductance calculated in 2.2.5 is only possible in limiting cases.

The local limit describes the case where the electron mean free path is short in comparison to the change of the electromagnetic field. In this case the field can be locally treated as constant. The penetration depth for thick films in the local limit is given for superconductors as

$$\lambda_{\text{local}} \approx 105 \text{ nm} \sqrt{\frac{\rho_n}{1 \mu\Omega \text{ cm}} \frac{1 \text{ K}}{T_c}} \quad (2.26)$$

where ρ_n is the normal state conductivity and T_c the transition temperature of the superconductor. The surface impedance can in this case be calculated as

$$Z_s(\omega, T) = Z_s(\omega, 0) \left[1 + \frac{i[\sigma_1(\omega, T) - i(\sigma_2(\omega, T) - \sigma_2(\omega, 0))]}{\sigma_2(\omega, 0)} \right]^{-x} \quad (2.27)$$

where $x = 1/2$ in the local limit. $Z_s(\omega, 0)$ is the surface impedance at zero temperature and is given as

$$Z_s(\omega, 0) = i\mu_0\omega\lambda = i\omega L_s \quad (2.28)$$

where L_s is defined as surface inductance here, which is a material parameter needed for electromagnetic simulation software. In thick superconductors, the electron mean free path can become considerably longer than the London penetration depth. This limit is called the extreme anomalous limit. The surface impedance can be calculated from eq. (2.27) with $x = 1/3$. The penetration depth in this case is given as

$$\lambda_{\text{e.a.}} = \lambda_{\text{local}} \left[\frac{\sqrt{3}l}{2\pi\lambda_{\text{local}}} \right]^{-1/3} \quad (2.29)$$

In the case relevant for this thesis, the film thickness is smaller than the respective penetration depth. In this case the eq. 2.27 with $x = 1/3$ is used to calculate the surface impedance. The penetration depth is modified by the thickness as

$$\lambda_{\text{thin}} = \frac{\lambda_{\text{local}}^2}{t} \quad (2.30)$$

where t is the thickness of the layer.

2.2.7 Fitting material parameters

The equations (2.24) and (2.25) will be fitted to own measurement data in 6.3 to get the values for α , Δ_1 and Δ_2 . The problem that occurs during the fitting procedure is that the three parameters are not entirely independent but correlated to a certain extend. The influence of the fitting parameters Δ_1 , Δ_2 and α is illustrated in fig. 2.6. Qualitatively

the quasiparticle binding energy, Δ_1 influences when the quality factor and frequency shift curves start to fall as it determines the onset of quasiparticle generation. Δ_2 sets the saturation value for Q_i , the measurement of $(f - f_0)/f_0$ does not depend on Δ_2 . α scales both parameters. Small changes in any parameter can however be mimicked by changing one of the other two parameters, as a slight decrease in Δ_1 can have the same effect as increasing α . The behaviour of (2.25) at low temperatures delivers the relation

$$\lim_{T \rightarrow 0} Q_i = \frac{\Delta_1}{\alpha \Delta_2} \quad (2.31)$$

which readily connects the kinetic inductance fraction to the complex gap parameter. The internal quality factor saturates at low temperatures and can be very easily determined from measurements. The detailed fitting procedure is described together with the analysis of the measurements in sec. 6.3.

2.2.8 The effect of high readout power

As mentioned before, the readout signal is usually in the range below 10 GHz. Therefore a single readout photon does not have enough energy to break a cooper pair. At the readout frequency, the superconductor is almost lossless and quasiparticles can not be created. In practice, it is observed that at high readout signal power the resonance shape starts to change and a discontinuity arises. This effect is shown in fig. 2.7. The description of this effect assumes a non-linear dependence of the kinetic inductance on the readout power which causes a shift in resonance frequencies. The hysteretic behavior of the resonator is explained by an elevated electron temperature caused by the readout signal [27]. Other sources develop a model including electro-thermal feedback processes [95, 96]. The microscopic explanations are usually not part of the models, but heating due to residual quasiparticles or multi-photon effects are candidates. The non-linear effects of the material under high power can be exploited to build devices like parametric oscillators or amplifiers [17, 99]. Some results of own measurements of a NbTiN resonator at high readout power are shown in Appendix A and in fig. 2.7

2.3 Noise sources in a kinetic inductance detector

Different fundamental and external effects cause noise in direct detectors. How the detector performance is specified and the noise sources which are most dominant is explained below.

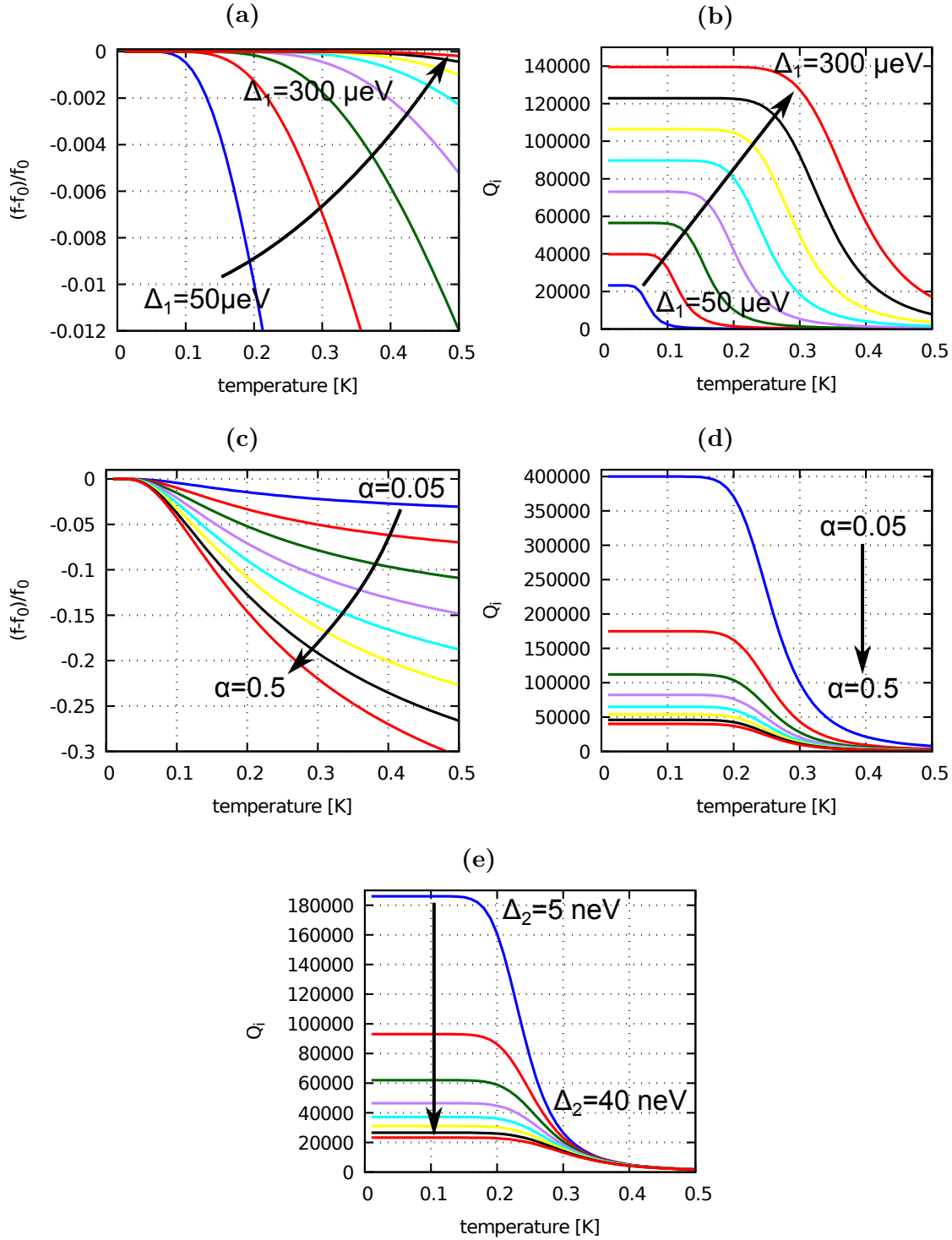


Figure 2.6: Calculation of the temperature dependence of the internal quality factor Q_i and the fractional frequency shift $(f - f_0)/f_0$ with using (2.23) in (2.24) and (2.25). The parameters are varied in equal steps. The constant parameters are: $\Delta_1 = 0.2 \text{ meV}$, $\Delta_2 = 10 \text{ neV}$, frequency $f = 1 \text{ GHz}$, $\alpha = 0.215$. (a) and (b) Variation of Δ_1 mainly changes the bending point on temperature. (c) and (d) The kinetic inductance fraction α merely scales in y-direction. For small changes, a decrease in Δ_1 can be simulated by an increase in α . (e) The loss parameter is obviously correlated with α shown in (d) for the saturation regime at low temperatures.

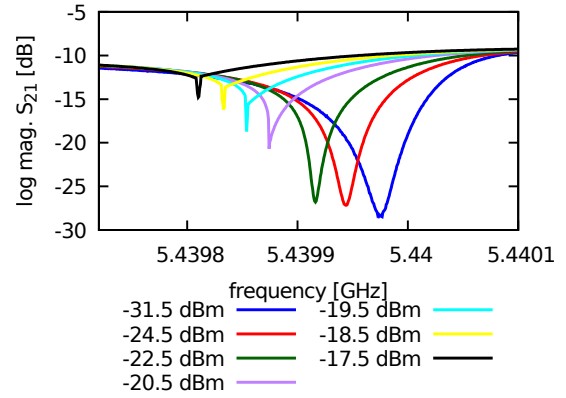


Figure 2.7: Measurement of a NbTiN resonator at high readout powers. The frequency is swept from left to right.

2.3.1 Power spectral density

The power spectral density $S_{XX}(f)$ of a time series signal $x(t)$ describes how the power of the signal is distributed with frequency. For stationary noise processes, the power spectral density can be calculated using the Wiener-Khinchin theorem. It states that the power spectral density is the Fourier transform of the autocorrelation function

$$r_{xx}(\tau) = \int_{-\infty}^{\infty} x(t + \tau)x^*(t)dt \quad (2.32)$$

which can be used to calculate the power spectral density. x^* is the complex conjugate of the time signal. The power spectral density is then given as

$$S_{XX}(\omega) = \int_{-\infty}^{\infty} r_{xx}(\tau)e^{-i\omega\tau}d\tau \quad (2.33)$$

This approach is necessary in theory because the Fourier transform of the time series $x(t)$ does not always exist for noise spectra without bandwidth limits. In real measurement of a finite number of discrete samples, a bandwidth limit always exists. For the calculation of the power spectra of the measured digitized time series, a discrete Fourier transform is used as described in sec. 6.5.3.

2.3.2 Noise Equivalent Power (NEP)

The performance of a direct detector like the MKID is measured in a quantity called Noise Equivalent Power (NEP). The NEP gives the amount of signal power at the input of the detector, that produces a signal to noise ratio of one at the output within bandwidth of 1 Hz, or, after an integration time of 1/2s. Consequently, a sensitive detector has to have a low NEP. Its definition allows to calculate the signal to noise ratio of a detector with

given NEP after an integration time T_{int} with an input signal power P_{sig} [84]:

$$\frac{S}{N} = \frac{P_{\text{sig}} (2T_{\text{int}})^{1/2}}{\text{NEP}} \quad (2.34)$$

The NEP is usually stated as a function of detector readout (chopping) frequency. It can be composed of the noise spectral density measured in Response/ $\sqrt{\text{Hz}}$ and the detectors responsivity measured in Response/ W . The 'Response' is the type of signal at the output of the detector. It usually is something like voltage or current, and is for MKID amplitude or phase, often encoded as a voltage. Another definition of the NEP can thus be stated as:

$$\text{NEP}(\nu) = S_R(\nu) \cdot \left(\frac{dR}{dP_{\text{sig}}} \right)^{-1} \quad (2.35)$$

Noise spectral density S_R and the responsivity dR/dP_{sig} are usually dependent on the readout frequency ν . The dynamic time constant limiting the speed of MKID is the quasiparticle recombination time. Therefore, the responsivity has the shape of a Lorentz-curve with time constant τ_{qp} . For many practical detectors, the input signal is thus chopped at the readout frequency of minimal NEP and the output of the detector is bandpass filtered at the chopping frequency to limit the electronic bandwidth. Often the NEP of a detector consists of contributions from a number of different effects. In case of MKID detectors, the fundamental effects are photon noise and generation-recombination noise. External effects are readout system noise and noise from the dielectric (TLS noise). Those effects are described in detail below. The combined NEP can be obtained by adding the individual components as absolutes:

$$\text{NEP} = \sqrt{\text{NEP}_{\text{GR}}^2 + \text{NEP}_{\text{phot}}^2 + \dots + \text{NEP}_{\text{X}}^2} \quad (2.36)$$

2.3.3 Generation-recombination noise

One of the two fundamental noise limits of the MKID is given by random generation and recombination of quasiparticles in the superconducting absorber material. This effect had been studied in 2001 by Wilson and Prober [102] in a superconducting "box" device. They used an aluminum strip separated by a tunnel junction and contacted using tantalum leads to trap the quasiparticles in the aluminum. They derived the frequency spectrum of the fluctuations of quasiparticles, which is a Lorentz-curve depending on the quasiparticle recombination time τ_{qp} . The spectral density of the fluctuations is given as:

$$S_N(\omega) = \frac{4N_0\tau_{\text{qp}}}{1 + (\omega\tau_{\text{qp}})^2} \quad (2.37)$$

with the single spin electron density N_0 and the angular frequency ω . This was verified experimentally at a temperature of 210 mK in the "box" device by examining the fluctuations of the tunneling current. The generation recombination noise was studied in a superconducting resonator by de Visser et al. [25, 26] with an aluminum transmission line resonator. The quasiparticle fluctuations can not be directly measured in a resonator, but their influence on the amplitude or phase response. The amplitude A or phase ϕ power spectrum is then given as product of eq. (2.37) with the change of amplitude/phase with quasiparticle number and a roll-off due to the resonator response time $\tau_{\text{res}} = \frac{Q}{\pi f_0}$ [25]:

$$S_A(\omega) = S_N \frac{(dA/dN_{\text{qp}})^2}{1 + \omega^2 \tau_{\text{res}}^2} \quad (2.38)$$

$$S_\phi(\omega) = S_N \frac{(d\phi/dN_{\text{qp}})^2}{1 + \omega^2 \tau_{\text{res}}^2} \quad (2.39)$$

The amplitude roll-off was measured over a temperature range from 100 mK to 360 mK, where the limiting frequency increases with temperature as the quasiparticle recombination time decreases.

The NEP of the generation-recombination noise can be stated as [105]

$$\text{NEP}_{\text{GR}} = \frac{2\Delta}{\eta_{\text{qp}}} \sqrt{\frac{N_{\text{qp}}}{\tau_{\text{qp}}}} \quad (2.40)$$

where N_{qp} is the remaining quasiparticle number in the detector volume, τ_{qp} the quasiparticle recombination time, η_{qp} the generation efficiency and Δ the gap parameter. In case the quasiparticle generation is governed by the photon arrival, the NEP becomes [105]

$$\text{NEP}_{\text{GR}} = \sqrt{\frac{2\Delta P}{\eta_{\text{qp}}}} \quad (2.41)$$

where P is the incoming photon stream power.

2.3.4 Photon noise

The nature of photon noise is introduced by R.W.Boyd as:

The sensitivity of a radiation detector is limited most fundamentally by the randomness of photon arrival times at the detector, and a detector whose sensitivity is limited predominantly by this effect is said to be photon-noise-limited. [19]

Real detectors are exposed to thermal background radiation which is always present in addition to the signal. The temperature of the background depends on the application of

the detector. In astronomy, one usually has to differentiate roughly between ground-based telescopes which have to observe through a hot atmosphere and space telescopes which are limited by the cosmic microwave background only. For ground based observatories the atmospheric transmission defines the background temperature, which depends on the frequency, the weather and the location. The requirement for a photon-noise-limited or background-limited detector for space application is therefore much lower noise. The derivation for the NEP caused by photon events gives [105]

$$\text{NEP}_{\text{photon}} = \sqrt{2Ph\nu(1 + \bar{n}_\nu \eta)} \quad (2.42)$$

where P is the incoming power, h is the Planck constant, η is the optical absorption efficiency and \bar{n}_ν is the photon occupancy, the mean number of photons per mode given by the Bose-Einstein statistics:

$$\bar{n}_\nu = \frac{1}{e^{\frac{h\nu}{k_B T}} - 1} \quad (2.43)$$

The term $\bar{n}_\nu \eta$ in (2.42) corrects for photon bunching causing excess noise in addition to the shot noise caused by individual photons [19]. This term can be neglected when $h\nu \gg k_B T$, but at a frequency of 350 GHz and at a temperature of 25 K, the photon occupancy reaches unity and the factor plays a small role in the detectors measured in this thesis. In practice, the photon-noise-limited criterion is, that the minimum NEP of a detector is lower than the NEP measured under the optical loading either for space-borne or ground based observation conditions [50, 52]. It is specified as a background limited detector at a certain limiting optical power. The actual background limited NEP is always linked to the telescope used, its efficiency and the atmospheric conditions. The argumentation in [12] calculates the NEP limited by the atmosphere as

$$\text{NEP}^2 = \int \frac{4\epsilon(\nu)}{\eta_{\text{MB}}^2 \alpha (1 - \epsilon(\nu))^2} k_B T h\nu \left[1 + \epsilon(\nu) \alpha \frac{k_B T}{h\nu} \right] d\nu \quad (2.44)$$

where $\epsilon(\nu)$ is the frequency dependent atmospheric emissivity, η_{MB} is the main beam efficiency of the telescope, α is the optical efficiency and T the blackbody temperature of the atmosphere. The integration goes over the frequency band which is received by the detector. An example for a 350 GHz for typical conditions on Mauna Kea yields a background NEP of $7.6 \times 10^{-16} \text{ W}/\sqrt{\text{Hz}}$ [12]. Generally, the background limit goes down if the input bandwidth decreases. For spectrometer applications which use direct detectors therefore very sensitive detectors are required.

2.3.5 Two-level systems

An excess phase noise whose power spectral density falls with frequency as $f^{-1/2}$ is described in [41]. It is attributed to a random distribution of two-level systems (TLS) which are present in amorphous dielectrics. The TLS react to the electric field, therefore their contribution is strongest in the capacitive sections of a transmission line resonator or the capacitor in a lumped element resonator. Even on crystalline silicon substrates, an oxide layer on the surface can be a source of TLS noise. The effect of amorphous dielectrics on the frequency noise of resonators is explicitly shown in [7], where NbTiN resonators are covered with various thicknesses of silicon oxides. The influence of TLS can be observed in the frequency noise, but also in the frequency shift vs. temperature measurements. At low temperatures, the TLS add an additional component ϵ_{TLS} to the effective dielectric constant. ϵ_{TLS} increases with temperature, therefore the resonance frequency of a superconducting resonator influenced by TLS first increases with temperature, before it decreases as predicted by the Mattis-Bardeen theory in (2.24). The dielectric constant changes as [7]

$$\frac{\delta\epsilon}{\epsilon} = -\frac{2p^2P}{\epsilon} \ln\left(\frac{T}{T_0}\right) \quad (2.45)$$

where p is the dipole moment of the TLS, P the density of states of the TLS and T_0 a reference temperature. The fractional shift in ϵ can in first order be translated to a shift in resonance frequency as

$$\frac{\delta f_0}{f_0} = \frac{\alpha}{2} \frac{\delta\sigma_2}{\sigma_2} - \frac{F}{2} \frac{\delta\epsilon}{\epsilon} \quad (2.46)$$

where the first term is caused by the quasiparticles and the second term is due to TLS. F is a factor which takes into account the active area of the resonator which is in contact with TLS. The effect will be shown and corrected for in measurements in sec. 6.3.2.

The contribution of TLS noise can be reduced by increasing the gap width of capacitive regions in the resonator to reduce the electric field strength which excites the TLS [88] and by special etching to remove substrate in regions with high electric field and treating of the surface to remove oxide layers [8]. Single crystal dielectric capacitors with applicable surface treatment have also been used [101]. A variation of my lumped element MKID design presented in chapter 4 has an interdigital capacitor where the substrate is completely etched away between the capacitor fingers.

2.3.6 Kondo effect

While not exactly a noise source, the Kondo effect is considered as an alternative explanation for the observed saturation of the quality factor at low temperatures and the

non-monotonic frequency shift described in (2.46) in [74]. Generally, the Kondo effect [57] describes the resistance of metals which include a low concentration of magnetic impurities.

Noguchi et al. [74] observed not just the non-monotonic frequency shift, but also an increase of the internal quality factor Q_i when the temperature is increased from about 100 mK till the quasiparticle generation starts and the quality factor goes down. This effect is not explained by TLS (sec. 2.3.5). From the Kondo effect, an expression for the internal quality factor can be derived as in [74]

$$\frac{1}{Q_i} = \alpha \frac{\sigma_1(T)}{\sigma_2(T)} - b \ln \left(\frac{T}{T_k} \right) \quad (2.47)$$

where T_k is the Kondo-temperature of the quasiparticles and b is a constant. The first term is the normal Mattis-Bardeen part. The resonance frequency can be expressed as

$$\frac{\delta f}{f_0} = \frac{1}{2} \left\{ \alpha \frac{(\sigma_2(T) - \sigma_2(0))}{\sigma_2(0)} - \omega_r \tau \left(\frac{1}{Q_i}(T) - \frac{1}{Q_i}(0) \right) \right\} \quad (2.48)$$

where $1/Q_i$ is calculated from (2.47) and therefore also gives a logarithmic dependence on temperature as seen for TLS in (2.46).

2.3.7 Readout system noise

The discussion of the readout system noise is fundamentally different as this noise does not occur in the detector device itself but is generated on the readout line behind the device. Noise generated in front of the device which may come down the readout line is neglected here because the first element in front of the device is a large attenuator at a temperature of 0.5 K, which defines the background noise on the readout line. The following discussion follows the argumentation in [10].

The noise of the individual high frequency components on the readout line is specified by their noise temperatures, which denotes the temperature a black body radiator at the input of the component would have to generate the noise of the component itself on its output. The motivation for this measure is, that in the Raileigh-Jeans limit $h\nu \ll k_B T$, the power output to a matched load of a resistor is immediately given by $k_B T$. The noise temperature of an attenuator is given as

$$T_N = T_{\text{att}} \frac{1 - G}{G} \quad (2.49)$$

where T_{att} is the physical temperature of the attenuator and $G < 1$ is its gain. The noise temperature for components like low noise amplifiers is usually given by the manufacturer.

If now several components are switched in series, the noise temperature of the whole system with N components is given as

$$T_{\text{sys}} = T_1 + \frac{T_2}{G_1} + \frac{T_3}{G_1 G_2} + \dots + \frac{T_N}{G_1 G_2 \dots G_{N-1}} \quad (2.50)$$

where T_i is the noise temperature of the i -th component and G_i the respective gain. From this equation it immediately becomes clear that in a chain where the first element is a high gain amplifier, the rest of the system hardly contributes to the system noise, as every following factor is divided by the gain of the first amplifier. If the first element has $G < 1$, the opposite effect happens and the noise contribution of the following components increased.

Now consider a readout system with a noise temperature T_{sys} determined using (2.50). Since the noise source is in this formulation expected to be a resistor, the noise power spectral density is expected to be flat within the relevant bandwidth of the system. The noise power spectral density generated at the detector which equals T_{sys} would then be

$$S^{\text{SSB}} = k_B T_{\text{sys}} \quad (2.51)$$

where S^{SSB} is the single sideband noise spectral density of the system in units of W Hz^{-1} . Because the influence of the system noise temperature on the amplitude and phase noise is crucial, the detection of the signal using homodyne detection and an in-phase-quadrature (IQ) mixer has to be taken into account (see sec. 3.3.2). In the IQ mixer, the noise spectrum is converted down to a frequency range between DC and about 1 MHz, split in two channels I and Q. The noise which is below the readout tone frequency would be converted to negative frequencies which means that it is swapped in the upper sideband, effectively doubling the noise. The split in two channels I and Q again divides the noise contribution by 2. Last, the noise is normalized to the readout signal power at the device to get rid of all the unknown factors in the processing chain. The relative, double sideband noise spectral density is then given as

$$S_{\text{I,Q}}^{\text{DSB,rel}} = \frac{k_B T_{\text{sys}}}{P_{\text{ro}}} \quad (2.52)$$

where P_{ro} is the readout power level at the device. From this relative noise in I and Q direction, the amplitude and phase noise relative to the carrier signal can be calculated from the radius in the I/Q plane r (see sec. 6.5.2) using the procedures explained in sec. 6.5.3 and sec. 6.5.4. Some additional normalization is necessary because the IQ mixer converts the incoming amplitude to voltages which are amplified and filtered before

digitization. The analysis of the readout noise of the setup developed within this thesis and a comparison to a measurement is shown in sec. 3.3.7.

2.3.8 A full MKID sensitivity model

The estimation of the real performance of the detector does not immediately emerge from the noise sources mentioned above. The fundamental noise sources like photon and generation and recombination noise do not immediately depend on design choices of the detector. In combination with the external noise sources from readout and TLS noise, the detector design decisions like the volume or the quality factor play a role. A noise analysis based on the disturbance of the input power to the detector is developed in [106] and reaches quite some level of complexity. For frequency or phase readout, the noise equivalent power is given as

$$\text{NEP}_{\text{freq}}^2 = \text{NEP}_{\text{phot}}^2 + \text{NEP}_{\text{GR}}^2 + \frac{8N_{\text{qp}}^2 \Delta_0^2}{\beta^2 \eta_o^2 \chi_c \chi_{\text{qp}}^2 \tau_{\text{qp}}^2} \frac{k_B T_a}{P_a} + \frac{8N_{\text{qp}}^2 \Delta_0^2 Q_i^2}{\beta^2 \eta_o^2 \chi_{\text{qp}}^2 \tau_{\text{qp}}^2} S_{\text{TLS}}. \quad (2.53)$$

In this equation, the first two terms are the photon NEP defined in eq. (2.42) and the generation-recombination NEP described in sec. 2.3.3. The third term shows the influence of the readout noise in terms of the amplifier noise temperature T_a at a readout power P_a and the fourth term the influence of TLS noise. The parameter N_{qp} is the quasiparticle number, Δ_0 the gap parameter at zero temperature, η_o the optical efficiency of the detector, τ_{qp} the quasiparticle recombination time, $\beta = \delta\sigma_2/\delta\sigma_1$ the ratio of change in conductivities under a small disturbance, $\chi_{\text{qp}} = Q_i/Q_{\text{qp}}$ is the part of the internal quality factor caused by quasiparticles and $\chi_c = \frac{4Q_c Q_i}{(Q_c + Q_i)^2}$ the coupling efficiency factor, where Q_i is the internal and Q_c the coupling quality factor.

It can be seen, that the photon noise and the generation-recombination noise are present independent of any design choices. The readout noise term shows that a low gap and a long quasiparticle recombination time lower the NEP. The same is true for the fourth term, which is unfortunately proportional to Q_i^2 whereas a high Q_i is desirable for good multiplexing properties. Therefore, the detector design should aim on low TLS noise as described in sec. 2.3.5. The volume is implicitly contained in N_{qp} , because in case of thermal excitation, quasiparticles are always created in the full volume while signal radiation always creates a number of quasiparticles per time. Low volume detectors therefore reduce the number of thermal quasiparticles.

The flaw of this model is, that for actually calculating a NEP, a number of parameters have to be known which can be only be estimated before an actual measurement has taken place. This starts at the material parameters like Δ_0 and Q_i and ends at parameters like

S_{TLS} whose origin is not sufficiently well understood. A frequency dependence is also not assumed in (2.53), but can be added by multiplying Lorentz functions with the resonator bandwidth and the quasiparticle recombination time as roll-off time constants.

2.4 Overview of MKID based instruments

2.4.1 NIKA 2

The New IRAM KID array (NIKA 2, [2]) is a two color MKID camera designed for the frequency bands around 150 and 240 GHz. The 150 GHz array has 616 pixels and the 260 GHz array has 2×1140 pixels, split by polarization. Each pixel is a lumped element resonator made of an aluminum thin film, which is deposited by electron beam evaporation. The shape of the inductive section of the pixel is a Hilbert-curve, that is matched to the free space impedance and makes the detector equally sensitive to both polarizations. The NIKA 2 instrument is currently installed at the IRAM 30 m telescope on Pico Veleta in Spain and (with its predecessor, NIKA [71]) is the one MKID instrument permanently in operation at a telescope and that achieves the expected sensitivity. It is available as a scientific instrument to the astronomical community. Within this thesis a test wafer of the NIKA 2 MKIDs is measured and analyzed. At the telescope, the instrument achieves a noise equivalent flux density of $33 \text{ mJy Hz}^{-1/2}$ at 260 GHz and $8 \text{ mJy Hz}^{-1/2}$ at 150 GHz. The NIKA 2 detectors are operated using a dedicated readout system called NIKEL.

2.4.2 A-MKID

This instrument is a new MKID camera for the APEX telescope. This ambitious camera has 3520 pixels at 350 GHz band and 21600 pixels in the 800 GHz to 900 GHz band [37]. The radiation from the telescopes secondary optics is coupled to double-slot antennas using one micro-lens array for each chip. The resonators are coplanar waveguide transmission line resonators. The sensitive section where the radiation is absorbed is made out of thin aluminum while the rest of the resonator is made of niobium titanium nitride (NbTiN). Air-bridges crossing the coplanar waveguide ensure the correct transmission mode. The A-MKID instrument was already deployed to the apex telescope but faced unforeseen problems, which delay scientific operation. The problems are assumed to be connected to the high pixel density and multiplexing factor.

2.4.3 MKID based multi color detectors and spectrometers

Planar superconducting electronics like on-chip filters, couplers or orthomode transducers can be coupled to MKID for the actual detection of the signal. The MUSIC instrument for example realizes a four color detector using an array of planar antennas coupled to four pass-band filters [88]. Other designs place a planar ortho mode transducer (OMT) to split up the polarizations at the output of a circular waveguide fed by a horn antenna [53]. The output of the OMT is separated in frequency by filters and the output of the filters is detected by MKIDs resulting in four MKID detectors per spatial pixel. The peak of that approach would be a filter bank spectrometer like DESHIMA [36] or SuperSpec [89]. There, the signal coming from a broadband antenna is filtered by a row of superconducting narrow-bandwidth filters, each with an MKID at the output. Each MKID in this case corresponds to one frequency channel.

2.4.4 The ARCONS near infrared camera

One different application than the previous examples of MKID based instruments is the ARCONS instrument [66]. It is designed for near-infrared wavelength and instead of adding filters or an dispersing element in front of the detector, it detects individual photon events and analyzes the pulse response to determine the photon energy. The idea of this technique is similar to the standard techniques in nuclear physics for analyzing high energy events. The ARCONS instrument has 2024 pixels which are sensitive to wavelength between 0.1 and 5 μm . The pixels are lumped element resonators with inductors made of titanium nitride. The quasi-particle lifetime of TiN is around 50 μs giving a compromise between time resolution, sensitivity and high kinetic inductance. The ARCONS instrument was tested successfully at the Palomar 200 inch telescope.

3 Measurement Setup

My workgroup has decades of experience designing and measuring SIS and HEB mixers. Building on this experience, I started working on MKID detectors basically from scratch, with some pre-development in my master thesis. I planned, implemented and tested the measurement setup described in the following.

The first considerable difference between the mixers and an MKID is the lower operation temperature which is supposed to be below $T_c/10$, meaning around 100 mK for aluminum MKID. For that, a new cryostat had to be bought and equipped for the measurements.

The most pronounced difference however is the completely different read-out scheme requiring a homodyne readout system. Also, the software required for my measurements had to be programmed.

The measurement setup described in this chapter has to be capable of measuring the sensitivity and noise of aluminum MKID detectors under conditions which are comparable to those on a telescope like CCAT-prime.

I first describe the Cryostat and the cold measurement setup. Then I introduce the implementation of the readout system and some basic measurement procedures. Since I measured three different devices in this thesis, I finally show the cold stage configurations necessary for each device.

3.1 ADR cryostat

The cryostat utilized to cool the MKID to temperatures below 100 mK is an HPD Rainier model 103 ADR cryostat. In this section the working principle and the technical details of the adiabatic demagnetization refrigerator (ADR) cryostat are described. The optimized operation procedure and the control software developed within this thesis are depicted in the following.

3.1.1 ADR principle

An adiabatic demagnetization refrigerator (ADR) is a cooling machine to cool experiments to low temperatures which can not be achieved by conventional refrigeration methods like

liquid cryogenics, Stirling or pulse tube coolers. Another cooling machine for achieving even lower temperatures is a dilution refrigerator [82]. The ADR relies on the magnetocaloric effect discovered in 1881 [33]. E. Warburg measured an increase in temperature if a strong magnetic field is applied to a paramagnetic material. This effect is used to realize a thermodynamic process using a paramagnetic salt pill instead of a gas and magnetic field instead of compression or expansion processes for cooling. The application as cooling machine was described by Debye [76] and Giauque [42] in 1926/1927.

As shown in fig. 3.1, an ADR system in principle contains one or more paramagnetic salt pills located inside a strong electromagnet. Each salt pill is thermally connected to a low temperature stage that is supposed to be cooled. A heat switch can connect the low temperature stages to the pulse-tube cooled stage which acts as a heat sink at constant temperature. The details and numbers given in the following procedure already apply to the HPD Rainier 103 cryostat used in this setup. The ADR cooling cycle goes as follows:

1. The heat switch thermally connects the mK stage to the pulse-tube cooler. The whole system is cooled to a temperature between 3 and 4 K.
2. With the heat switch closed, the electromagnet is slowly ramped to full current of 9.4 A and magnetizes the paramagnetic salt pills.
3. The current is kept at maximum for 15 min up to a few hours of time depending on the desired hold time. The spins in the magnet are forced to align to the field and generate heat by reducing their entropy. This heat from the magnetocaloric effect is dissipated by the pulse tube cooler via the heat switch.
4. Now the heat switch is opened and the cold stage is thermally isolated from the pulse tube. Then the magnet current is reduced slowly, reducing the external magnetic field in the salt pill. The spins are allowed to become more and more disordered again. The process of disordering the spins is endothermic and the only source of energy is the thermal energy of the salt pill and the mK stage. That way the salt pill cools down the mK stage to temperatures below 40 mK. When the magnet current is at 0 A, the full cooling capacity is available.
5. When the salt pills are fully disordered, their cooling charge is exhausted and the cycle has to be started over again.

The temperature of the mK stage and the magnet current of a typical ADR magnet cycle is shown in fig. 3.3.

The material properties of the salt pill are decisive for the temperatures that can be achieved. For the cooling capacity the magnetization of the salt pill is the determining

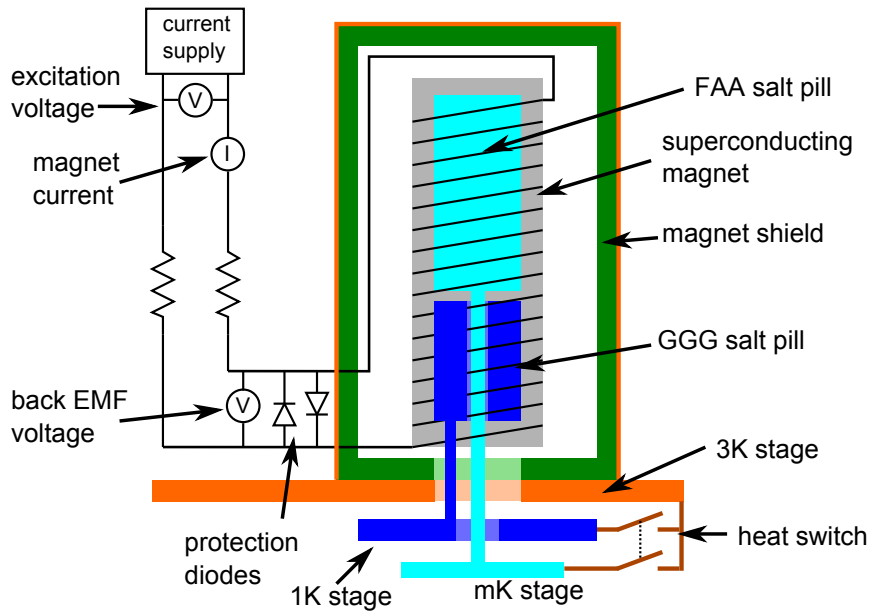


Figure 3.1: The principle construction of the ADR including two salt pills for the 1 K and the mK stages as it is the case in the HPD Rainier 103 system. Two salt pills made of gadolinium gallium garnet (GGG) and ferric ammonium alum (FAA) cool down to different temperatures. The colors depict the three different temperature stages, 3 K stage is orange, the 1 K stage is dark blue and the mK stage turquoise. The heat switch connects both stages to the 3 K stage. The superconducting magnet (grey) is mounted on the 3 K stage and shielded (green) to prevent field leaking to the experiment. The backward electromotive force (back EMF) voltage is the voltage across the superconducting magnet caused by the inductance resisting current changes. The back EMF voltage must not exceed the trigger voltage of the diode clamps. The excitation voltage is delivered by the current supply and is caused by the resistance of the normal conducting leads.

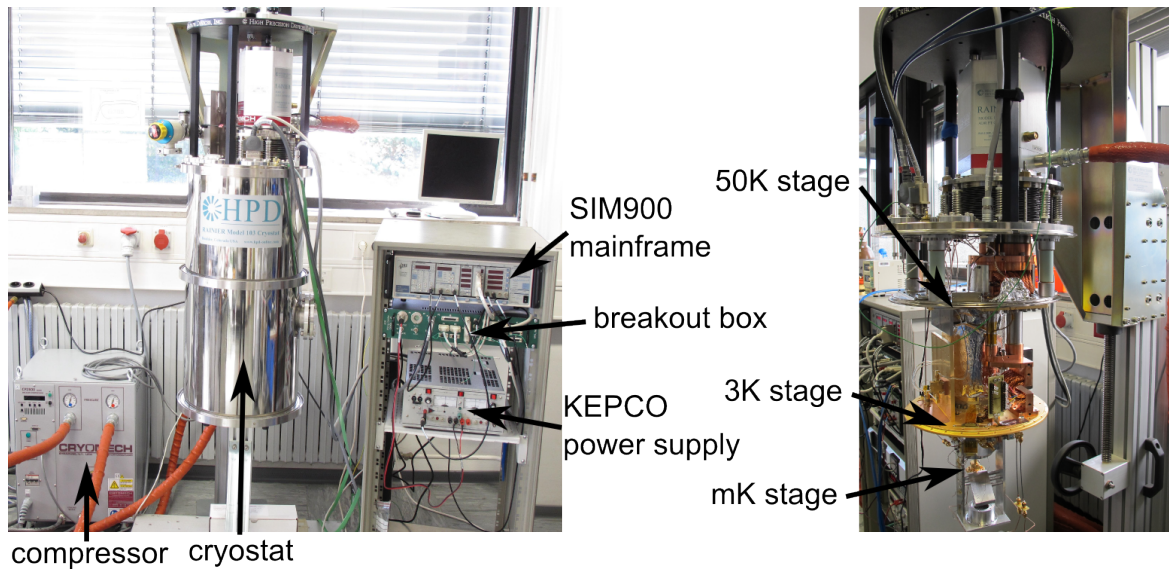


Figure 3.2: Left: The external components of the ADR cryostat. The compressor powers the pulse-tube cooler to pre-cool the system to 3 K. The rotary valve is on a separate stand behind the cryostat to minimize vibrations. The electronics rack contains the SIM900 mainframe with the temperature readout and the PID controller which programs the KEPCO magnet power supply. **Right:** The inside of the ADR cryostat. The ADR magnet is mounted on the 3 K stage wrapped in super insulation.

factor and for the minimum temperature the temperature dependence of the magnetic susceptibility as the salt has to stay paramagnetic down to the required base temperature.

3.1.2 The HPD Rainier model 103 cryostat

The HPD Rainier model 103 (see fig. 3.2) is a commercial system developed by High Precision Devices (HPD). Its specifications are summed up in table 3.1. It features a pulse-tube pre-cooled cryostat with a 10 A, 4 T superconducting ADR magnet. It has two salt pills, a gadolinium gallium garnet (GGG) pill that achieves a minimum temperature of 0.5 to 1 K (subsequently called 1 K stage) and a ferric ammonium alum (FAA) salt pill that achieves temperatures below 40 mK (called mK stage). The GGG salt pill has a factor of 10 larger cooling capacity and is used to heat sink all connections to the mK stage. Dual diode clamps on the magnets electric leads protect the magnet and the warm electronics in case of a quench. The current leads between the 50 K stage and the 3 K stage are made of a high temperature superconductor to minimize thermal conductivity. The Cryomech pulse tube pre-cooler achieves a base temperature of about 47 K on the first stage and 3.0 K at the 3 K stage. A minimum ADR temperature for the mK stage of 36 mK was measured. The system promises 150 h hold time at 100 mK for one ADR cycle

parameter	spec./typ.	measurement
pulse tube stage 1 base temperature	52 K	47 K
pulse tube stage 2 base temperature	2.7 K	3.0 K
1 K stage base temperature	< 0.5 K	–
mK stage base temperature	< 50 mK	38 mK
GGG salt pill cooling capacity	≈ 1 J	–
FAA salt pill cooling capacity	≈ 0.1 J	–
hold time at 100 mK	> 150 h	149 h
max. mass on mK stage	2 kg	–

Table 3.1: Specifications of the HPD model 103 Rainier ADR cryostat. [47]. The slight discrepancy to the measured values are due to the fact that parts of the cables are already installed at the test run. The hold time and the mK stage are determined at regulated temperature of 100 mK as described in sec. 3.1.5.

without thermal load which I verified. Mechanically, the 1 K stage and the mK stages are held in place by strong Kevlar strings only to minimize the thermal conductance to the 3 K stage. The low temperature stages are gold plated Copper rods mounted to the salt pills. The stages are split such that experiments can be mounted facing the side of the cryostat and facing downwards, where larger experimental space is available.

The system comes with a Stanford Research Systems SIM900 mainframe which includes a SIM921 AC resistance bridge connected via a SIM925 multiplexer to the Ruthenium Oxide temperature sensors for the mK and 1 K stages. The temperatures of the pulse-tube stages and the magnet are measured with silicon diode sensors and a SIM922 diode temperature monitor. The mainframe also includes a SIM970 digital voltmeter to measure the magnet voltage and current and a SIM960 PID controller to program the magnet current generated by an external KEPCO BOP20-10 power supply. Every instrument in the SIM900 mainframe can be controlled and monitored via a RS232 serial interface. All electric connections to the cryostat are conveniently done through a breakout box. With the SIM900 mainframe and the power supply, the ADR system can in principle be operated manually without an external computer.

3.1.3 Increasing and decreasing the magnet current

The method to ramp up the magnet current as proposed by the manufacturer is to determine the lead resistance, calculate the voltage required for a target current of 9.4 A and slowly ramp up the excitation voltage that programs the KEPCO magnet power supply to the calculated value while keeping the backward electromotive force voltage (back EMF, voltage of the magnets inductivity resisting current change) below 0.45 V. The current fol-

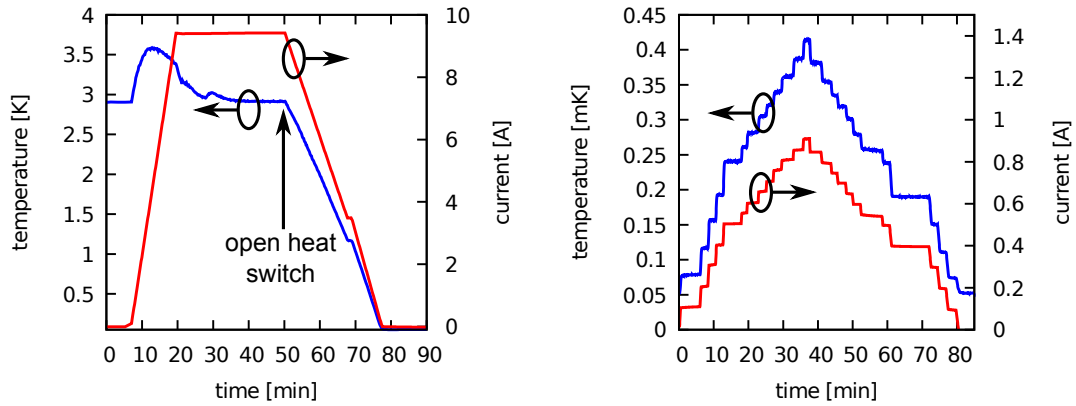


Figure 3.3: Left: mK stage temperature (left axis) and magnet current (right axis) during a magnet current cycle using my ramping method holding the back EMF voltage constant. The heat switch is closed during the ramp up and hold of the current. During the ramp up the temperature rises slightly because of the magneto caloric effect. This heat is dissipated by the 3 K stage. **Right:** mK stage temperature and current during a temperature sweep. The current is proportional to the temperature with a small drift caused by the slow depletion of the cooling capacity on a longer timescale than visible in the plots.

lows a limited growth function and it does never reach the desired value, therefore manual tweaking is necessary after the ramp.

The voltage across the protection diodes, the back EMF voltage, is the limiting value when increasing or decreasing the ADR current in order not to trigger the diodes and quench the magnet. The ramping method developed within this thesis keeps the back EMF voltage constant during current changes. This can be easily implemented in a control loop because the programming voltage (excitation voltage) is the back EMF voltage with an offset caused by the lead resistance, without any time constant or non-linearity involved. The back EMF voltage is kept constant at a defined value determining the ramping speed, until the current is achieved. Then the excitation voltage is reduced such that the back EMF voltage is 0 V and the ramp is finished. This method provides two advantages: The fastest possible ramp with the given limit on the back EMF voltage and the linear increase of the current up to the target. The new ramping method is shown in fig. 3.3. Ramping down the current is implemented in the same way by applying negative voltages.

3.1.4 Operation and monitoring software

The system manufacturer did not deliver automatic operation and temperature monitoring software. Thus a control and monitoring software was developed within this thesis and integrated in the framework of the measurement software described in sec. 3.3.6. The software logs all temperatures of the low temperature stage and the diode temperature

monitor and the voltages of the digital voltmeter in adjustable time intervals. It also implements ramping up and down the magnet current by the method described in sec. 3.1.3. As security interlocks, the software forbids back EMF voltage above 0.45 V as recommended by the HPD manual and currents above 9.45 A. This gives an additional limit to the hardware limits implemented in the KEPCO supply. The software also prevents ramping up the current while the magnet temperature is above 3.5 K.

The software connects to the SIM900 mainframe and its individual instruments using a serial interface and reads out all relevant parameters once a second. Control commands are also sent on this interval. Besides the SIM900, the ADR control software also connects to a CryoCon C44 temperature controller for additional temperature sensors installed in the experiments mounted in the cryostat.

3.1.5 Temperature control and stabilization

The demagnetization process is reversible to a certain extent and therefore called adiabatic. If the magnet current is increased using the magnet power supply, the temperature of the mK stage temperature starts to rise. The big advantage of regulating the temperature by ADR magnet current is that that way no cooling energy stored in the salt pill is wasted as it would be the case using a heater. The magnetic field actually reduces the disordering rate of the spins in the salt pill leading to longer experimentation time per magnet current cycle. Using the magnet, temperatures between 3 K and the lowest temperature can be set. This is shown in fig. 3.3 on the right. The downside is that the magnetic field from the ADR magnet may interfere with the experiment. This is especially probable at high temperatures requiring high currents, therefore the temperature sweeps are usually done only up to 500 mK, which is sufficient to make resonances of aluminum resonators basically disappear. When the magnet current is ramped down, the mK stage cools to its base temperature again.

The mK stage temperature is not stable at zero magnet current and rises with time due to unavoidable heat input from connections and radiation. For experiments at constant temperature it is therefore necessary to stabilize the mK stage at higher temperature using a bit of magnet current. For that, at 0 A current a $10\ \Omega$ resistor is switched in between the power supply and the magnet to increase the dynamic range of the control loop. The PID controller is used to regulate the magnet current. The PID input is the temperature reading of the mK stage. The PID ramps up the magnet current to a certain value causing the mK stage to settle on a corresponding temperature. If the temperature now starts to rise, the PID *decreases* the current which then increases the cooling power of the mK stage. When the PID decreased the current to 0 A, the charge of the salt pill is depleted.

This temperature stabilization can be done up to temperatures of about 180 mK which requires magnet currents of about 300 mA.

3.1.6 ADR security precautions

The operation of a dry ADR cryostat is not exceptionally dangerous as no liquid cryogens have to be handled. During the magnetization phase one has to be aware that the magnet (4 T field) stores a lot of energy. Since the magnet is a huge inductivity, a sudden voltage drop by cable failure, power outage of the magnet supply or operation mistakes will cause the magnet to release its inductive energy instantly (quench) what may damage the magnet itself or anything attached to it. To prevent a high voltage surge to propagate through the system, a diode voltage clamp is located directly in front of the magnet and will short out any voltages above about 0.7 V. This protection however also causes a risk, because if the back EMF voltage above 0.7 V is applied externally (while ramping up the current) the diodes will switch on and short the magnet. Then, depending on the current, at least the diode is damaged and the cryostat has to be opened and cleaned. A power outage of the control electronics is excluded with a zero-latency uninterrupted power supply (UPS) giving a bridge time of approximately 15 minutes which is sufficient to ramp down the magnet current without triggering the protection diodes.

Another scenario to be considered is failure of the pulse-tube or the helium compressor. In this case the temperature of the magnet will start to rise and the current rating of the magnet falls. Because of that, the cryostat should not be left unattended while under full current. After a pulse-tube failure the operator has 5 to 10 minutes of time to manually ramp down the magnet current.

The magnet could also be quenched by applying too high current which is prevented by a hardware current limit of 9.6 A in the KEPCO power supply. Generally, the system operator has to be aware of the fact that in case of a problem the panic reaction of turning everything off is exactly the wrong thing to do and that the magnet current always has to be reduced slowly keeping the voltage across the magnet below 0.7 V.

3.2 General cold measurement setup

The characterization of MKID devices takes place at temperatures around 100 mK which can be achieved using the ADR cryostat described above. The MKID devices are characterized under dark conditions without any optical signal and under thermal loading. The dynamic response is investigated using LED pulses. These setup parts which are located in the cryostat and were designed and implemented within this thesis are described in the

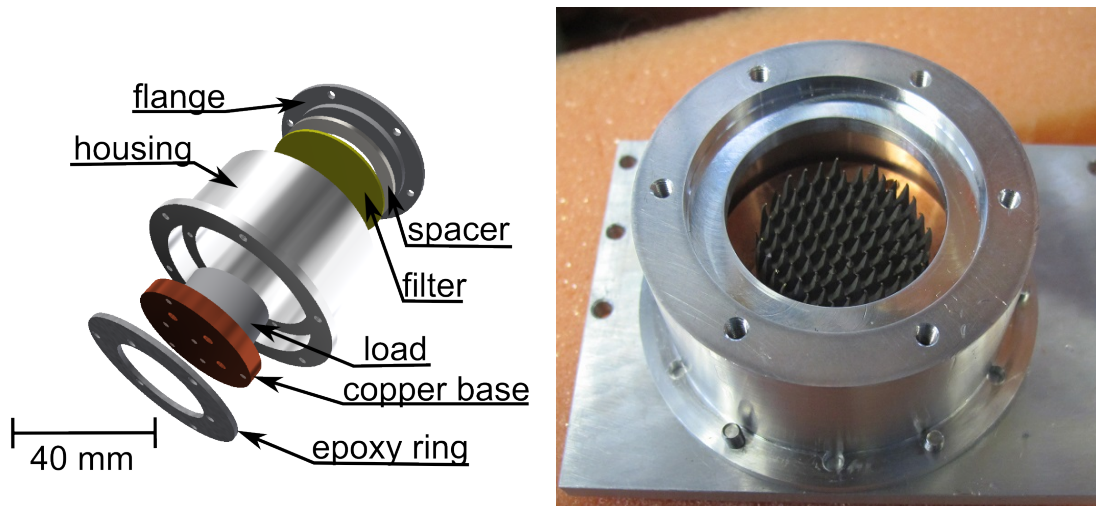


Figure 3.4: **Left:** CAD drawing of the heatable load. The heater and temperature sensor will be screwed to the Copper base, where also the load itself is fixed. It is separated from the housing by a ring milled out of epoxy PCB material. **Right:** Photograph of the assembled load without the filter, as used during the NIKA measurements.

following. Some parts of the cold measurement setup are discussed in sec. 3.5 because they are dedicated to measurements of one specific device.

3.2.1 Heated black body load

The detectors optical NEP is going to be characterized by applying a defined amount of radiation to the detector. To do this, the black body absorber (load) shown in fig. 3.4 can be varied in temperature between the pre-cooler base temperature of 3 K up to about 30 K. The aluminum housing of the load is connected to the base plate with solid aluminum pieces. The inside of the load with a Copper puck and the actual absorber is isolated from the housing with a ring milled from FR4 circuit board material. The time constant of the load should be such that it can be easily heated up without excessive thermal load on the pre-cooler stage and should also cool down in reasonable time for a fluent experimental work. Since the material properties like thermal conductivity and heat capacity are tedious to investigate exactly for temperatures below 4.2 K, the design is based on estimated heat transfer between the 3 K stage and the Copper puck. In an experiment, the load heats up without significantly loading the 3 K stage and cools down again in about 15 minutes, which is adequate for experimentation. On top of the aluminum outer housing a 600 GHz low pass filter can be mounted which stands at an angle to the beam axis to reduce standing waves.

3.2.2 LED pulse setup

To analyze the time response of MKID detectors, mainly to measure the lifetime of the quasiparticles, the chip is illuminated with optical pulses from an light-emitting diode (LED) [11]. LEDs do not generally operate at 3 K¹, therefore it is mounted on the room temperature stage of the ADR cryostat. Problems with vacuum are not known, therefore the effort of an sealed feed trough through the vacuum shield is not made. The LED radiates in red and is directly screwed on an optical fiber which then transports the light to the 3 K stage. The material of the fiber is non-metallic and has a low thermal conductivity. Impact on the cryostat performance is not noticed. Inside the 3 K shield the fiber is fed through a Copper pipe which is bent to point directly on the device to be measured. The Copper pipe prevents excess radiation inside the cold stage coming from the eventually warm fiber. It is also a stable mechanical support for the fiber. The fiber does not touch the low temperature stages where the MKID devices are mounted, but is just aimed at the device. The radiation only reaches the devices under test through small holes in the shields which limit the energy input from the 3 K surrounding and from the fiber (see sec. 3.5.2)

The LED is powered by a driver circuit which is triggered by a 5 V pulse from the data acquisition system. The circuit is galvanically separated from the data acquisition system with an optocoupler to prevent interference with the grounding. The LED current can be set by an potentiometer on the circuit. The circuit is developed and build by our in-house electronics workshop.

3.2.3 R/T setup

Besides the optical tests of the detector, the ADR cryostat also has to be used to perform DC tests on the superconducting aluminium used in the WGKID detector and other material characterization tasks. If the material properties only have to be tested down to 4.2 K, the experiments are performed with a dipstick which is submerged in liquid helium. Since aluminum has a critical temperature around 1.2 K (bulk) or around 1.4 K (thin film), the aluminum samples have to be measured in the ADR. The main parameter of interest during these measurements is the resistance of the thin film layers used in the MKID at different temperatures to find a possible transition to the superconducting state to determine the critical temperature T_c . The voltage and current to calculate the resistance are measured with two low noise lock-in amplifiers avoiding any drift, which is especially necessary for low resistance samples like van-der-Pauw structures. If of interest, also the current volt-

¹I actually tested one successfully at liquid nitrogen temperature (77 K) but could not get any current through the LED at 3 K.

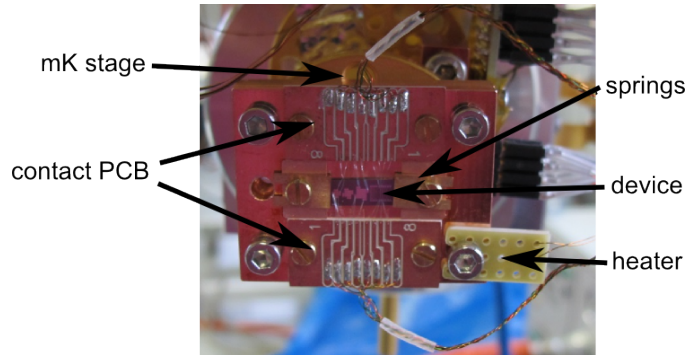


Figure 3.5: The cold fixture for resistance vs. temperature measurements mounted on the side stage of the ADR. The temperature sensor is mounted on the back of the mK stage.

age characteristics of the samples can be measured (IV). The experiments take place on the side stage of the ADR so the MKID measurement can in principle take place on the same cool-down. During one cool-down currently 4 samples can be measured in four-point measurement configuration (fig. ??). The samples are clamped to the mounting block using Copper-beryllium springs since glued connections are not trustworthy at temperatures below 4 K. To enhance thermal conductivity, a very small amount of Apiezon N cryogenic vacuum grease is applied to the block. The electrical contacts are made with aluminum wire bonds. The multiplexer that switches between samples is outside the cryostat. The wires from the mK stage are AWG 36 Lakeshore phosphor bronze cables for low thermal conductivity. The wires are heat sunk on the 1 K stage before going to a contact panel on the 3 K stage and out of the cryostat.

3.3 MKID readout system

An essential and time consuming part of the MKID measurement setup development I did within this thesis are the cold and warm readout electronics. The readout system generates a probe tone which is modified by the MKID resonators and analyzed in amplitude and phase. As described below, two different mechanisms are used for MKID measurements. A vector network analyzer (VNA) and an IQ mixer setup together with a synthesizer. For large detector arrays, complex digital systems based on fast ADCs and DACs in combination with individually programmed FPGA are in use that generate and analyze thousands of readout tones [18,69]. For the setup used in this thesis, a single resonator readout system is required and a purely analog approach is chosen which also gives a high experimental freedom.

3.3.1 Vector network analyzer readout

The most straightforward way of measuring an MKID device is a vector network analyzer (VNA) transmission measurement. In a simplified picture the VNA generates a probe tone which is swept in frequency. The probe tone goes through the cryostat and the MKID and back to the VNA, where it is analyzed in amplitude and phase. The VNA measurements are very useful to measure the shape of resonances because it is fast and well compensated for its internal errors. External components can be corrected for using the VNA build-in calibration features. Therefore, resonance frequencies and quality factors of the MKID resonators can be measured easily.

3.3.2 IQ mixer readout mode

The purpose of the IQ mixer readout is to measure dynamic properties like the quasi particle lifetime and time domain data for noise analysis of the MKID. The IQ mixer can be used for frequency sweeps as well but is especially useful for operation at a single frequency and measurement of fast processes as mentioned.

The ideal IQ mixer as shown in fig. 3.6 (left) generates DC voltages at its outputs which are proportional to the in-phase and the quadrature (90° phase shifted) components of the signal. The voltages would ideally be

$$V_I = V_0 \cos \phi \quad (3.1a)$$

$$V_Q = -V_0 \sin \phi \quad (3.1b)$$

where ϕ is the relative phase between local oscillator (LO) and signal port, $V_0 = V_{\text{signal}}V_{\text{LO}}$ is the product of the amplitudes of signal and LO. The IQ mixer is used for measurements of a MKID as shown in fig. 3.6 on the right. This detection scheme is called a homodyne detection because from one signal generated from a synthesizer a small portion is split off in an directional coupler. The through port of the coupler goes to the LO input of the IQ mixer while the split off fraction goes into the cryostat and through the MKID device. After amplification, the split part goes out of the cryostat to the signal input of the IQ mixer and is down-converted with the other part of the signal that goes to the local oscillator input. The IQ mixer generates V_I and V_Q , which are voltages proportional to the in-phase and quadrature component of the signal relative to the LO. These voltages are amplified, filtered and digitized. When V_I and V_Q are plotted against each other in a polar diagram, the radius of the point resembles the signal amplitude and the angle the phase. In contrast to the simple model, real IQ mixers suffer from internal errors as gain and phase imbalance. The full model applied for analysis of IQ mixer measurements is

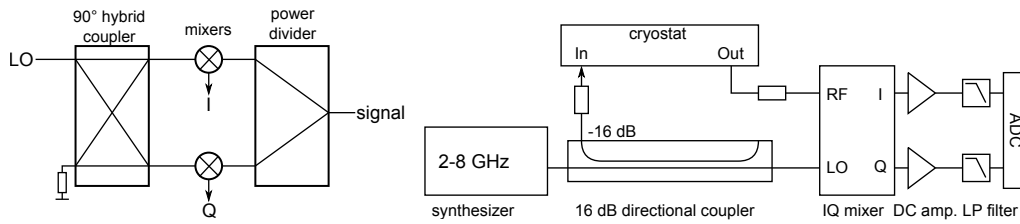


Figure 3.6: **Left:** Internal schematic of the IQ mixer. **Right:** The reduced schematic of the IQ mixer setup.

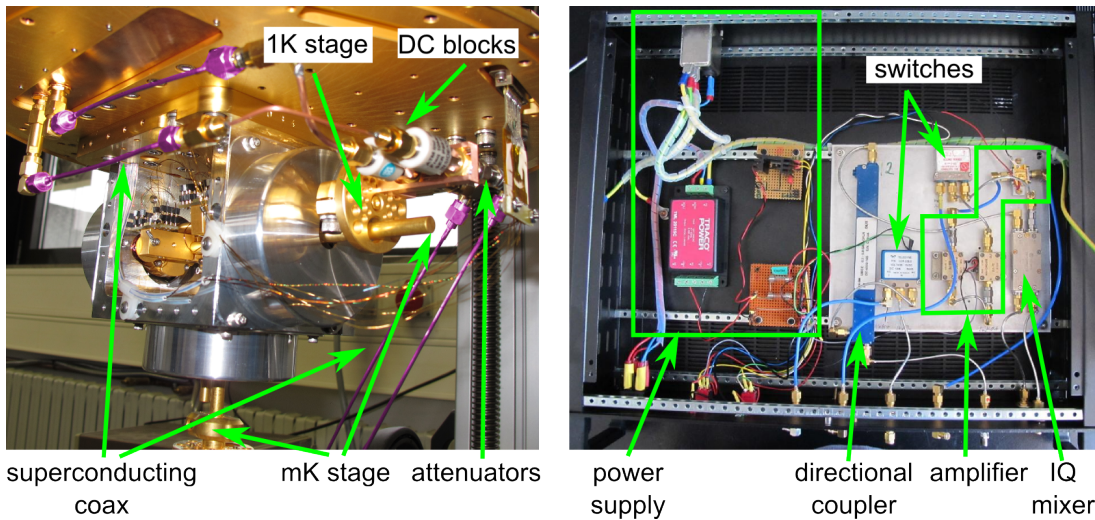


Figure 3.7: **Left:** Picture of the 3 K stage with the coaxial cables to the 1 K stage and the mK stage. The superconducting NbTi coax cables thermally insulate the stages from each other and are tinted in the picture. **Right:** The inside of the warm readout processor. The schematic is shown in fig. 3.10

shown in 6.5.2 and the detailed implementation of the setup is described below in 3.3.3 and 3.3.4. The low pass filters are described in 3.3.5.

3.3.3 Cold readout system

The job of the cold readout system is to transport the probe tone to the device and the response signal to the low noise amplifier (LNA) and back outside while introducing a minimal amount of thermal load and noise on the device. A schematic of the setup is shown in fig. 3.8. A picture of the wiring between the 3 K stage and the mK stage is shown in fig. 3.7 on the left.

The probe signal enters the cryostat via a hermetic SMA feed-through with a 10 dB attenuator. Between the vacuum hull and the 50 K stage are ca. 20 cm of stainless steel

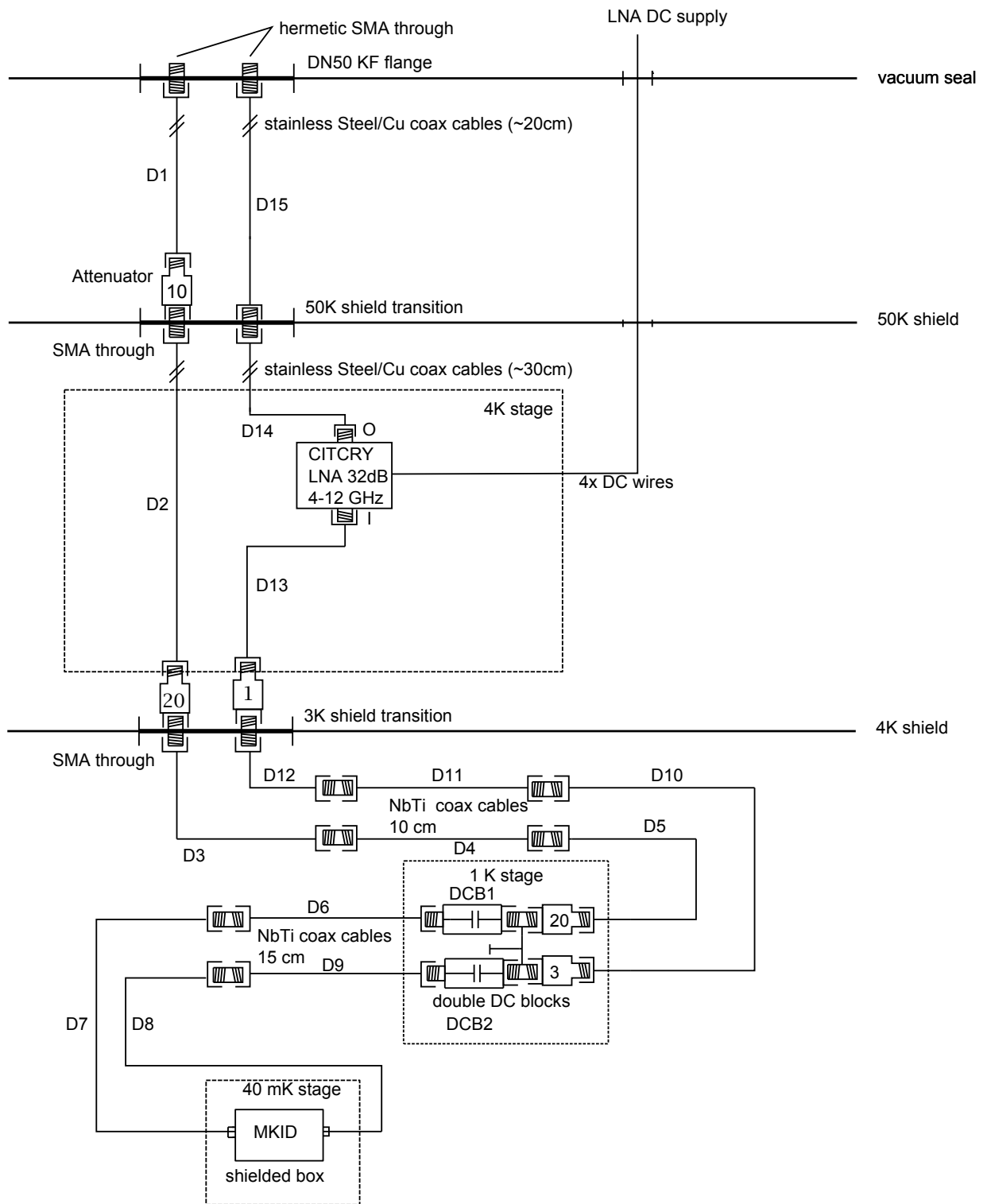


Figure 3.8: Schematic of the cold RF setup mounted inside the cryostat.

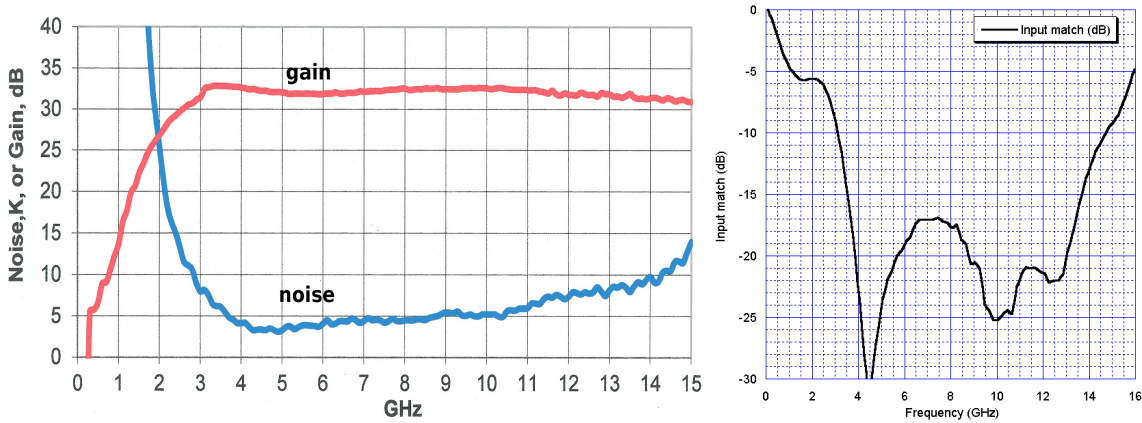


Figure 3.9: Left: Gain and noise performance of the used LNA CITCRYO4-12 516D measured at 22 K. **Right:** Input match of the LNA (typical) measured at 11 K. All data is as provided by the vendor. The input reflection and the noise performance gets considerably worse in the frequency range below its designated operating band of 4 GHz to 12 GHz while the gain is still acceptable.

coax cable with Copper center conductor. The center conductor is thermalized with a 10 dB attenuator on the 50 K stage. Using subsequently ca. 30 cm stainless steel cable the signal goes to the 3 K top shield. Another attenuator on 3 K helps thermalizing the cable. Now between the 3 K stage and the 1 K ADR stage, 10 cm superconducting NbTi coax cables are used for transporting the readout signal while maintaining good thermal insulation. They are fabricated by Coax Co in Japan. On the 1 K stage, a 20 dB attenuator is supposed to thermalize the center conductor while a double DC break electrically and thermally insulates the ADR stages. 15 cm superconducting coax cables are used to connect to the mK stage. The probe signal then goes through the MKID, and back via the 1 K stage to the low noise amplifier (LNA) at 3 K. In the return path the same length of superconducting cables are used, but not as much attenuation as in the entry path because the signal is already weak and the signal to noise ratio would suffer. The LNA is a CITCRYO4-12 HEMT [5] cryogenic amplifier cooled to 3 K. Its specs are shown in fig. 3.9. Then the signal goes back through the 50 K stage to the cryostat vacuum flange using stainless steel coax cables with Copper center conductor again.

3.3.4 Room temperature switchable readout processor

The room temperature readout processor designed and build within this thesis is shown in fig. 3.7. The full schematic is shown in fig. 3.10. It is conveniently mounted in a 19" rack casing where the external hardware is connected. It contains a series of necessary amplifiers to bring the signal coming from the LNA to a level which is suitable for the IQ

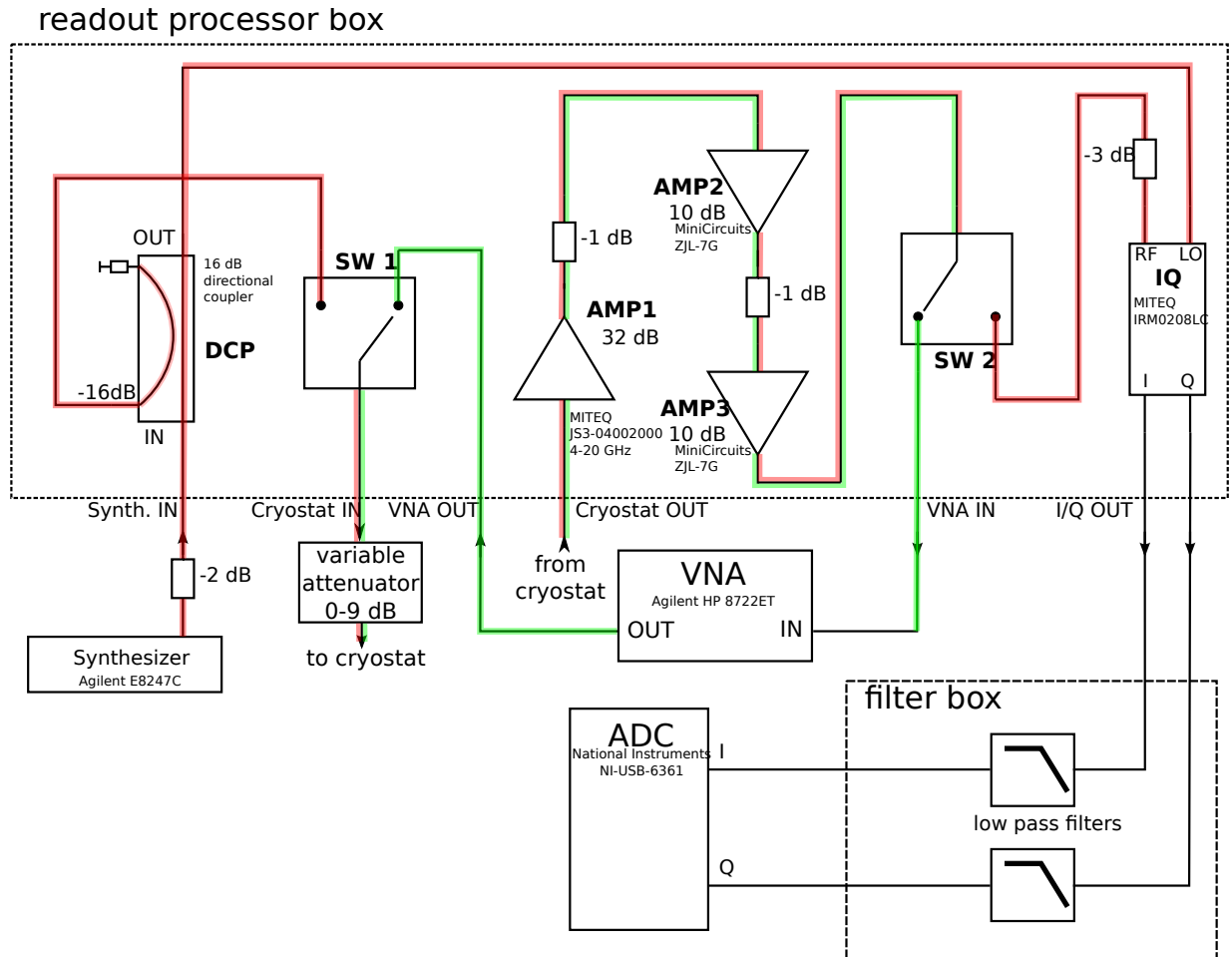


Figure 3.10: Schematic of the readout processor. The two switches are set to network analyzer readout mode. The signal paths for the two readout modes are described in detail in sec. 3.3.4. The VNA readout signal path is marked in green, the IQ readout signal path in red. Both signal paths share the cold electronics and the amplifier chain.

mixer and the VNA. All necessary devices like the VNA, the synthesizer for IQ readout (see sec. below) and the cryostat are connected to the readout processor. The system can be switched between VNA readout and IQ mixer readout with the two SMA switches inside the box which are toggled with one switch at the front panel. The schematic shows the system in VNA readout mode. The active mode is indicated with an LED at the front panel as well.

Network analyzer readout As shown in green in fig. 3.10, in this readout mode the signal generated by a Agilent 8722ET vector network analyzer goes to switch SW1 and is connected to the cryostat input. The return signal coming from the cryostat through the amplifier chain (AMP1-AMP3) where it is amplified by a total gain of 50 dB. Attenuators between the amplifiers dampen possible standing waves. Switch SW2 then directs the signal to the VNA output from where it goes back to the VNA transmission port.

IQ mixer readout The signal path within the readout processor is shown in fig. 3.10 in red. The probe tone is generated by a Agilent E8247C synthesizer which is connected to the readout box using a semi-rigid Copper cable. This connection has shown to be a source of excess low frequency amplitude noise in the spectrum probably due to modulation of standing waves, so a rigid cable was chosen here. In the readout processor, -16 dB of the signal are split off using a directional coupler and directed to the cryostat as probe tone for the MKID via switch SW1. The remaining signal is used as a local oscillator signal for the MITEQ IRM0208LC IQ mixer. Its operation bandwidth goes from 2 GHz to 8 GHz. The IQ mixer needs 10-12 dBm LO power, thus the synthesizer is set to 13 dBm output power. The amplitude at the cryostat input can be reduced with a variable attenuator. The signal path in the cryostat is the same as for VNA readout and explained in sec. 3.3.3. The return signal coming from the cryostat is amplified by 50 dB using the amplifiers Amp1 to Amp3 and connected to the IQ mixers signal port via switch SW2. 3 dB attenuation are inserted here because the IQ mixers signal port is not very well matched and can be a cause of standing waves. In the IQ mixer, the LO and signal are converted to an in-phase (I) and quadrature (Q) component. To be able to compare the VNA and IQ mixer measurements, the synthesizer delivers the 10 MHz reference frequency to the VNA. That way it is ensured, that both measurements are on the same frequency axis.

3.3.5 Analog to digital converters and low pass filters

The IQ mixer generates analog voltages which are proportional to the in-phase (I) and quadrature (Q) parts of the input signal in a frequency range between DC and in principle

500 MHz, which is the output bandwidth of the IQ mixer. For the measurements only the first 500 kHz of the signal that can be digitized are of interest. If these voltages would be directly attached to the analog to digital converters (ADC) which sample at 1 MHz, the broadband noise above the Nyquist limit of 500 kHz would fold back into the band and increase the overall noise level significantly. Therefore, low-pass filters have to be used in front of the ADCs. In my setup, the filters also include amplifiers to boost the signal level to a level adequate for the ADC.

Filter design Before reaching the amplifiers, the voltages are pre-filtered with ferrites to reject the high frequency content. Then they are amplified by a factor of 11 and fed into the low-pass filters. These filters are active 4-pole Chebychev filters using operational amplifiers [49] designed within this thesis and build and optimized by our in-house electronics workshop. This design is selected for its steep transition to the stop band. The amplifiers and filters have a total voltage gain of 46 and $50\ \Omega$ input and output impedance.

Two sets of low-pass filters with 1 kHz and 260 kHz are build to limit the input signal of the following ADC and by that prevent signal aliasing. The ADC is a National Instruments NI-USB 6361 USB interface with BNC inputs. The maximum sample rate for multiple channel input is 1 MHz at a resolution of 16 bit. For measurements at the full sample rate, the 260 kHz filter is used, while the 1 kHz filter is used for long measurements at a sample rate of 4 kHz. Because of the amount of data acquired, measurements longer than about 10 seconds are not possible at 1 MHz sampling rate. Both sampling rates are a factor of 4 above the filter frequencies. The Nyquist limited bandwidth is therefore still a factor of 2 above the filter cutoff frequencies. The 4-pole low-pass filters should have a steepness at the stop-band transition of 12 decibel per octave. Therefore, the contribution of out-of-band signal which folds back into the signal band at the ADCs is limited to less than 6 %.

3.3.6 Measurement and control software

The center of the measurement setup is the measurement and control software which I developed within this thesis to acquire the data for the different measurement modes and remote control parts of the setup. A screen shot of the software GUI is shown in fig. 3.11. The software is written in Visual Basic for a Microsoft Windows operating system. It uses the National Instruments libraries for the graphical user interface and the NI DAQmx library for interfacing the ADC/DAC. The NI Enterprise Analysis Library is also used for some calculations. Listed below are the main features of the measurement software.

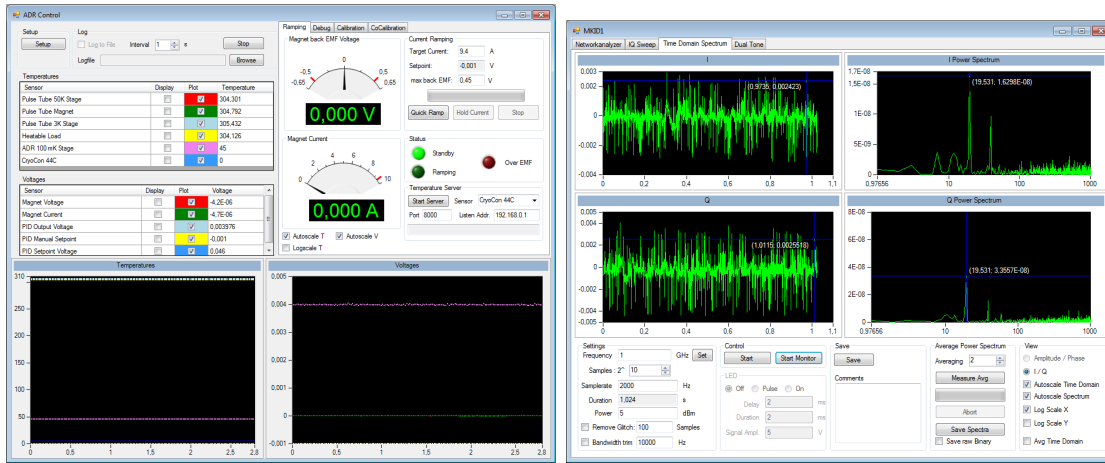


Figure 3.11: Screenshots of the measurement software GUI. **Left:** The ADR monitor and control window. **Right:** The Time domain measurement window.

VNA readout mode This part of the software uses the VNA GPIB interface to get the data from the VNA, display and save it without any advanced processing. The VNA is also remote-controlled via the GPIB interface. As an additional feature, lists of scan ranges can be saved and measured at high resolution to repeat measurements with many resonators.

IQ sweep mode The software remote controls the synthesizer which is necessary to perform frequency sweeps with the IQ mixer. The I and Q signals are read from the ADC, averaged and stored as described in sec. 3.4.2. Once the data is digitized, errors of the IQ mixer such as phase and amplitude imbalance and DC offsets can be corrected as will be shown in sec. 6.5.2.

Noise measurement mode This mode implements the measurement procedure described in sec. 3.4.3. In addition to that the software also includes preview mode which measures and displays the spectrum continuously like a spectrum analyzer. This mode is mainly useful for debugging and location of grounding problems. The GUI of this mode is shown in fig. 3.11 (right).

LED pulse mode This measurement scheme is closely related to the noise measurement, as it used the IQ mixer for a time domain measurement at a high sampling rate. It implements the procedure described in sec. 3.4.4.

ADR control As mentioned in sec. 3.3.6, the ADR control software is linked to the measurement software parts. With every measurement, the temperatures of all stages are

saved. This module also contains a small web server to transmit the temperature to the RT setups computer which is connected to the lock-in amplifiers for the resistance measurement. This allows resistance/temperature measurements with the ADR temperature sensors. The GUI of this mode is shown in fig. 3.11 (left).

Dual tone measurement mode This mode offers some experimental features for measurements with a second, strong probe tone used to excite the MKID. The software can perform power sweeps of the second probe tone and frequency sweeps in up- and downward direction interleaved with VNA measurements as described in appendix A.

3.3.7 Estimation of readout system noise

As described in sec. 2.3.7, the noise contribution of the readout system mainly depends on the first components behind the detector. In the case of my setup this would be the cables between the mK stage, the 3 dB attenuator and the DC block on the 1 K stage, the cables to the 3 K stage and of course the low noise amplifier. The performance of the LNA is shown in fig. 3.9 and indicates that the noise performance degrades at the low end of the designated operation frequency band. The transmission of the cables is measured in using a VNA at room temperature. The cables that connect stages with different temperatures are treated to be at the temperature of the respective warmer stage. The estimation of noise temperature is therefore rather conservative.

The attenuation and the noise temperature are calculated for 2.5 GHz and for 5 GHz readout frequency. The resulting noise temperatures for the setup are 89 K and 55 K respectively. Leaving out the 3 dB attenuator on the 1 K stage, the noise temperatures would immediately reduce to 45 K and 28 K. Because of the bad input match at low frequencies, this may cause problems with standing waves. At an estimated readout power at the device of -69 dBm at 2.5 GHz and -71 dBm at 5 GHz, the resulting amplitude and phase noise would be -110 dBc/Hz. The effect of the lower noise temperature at 5 GHz does not make a significant difference here. A measurement of the noise spectral density at a frequency around 2.3 GHz measured as explained in sec. 6.5.1 is shown in fig. 3.12. As this measurement is done at a frequency where no resonance feature is present, only the setup noise is visible. The measurement result shows a strong low frequency noise contribution that saturates above 5 kHz at -105 dBc/Hz. This is a bit higher than the estimation above. The roll-off above 100 kHz is due to the filters in front of the ADC and shows that the system noise is dominated by the high frequency setup and not by the filters or the ADC.

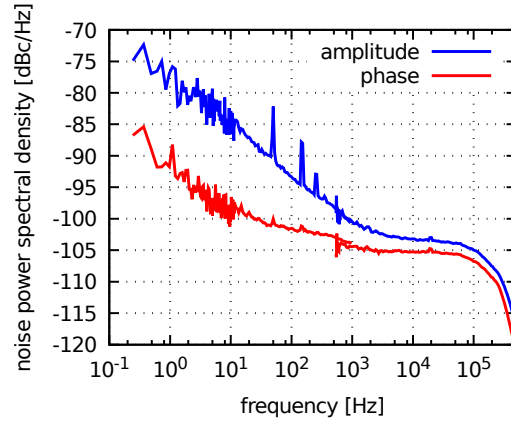


Figure 3.12: Amplitude and phase noise of the setup measured with one of the NIKA 2 devices (chapter 6). The prediction for the setup noise is -110 dBc/Hz. The roll-off above 100 kHz is due to the filters in front of the ADC.

3.4 Measurement procedures

The different measurements on MKID devices follow determined procedures which are generally described in the following. Individual parameters of the procedures can vary, but will be mentioned explicitly in the chapters describing the actual measurement.

3.4.1 VNA transmission measurement and temperature sweep

The VNA measurements are used to get a first impression of the functionality of the mounted device and for detailed zoom-in scans of the individual resonances at high resolution. All measurements are generally taken at the full resolution of the VNA, which is 1601 samples over the selected band. The sweep time of 800 ms is sufficiently long to compensate for the length of the cables between the VNA terminals, meaning that the transmission spectrum does not change on longer sweep time settings. The general procedure for the initial measurement of a chip is the following:

- Dependent on the chip, the 3 K transmission is measured over a wide bandwidth, usually the full system bandwidth 1 GHz to 12 GHz at the native VNA resolution of 1601 samples. If the device under test is made of a material which is resistive and normal conducting at 3 K, no transmission is measured.
- The device is then slowly cooled to the ADR base temperature doing an ADR magnet cycle (sec. 3.1.1). In some samples the critical temperature T_c of the read out line is below 3 K. Then the superconducting transition of the readout line can be observed in the transmission spectrum during cool-down.

- At the ADR base temperature, usually below 50 mK the wide band measurement is repeated. Then the individual resonators are measured in a narrow frequency band around the resonance frequency. Using a feature of the software, once the frequency ranges are defined they can be remembered and measured over and over again.
- The current on the ADR magnet is increased to increase the sample stage temperature as described in sec. 3.1.5 The resonances are measured at each temperature step again. The temperature behaviour of the resonances usually distinguishes the real KID resonances from spurious resonances of the box or cables.

The above procedure has to be understood as a summary of the measurements done in the context of this thesis. The real procedure is always adapted to the sample to be measured.

3.4.2 Measurement of IQ mixer frequency sweeps

Frequency sweeps using the IQ mixer are necessary to calibrate the time domain data locally, meaning in a certain frequency range around the resonance. The procedure for recording IQ mixer frequency sweeps is:

- The mK stage temperature is set as described in sec. 3.1.5.
- The desired frequency range is determined from a VNA measurement. The readout box is switched to IQ readout mode. The 1 kHz filter is used in front of the ADC. The resolution, an averaging factor (≈ 20) a delay (100 ms) and a sample rate (4 kHz) are set in the software.
- From start and stop frequency and the resolution the frequencies at which measurements are made are calculated. For each frequency:
 - The synthesizer is programmed to the next frequency to generate the signal.
 - The software waits for the selected delay to make sure the communication with the synthesizer is finished and the synthesizer can set and stabilize the frequency.
 - A number of samples given by the averaging factor is recorded from the ADC from the I and Q channels.
 - The samples are averaged and stored together with the frequency
- The acquired IQ data is saved for later correction and processing.

The resolution of the measurement is specified by the number of frequencies to record in the given interval. The start and stop frequencies, the sample number, the delay, the

synthesizer power, the sample rate and the averaging factor are adjustable parameters. The values given above are typical for most measurements done in the following. The sample number has the strongest influence on the measurement time and has to be set to the need of the measurement, as for resolving individual resonances, high resolution is required while for sweeps intended for calibration of the IQ mixer, a more coarse resolution is favorable.

3.4.3 Measurement of time domain data for noise analysis

The noise power spectral density is calculated from time domain measurements. To achieve a good coverage of the high and low frequency sides, the time domain measurements are split in two measurements at two sampling frequencies. The typical time domain measurement procedure is:

- The temperature of the mK stage is set as described in 3.1.5.
- The resonance frequency of the resonator is determined from the lowest point in a VNA scan of the resonance. Since the synthesizer and the VNA use the same reference oscillator, the frequency axes match.
- An IQ mixer frequency sweep (3.4.2) that covers the resonance and a bit of the frequency range around the resonance is measured. This measurement should contain a few revolutions in the IQ plane caused by the cable length. This data is used later for error and offset correction.
- The readout tone is set to the resonance frequency and the 1 kHz filter is attached to the ADC. Then 10 times 8 seconds of data is recorded at 4 kHz sampling frequency.
- The readout tone is set at a frequency close to, but off the resonance frequency to record a reference.
- Now the 260 kHz filter is connected to the ADC and the above two measurements (on and off resonance) are repeated. 30 times 0.16 s of data are measured on and off resonance at 1 MHz sample rate.

The recorded data is saved in a binary format containing the full time domain data set. An ASCII file containing only the averaged spectrum is also saved which is useful for a quick look at the data. The binary format is chosen for the full set to reduce the hard disk space requirement and processing speed in comparison to ASCII files. The binary archives easily reach sizes of 200 megabytes already for one measurement. These files together with

the IQ measurements are then further processed by my analysis software as described later in sec. 6.5.3.

The recording sample rate can be set freely in the software, but the two values mentioned in the process above are consistently used. The sample number resulting in the record duration is limited to powers of 2 to allow for the use of a real fast Fourier transform (FFT) algorithm on the discrete time domain data which considerably speeds up the later processing in comparison to a slower discrete Fourier transform (DFT). The run time of the FFT algorithms generally scales with $\mathcal{O}(N \log N)$ where N is the number of time domain samples while the standard DFT run time scales with $\mathcal{O}(N^2)$. The synthesizer output power is kept at a constant value of 13 dBm which gives the required input power for the IQ mixer.

3.4.4 LED pulse

In this measurement the detector is excited with an optical pulse from an LED coupled to an optical fiber and the time domain response of the detector using the IQ mixer.

The pulse is generated from a DAC in synchronization with the ADC. The pulse signal drives an LED driver circuit with variable output current. For the following measurements, the 260 kHz filter is used in front of the ADC.

The measurement of a single pulse is done as follows:

- The temperature of the mK stage is set as described in 3.1.5.
- The synthesizer frequency is set to the resonance frequency of the resonator to be measured which is previously determined by VNA measurements.
- The LED current is set using a potentiometer on the driving circuit. The readout tone of the synthesizer is set exactly on the lowest point of the resonance feature.
- The DAC and ADC are started synchronously with a sampling frequency of usually 1 MHz. The ADC records the I and Q signals.
- After a delay to get the baseline before the pulse, the DAC generates a rectangular 5 V pulse with adjustable duration of usually 50 μ s.
- The acquisition is stopped after a few ms and the whole process is repeated 20-100 times to average the pulses.

The delay, the pulse duration, the sampling frequency and the averaging can be set in the measurements software. The pulse duration is chosen to a minimum where the pulse is

still clearly detectable. If the pulse is too short, the capacity in the driving circuit and the cables will distort the signal. The response of the driving circuit is verified in a separate measurement without an LED.

3.4.5 Search for Cosmic ray events

Dependent on the substrate volume on the devices, radioactive high energy particles or photons as they occur in the cosmic rays generated in our atmosphere can excite resonators. These appear as strong peaks in the IQ data of some measurements and tend to disturb noise measurements. To prevent disturbance of e.g. the calculated power spectra, the time domain data is visually inspected for strong peaks. The contaminated data sets are then removed from the later analysis.

On the other hand, cosmic ray events can be used as a diagnostic tool when measuring quasiparticle lifetime as they offer another way to excite the device. To actively search for cosmic ray events, data is acquired using the IQ mixer setup with the readout tone set on a resonance. Then chunks of 10 seconds are recorded at a sampling frequency of 100 kHz. The digitized I and Q data is then inspected for peaks. 1 MHz would give higher resolution, but would also need a factor of 10 more memory and 100 kHz is sufficient to see and analyze these events because the time resolution of 10 μ s resolves the \approx 100 μ s pulses.

3.5 Measurement setup for different devices

Three different MKID device types are measured and analyzed in this thesis. Each of them requires adaptations of the measurement setup at the mK stage to accommodate for the different dimensions and designs. The setup of the mK stage and the mounting of the devices is described in the following sections for the three designs.

3.5.1 Cold setup for waveguide coupled devices

The design of the WGKID devices is described in chapter 4. The devices are mounted in detector blocks which are fabricated in our institutes workshop. In the blocks, the waveguide back short and the substrate channel are created by consecutive stamping and milling steps till the desired depth is achieved. The broad side of the substrate channel is completely milled. The blocks are processed on a Kern Evo milling machine out of Copper-tellurium. A microscope image of the waveguide and substrate channel and a photograph of a complete block is shown in fig. 3.13 and 3.14.

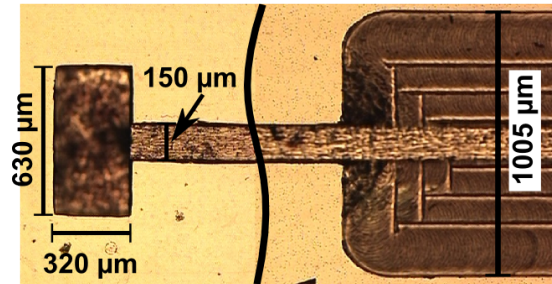


Figure 3.13: The waveguide and substrate channel in a Copper-tellurium metal block. The waveguide on the left and the substrate channel are machined using a stamping and flat milling process. The wide area for the readout part of the substrate is milled using a 100 μm diameter milling tool on a Kern high precision 5 axis milling machine.

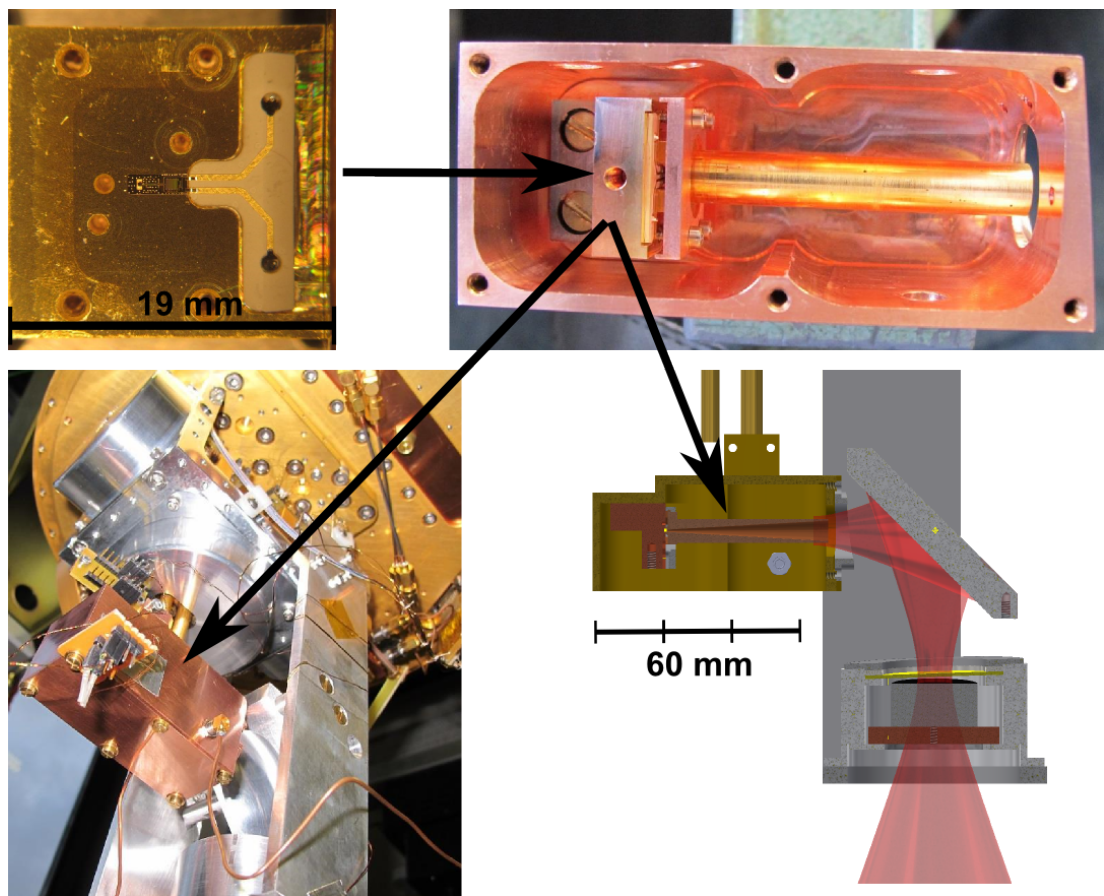


Figure 3.14: **Top left:** The TMKID device on a 9 μm silicon membrane is mounted in a Copper-tellurium block using ultrasonic bonding. **Top right:** The block with the horn antenna is mounted in a OFHC Copper outer box. **Bottom left:** The outer box is mounted on the mK stage of the ADR. **Bottom right:** The horn antenna looks through a mirror and two filters at the black body load described in sec. 3.2.1. The cut shows the propagation of the 350 GHz gaussian beam.

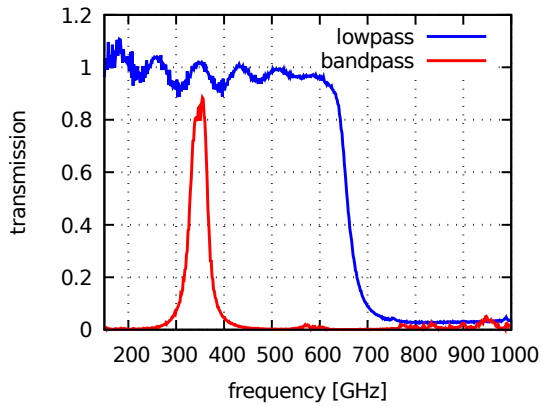


Figure 3.15: Transmission of the QMC 650 GHz low pass filter and 350 GHz low pass filter measured with our Menlo Systems terahertz time domain spectrometer. The peaks in the stop band are artifacts of the normalization resulting from low output power probably due to water line absorption. These features are not visible in the raw data.

The readout connection of from the device to SMP connectors is done using a milled TMM 10 circuit board, to which the screw-in SMP jacks are soldered. It was verified in simulations that no significant crosstalk of the lines on the circuit board takes place.

The device is mounted in the block such that the waveguide probe aligns with the stamped waveguide in the block. The device is fixed with ultrasonic bonding impulses on the beamleads. On top of the device the horn is mounted such that the horns waveguide directly matches the blocks waveguide.

Since it has been proven that good radiation shielding is essential for low noise MKID detectors, the detector block with the horn is mounted in a Copper housing also cooled down to the MKIDs temperature of about 100 mK.

The MKID will be illuminated with thermal radiation from the black body calibrator described in sec. 3.2.1. A QMC instruments 650 GHz low pass filter mounted directly on the housing of the load limits the output band of the thermal radiation. The radiation can enter the Copper block via a cold 350 GHz band pass filter also made by QMC instruments. The performance of the two filters on the load and on the Copper housing was verified with a terahertz time domain spectrometer shown in fig. 3.15. At 350 GHz, the combined transmission of the two filters transmission is 84.3% and nearly fully determined by the band pass filter, since the low pass has an upward fringe right at that frequency.

Since the heatable black body load could not be mounted in line to the housing, a refocussing mirror is necessary to transform the horn beam onto the load. The elliptical mirror is CNC milled out of aluminum. The beam waist is considerably smaller than the load diameter, therefore the load is considered to fill the detectors aperture completely. The optical arrangement will also allow the detector beam to protrude to the outside of the cryostat when the load is removed and windows are installed. This will be necessary in later stages of the MKID development.

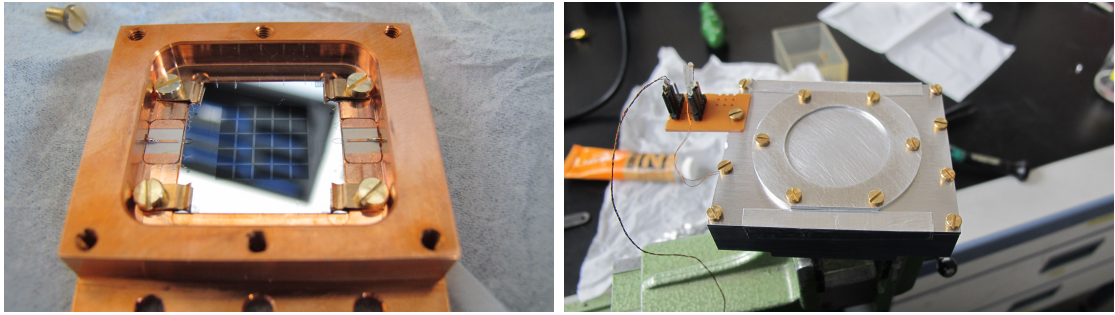


Figure 3.16: Left: The copper fixture manufactured at our in-house workshop with an NIKA chip mounted using beryllium copper springs. **Right:** The dark setup. The box is closed with a aluminum disk containing a 0.1 mm hole in the center.

3.5.2 Cold NIKA chip measurement setup

Since the NIKA 2 MKID is a completely different device than my waveguide coupled MKID, a new housing for mounting the chip on the mK stage of the ADR cryostat is designed and manufactured in our workshop. The housing is made of OFHC Copper for optimal thermal conductivity. The chip is fixed in the housing with four Beryllium-Copper springs and a slight amount of Apiezon-N grease is used underneath the chip to improve the thermal contact to the milled surface. The chip mounted in the Copper housing is shown in fig. 3.16. Because the devices are sensitive to magnetic fields, the Copper box is again mounted in an outer aluminum box. Aluminum becomes superconducting at temperatures below 1.2 K and a closed box provides a good magnetic shield due to the Meissner effect. Superconductors have a low thermal conductivity in the superconducting state, therefore a plug made of oxygen free Copper (OFHC) connects the inner Copper fixture to the mK stage as can be seen in fig. 3.17. To maintain the magnetic shield, the Cooper plug is coated with 200 nm sputter deposited aluminum. The whole assembly is then mounted on the ADR mK stage.

Dark setup For minimal optical loading, the copper box is closed with a lid containing a 1 mm hole in the center to allow excitation of the chip with an optical pulse. The copper box is then placed in a second box made of aluminum for shielding the magnetic field. To enhance the thermal conductivity between the inner box and the cold finger of the cryostat, a copper plug on the bottom of the outer package is used. It is sputtered with aluminum to maintain the magnetic shield (fig. 3.17). A Lakeshore ruthenium-oxide temperature sensor type RX-102B-CB is mounted on the inner copper box and consecutively used to determine the sample temperature. The aluminum box is closed with a lid containing a 40 mm socket to hold a QMC instruments wire mesh filter. For the dark measurements,

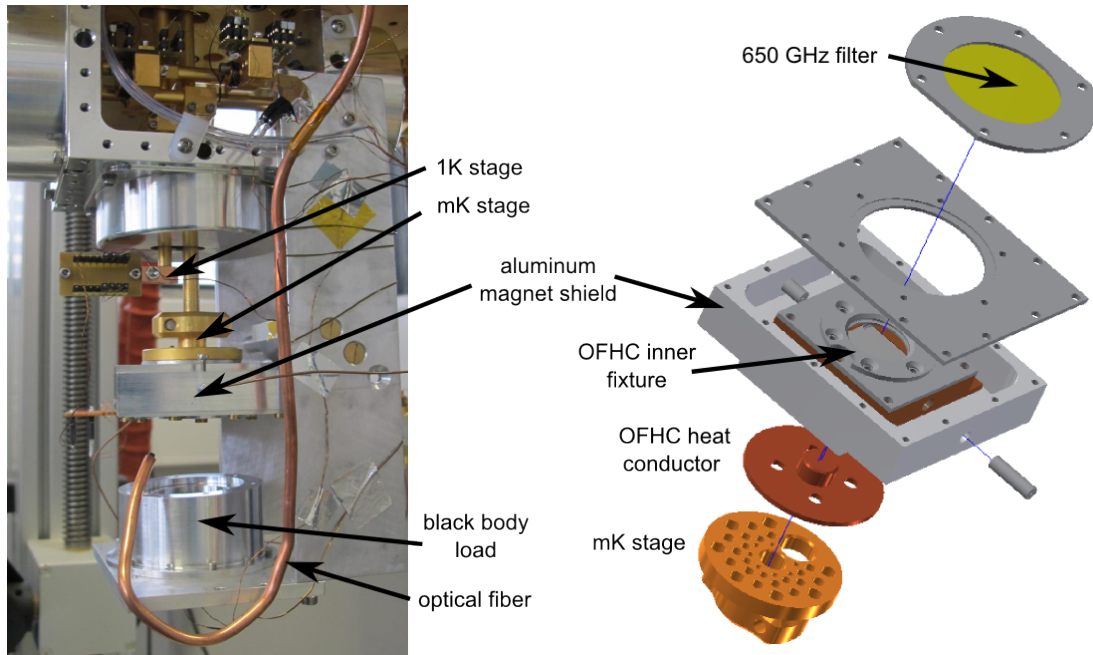


Figure 3.17: **Left:** The NIKA housing mounted on the mK stage of the ADR. The heatable black body load is mounted in front of the optical access. The copper tube guides the optical fiber which points at the device. **Right:** CAD drawing illustrating the assembly of the NIKA fixture. The aluminum package shields magnetic fields but has inferior heat conductance at low temperatures, therefore an OFHC copper plug sputtered with a thin aluminum layer thermally connects the mK stage with the sample fixture.

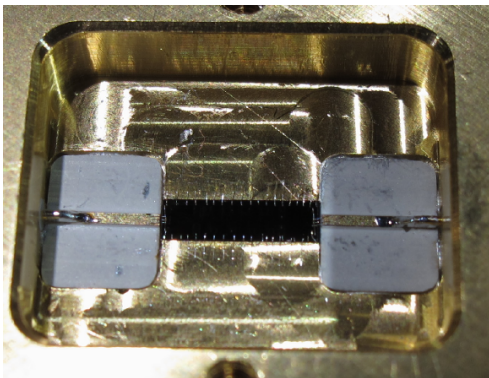


Figure 3.18: Inside of the NbTiN test chip. Wire bonds establish the electric connection for signal and ground. The signal connections lead to two TMM 10 circuit boards to which screw-in SMP connectors are soldered.

the filter is replaced with an aluminum disc containing a 0.1 mm hole in the center that acts as a high pass filter [9]. It is designed to block thermal radiation of the 3 K background of the surrounding shield but let an optical pulse pass. The whole package is mounted on the cold finger of an ADR cryostat that reaches a base temperature of about 40 mK.

Optical setup For measurement of the chip under optical loading, the copper fixture is left open and the aluminum magnetic shield is closed with a 650 GHz low pass filter. For this setup, the black body load (sec. 3.2.1) is placed directly in front of the opening in the aluminum magnetic shield. The load is however considerably smaller than the limiting aperture of the copper fixture, therefore to calculate the power which is received by the chip from the load, the solid angles associated with the geometry has to be calculated in detail.

niobium magnetic shield As one of the final modifications to the measurement setup, a film of niobium is sputter deposited on the inside of the outer aluminum package shown in fig. 3.16. The thickness of the film is between 80 nm on the vertical walls and about 300 nm in the center. The purpose is to shield magnetic fields above the transition temperature of the test devices which is higher than the transition temperature of bulk aluminum (1.4 K vs. 1.2 K). The transition temperature of the niobium produced in our sputter deposition system usually exceeds 8 K and is far above the value for aluminum. Therefore the niobium is supposed to shield the samples before they become superconducting and can freeze in flux, which deteriorates the performance of an MKID [38].

3.5.3 NbTiN test chip setup

The NbTiN test chip was developed and tested in my master thesis. The measurement is described in Appendix A. The chip is mounted in an OFHC copper fixture with a bit of Apiezon N cryogenic grease to improve the heat conductance (see fig. 3.18). The chip is electrically mounted to the fixture and the read out lines using aluminum wire bonds. Many bond wires are placed on the long sides of the 2 mm by 8 mm devices. The signal connection between the device and the SMP connectors are made with milled circuit boards made of Rogers TMM 10 high frequency laminate. The fixture is closed with a copper lid to prevent stray radiation from reaching the device. The fixture with the chip is mounted on the ADR mK stage using an adapter.

4 Design and simulation of a waveguide coupled MKID

The long-term goal of the MKID development is to design a camera for an instrument like prime-Cam on the CCAT-prime telescope. The most striking argument for using MKID is their intrinsic aptitude for frequency multiplexing. This on the other hand means, that an MKID camera has to exploit the limits of pixel density to compete with technologies like the TES bolometer, which also achieves background limited sensitivity. A competitive MKID instrument needs pixel numbers exceeding 10000, ideally with the potential to enter the mega-pixel range.

The A-MKID instrument already mentioned in sec. 2.4 goes in that direction. Unfortunately, the instruments showed erroneous behavior on the telescope which is not diagnosed up till now. My approach is to take a step back and investigate the absorption process in MKID in more detail to increase the understanding of MKID sensitivity under optical conditions. Since our research group has a lot of experience with waveguide coupled heterodyne mixers, my idea is to build an MKID with the same high frequency design that has proven to work with an SIS mixer. That way I can be sure that the optical coupling to the detector is working and focus the experiment on the absorption and detection process.

In this chapter the design of a 350 GHz waveguide-coupled MKID is described. First the design goals and constraints are defined and the basic high-frequency components are described briefly. Two different MKIDs are designed in this chapter. First, a waveguide coupled lumped-element MKID is presented. Then the design of a waveguide coupled transmission line resonator MKID is shown. Finally, the steps towards the fabrication of the devices are outlined.

4.1 A waveguide coupled MKID Detector

The intention of the waveguide coupled MKID design is to understand the limits of sensitivity by reducing the number of unknown parts of the detector. This sets the focus of the measurement and analysis on the absorption and detection process. This is achieved

by using a waveguide and antenna design that has proven to achieve nearly quantum limited sensitivity with SIS mixers at 350 GHz [3]. Focus of the new design is an efficient absorption of the signal in the sensitive volume of the detector in combination with a low detector volume. Other existing MKID designs which use a waveguide and a horn antenna can be found in [20, 29, 68].

4.1.1 Design decisions and constraints

The design goal presented above has to obey some practical and physical constraints that have to be accounted for during the design process.

- The center frequency of the sensitive detector band is decided to be set to 350 GHz, which is a frequency of scientific interest for ground based observations. Our group already build SIS detectors with quantum limited sensitivity for that frequency and thus has experience in design and measurement. Also, suitable measurement equipment is already available.
- The readout frequency should be low to prevent excitation of the MKID by multi photon events and reduce TLS noise [106]. A low resonance frequency requires large capacitors and inductors and increases the size of one detector pixel. As a compromise and to stay in the operating frequency range of the existing read-out electronics we choose 2.5 and 4 GHz resonance frequency variations.
- The superconductor has to be lossy at the design frequency of 350 GHz and still be superconducting at the maximum readout frequency of 4 GHz (sec. 2.1). On the practical side it should be available for thin film processing and sufficiently robust to make thin films on silicon substrates. We choose aluminum as inductor material, because the results of other groups show outstanding performance with this material [2, 37].
- The signal radiation has to be efficiently absorbed in the inductor. Since the quasi-particle density is the important parameter, a low inductor volume increases the response of the detector. Both can be helped by reducing the thickness, but there are mechanical limits. Preparatory experiments show that 40 nm aluminum films can be fabricated in our microfabrication laboratory with good quality and yield.
- The substrate on which the detector circuit is based on must be suitable for 350 GHz, which specifically means that it has to be considerably thinner than the wavelength in silicon at this frequency. Considering the frequency, mechanical stability of the chip and the available technology, 9 μm thick silicon membrane substrates are chosen.

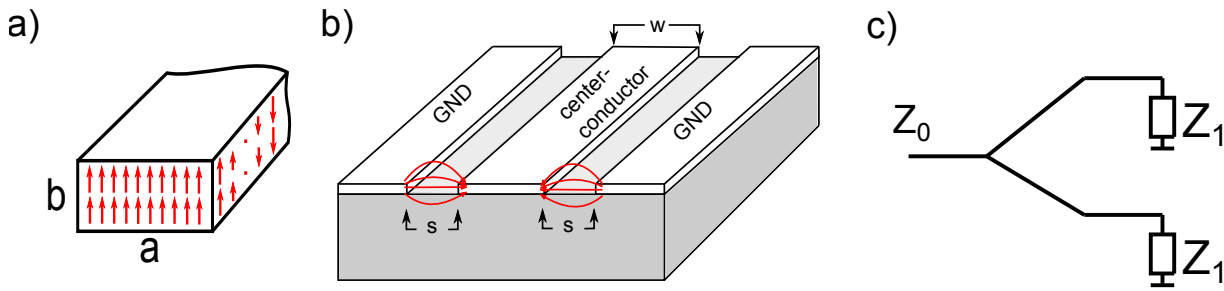


Figure 4.1: (a) Sketch of a rectangular waveguide. Indicated in red is the electric fields in its TE₁₀ mode, which is commonly used. (b) Drawing of a coplanar waveguide transmission line cut at the front and at the sides. (c) Schematic of a simple power divider terminated into loads Z_1 .

4.1.2 Simulation software

The design process of the MKIDs is supported by advanced electromagnetic simulation software. The software used is industrial standard for designing high frequency circuits. My simulations go beyond the usual application because the frequencies for the RF circuit exceed those of industrial interest and the superconductors in the readout circuit have to be simulated correctly.

For designing the 350 GHz parts like the waveguide, the waveguide probe, and the absorber lines, the software CST microwave studio [92] is used. This software does a full 3D simulation of the circuit on the chip and of the surroundings. For simulating a superconductor, the surface impedance is calculated using the standard Mattis-Bardeen theory (see sec. 2.2.5) and fed into CST as a tabulated surface impedance for the required frequency range. Internally, this impedance is fitted as a polynomial and used as a material parameter for the superconductor. For all CST simulations the transient solver is used, combined with adaptive mesh refinement for the final simulations. The model is usually created fully parametrized which allows the use of parameter sweeps in CST to optimize the design. The diagnostic features allow to view the field and current distribution at preselected frequencies which is helpful to ensure that the circuit operates as expected. The results are the scattering (S) parameters to and from the defined ports.

The low frequency parts like the resonator and the feed line couplers are simulated using Sonnet EM [35]. This software is better suited for simulations of two-dimensional circuits with multiple layers. The simulation environment is always a rectangular box, therefore only sections of the circuit are simulated as the full chip geometry can not be implemented. The superconducting material properties can be included defining an arbitrary impedance metal with a certain surface impedance. No frequency dependence can be inserted here, therefore care must be taken for wide-band simulations. The frequency range of interest

here is far below the superconducting gap and does not change significantly. The solver of Sonnet EM calculates a full solution of the circuit in the frequency domain at a few frequencies. It then uses fast adaptive methods to interpolate between the full solutions to obtain the transmission and reflection to and from the defined ports. Also the surface current distribution can be calculated for diagnostics.

4.2 Transmission lines

High frequency signals are transferred using special transmission lines. Two transmission lines are predominantly used in my design, the rectangular waveguide fed by a horn antenna and the coplanar waveguide on chip.

4.2.1 Rectangular waveguide

The rectangular waveguide is a high frequency transmission line that guides the signal through a rectangular conductive cavity (see fig. 4.1 a). Unlike other transmission lines, the cavity is the only conductor and no 'second wire' is needed. The propagating modes are either transversal electric (TE) or transversal magnetic (TM). The mode with the lowest propagation frequency is the TE₁₀ mode, that is illustrated in the figure. This mode is usually the desired one for waveguide operation. Each mode has a specific frequency band at which it can propagate, set by a low cutoff frequency at the wavelength defined by the dimensions of the waveguide a and b and the mode indices m, n . The cutoff wavelength for the TE _{m n} modes are given as [63]

$$\lambda_{ci} = \frac{2\sqrt{ab}}{\sqrt{m^2\frac{b}{a} + n^2\frac{a}{b}}} \quad (4.1)$$

The high frequency end of the operation band is reached when the wavelength becomes comparable to the waveguides dimensions. Then the waveguide becomes overmoded, and higher modes are excited. Consequently, the power is lost in the fundamental mode which is the one that can be extracted by waveguide probes. Waveguides in single mode operation have several advantages that are utilized in this application:

- Waveguides are usually coupled to free space using horn antennas. These are designed to give a very clean Gaussian shaped beam that can be directly processed by the attached optics.
- Because of the large conductor area, waveguides have rather low loss, but can still not compete with superconducting transmission lines.

- Signals in a single mode waveguide can be efficiently extracted to an integrated circuit, like a MKID using waveguide antennas.
- Rectangular waveguides in single mode operation have a distinct polarization along the short side (E-plane) of the rectangle.
- The waveguide cutoff frequency is a very efficient low-pass filter.

Besides rectangular waveguides, also circular or more seldom elliptical waveguides exist.

4.2.2 Coplanar waveguide transmission line

The coplanar waveguide (CPW) line is a planar transmission line for high frequency signals. Its layout is shown in figure 4.1 b). The CPW is patterned in one single metal layer and does not require additional dielectric, besides the substrate where it rests on. The reverse side of the substrate can also have a metal coating, then one talks of a conductor backed CPW. The desired transmission mode of the CPW is a symmetric (quasi) TEM mode where the electric field is always in the image plane perpendicular to the line, located in the slots between the center conductor and the ground planes. If excited asymmetrically or when confronted with discontinuities, odd modes where each of the slots behaves like a slotline transmission line can occur. To prevent odd-mode excitation, conductive bridges can be placed across the CPW which connect the ground planes on both sides. The bridges enforce a common ground potential and suppress the odd mode. The impedance of the CPW is determined by the capacity given by the gaps and the dielectric substrate and the line inductivity of the center conductor. A low impedance line has narrow gaps and a wide center conductor while a high impedance line has wide gaps with a narrow center conductor. The impedance of the line can be calculated analytically as shown in [91], but because of the special requirements (very high frequencies and superconducting or lossy materials) the impedance is determined using parameter sweeps in EM simulations, which are computationally cheap to perform and more accurate. This way also the lossy center conductor of the absorber line can be easily analyzed.

4.3 The waveguide coupled lumped element MKID (WGKID)

As mentioned above, the detector designed here is a waveguide coupled MKID. Two main variations are designed: One MKID design attaches a lumped-element type resonator to

the waveguide antenna and the other uses a transmission line resonator. The latter one is described in sec. 4.4.

The lumped element MKID detectors (LEKIDS, [31]) are usually used to shape the inductive section of the MKID such that it can immediately be matched to the free-space impedance. In my horn-coupled design, the freedom of choice of the inductive section is used to shape an efficient absorber. Also, the current density in an LEKID is uniform over the length of the inductor. The response to changes in kinetic inductance is only detectable in the parts of the resonator where the current is high. Therefore, it is expected to have a good response to generated quasiparticles in my design as they can not diffuse out of the high current parts. By making only the absorber lines out of aluminum and the rest of the circuit out of niobium, quasiparticles generated in the aluminum will be trapped as they do not have enough energy to enter the niobium, because the gap energy is higher in the niobium film.

The rough idea of the detector with a lumped element type resonator is sketched in fig. 4.2. The 350 GHz signal coming from the telescope is received by the horn antenna and fed into a waveguide. From there it is extracted by a waveguide antenna onto the 9 μm thick silicon chip with the MKID circuit on. The 350 GHz signal is split into two absorber lines made of aluminum. The center conductor of these lines forms one turn of an inductor, which together with an interdigital capacitor forms a superconducting resonator at the readout system frequency. This lumped element type resonator probes the kinetic inductance in the aluminum absorber lines.

The 350 GHz signal path is followed starting at the antenna in the description of the parts of the complete design. A CAD rendering of the finished WGMKID design is shown in fig. 4.3.

4.3.1 Horn antenna and waveguide

The horn antenna to couple the free space radiation into the waveguide is a corrugated spline profile feedhorn designed for 350 GHz and verified in heterodyne measurements. The horn antenna is positioned on the top of the chip such that the waveguide aligns perfectly to the waveguide in the bottom part of the fixture and to the chip. The dimensions of the signal input waveguide are (fig. 4.3 a) 315 μm by 630 μm , optimized for the TE₁₀ mode for 350 GHz. Using (4.1), the low cutoff frequency is calculated as 238 GHz. A waveguide back short located 240 μm behind the substrate matches the waveguide antenna to the waveguide.

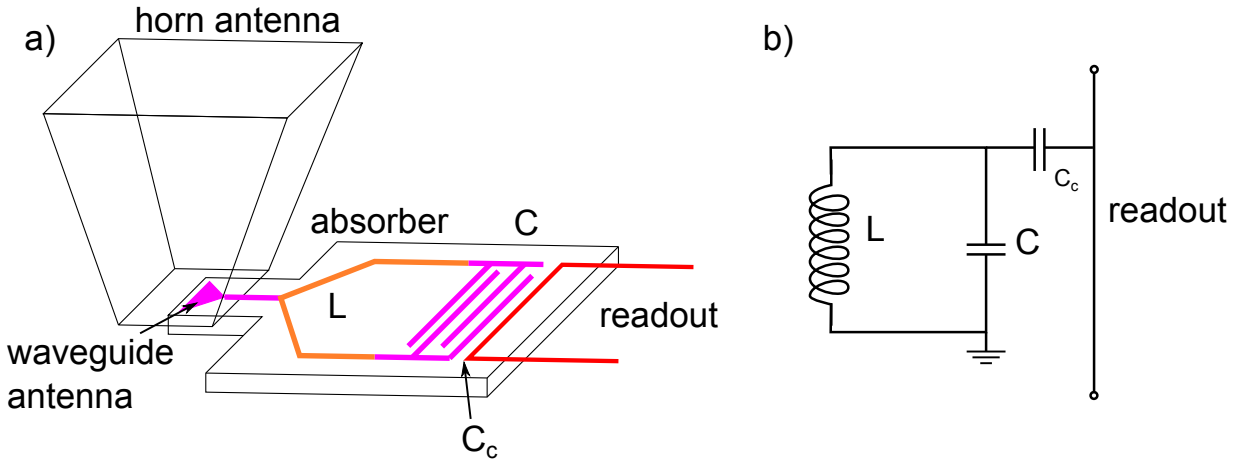


Figure 4.2: (a) Schematic overview of the new waveguide coupled MKID design with the lumped element resonator. The signal is collected from free space using a feed horn on a waveguide and coupled to the detector chip using a superconducting waveguide probe. Then it is absorbed in the low- T_c inductive section of the LEKID resonator. (b) Equivalent circuit diagram for the lumped element type resonator.

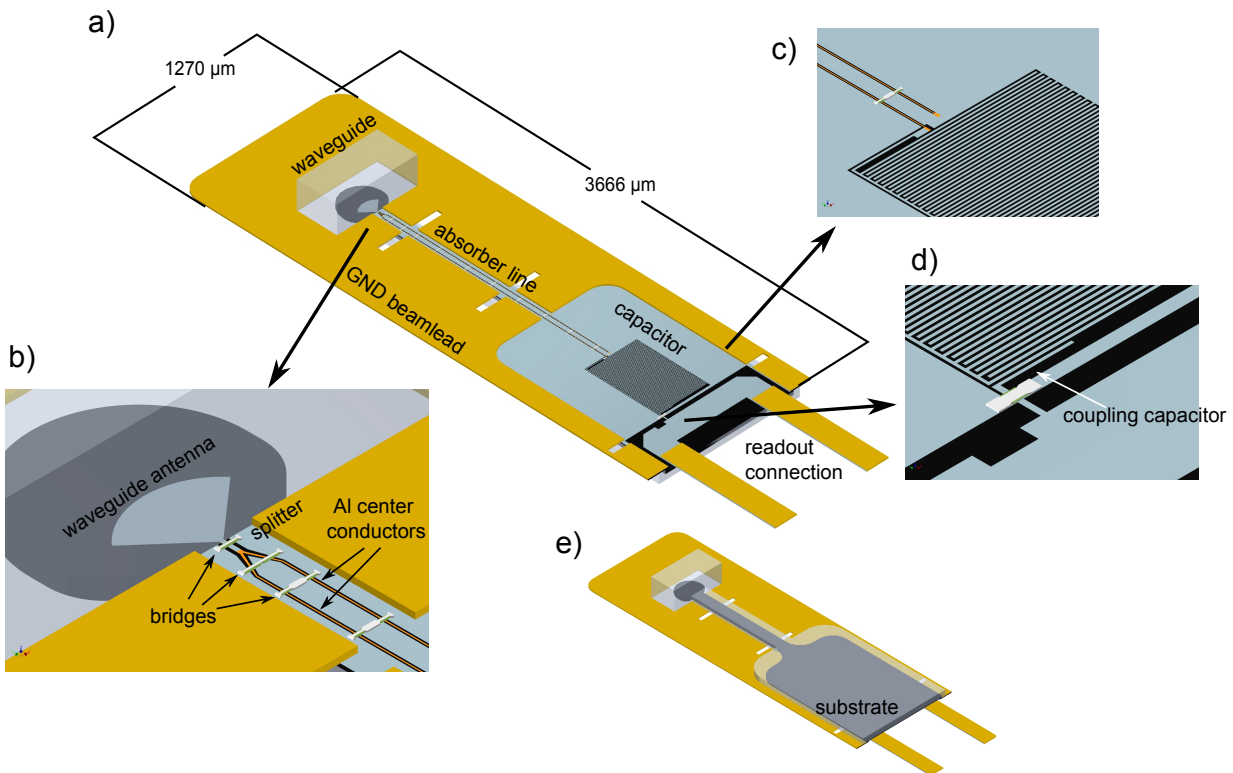


Figure 4.3: CAD rendering of the finished WGKID Chip. The layer thickness is exaggerated for better visibility. The materials are: Silicon: black, gold: yellow, niobium: blue, aluminum: orange, SiO_2 : green. The waveguide and surrounding substrate channel are indicated with transparent shapes. For a full description see sec. 4.3.

4.3.2 Waveguide probe and substrate

The probe design is adapted from a 350 GHz SIS mixer [3] developed in our group and modified to a different impedance on the output. It is a radial wide band probe as described in [58]. The antenna requires a 9 μm thin silicon substrate which is specially shaped and protrudes the waveguide from the broad side. The radial probe has a radius of 109 μm and an arc angle of 98° , which is 1.7 rad. This is shown in fig. 4.3 a) and b). The antenna impedance is matched to the impedance of the coplanar waveguide line (CPW) at its output, which is $35\ \Omega$. It has a center conductor width of 6 μm and a gap width of 5 μm . A first bridge of made of niobium on 400 nm SiO_2 dielectric spans the coplanar waveguide line to prevent the excitation of odd modes. Since the Antenna and the connected CPW line are not part of the sensitive area of the detector, no radiation should be absorbed there. Therefore, these parts are made out of superconducting niobium for minimum loss at 350 GHz. The antenna and the CPW dimensions are optimized using a CST microwave studio 3D simulation.

4.3.3 Symmetric 3 dB power splitter

The coplanar waveguide from the waveguide probe is split into two absorber lines which then form the inductor for the readout resonator. For that, a symmetric power divider is used in its most simple form as shown in fig. 4.3 b). The output impedance of the power divider can be simply analyzed by assuming the two output lines are each terminated with a characteristic impedance Z_{out} (see fig. 4.1 c). Then the input impedance is related to the output as

$$Z_{\text{in}} = Z_{\text{out}}/2 \quad (4.2)$$

The electrodynamics of the actual geometrical shape of the splitters can not be described analytically in such a simple way, therefore for the design a CST simulation is done. The advantage of this splitter is that it does not need any resistive components like a Wilkinson power divider and is therefore lossless. On the other hand, the output impedances are different than the input impedance and this splitter does not perform well if it is driven asymmetrically from one of the output ports.

The absorber line impedance is connected to the antenna impedance by eq. (4.2). The absorber line impedance has to be chosen such that the impedance at the antenna output is not too low to be matched to the antenna and that the absorber line impedance is not too high. If the gaps of the absorber lines become too wide, the capacity to the top metal cover, which is only 3 μm apart from the circuit, will dominate and the line will behave like a microstrip. This is expected to degrade the quality factor of the resonator because the

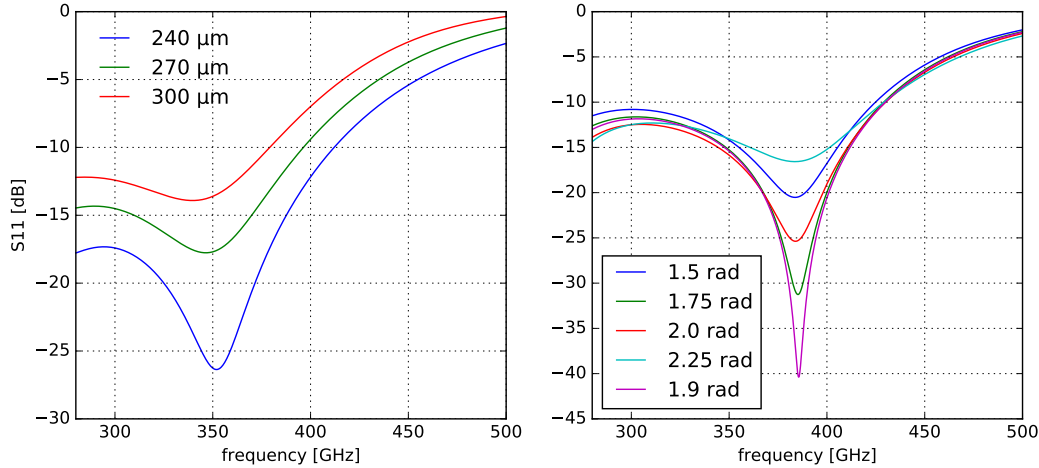


Figure 4.4: **Left:** Input reflection seen from the waveguide for different depth of the backshort. The antenna angle was set on 98° and the distance between the coupler and the antenna is $22.5\ \mu\text{m}$. **Right:** Input reflection seen from the waveguide for different opening angles of the waveguide antenna arc segment. The distance between antenna and coupler here is not optimal yet, therefore the overall transmission is low.

top wall of the detector fixture, which is made of normal conducting copper, would also be part of the transmission line. As an compromise, an antenna CPW impedance of $35\ \Omega$ and an absorber line impedance of $70\ \Omega$ are chosen. The ground plane between the arms of the splitter has to be properly connected to the system ground using dielectric bridges. The inner conductor of the splitter is part of the inductor loop of the readout resonator and is therefore part of the sensitive volume of the detector. Because of that, the inner conductor is made of thin ($40\ \text{nm}$) aluminum and the ground planes, which are not part of the inductor are made of niobium.

The simulated performance of the waveguide, antenna and splitter for different antenna parameters is shown in fig. 4.4. This plot shows the input reflection at the waveguide port. Both absorber lines are terminated with simulated waveguide ports which produce a good match. The simulation was performed for different waveguide backshort depths and antenna angles using CST microwave studio. The chosen dimensions for the design are $240\ \mu\text{m}$ backshort depth and 98° ($1.7\ \text{rad}$) antenna angle. As can be seen, a detuned backshort impedes the signal coupling generally, while the antenna angle is related to the resonance feature at $380\ \text{GHz}$. The usable band of this circuit section is at least $280\ \text{GHz}$ to $420\ \text{GHz}$, which gives enough margin to keep the design frequency of $350\ \text{GHz}$ in the band in case of detuning in the real device.

abs. length [μm]	center w. [μm]	gap w. [μm]	total absorption [dB]
820	0.4	0.6	-32.4
	0.8	1.2	-20.9
1750	1.2	2.0	-31.5
	1.6	2.2	-26.2

Table 4.1: Variations of the CPW absorber line dimensions. The absorption has been simulated with Sonnet EM in a planar environment with the normal state aluminum resistance measured at 4.2 K and a thickness of 40 nm. Thin lines are good absorbers but are also very fragile and hard to fabricate, therefore the very narrow lines are shorter to increase fabrication yield.

4.3.4 Absorber lines

The absorber lines are two coplanar waveguide (CPW) lines, where the center conductor is made out of 40 nm thick aluminum and the outer conductors are made out of superconducting niobium. That way the absorption of the antenna signal only takes place in the center conductor which doubles as the inductor of the MKID resonator and quasi-particles are only generated in that sensitive volume. As described above, the absorber line impedance is chosen to be 70Ω . With CPW lines, this impedance can be realized with a variety of center conductor and gap widths. In total, four variations are designed, which are shown in table 4.1. The absorption of these lines is determined by a Sonnet EM simulation assuming a conductivity of the aluminum of $1.35 \mu\Omega \text{ cm}$, which is a value measured for test structures at 4 K before. The two variations with a center conductor width below $1 \mu\text{m}$ have sufficient absorption that the length of the absorber line can be reduced to $820 \mu\text{m}$. This reduces the active volume of the detector and thus increases the responsivity. The shorter lines also reduce the risk of fabrication failures, which is considerable for the small dimensions. The variations with center line dimensions above $1 \mu\text{m}$ use the full length of the absorber line which is $1750 \mu\text{m}$ to get sufficient absorption of the signal. The larger dimensions are expected to be risky to fabricate as well.

To maintain a clean CPW mode, dielectric bridges are placed across the two absorber lines. Each bridge loads the line with a capacitive discontinuity and is a fabrication risk of failing and shorting the center conductor to ground. In this design bridges with 400 nm thick SiO_2 dielectric and niobium top metal are used. The spacing of the bridges is increased with distance from the antenna, because when most of the signal is already absorbed, the problem with odd-mode excitation becomes less severe.

Figure 4.3 e) shows the reverse side of the chip. The $9 \mu\text{m}$ silicon substrate is tailored at the antenna side, since a large air volume under the chip would invite box resonances or signal traveling under the substrate, which should rather be absorbed in the CPW line.

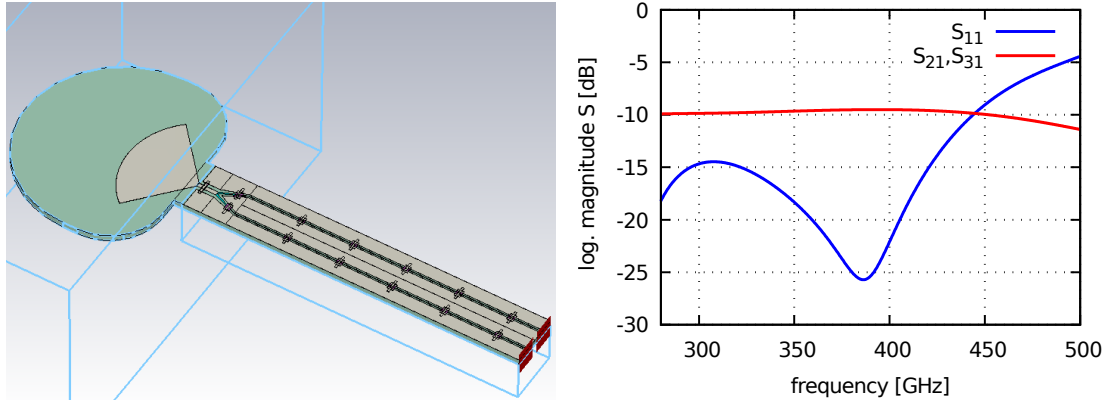


Figure 4.5: **Left:** Picture of the model simulated in CST microwave studio. Port 1, located on top of the waveguide outlined in blue is not shown here. Ports 2 and 3 are at the respective ends of the absorber lines. **Right:** CST simulation results of waveguide, antenna and 450 μm of absorber line with a width of 800 μm . The input reflection is better than -15 dB up to 420 GHz. Actual absorber line length are 1750 μm and 820 μm , therefore the actual absorption will be up to 88 % and 98 % respectively. Note that the simulated line is one of the widest of the design and more narrow lines are much more lossy. Furthermore it is expected that the remaining signal is mostly reflected at the capacitor end and will pass parts of the absorber again.

4.3.5 Lumped element resonator

The readout LC resonator of the MKID is formed by the center conductor of the absorber lines which is superconducting for the frequency of the readout signal and the interdigital capacitor (4.3 c). The connection of the readout line to the capacitor section is made as following. One side of the inductor is just grounded, as one side of the capacitor is always connected to ground as well. The other side goes to the open port of the capacitor. To reduce risk of contact failure between the thin aluminum and the niobium on top, the contacts are all made with pads of larger area.

The capacitor is a so called interdigital or finger capacitor, where the electrical field is located between the fingers which are connected to the two ports of the capacitor. The advantage of this type of capacitor is that it can be fabricated in one layer of metal. It also is not as sensitive to TLS noise as parallel plate capacitors, since the electrical field strength between the fingers is quite low. This also implies the main disadvantage, namely the low capacity per chip area that makes packing chips with thousands of pixels more challenging. To even improve the properties it is planned to etch away the substrate between the capacitor fingers in one design variation. The width of the fingers and the gap between the fingers are 4 μm for 2.5 GHz resonance frequency and 8 μm for 4 GHz resonance frequency.

Because the shape of the inductor is fixed by the absorber line design, the capacitor is

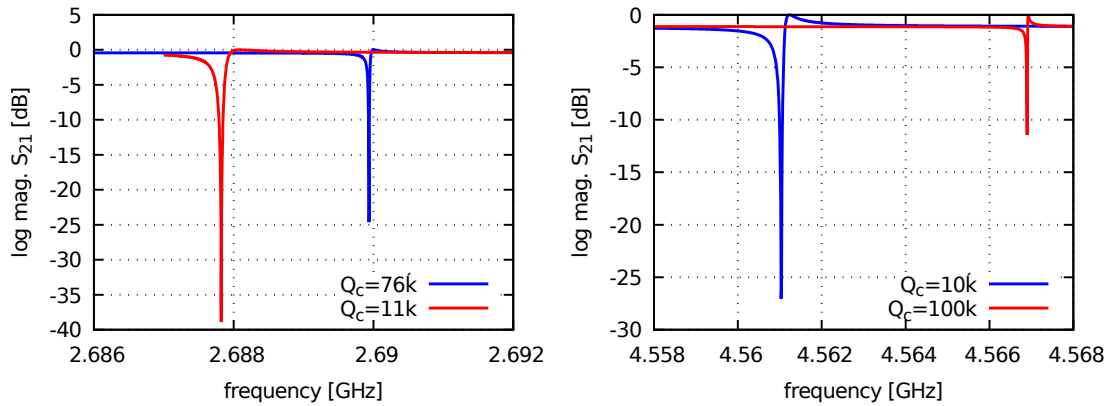


Figure 4.6: Simulated resonance frequencies for the lumped element resonators at different coupler dimensions. The stronger coupled resonances are deeper in this plot because they are better resolved by the simulation. Because the simulation assumes lossless materials, the depth of the resonances has no physical meaning here. **Left:** 2.5 GHz design. The simulated resonance frequencies for low and high Q_c are at 2.687 GHz and 2.689 GHz respectively. **Right:** 4 GHz design. The simulated resonance frequencies are 4.566 GHz and 4.567 GHz.

used to tune the readout frequency to 2.5 or 4 GHz, which are the two selected values. The exact kinetic inductance of the aluminum inductor is unknown during the design phase since the films will be produced on a new sputtering machine not yet available at this point. For initial tuning of the resonance frequency, the kinetic inductance is neglected. For an estimation, the film properties of aluminum from a different sputtering machine is used which gives a kinetic inductance in the thin film limit of 0.36 pH/sq, which can be simulated in Sonnet defining a generic metal (fig. 4.6). The resulting resonance frequency is about 100 MHz lower, which suggests a kinetic inductance fraction of 8%. The real film properties can be determined once real devices are produced.

4.3.6 Connection to the readout system

The resonator is coupled to a readout line using a small capacitor on the bottom of the large interdigital capacitor (fig. 4.3 d). The length of the lines and the gap width define the capacity and thus the coupling strength which limits the coupling quality factor of the resonator, as discussed in sec. 2.2.1. The coupling quality factor can be determined by a simulation where all metals and dielectrics are set as lossless. The width of the simulated resonance feature then is only determined by the coupling.

The readout signal enters the chip via one of the beamleads as shown in fig. 4.3. The line on the chip represents a coplanar waveguide line bent in a U-shape. The width of the line is 170 μm and the gap width is 32 μm . The edges of the line in the bends are cut to

compensate for excess capacity in the corner. Because the length of the line is relatively short in comparison to the readout signal wavelength, this line is not very critical. The readout line is made of niobium and gold to have good transmission of the readout signal even at room temperature. This is very convenient for testing the setup before closing the cryostat.

4.3.7 Inductively coupled design

For experimental reasons as presented in [100] it is interesting to examine MKIDs with an external bias DC current on the resonator line. However, this is not possible if capacitive coupling is used because any extra bias line would automatically load the resonator and lead to a low Q . High impedance can also be realized with large inductance which have low impedance for the DC bias and high impedance for the readout signal to achieve weak coupling. An image of the inductively coupled resonator with an equivalent circuit diagram is shown in fig. 4.7.

The inductively coupled design as realized here has two disadvantages: First the inductors need high inductance to keep the coupling strength low. This requires inductors with large areas and winding numbers, that need a lot of space on the chip and are prone to extra resonances because of the line length. Second, the coupling inductor will form a resonator with the MKID capacitor. This will create even more extra resonances which have to be distinguished from the main MKID resonance. This should however be possible because a much lower Q is expected due to the strong coupling to the feedline than from the main MKID resonance.

The way inductive coupling is implemented here maintains a DC contact to the resonator. It is an option for purely experimental devices with single detectors, but the extra resonances will make it very cumbersome for arrays with many pixels. Coupling the feed line to the inductor instead of the capacitor using an air gap is however more commonly practiced, for example in the NIKA 2 devices also measured in this thesis in chapter 6.

The inductively coupled devices were only designed in this thesis, but could not be measured anymore.

4.4 The waveguide coupled transmission line resonator design (TMKID)

This design uses a quarter wavelength transmission line resonator for measuring the change in kinetic inductance. As an overview, the signal from the waveguide is absorbed in an

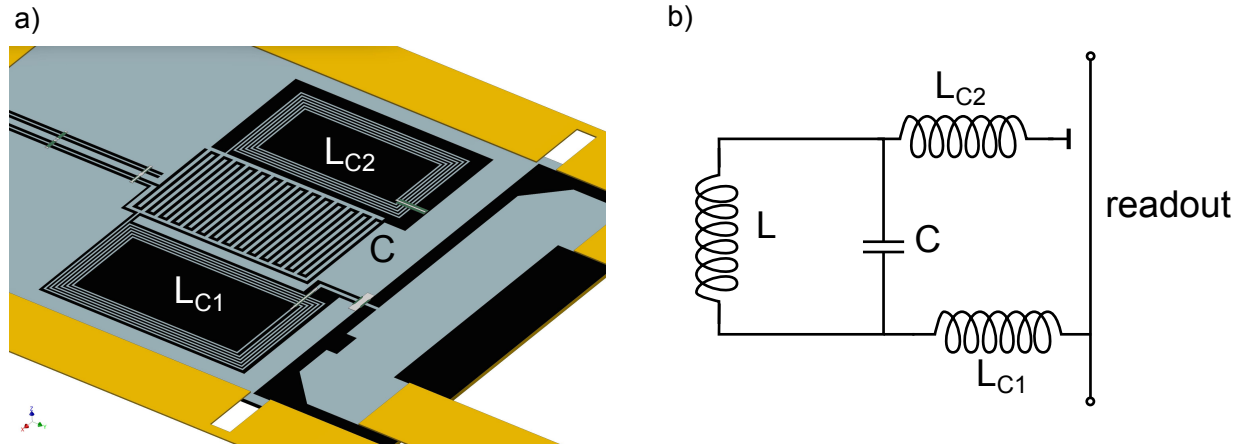


Figure 4.7: (a) rendering of the resonator section of the inductive coupled MKID. The RF design is identical with a TMKID with a short absorber line. L_{C1} and L_{C2} are the coupling inductors. (b): equivalent circuit diagram.

absorber line which is part of a transmission line resonator. The resonator is capacitively coupled to the readout line. A CAD drawing of the design is shown in fig. 4.9. In the following, the description follows the signal path.

4.4.1 Waveguide and antenna

The signal from the telescope is coupled into a waveguide using a horn antenna. To get the signal on the chip, the waveguide probe described in 4.3.2 is used. The radius of the probe is $106\ \mu\text{m}$ and the arc angle is 98° . The probe extracts the signal to a $50\ \Omega$ coplanar waveguide (CPW) transmission line on the $9\ \mu\text{m}$ silicon substrate. It has a center conductor and gap width of $5\ \mu\text{m}$ which compensate for the first dielectric bridge (see fig. 4.9 a). This line is then tapered down to the width of the aluminum absorber line.

4.4.2 readout ground stubs

One challenge of this design is that the transmission line resonator requires a short circuit at the antenna side. This is necessary since the current in a quarter wave resonator is highest at the shorted end, where the resonator is in particular sensitive to a change of kinetic inductance. This short circuit is realized with two coplanar waveguide stubs. The length is approximately $1/8$ th of a wavelength at the signal center frequency of $350\ \text{GHz}$. The two stubs are just a short circuit for the readout frequencies in the range of GHz but transform into an open circuit at $350\ \text{GHz}$ and do not disturb the signal. Dielectric bridges ensure the continuity of the ground plane. The input reflection and transmission of the waveguide, the antenna and the stubs is shown in fig. 4.8.

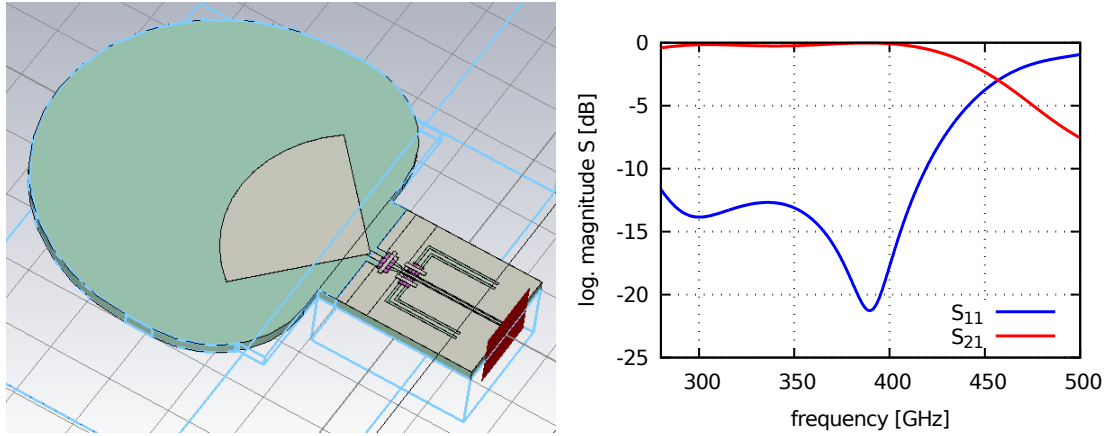


Figure 4.8: **Left:** Model of the TMKID design in CST microwave studio. Only the waveguide, the waveguide antenna and the ground stubs are simulated. **Right:** Simulated reflection and transmission from the waveguide to the beginning of the absorber line. Simulated with CST microwave studio.

4.4.3 Absorber line

The absorber line made of a coplanar waveguide line with an aluminum center conductor is connected to the taper coming from the antenna as shown in fig. 4.9 a). The center conductor has a width of $2\ \mu\text{m}$ and the gap width is $1\ \mu\text{m}$. The total length of the absorber line is $730\ \mu\text{m}$. As determined from Sonnet EM simulation and using the normal state resistance of aluminum determined from DC measurements of $1.35\ \mu\Omega\ \text{cm}$, the line is supposed to have a total attenuation of 11.7 dB. It is however expected that the signal gets reflected at the end of the absorber line resulting in a larger total absorption.

4.4.4 Resonator and Coupler

The absorber line then ends in taper leading to a coplanar waveguide made only of niobium as shown in fig. 4.9 d). The taper transforms the narrow absorber line to a coplanar waveguide with a center line width of $12\ \mu\text{m}$ and a gap width of $4\ \mu\text{m}$. Because the resonator is several cm long, it is meandered for geometrical compactness. Bridges across the CPW suppress the propagation of an odd-mode on the line. The CPW resonator is coupled to the readout line with an elbow-style coupling capacitor (fig. 4.9 d). Four variations of the resonator are designed as combinations of the resonance frequencies of 2.5 GHz and 4 GHz and two coupling quality factors of 10000 and 100000. For varying the resonance frequency, the length of the niobium part of the resonator is changed. The coupling quality factor is varied by changing the length of the elbow coupler. The readout line is identical to the WGKID design and described in sec. 4.3.6.

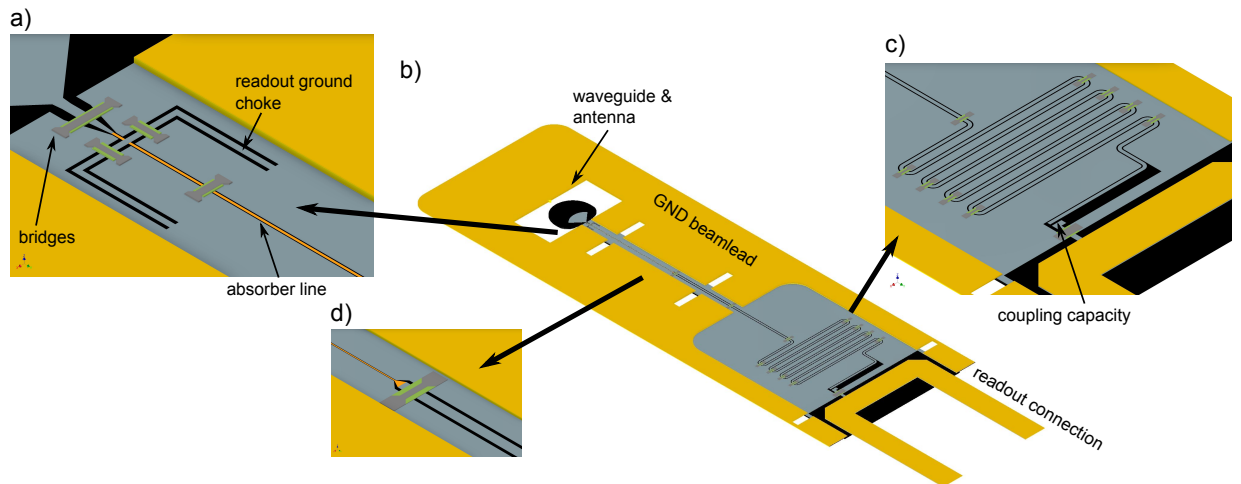


Figure 4.9: Rendering of the finished transmission line resonator (TMKID) design. The layer thickness is exaggerated for better visibility. The materials are: Silicon: black, gold: yellow, niobium: blue, aluminum: orange, SiO₂ : green.

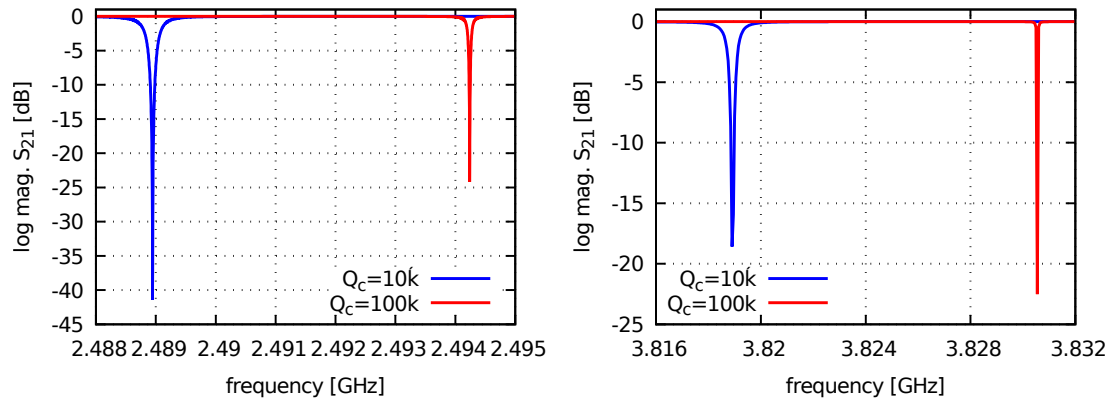


Figure 4.10: Simulated resonance frequencies for the transmission line resonators at different coupler dimensions. The stronger coupled resonances are better resolved by the simulation. Because the simulation assumes lossless materials, the depth of the resonances has no physical meaning here. **Left:** 2.5 GHz design. The simulated resonance frequencies for low and high Q_c are at 2.489 GHz and 2.494 GHz respectively. **Right:** 4 GHz design. The simulated resonance frequencies are 3.818 GHz and 3.830 GHz.

row	design	f_0 [GHz]	$Q_c \times 1000$	l [μm]	c [μm]	g [μm]	comment
A	WGKID-L	2.5	76/11	1750	1.6	2.2	
B	WGKID-L	4	100/10	1750	1.6	2.2	removed substrate in cap.
C	WGKID-S	2.5	76/11	820	0.8	1.2	
D	WGKID-S	4	100/10	820	0.8	1.2	removed substrate in cap.
D	TMKID	2.5	100/10	730	2.0	1.0	
F	TMKID	4	100/10	730	2.0	1.0	
G	INDKID	4	8	820	0.8	1.2	

Table 4.2: Device list for the selected devices which will be fabricated. Each row contains seven devices of which three are of the lower coupling Q_c and four of the higher Q_c . l is the length of the absorber line, c the absorber lines center conductor width and g the gap width. In rows B and D, the substrate between the fingers of the interdigital capacitor is etched away for two of the seven devices.

4.5 Preparing fabrication

The ultimate goal for any design is to become a real detector. After the design process described above there is a assembly of dimensions and CAD drawings that have to be now converted into a lithography mask. The order of fabrication steps, the materials and layer thicknesses (the critical parts are already considered at the beginning of the design process) have to be ultimately fixed and thoughts have to be spent on the global wafer layout and alignment of consecutive layers.

4.5.1 Selection of variations

From the two main designs, the transmission line resonator (TMKID) and the lumped element resonator (WGKID), variations in absorber line width and length, in resonance frequency and in the coupling factor are designed. The device variations selected for fabrication are presented in table 4.2. The selection is rather conservative in the sense that the less critical dimensions are chosen where possible. Each row on the wafer contains seven devices.

4.5.2 Layer order and thicknesses

For patterning the layers, two lithography methods are used. The necessary information during the design stage is that with ultra violet lithography (UV) all large structures have to be patterned. The alignment accuracy between two layers is about $2\mu\text{m}$. For very critical structures, electron beam lithography (EBL) is used. Only small structures can be patterned, but the alignment accuracy between any layer and an EBL layer is better than

step #	layer	lithography	material	thickness
1	alignment marks	UV	gold	120 nm
2	absorber line	EBL	aluminum	40 nm
3	precision GND	EBL	niobium	80 nm
4	resonator and GND	UV	niobium	150 nm
5	dielectric	EBL	SiO ₂	400 nm
6	bridges	EBL	niobium	400 nm
7	beam lead seed	UV	gold	200 nm
8	alignment mark etch	UV		
9	beam lead electroplating	UV	electr. gold	3 μ m
10	device separation	UV		

Table 4.3: The lithography steps necessary to produce a waveguide coupled MKID. The lithography methods are ultraviolet lithography (UV) or electron beam lithography (EBL). All material layers are fabricated using sputter deposition.

50 nm.

The order of the layers with their respective thicknesses is shown in table 4.3. The critical thought when ordering the layers is which layer will easily cover the layers below and make good electrical contact. Its potentially easier for thick layers to cover thin ones, therefore the first layer is going be the aluminum absorber line with its 40 nm thickness. Since this line is patterned using electron beam lithography, one UV lithography layer before that is necessary with alignment marks to give a global reference. This layer is also used for UV alignment marks and contacts on the wafer. After the aluminum, niobium parts such as the ground plane of the lines are deposited which have to be accurately aligned to the aluminum. The main niobium parts like the large ground plane and the MKID capacitor are than patterned using UV lithography. After that follow two EBL steps for the SiO₂ dielectric and the top of the bridges mainly because the bridges have very low tolerance in the antenna area. Then the beam lead seed layer is defined with UV lithography. Because the seed layer also contains gold contacts which should not be electroplated with 3 μ m of gold, another UV lithography step to define the beam lead shape is necessary.

4.5.3 Tolerance analysis

The most critical part of the circuit is the section with waveguide antenna and the splitter. The main deviations in production of thin film structures is the alignment accuracy between subsequent layers. The new layer always has to be adjusted to the previous ones, where translational and rotational deviations can occur. In critical sections of the design these deviations have to be accounted for, and where necessary, a less critical design has to be

layers	description	lithography	tolerance [μm]
2-3	absorber-GND	EBL	0.1
3-4	line - GND plane	UV	2
4-5	line - bridges	EBL	1
5-6	dielectric - bridge	EBL	0.8
4-7	beamleads	UV	2

Table 4.4: Tolerances between the critical layers. The list of layers is found in table 4.3.

chosen. A summary of the tolerances is given in table 4.4.

The absorber lines are the most difficult parts of both designs, because the line gaps are as small as $0.4 \mu\text{m}$ and the center line and the ground plane are also on different layers. In addition the lines are very long. Small deviations in the gaps do not change the line impedance a significantly, but short circuits have to be prevented along a distance of about 1 mm. Because of that the absorber lines are created with electron beam lithography. If the tolerances can not be met, the line parameters can be changed without the need of a new lithography mask.

The bridges are critical in the sense that the top metal needs dielectric underneath to prevent a short circuit. The dielectric is $2 \mu\text{m}$ wider than the bridge. The alignment tolerance has been set to $0.8 \mu\text{m}$.

The niobium ground and resonator layer (layer 4) is critical at the antenna where it interfaces with layer 3. The effect of misalignment is shown in fig. 4.11 on the right and does not have a negative effect. Since the line and its ground is completely done in EBL and the overlap is quite generous, this layer does not affect the absorber line directly. The resonator is completely patterned inside this layer. If the width of the capacitor strips changes, only the resonance frequency will change which does not affect the performance of the detector at all.

Alignment inaccuracies most certainly also occur when the device is mounted in a copper block. A movement around the long axis of the device has been simulated and is shown in fig. 4.11 on the left. Movement out of the waveguide are quite tolerant while movement in the waveguide direction is immediately visible. $2 \mu\text{m}$ variation are still tolerable here. The influence of shifting the device along the short axis in the waveguide did not show any significant effect beyond $10 \mu\text{m}$.

4.5.4 Wafer layout and test structures

The production wafer size of 30 mm in diameter allows for a total of 56 devices and divides up in 4 sectors. Two sectors of 16 devices each are for the WGKID devices with long and

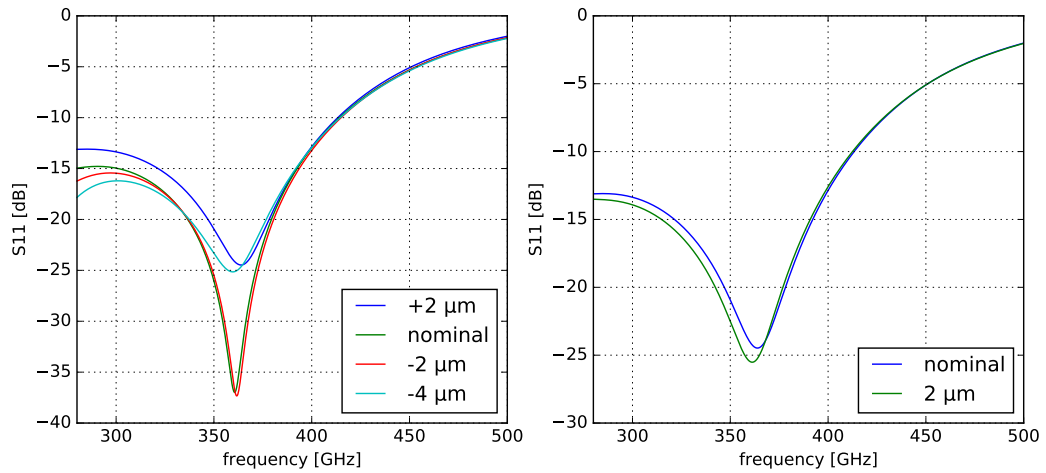


Figure 4.11: Left: Performance of the antenna and splitter section if the device is moved out (positive direction) of the waveguide. **Right:** Performance if the antenna is misaligned to the line. $2 \mu\text{m}$ is already nearly half of the line and a visible misalignment.

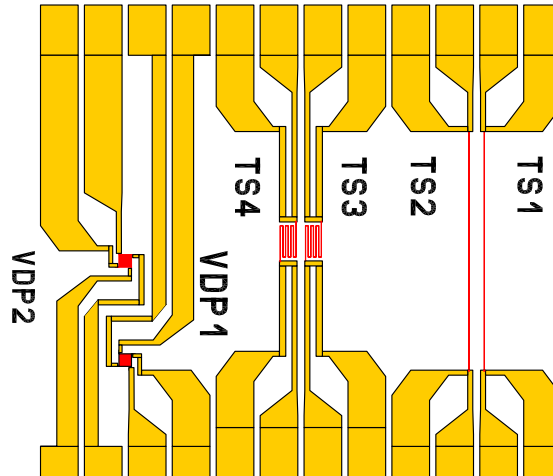


Figure 4.12: The test structures used to determine the properties of the aluminum films. The yellow parts are made of gold and the red parts are made of aluminum. The van-der-Pauw structures VDP1 and VDP2 are for determination of the resistivity and the test stripes are for measurement of the transition temperature mainly. The wafer contains two of the blocks shown here.

short absorber lines, one sector for the TMKID devices and one sector is shared between the inductively coupled KIDs and test structures.

Three kinds of test structures for aluminum are on the wafer. They are shown in fig. 4.12. First, there are van-der-Pauw [98] structures which are squares with a side length of $100\ \mu\text{m}$. They are contacted at the four edges and allow a real four-point measurement of the aluminum film. The other test structures are $1900\ \mu\text{m}$ long and $2\ \mu\text{m}$ wide lines. They are contacted with gold at both ends to allow a connection using bond wires. Straight lines are used to exercise specifically the stitching of write-fields which is necessary for the electron beam lithography. As a variation, the long line is meandered such that less stitching is necessary. The lone lines are primarily useful to measure the transition temperature of the superconductor. They are also used to compare the aluminum films to the van-der-Pauw test structures to see if the geometry has an influence on the films resistivity and transition temperature. The long lines are contacted to the gold terminals such that a possible contact resistance between gold and aluminum is also measured. The aluminum lines and the van-der-Pauw structures are defined using electron beam lithography.

Besides the four sectors with the MKID and test devices, the mask also contains eight larger van-der-Pauw structures for the bottom niobium layer (4) and the beamlead seed gold layer (7). With those the resistance can also be checked for the layers mainly responsible for the resonator properties.

5 Measurement and diagnosis of waveguide coupled MKID devices

In the previous chapter, the design of waveguide coupled MKID detectors used as a prototype to investigate the optical sensitivity of MKID is presented. In this chapter, the fabrication of these devices done by Dr. Karl Jacobs in our microfabrication laboratory and my measurements are described. I have to anticipate here, that the planned optical measurements could not be performed on the fabricated devices, therefore the diagnosis based on the results from DC and VNA measurements will also be covered in this chapter.

5.1 Fabrication of devices

The preparations for fabrication and the tolerance analysis mentioned in sec. 4.5 are the basis for the following discussion. First the lift-off process and the SOI-technology are briefly explained. Then the fabrication process is described in greater detail.

5.1.1 Lift-off process

All material layers which are deposited are patterned using the lift-off process sketched in fig. 5.1. For this process the substrate (I) is coated with photoresist (II) which is patterned into the inverse shape of the structure. Thereby the areas of the photoresist where the structures will be are holes in the photoresist layer. The material layer is deposited (IV) on top of the substrate with the developed photoresist. It is important that the thickness of the material is considerably less than the thickness of the photoresist layer. The last step is the actual lift-off step. The wafer is placed in a solvent which removes the entire photoresist, often aided by ultrasonics (IV). Only the material being in direct contact with the wafer stays, whereas all the material which is on the photoresist is removed (V).

Possible problems of the lift-off process can arise at the edges of the material of the defined structures, at which material may accumulate along the walls of the photoresist during the deposition. This creates thin walls of material at the edges. Another problem

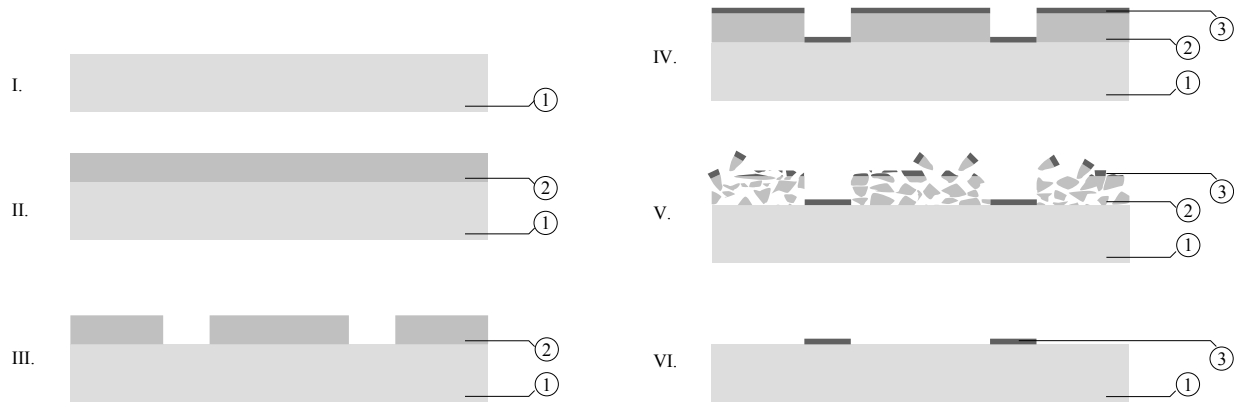


Figure 5.1: Sketch of the typical lift-off process. Legend: (1) substrate, (2) photoresist, (3) deposited layer. Image: By Twisp [public domain], Wikimedia Commons. For description see sec. 5.1.1.

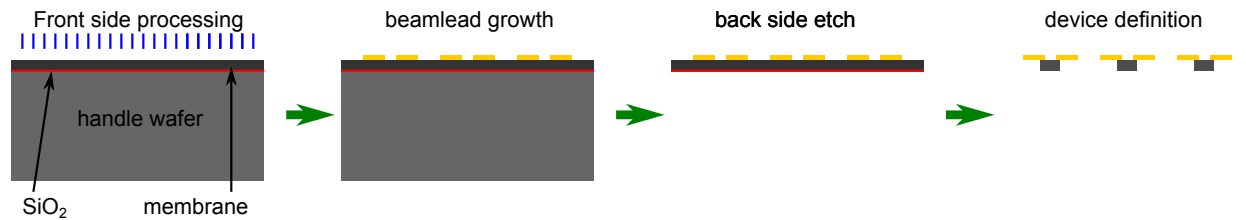


Figure 5.2: Very simplified sketch of the SOI process with beamlead deposition. The front side processing can be done like on standard wafers. Finally the seed layer for the beamleads is deposited, before in the next step the gold is thickened by electroplating. Then the handle wafer is etched away. The remaining SiO_2 layer can be removed with an etch in buffered HF. The device shape can then be patterned on the backside and the devices are etched out.

is that the lift-off process (V) does not work well for small enclosed structures. These have to be prevented during the design process already.

During the deposition of the material on the photoresist, contaminations can be implanted in the material, which can be problematic for thin superconductors like the aluminum absorber lines. Since the contamination mainly occurs at the beginning of the deposition, there is always sufficient clean material for thick structures, whereas for thin structures, the whole layer can be affected.

5.1.2 Silicon On Insulator (SOI) technology

The design of high frequency integrated circuits is always closely related to capabilities and limits of fabrication. One critical limitation is the dielectric substrate which has a thickness usually defined by the commercially available wafers around between 200 and 550 μm . At high frequencies, the substrate thickness becomes comparable to (half) the

wavelength and can hence act as a dielectric waveguide in parallel to the actual circuit on top of the substrate. The desired substrate thicknesses are below $9\ \mu\text{m}$ for my 350 GHz case and can go down to $2\ \mu\text{m}$ for circuits up to 4.7 THz [21].

To actually fabricate on such thin substrates, wafers with a special layer combination are used. These wafers are called silicon on insulator (SOI) wafers and are bought commercially. On top of the wafer is the thin high resistivity silicon membrane production layer. It is separated by a silicon dioxide barrier from a thick handle wafer (see fig. 5.2). The processing is done on the membrane side of the wafer, just like on a thick substrate. As one of the last process steps, the thick wafer on the back is completely etched away down to the SiO_2 which is an etch stop layer. This etch stop layer is removed using buffered Hydrofluoric Acid, which does not etch the silicon. Now only the thin top wafer is left and the shape of the device can be defined in another etch step. An important advantage of the SOI technology is that the device shape can be freely designed and is not restricted to mainly rectangular shapes that can be diced on a wafer saw.

The thin silicon chips can not be contacted by using wire bonds, therefore beam leads are used. Beam leads are $2\ \mu\text{m}$ to $3\ \mu\text{m}$ thick gold flaps that are defined with a thin gold seed layer and then gold is grown by electroplating to achieve the desired thickness. When the substrate underneath is removed during device definition, the Gold flaps are free standing elements and can be used for ground and signal connections. As can be seen in fig. 4.3 e), the ground beamlead surrounds the whole chip while the substrate is only in the center section. Because of the large contact area, they allow a much more reliable and low inductance connection to the surrounding circuit and the fixture than bond wires, which is desirable especially for the ground connections at high frequencies.

5.1.3 Description of the micro-fabrication process

The fabrication follows the procedure outlined in sec. 4.5.2. The lithography steps are shown in table 4.3. Microscope photos of fabricated devices are shown in figures 5.3 and 5.4. All of the fabrication is done in our in-house microfabrication laboratory.

On the cleaned SOI wafer, the first gold layer containing alignment marks is created using the lift-off process and UV lithography. The alignment marks are necessary to establish a reference frame for the following electron beam lithography (EBL). The gold is deposited in an ultra high vacuum chamber by DC magnetron sputtering. Layer 2 uses EBL to define the absorber lines made of 40 nm thick, sputter-deposited aluminum. Layer 3 is the sputter deposited niobium ground plane with a thickness of 80 nm which has to be precisely aligned to the aluminum layer and is also defined by EBL. Since the niobium has to make electrical contact to the aluminum, the native aluminum oxide layer has to

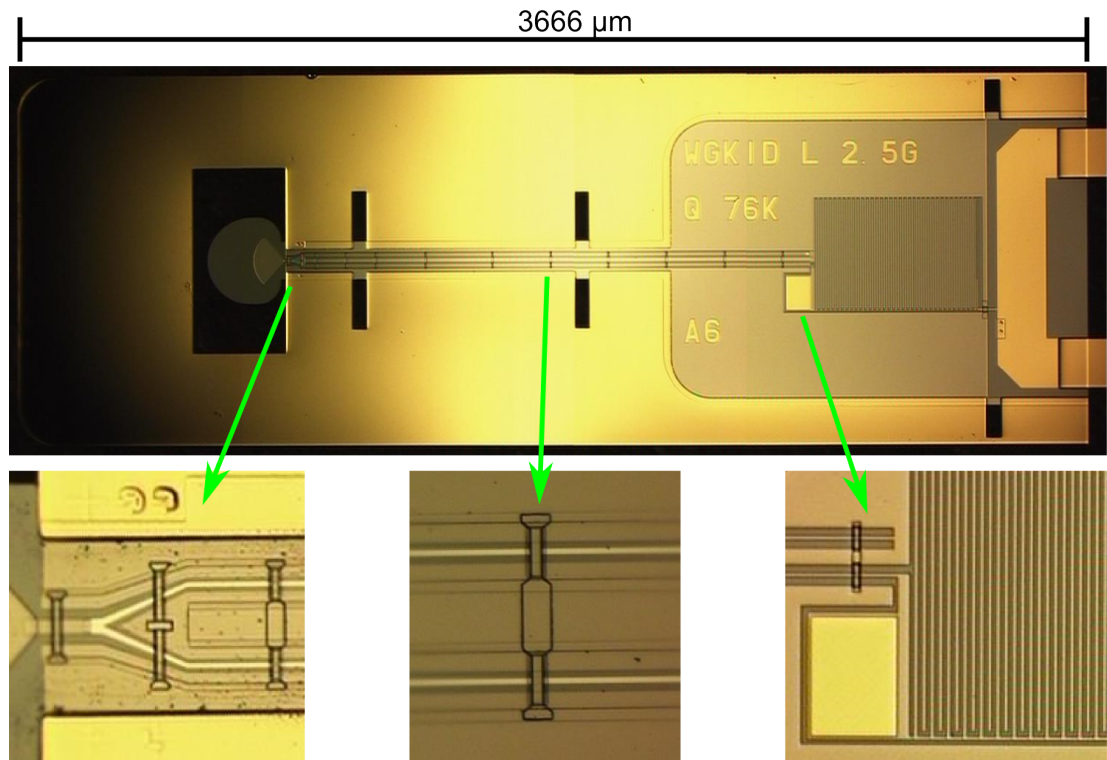


Figure 5.3: Microscope photograph of a fabricated waveguide coupled MKID with lumped element resonator (see sec. 4.3). The zoomed regions are, from left to right, the RF splitter, the absorber lines with dielectric bridges and the transition between the inductor and the capacitor. The large golden areas are the beam leads. For details see fig. 4.3.

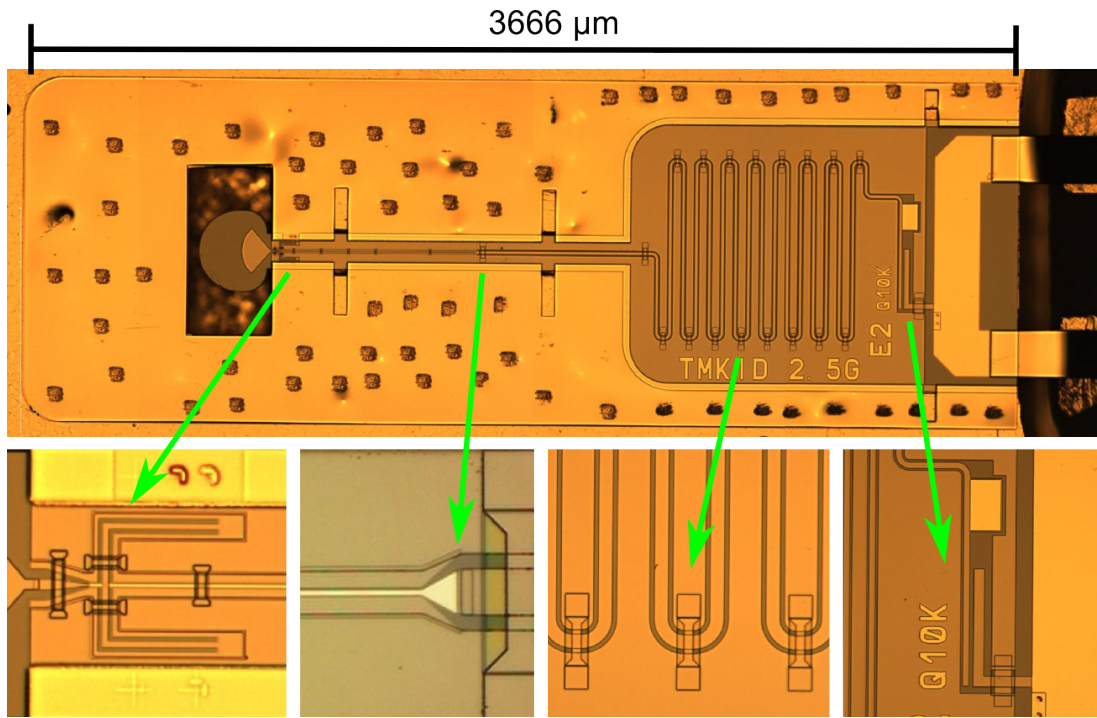


Figure 5.4: Microscope photograph of the fabricated device of the waveguide coupled transmission line resonator design (sec. 4.4) mounted in a detector fixture. The marks on the beam leads are the locations where the needle of the bond machine fixed the chip to the copper block using ultrasonic impulses. The zoomed pictures show, from left to right, the coupling from the antenna to the line, the transition between the aluminum part of the resonator and the niobium part of the resonator, the meandered part of the resonator and the coupler to the readout line. For details see fig. 4.9.

be removed. This is done by a cleaning process using an argon plasma before deposition of the niobium. The cleaning process must not be too aggressive because thin photoresist is used for the EBL, which can be damaged by the plasma.

The following fourth layer now contains the large structures of the resonator and the ground plane made of niobium. UV lithography is used for structuring this layer. The structures have to make contact to the aluminum line at the capacitor in the WGKID design or at the transition to the remaining transmission line resonator in the TMKID design. At these contact areas, the aluminum would be exposed to the chemical developer for the UV photoresist, which has a large etch rate for aluminum. It is therefore protected by an additional niobium layer. The EBL developer does not attack the aluminum and the extra niobium protects the aluminum from the developer for the UV lithography. At the ends of the absorber line now two interfaces are present. First the contact between the aluminum and the EBL niobium and second between EBL niobium and UV niobium.

Layer 5 defines the SiO₂ for the dielectric bridges using EBL. The dielectric thickness is 400 nm and the SiO₂ is deposited using RF sputter deposition. The developer necessary for the thick layers also attacks the aluminum layer, therefore first a very thin protective layer of PMMA photoresist is used to protect the aluminum before the actual photoresist is spun on. Before deposition of the SiO₂ the PMMA is removed using an Oxygen plasma etch followed by a cleaning step using argon plasma. The bridges themselves are defined in layer 6. They are made of 400 nm thick, sputter deposited niobium. The thickness is necessary to cover the large step onto the 400 nm dielectric.

Layer 7 is the seed layer for the beamleads and also contains the readout line. It is defined using UV lithography which is not problematic here since the aluminum line is not exposed here. The gold is sputter deposited with a thickness of 200 nm. Layer 8 contains UV defined photoresist which covers all areas that are not supposed to be covered by the 3 μm thick beam lead gold. The thick gold layer is grown by electrolytic plating.

The substrates of the devices are 9 μm thin silicon membranes which are processed using the SOI technology described in sec. 5.1.2. The next step is now to etch alignment marks in the substrate using deep reactive ion etching (DRIE). They are necessary to define the shape of the devices when the wafer is turned around. At the same time the substrate between the capacitor fingers of the WGKID 4 GHz design is removed (see sec. 4.3.5). The handle wafer is removed using DRIE as well. The remaining oxide layer is removed using buffered HF. Now the last UV lithography step defines the final shape of the devices which are then subsequently etched out and separated. After a visual inspection a device can be mounted in a fixture as described in 3.5.1

In total four batches were fabricated. They are named MKID-SOI-1 to MKID-SOI-4 in the following. The first two batches were still early process development and did not

yield any devices. The batches 3 and 4 were measured, but the following measurement concentrate on batch MKID-SOI-4, because batch MKID-SOI-3 showed contact problems between subsequent layers.

After fabrication, the MKID devices are separated and sorted. Then an inspection using an optical microscope is done. The capacitor/meander, the coupler to the feedline and the antenna are inspected at medium magnification of 100-200 times. The absorber lines are inspected closely using 500-1000 times magnification for any interruptions in the line. Damage of the absorber line is found in approximately 25 % of the inspected devices. If the device passes the inspection, it is mounted in a detector block as explained in sec. 3.5.1.

5.2 DC measurement of test structures

Before any measurements of the MKID devices are attempted, DC measurements of the test structures on the wafer are done to yield initial information of the superconducting thin films. DC measurements allow to measure material properties and to diagnose initial problems. This is especially important, if the subsequent measurements of the devices fail, providing the only source of information in that case.

5.2.1 Measurement of transition temperature and resistivity

The fabricated wafer with the WGKID and TMKID devices contains dedicated test structures to measure the properties of the thin aluminum film of which the absorber lines are made. The test structures are shown in fig. 4.12. The structures are diced out while they are still on the thick handle wafer and measured in the setup described in sec. 3.2.3. 16 DC wires are available, therefore four samples can be measured in one cool-down. The van-der-Pauw structures are measured in a real four-point configuration while the test strips are measured including the contact between gold and aluminum.

For the measurement of the resistance vs. temperature curve (RT), the bath temperature of the ADR is varied by either increasing or decreasing the ADR magnet current as described in sec. 3.1.5, but slowly and continuously to give the setup time to thermalize. The RT curves of two van-der-Pauw structures and two test strips are shown in fig. 5.5. The excitation current for the test strips is chosen to be 1 μA and for the van-der-Pauw structures 53.9 μA to get a sufficient voltage reading. The measurements are once done starting at the lowest temperature and increasing the temperature and once starting at 3 K and decreasing the temperature. From a possible asymmetry between the upward and downward temperature curves, bad thermal coupling between the temperature sensor and

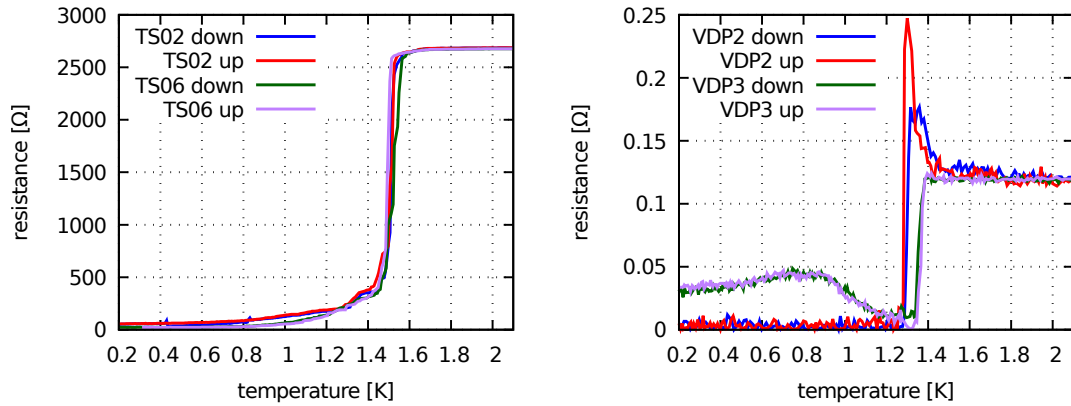


Figure 5.5: Left: Resistance vs. temperature measurement of two test strips of batch MKID-SOI-4 which are $1900\ \mu\text{m}$ long and $2\ \mu\text{m}$ wide. The excitation current is $1\ \mu\text{A}$. The measurement is once done with increasing temperature (up) and once with decreasing temperature (down). **Right:** The same measurement for two van-der-Pauw structures at an excitation current of $53.9\ \mu\text{A}$.

the sample can be identified. This is not the case in my measurements

The resistivity measured using a symmetric van-der-Pauw structure can be determined as [98]

$$\rho = \frac{\pi d}{\ln 2} R_{\text{ab}} \quad (5.1)$$

where d is the thickness of the film and R_{ab} the measured resistance in the four point measurement. The resistance at 3 K assuming a film thickness of 40 nm is $\rho_3 = 2.16\ \mu\Omega\ \text{cm}$ and at room temperature $\rho_{300} = 5.6\ \mu\Omega\ \text{cm}$. This gives a residual resistance ratio $\text{RRR} = \frac{R_{300}}{R_3} = 2.3$. The transition temperature is determined in the RT measurement the inflection point of the slope between the high resistance of the normal state to the low resistance of the superconducting state. The measured resistivities and transition temperatures are summed up in table 5.1.

5.2.2 Measurement of current-voltage characteristics

The current-voltage (IV) relation of the devices is measured to get more insight into the influence of the excitation current on the device. The measurement is done directly after the aforementioned RT measurements in the same setup. The result of the current-voltage measurements is shown in fig. 5.6. One of the test strips is also measured at different temperatures. At the lowest temperature, the transition to the normal state resistance happens at a current of $18\ \mu\text{A}$ for the test strips. Knowing the width and the thickness of the strip, a critical current density of $25\ \text{kA}\ \text{cm}^{-2}$ is calculated. The van-der-Pauw

device	ρ_{300} [$\mu\Omega$ cm]	ρ_3 [$\mu\Omega$ cm]	RRR	R_{mK} [Ω]	T_c [K]	I_c
TS2	9.8	5.6	1.7	59	1.50	21.5 μ A
TS6	9.6	5.6	1.7	50	1.50	22.3 μ A
VDP2	5.7	2.2	2.6	0.000	1.31	1.7 mA
VDP3	5.8	2.2	2.6	0.012	1.32	1.7 mA

Table 5.1: DC parameters of measured test structures for batch MKID-SOI-4. The TS-devices are straight test strips which are 1900 μ m long and 2 μ m wide. The VDP devices are van-der-Pauw structures which are squares with 100 μ m edge length. Measured parameters are the resistance ρ at 3 K and at 300 K, the residual resistance ration RRR, the resistance measured below the transition to the superconductig state R_{mK} , the transition temperature T_c and the critical current I_c at 68 mK bath temperature which is determined from the IV measurements.

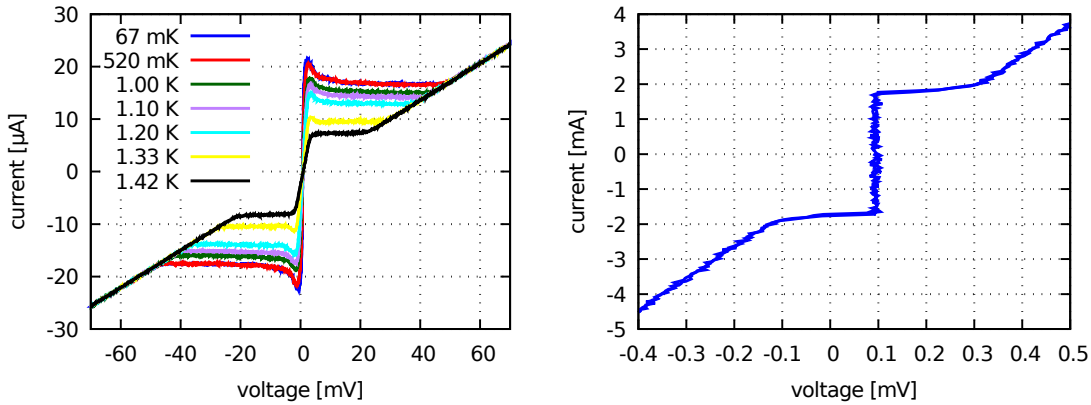


Figure 5.6: **Left:** current-voltage (IV) curve of device TS6 measured at different bath temperatures. **Right:** The IV curve of device VDP2 measured at 67 mK. Both devices exhibit a switching current at which the resistance of the device switches to the normal state value.

structures can support a critical current of 1.7 mA. If one calculates a current density neglecting the contacts at the edges and just taking the cross section of the van der Pauw structure into account, the critical current density would be 42.5 kA cm^{-2} .

5.2.3 Experiment to reduce contact resistance

This experiment was done on the test devices of batch MKID-SOI-3. During the first measurement, the van-der-Pauw structures and the test strips showed a very high resistance in the range of mega-ohms while kilo-ohms were expected. On some devices, the resistance suddenly changed to a lower value in the expected range of kilo Ohms as a multimeter was repeatedly attached and detached. Then a voltage source set to 15 V with a resistor in series to limit the current was connected to each device for about half a second. The current applied during this procedure was in the range of a few mA for the VDP test structures. Afterwards the device always showed lower resistance and does not change back to the mega-ohm resistance initially measured. With the 'electrocuted' devices, normal R/T measurements and the determination of a transition temperature was possible. However, the devices of batch MKID-SOI-4 already showed a lower resistance and the treatment above did not change the initially measured resistance anymore.

5.3 VNA transmission measurements

A first health check of a MKID is the transmission spectrum. As an MKID is a superconducting resonator, the presence of the resonance feature in the transmission spectrum is the first test that shows if the detector can work at all. Since the readout line of the detector is made out of niobium and is also covered with gold, transmission through the device can be measured even at room temperature. A part of the resonator is made of aluminum with a transition temperature of about 1.5 K, as measured in sec. 5.2. Therefore the MKID resonance feature can only be visible below that temperature.

For the initial test, no horn antenna but only an aluminum cap for mechanical protection is put on the device. Then the device is mounted in the ADR cryostat and cooled down.

The measurement procedure is adapted from the procedure explained in sec. 3.4.1. Although the devices are designed for a resonance frequency of either 2.5 or 4 GHz, they are largely unknown yet. Therefore a wide band VNA frequency sweep ranging from 1 GHz to 12 GHz is done at a temperature above T_c first, where the aluminum in the resonator prevents the resonance to be visible. Subsequently, a second run at the ADR base temperature of 67 mK is done. From the comparison of the two spectra a MKID resonance can be identified.

To increase the frequency resolution of the spectrum, it is measured in spans of 2 GHz at the full VNA resolution of 1601 samples. Before analysis, the full 1 GHz to 12 GHz spectrum is stitched together from the measured spans.

If the comparison between the low and elevated temperature spectra does not give a clear result, the transmission spectrum is closely inspected using the VNA and a frequency span of 500 MHz. That way, also narrow and weak resonance features can be found. The main criterion for a MKID resonance is its narrow width in comparison to other features like standing waves or box resonances on the transmission spectrum. Each potential MKID resonance need to be verified through a transmission measurement at a temperature above the T_c of Aluminium. If the resonance disappears, the identified resonance feature belongs to the MKID resonator. This measurement procedure is repeated for three devices of batch MKID-SOI-3 and for three devices of batch MKID-SOI-4. Mainly, the results for MKID-SOI-4 are shown in the following.

5.3.1 Measurement of WGKID devices

The measurements presented here are performed on two devices from batch MKID-SOI-4, which are based on the lumped element design described in sec. 4.3. As device A5 did not stick to the fixture during the mounting process and had to be mounted upside down, I will focus on the measurement of device A3. The transmission through the device is shown in fig. 5.7. A stitched measurement as described above is once done at a bath temperature of 40 mK and then repeated at 410 mK. At the high temperature, the quasiparticle density in the aluminum inductor of the resonator should have considerably increased. Because of that, the resonance frequency should be visibly shifted to lower frequency and the quality factor of the resonance should have decreased.

The designed resonance frequency for device A3 is 2.5 GHz with a coupling quality factor of 11 000. The design with the lower coupling factor is chosen here because it is more likely that the resonance is still visible on the spectrum if the unknown internal quality factor of the resonator is low. The measurement result shows narrow features around 6 and 10 GHz which could originate from a superconductor, but as the features are nearly unchanged at 410 mK, they can only be some spurious resonances in the niobium structures. The lack of any MKID resonance makes further optical measurements of the devices pointless.

The measurement of device A5 and the of batch MKID-SOI-3, where also a device with 4 GHz resonance frequency is measured, qualitatively show the same behavior. That is, the main resonance feature is not present.

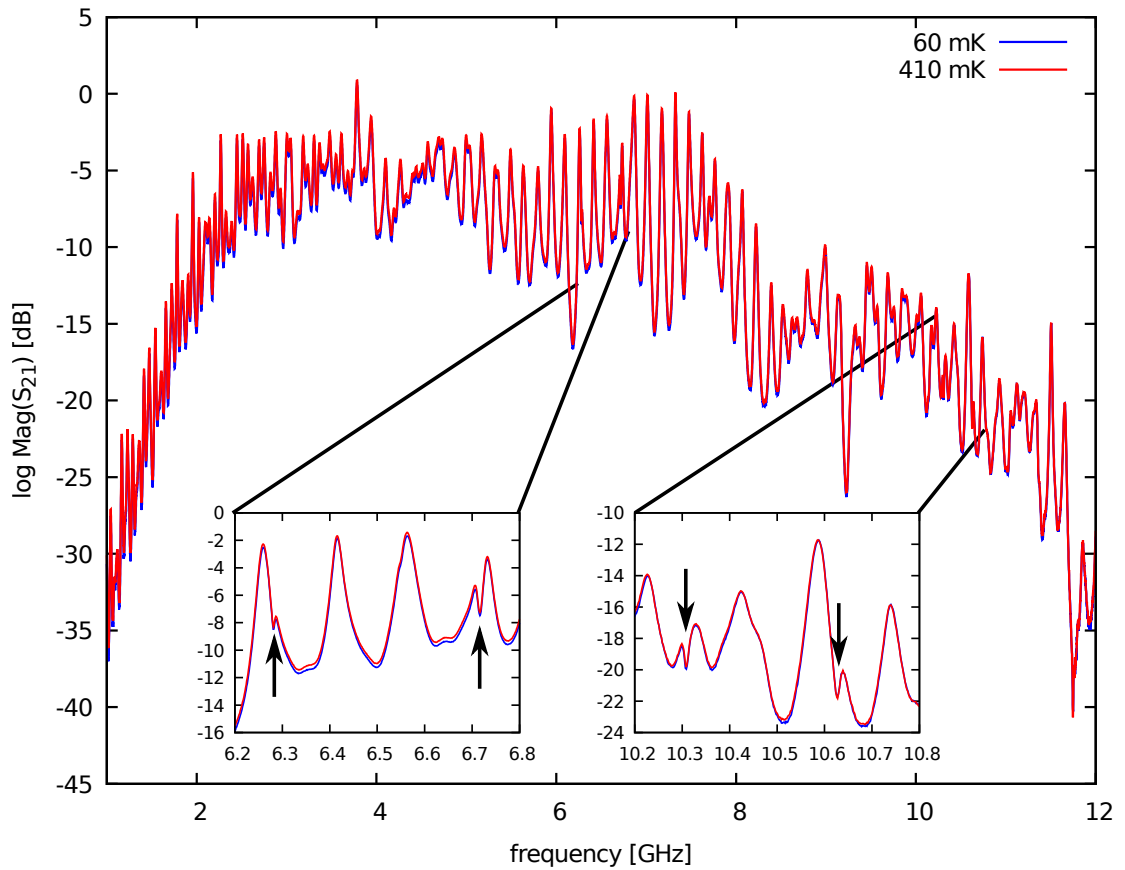


Figure 5.7: Result of the VNA transmission measurement for device A3 of batch MKID-SOI-4. This device is of the lumped element resonator design with a designed resonance frequency of 2.5 GHz and an external quality factor of 11000. The features identified here turn out not to be MKID resonances.

5.3.2 Measurement of TMKID devices

The following section presents the measurements of two devices of batch MKID-SOI-4 based on the transmission line resonator design presented in sec. 4.4. As described in sec. 5.3, the VNA transmission of the devices is measured at both, the minimum ADR bath temperature and at elevated temperature to identify aluminum resonances. The results for the devices E1 and F1 are shown in fig. 5.4. Device E1 is designed to have its resonance frequency at 2.5 GHz and a coupling quality factor of 10000. F1 has a designed resonance frequency of 4 GHz and a coupling quality factor of 10000. Device E1 shows two resonances at 5.24 GHz and 10.4 GHz which look like superconducting resonance because of their narrow width. Device F1 shows one resonance around 8.77 GHz. The resonances however do not respond to the increasing bath temperature as to be expected from aluminum resonators. At 1.8 K, an aluminum resonator would not show a resonance anymore, because it would be fully normal conducting.

With increasing temperature, the resonance frequency should decrease due to the onset of quasiparticle generation, which increases the kinetic inductance. Instead, the resonances actually show a slight increase in resonance frequency at the higher temperature, which can be explained by a reduction of the TLS permeability (see sec. 2.3.5). This observation means that no quasiparticles are generated, thus the aluminum film is not part of the probed resonator.

Using the fitting method described later in sec. 6.2.2, the internal and coupling quality factors could be extracted from the resonances. For device E1, the measured quality factors of both resonances are close to 2000. The coupling quality factors are 2200 and 2500 for the 5 GHz and 10 GHz resonances respectively. The resultant internal quality factors are 9900 and 8300, respectively. The resonance of device F1 at 8 GHz has a total quality factor of 2900, a coupling quality factor $Q_c = 3800$ and an internal quality factor $Q_i = 11800$. The coupling seems to be a bit too strong, but it has to be respected that at double the frequency, the impedance of the coupling capacitor is half. The internal quality factors are relatively low. Any further optical or noise measurements do therefore not make any sense here, as no response from the aluminum is measured.

5.4 Hypotheses for possible failures of the devices

The measurements above reveal that the devices measured from batch MKID-SOI-4 can not be used as detectors because none of them response from the aluminum part of the resonator. The transmission line resonator exhibits resonances which are far off the design frequency and do not respond to an increasing bath temperature. The 40 nm thin and less

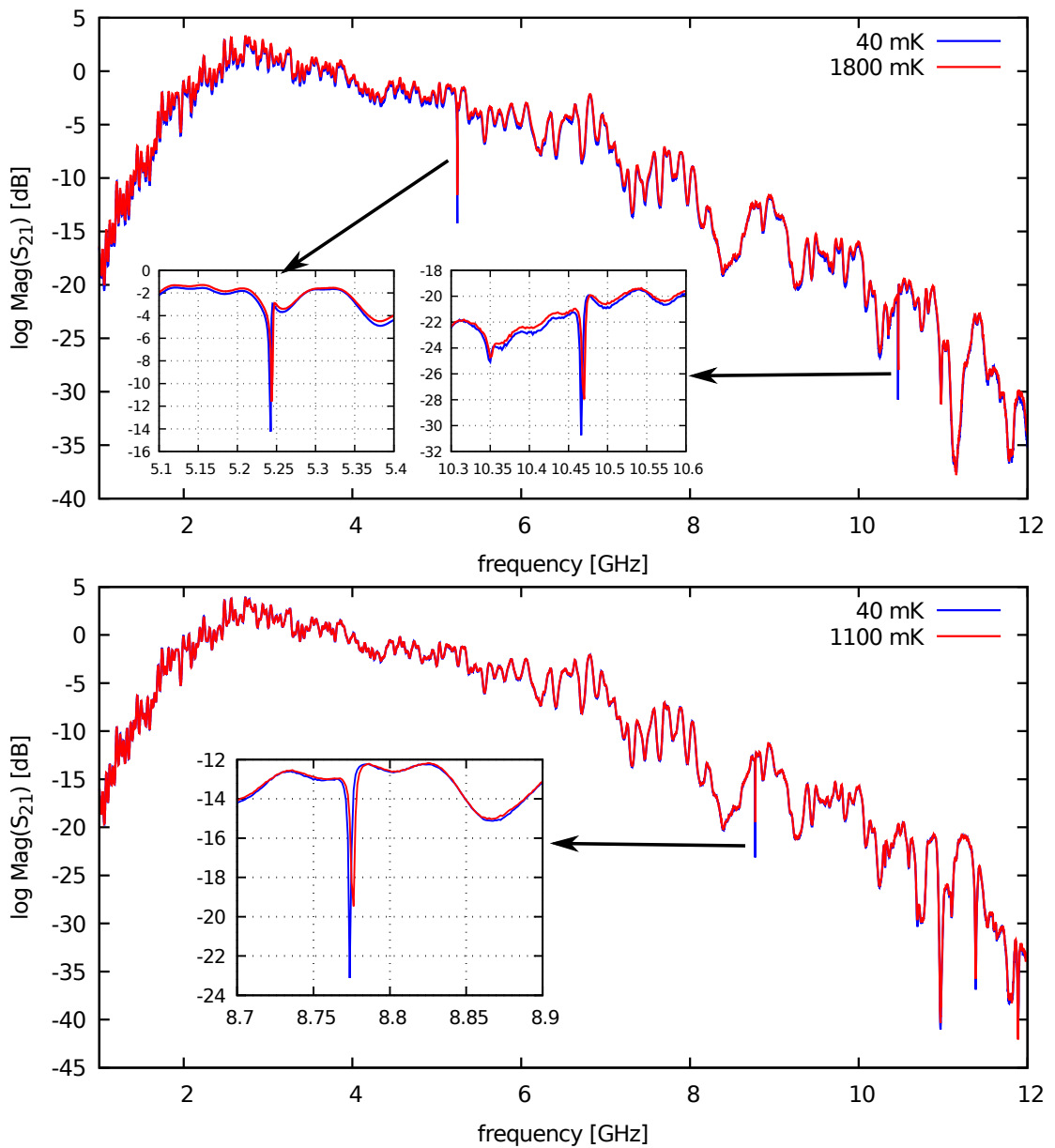


Figure 5.8: Result of the VNA transmission measurement of the transmission line resonator devices of batch MKID-SOI-4 for different bath temperatures. **Top:** Transmission of device E1. This device has a designed resonance frequency of 2.5 GHz and an external quality factor of 10000. Two apparently superconducting resonances are identified at 5.24 GHz and 10.47 GHz. The resonances do not vanish at the higher temperature (red curve) as expected for aluminum. **Bottom:** Transmission of device F1 with a designed resonance frequency of 4 GHz. The designed external quality factor is 10000. This measurement shows a resonance at 8.77 GHz which also does not respond to temperature as expected from aluminum.

than $2\ \mu\text{m}$ wide aluminum absorber lines are the most critical parts of the resonator and can be easily mechanically or chemically damaged. The visual inspection can only reveal mechanical damage of the parts of the line not being covered.

In the following two hypotheses for the device failure will be evaluated. The possible failure causes concerning the aluminum absorber lines are:

1. The long and narrow aluminum absorber lines are damaged or contaminated during the processing making them not superconducting or having an unusual high RF loss.
2. The electrical contact between the aluminum absorber lines and the resonator made of niobium is faulty due to the oxide layer on the surface of the aluminum. Also, the contact between the thin niobium defined by electron beam lithography (layer 3) and the thick aluminum ground plane could be faulty (layer 4).

The DC and VNA measurements made above are in the following evaluated against the background of both hypotheses.

5.4.1 Interpretation of DC measurements

The resistance vs. temperature measurements presented in sec. 5.2 enable to specify the critical temperature for the van-der-Pauw structures and the thin test strips as shown in table 5.1. For aluminum films, a thinner film exhibits a higher T_c than thick aluminum [79]. This is because a larger grain size exhibits enhanced superconductivity expressed by a higher T_c . The van-der-Pauw structures have a 20 % lower T_c than the test strips although they have the same thickness. Consequently, the films of narrow strips are somewhat different in their internal structure which would support hypothesis one.

An unexpected observation in the resistance vs. temperature measurement of the test strips is the considerable residual resistance below the transition temperature. The van-der-Pauw structures show a nearly immeasurable resistance while the test strips have a resistance around $50\ \Omega$. In contrast to the four-point measurements of the van-der-Pauw structures avoiding any contact resistance, the test strip measurements do include the contacts between gold and aluminum. The high residual resistance is therefore attributed to the contacts and would support hypothesis 2. The comparison of the resistivities and the RRR to other publications supports the first hypothesis to some extent. The aluminum film published in [26] shows a resistivity at 3 K of $\rho_3 = 0.8\ \mu\Omega\ \text{cm}$ and a RRR of 5.2, but on a sapphire substrate. My film has a resistivity of $\rho_3 = 2.1\ \mu\Omega\ \text{cm}$ and a RRR of 2.6.

The IV measurements from sec. 5.2.2 show a current density for the test strips of $25\ \text{kA}\ \text{cm}^{-2}$. The maximum supercurrent which could pass through the strips is around $18\ \mu\text{A}$ while the current through the van-der-Pauw structures can reach up to $1.7\ \text{mA}$

despite also having contacts between gold and aluminum in the current path. The current density of 42.5 kA cm^{-2} is not far away from the value for the test strip. This implies, that the current is not limited by the film, but by the contacts, which would support hypothesis two.

The contact resistance experiment described in sec. 5.2.3 is only applicable to the batch MKID-SOI-3. It suggests a contact problem exists that can be influenced by a moderate voltage surge. The electrocuted devices are not expected to suddenly exhibit perfect electrical contact. As the new batch MKID-SOI-4 does not change after treatment, I conclude that that in this batch the contact problems which respond to the surge are already cured. The fact that this experiment was at all successful shows that the devices are prone to contact problems. It consequently supports hypothesis two as well.

5.4.2 Interpretation of VNA measurements

The VNA measurement results of the lumped element resonator shown in sec. 5.3.1 do not yield much lot of information. The resonance feature is not visible in the spectrum. The expected effect of bad contacts between the aluminum inductor and the niobium capacitor is tested doing a qualitative simulation with Sonnet EM. In a model the absorber line is disconnected from the capacitor by a small gap. The simulation result does not show a resonance. From the measurement it is not uniquely possible to distinguish between an open contact or resistance on the line which both would lead to an invisible resonance.

The VNA measurement results of the transmission line resonator design measured in sec. 5.3.2 yield more information. Both chips show resonance features which do not respond to the increasing temperature as expected from aluminum resonators. The designed resonance frequency of device F1 is 4 GHz and the first resonance in the spectrum is measured at 8.77 GHz which is roughly double the designed frequency. The spectrum of device E1 with a designed resonance frequency of 2.5 GHz shows a first resonance at 5.24 GHz and a second one at 10.47 GHz. The first resonance feature is again roughly twice the design frequency and the second resonance is exactly twice the first frequency which qualifies it as the next higher mode of the transmission line resonator. The resonator is designed as a quarter-wave resonator which is open at the coupler end and shorted at the waveguide antenna. In case the contact between the aluminum line and the niobium is an open circuit, the resonator has two open ends and becomes a half-wave resonator. The contact point is shown in fig. 5.4 in the second picture on the bottom. The lowest mode on the half-wave resonator has twice the resonance frequency than the lowest mode on the quarter wave resonator. This resonator is also a little bit shorter than designed because the aluminum line is detached which would explain that the measured resonance frequencies are systematically higher

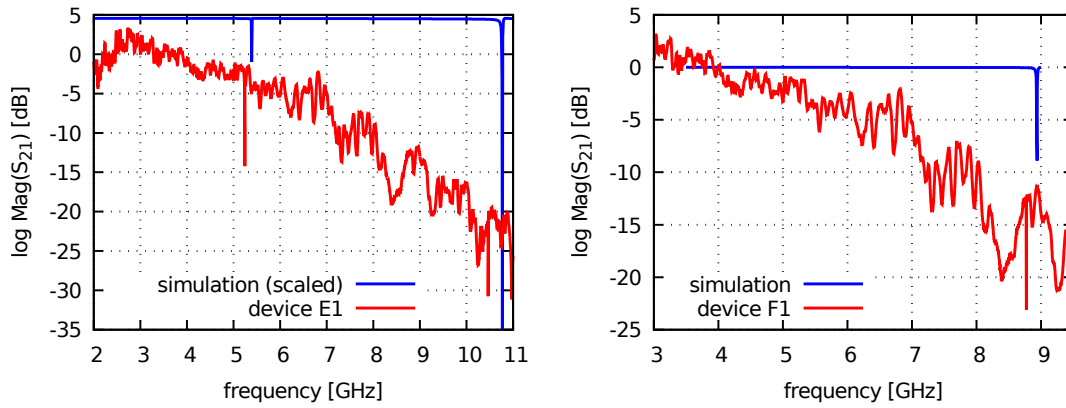


Figure 5.9: Sonnet EM simulation of devices E1 (**left**) and F1 (**right**) with broken contact at the absorber line compared to real measurements.

than double the designed resonance frequency. The measured internal quality factors in the range of 10000 show that the resonator still has reasonably low loss, which means that the contact point can not be resistive. It is rather a relatively good open circuit.

A Sonnet EM simulation of a transmission line resonator with a gap at the transition between the narrow part with the aluminum center line and the wider niobium part of the resonator was done. The results are shown in fig. 5.9. For faster calculation, the niobium is simulated as perfect electric conductor (PEC), which neglects the kinetic inductance in the niobium resulting in a slightly higher resonance frequency. For both devices the simulation shows no resonance at the designed frequency of 2.5 GHz or 4 GHz. The first visible resonance feature is at double the designed frequency and for the 2.5 GHz design, the higher mode is visible. Since the material is not simulated as a superconductor, an exact correspondence to the measured resonance frequency is not expected. The simulation agrees with the theory of broken contacts at the transition between aluminum and niobium. The whole VNA measurement therefore strongly supports the hypothesis two made in the beginning of sec. 5.4.

5.5 Conclusion and suggestion for improvements

Four batches of the waveguide coupled MKID devices were fabricated in our microfabrication laboratory. The devices look as expected in an optical inspection and are mechanically in a good shape. The VNA transmission measurement I did in sec. 5.3 show that the waveguide coupled MKID devices of the batch MKID-SOI-4 can not be used as detectors. They have transmission showing that the readout line is intact and that the surrounding measurement setup works. They do not show a resonance feature which makes it impossi-

ble to read out the detector. Even if the detector would absorb photons in the aluminum absorber lines, the change of the kinetic inductance from the outside can not be measured without a functional resonator. Together with the the DC measurements I did, presented in sec. 5.2, two hypotheses are developed. The analysis of the measurements in sec. 5.4 suggests that the second hypothesis made in sec. 5.4 is very likely. Therefore, the first attempts towards an improvements of the device should focus on the contact between the aluminum and the niobium layer. The second hypothesis of bad material characteristics can not be entirely discarded yet, but has to be investigated further as soon as the contact problems are solved.

The higher order resonances of the transmission line resonator design are expected at double the design frequency. Calculating back, the measurements show that the measured resonance frequency is even without correction for the missing aluminum line within 5% for the 2.5 GHz design and within 10% for the 4 GHz design. The real resonance frequencies can therefore not be far off the design which is important information for future measurements because finding a resonance shifted by a few GHz should not be expected.

The transmission line resonator shows a slightly increased resonance frequency at the higher measured temperature which hints to the presence of two-level systems (TLS) (see sec. 2.3.5 close to the resonator. These could be in the SiO₂ dielectric or as a remaining layer on top or below the substrate.

6 Measurement and analysis of NIKA 2 MKID test arrays

One of the main tasks of my thesis is the establishment of a measurement setup which is suitable for testing MKID with state of the art performance. While the devices designed in chapter 4 were still under development I had the opportunity to verify my measurement setup with experimental MKID arrays designed for NIKA 2 [2] instrument development. They were supplied by E. Driessen and S. Shu from IRAM in Grenoble. As mentioned in the introduction in chapter 1, the NIKA 2 MKID camera is one permanently operating MKID instrument reaching the expected sensitivity and is in scientific operation. Two main questions should be investigated with these test devices:

1. Is the measurement setup suitable to measure the sensitivity of aluminum based MKID detectors?
2. What is the quasiparticle lifetime in the aluminum thin film of which the NIKA 2 detectors are made?

The straightforward way to answer question 1 is to try to measure the NEP (sec. 2.3.2) of the detector in my setup and compare it to published results. Question 2 will have to be answered on the way because the quasiparticle lifetime is a required parameter for calculating the NEP.

In total three NIKA 2 chips were measured. During the measurements, continuous improvements on the measurement setup and the procedures were made. The first chip became damaged and is therefore omitted. During the measurements of the second chip (called CPWO1), the measurement procedure was optimized and the setup was improved step by step. Of the third chip called CPWO2, measurements of two runs are presented and analyzed. The measurements were done in two setup configurations. The first configuration uses the setup described in sec. 3.5.2 in combination with permanent magnets attached to the outer hull of the cryostat. As described in sec. 6.2.4, excellent quality factors were measured with this configuration, therefore the whole sensitivity measurement is done with this setup. The second configuration is without the external magnets but with a niobium

film, which is sputter deposited on the inside of the aluminum device package. This is supposed to shield the device from any outer magnetic fields.

In total, the NIKA measurement campaign contained 12 successful cooling cycles of the ADR and some additional runs where electrical contacts failed or thermal problems occurred, which prevented that the base temperature could be achieved. Each cool-down required about one week of preparation and measurement, followed by analysis and changes or improvements on the setup. In the following, a description of the chip, the measurement results and the analysis are presented.

6.1 Description of the NIKA 2 test devices

The NIKA2 test devices measured here are designed to investigate a reduction in pixel size for the New-Iram KID array [90]. The chips (fig. 6.1) have an outer dimension of 20 mm by 20 mm and the resonators are patterned into a layer of evaporated aluminum with a thickness of 20 nm on a 250 μm thick high resistivity silicon substrate. One chip contains 25 resonators arranged in a regular 5x5 matrix. The readout line (feedline) connecting the resonators with the readout system is a coplanar waveguide and is inductively coupled to the inductor of each resonator. The feedline is tapered at the left and right edges of the chip to allow connection to the outside with bond wires.

The resonators are lumped element kinetic inductance detectors (LEKIDS, [31]) and have resonance frequencies in the range between 1.4 and 2.5 GHz. The inductor is designed to match free space impedance to efficiently absorb incoming radiation of the 150 GHz or the 260 GHz bands, selected by the substrate thickness [90]. The substrate thickness of my test chips is close to the designated thickness of the 260 GHz design, therefore the absorption band of my devices is expected to be close to that frequency as well. The width of the resonator lines is 2 μm and the capacitor finger width is 6 μm . The resonance frequencies are tuned solely by changing the capacitors, meaning that the inductor dimensions for all 25 resonators on one chip are identical. The chip and a microscope image of a resonator is shown in fig. 6.1.

The resonance frequencies are designed such that each row of resonators on the chip corresponds to one group of resonance frequencies in the transmission spectrum. The resonances are therefore addressed in the following by their group and resonator number, meaning "G5R3" is the third resonator of group 5. The geometrical layout of the chip is such that the bottom left resonator has the lowest resonance frequency (G1R1) and the top right resonator the highest resonance frequency (G5R5). The measurement setup for the NIKA2 devices is described in sec. 3.5.2.

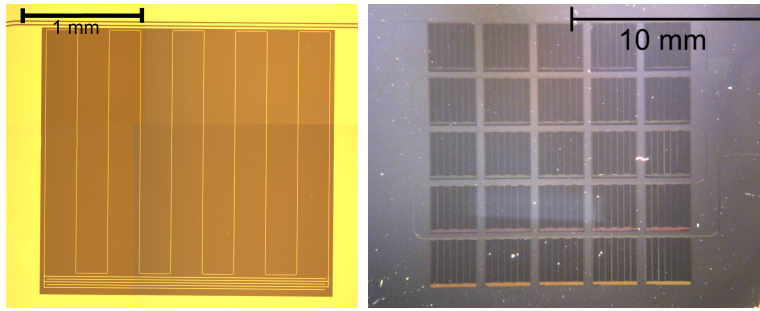


Figure 6.1: **Left:** Microscope image of one NIKA 2 LEKID resonator. **Right:** 5 by 5 resonators are connected to one feedline. The bottom left resonator has the lowest resonance frequency (G1R1) and the top right the highest resonance frequency (G5R5).

6.2 Measurement of resonance frequency and quality factors using the VNA

The following measurements are made using a vector network analyzer in transmission measurement mode (see sec. 3.3.4). Since the readout setup is not specifically designed for the NIKA 2-devices, the following measurements have to concentrate on the overlapping frequency range above 2 GHz. The VNA is set to its full native resolution of 1601 samples for all the following measurements. The sweep time is set to 800 ms which is sufficiently long to avoid distortion of the measurement due to the considerable cable length in the setup. The readout power setting is kept at -5 dBm, which results in an approximate power at the device of -70 dBm and is far below the onset of non-linearity, where the readout signal distorts the resonance.

6.2.1 Transmission of the chip

The full transmission of the test chip CPWO2 at a temperature of 63 mK is shown in fig. 6.2. The main purpose of this measurement is a health check of the chip and the setup. The resonance frequencies and quality factors of each resonance are determined in a detailed measurement presented in section 6.2.5. The resonances are arranged in 5 groups with 5 resonance features each which correspond to their geometrical position of the chip. The features around 1.7 GHz do not seem to be MKID resonances, because of their low quality factors and strong coupling (high depth). Probably they are resonances on the readout line or resonances in the copper fixture. The y-scale in dB is not calibrated to the device level.

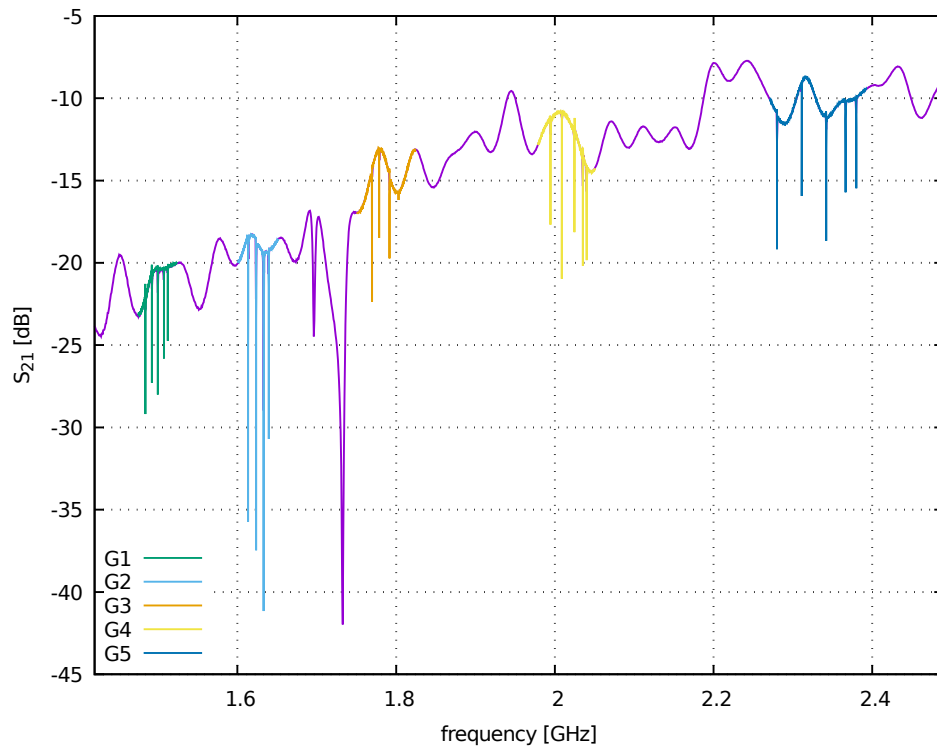


Figure 6.2: VNA transmission measurement result of the NIKA CPWO2 chip showing the whole band at 63 mK. Each row of resonators corresponds to one group of frequencies. The broad feature at 1.7 GHz is expected to be a box resonance in the copper housing.

6.2.2 Fitting procedure

To analyze the measured resonance features, the model described in 2.2.3 is used. The VNA transmission measurement data measured in the 'log Mag.' format is related to the S-parameters as

$$S_{21}^{\text{dB}} = 10 \log_{10} (|S_{21}|^2) = 20 \log_{10} (|S_{21}|), \quad (6.1)$$

$|S_{21}|^2$ is calculated from eq. 2.21. The formula used for the fit is

$$|S_{21}|^2 = \frac{1 + \frac{Q^2}{Q_c^2} - 2\frac{Q}{Q_c} \left(\cos \phi + 2\frac{\delta\omega}{\omega_0} Q \sin \phi \right) + 4Q^2 \left(\frac{\delta\omega}{\omega_0} \right)^2}{1 + 4 \left(\frac{\delta\omega}{\omega_0} \right)^2 Q^2} + T_0 \quad (6.2)$$

where Q is the total quality factor of the resonator, Q_c is the coupling limited quality factor, $\delta\omega/\omega_0 = (f - f_0)/f_0$ is the fractional frequency shift with respect to the resonance frequency f_0 and ϕ an angle describing the asymmetry of the resonance. T_0 is a normalization constant.

The fitting procedure is implemented for batch processing in a gnu Octave [34] script. In addition to the fitted parameters, the script generates a plot containing the model and the data for a quick inspection of the quality and convergence of the fit. The script can process multiple input files which each contains one resonance in one run. The fitting algorithm is a Levenberg-Marquardt non-linear regression fit with Q , f_0 , Q_c and ϕ as free parameters. The steps of the analysis are as follows

- The data is normalized choosing T_0 such that the maximum is at 1 (0 dB).
- Starting values are determined for the resonance frequency (point of minimum transmission) and the quality factor (from FWHM).
- The resonances are fitted to the model described above using the implementation of the Levenberg-Marquardt algorithm of the octave-forge `leasqr()` function.

Two resonances with the fitted models are shown in fig. 6.3. Since very many resonances are fitted, only representative examples can be shown as illustration of the accuracy of the model. Before the results of the fit are used in further calculations, each fit is quickly inspected visually for false convergence or other errors like bad data. However, bad fits become also immediately apparent in the fitted parameters like unrealistic resonance frequencies or quality factors. The following sections show results based on this fitting method.

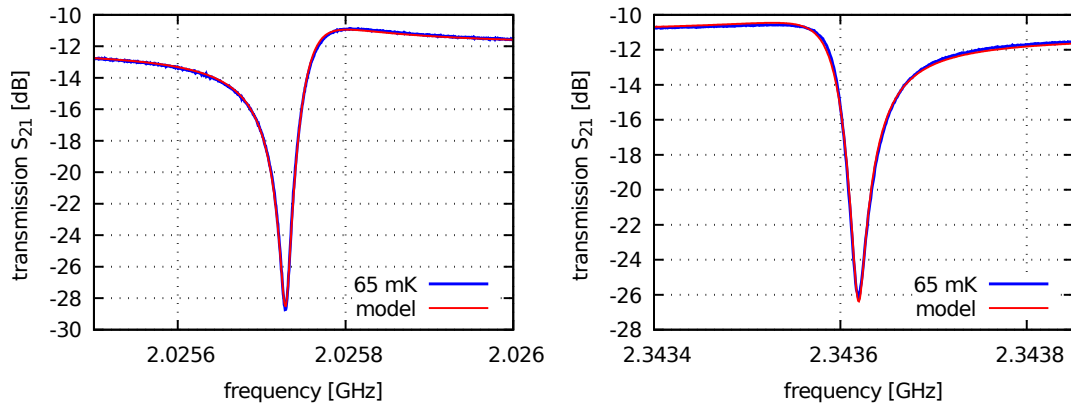


Figure 6.3: Measurement results of VNA measurements for resonators G4R3 (left) and G5R3 (right) with the respective fits of eq. 6.2. The fitted parameters for G4R3 are $f_0 = 2.02574$ GHz, $Q = 32760$, $Q_i = 192000$ and $\phi = -0.580$ rad. For resonator G5R3 the parameters are $f_0 = 2.34360$ GHz, $Q = 36360$, $Q_i = 196000$ and $\phi = 0.452$ rad.

6.2.3 Reduction of quality factor over time

The NIKA 2 devices were measured over a time span of about 1.5 years, and quite a number of cool-downs have been done with the chips. The second NIKA 2 chip CPWO1 was mounted in the copper fixture around the 30th of March 2017. During that measurement, the best quality factors were measured even though the cryostat base temperature was not optimal. In the following month, several additions to the measurement setup were made like the outer aluminum magnetic shield. However, the internal quality factor did not increase during the next measurement, therefore it was decided to exchange the chip with the third one (CPWO2) that spent the time after dicing in a desiccator, covered with photoresist. Immediately, better quality factors were measured, therefore it has to be suspected, that the chips age, at least with each cool down or each time the cryostat had to be opened and the chip is exposed to air and humidity. The mounted chip (CPWO1) was stored under normal atmosphere for quite some time, since the aluminum layer was expected to be protected by its native oxide layer. The internal quality factor measured at different dates is shown in fig. 6.4. From initial quality factors above 120000 the value dropped below 40000 after some measurements.

6.2.4 Qualitative investigation of the influence of external magnetic field

To examine the qualitative effect of an external magnetic field on the resonators, two permanent magnets are placed on the outer shell of the cryostat in different field directions.

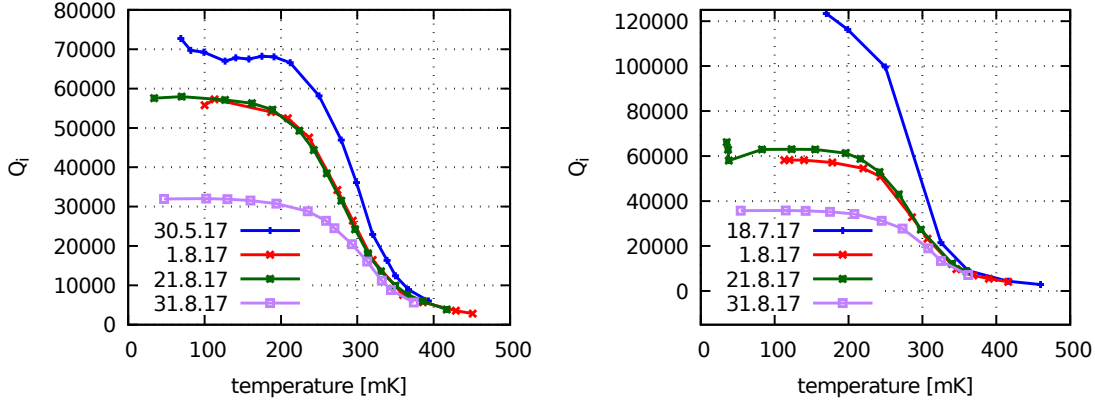


Figure 6.4: Internal quality factor of two resonances at different measurement dates. **Left:** R3G4. **Right:** G5R1. Group 5 was not measured at the first measurement date and Group 4 not at the second.

The north poles of the two magnets always point in the same direction to create a roughly homogeneous field in the cryostat.

The setup in the cryostat is described in 3.5.2. To change the measurable field configuration, the sample is warmed up above its critical temperature and then cooled down to the ADR base temperature again with the magnets in place. Then the transmission of the resonances is measured using the VNA. This is repeated for different field directions, towards north, south, east and west. Before the magnetic configuration is changed, the sample stage has to be warmed up above the T_c of the aluminum shield, which effectively shields the sample from changes in external field. The resulting resonance shapes are shown in fig. 6.5. From these measurements, it can be seen that the magnetic field in western direction gives the visibly most narrow resonance.

In addition, measurements are done with an additional sputtered Niobium thin film on the inside of the aluminum housing, as described in sec. 3.5.2. The measurements mentioned above with external magnets are repeated with this setup. This measurement has been done 10 month after the measurement without Niobium. The results are shown in fig. 6.5 on the bottom.

The measurement result shows, that for the magnetic shield in western direction, the maximum quality factors are measured. The quality factors measured with the Niobium shield are lower than the results for the setup with aluminum shield only and external magnets. Therefore all measurements of quasiparticle lifetime and NEP are done with the optimized external field configuration. The resonance frequency of the measurement with Niobium shield is about 12 MHz lower than the frequencies measured before. The following VNA measurements are done for both configurations, if not noted otherwise.

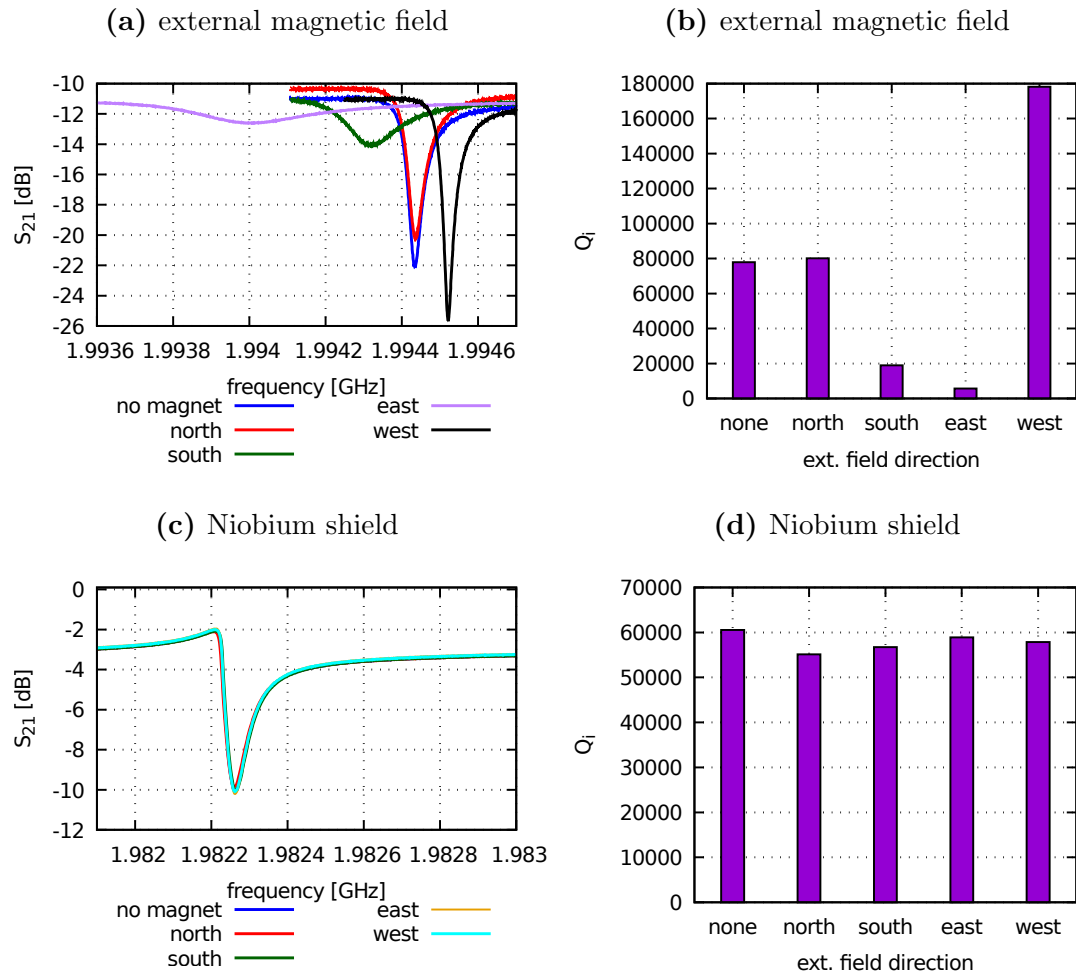


Figure 6.5: (a) Shape of the resonances of G4R1 under different magnet configurations. (b) The internal quality factor of resonance G4R1 under different magnet configurations. (c) Shape of resonance G4R1 with Niobium magnetic shield with external magnets applied in different directions. (d) The fitted quality factor with Niobium magnetic shield.

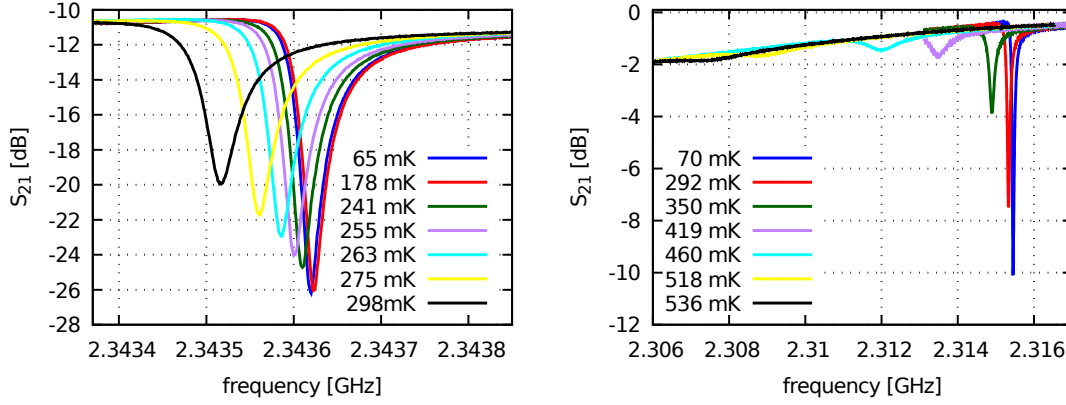


Figure 6.6: **Left:** Measurement result of transmission measurement of resonator 3 in group 5 of the NIKA 2-chip, measured with optimized external magnetic field. **Right:** The same measurement covering a larger temperature range with Niobium magnetic shielding.

6.2.5 Measurement of temperature dependence of resonance frequency and quality factor

The change of the resonance frequency and the quality factor with temperature is of great interest for the device analysis, as it yields information about the gap parameter of the superconductor, which will be extracted from the following measurements in the analysis in sec. 6.3. The transmission of the individual resonators is measured as a function of the temperature of the device as described in sec. 3.4.1. The measurements are done for the two setup configurations mentioned above. First, the measurements are done with the sample surrounded by an aluminum magnetic shield with external magnets applied in western direction. This measurement is labeled "opt. mag." in the plots below. The second measurement is done with an niobium layer on the aluminum shield acting as an extra magnetic shield layer.

The measurement result for resonator G5R3 for the two configurations is shown in fig. 6.6. For both measurements the resonance frequency shift and the internal quality factors are fitted using eq. (6.2). The measurements are done on resonator groups 4 and 5 only, since at resonance frequencies below 2 GHz the used LNA (see sec. 3.3.4) is too far out of its design band. Below 2 GHz, the LNA input reflection increases rapidly, as does the noise temperature. The measurements with optimized field are done up to 300 mK and the measurement with Niobium shield up to 530 mK which makes a visible difference in the amount of frequency shift and quality factor reduction.

The results for G4 and G5 of chip CPWO2 are shown in fig. 6.7. Generally, measurement with optimized magnetic field shows higher quality factors than the Niobium

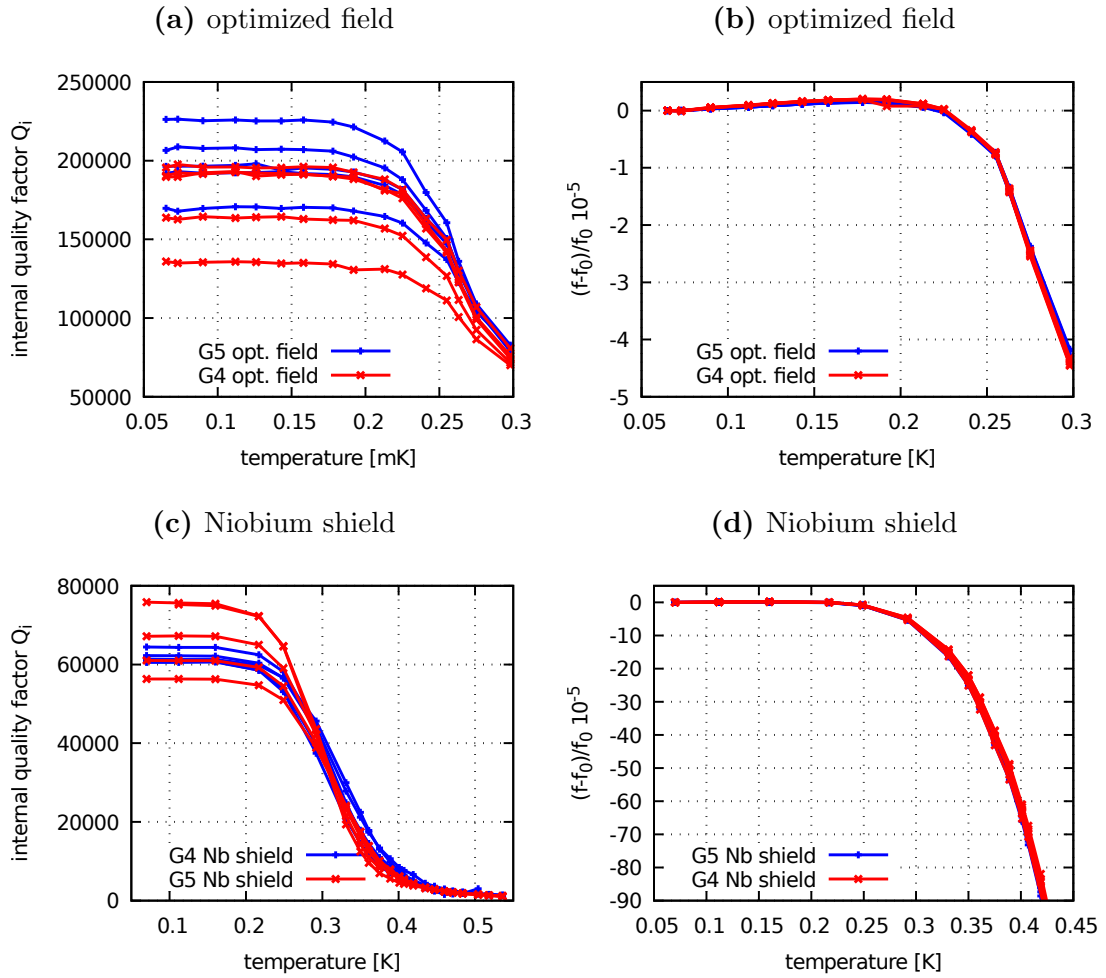


Figure 6.7: Internal quality factors for all resonances in G4 and G5 measured with optimized external magnetic field (a) and with Niobium shielding (c). The measured temperature range for the shielded measurement was wider. (b) and (d) Measurement of fractional frequency shift $(f - f_0)/f_0$ for the two configurations for all resonators in G5 and G4.

shield measurement, with quite some spread between the individual resonators. For all resonators, the quality factor saturates below 0.2K. At high temperatures, the spread between the individual resonators reduces. The fractional frequency shift in contrast behaves very uniformly with temperature for all resonators.

6.3 Determination of the complex gap parameter

One important material parameter is the superconducting gap parameter which gives the binding energy of cooper pairs. The complex gap parameter $\Delta = \Delta_1 + i\Delta_2$ as introduced in [75] contains the usual superconducting gap parameter Δ_1 and a parameter Δ_2 which limits the internal quality factor of the resonators at low temperatures. The complex

gap parameter can be determined from the VNA measurements analyzed in sec. 6.2.5 as described below.

6.3.1 Simulation of the kinetic inductance fraction

For my measurements the gap parameter Δ_1 can not be treated as a constant only dependent on T_c . Looking at the fitting procedure in sec. 2.2.7, one can quickly see that the gap parameter and the kinetic inductance fraction α are strongly correlated in the fit for small changes. Because of that, the gap parameter Δ_1 and the kinetic inductance fraction α can not be fitted simultaneously. The kinetic inductance fraction α is therefore determined from a numerical simulation using Sonnet EM first.

From the CAD design of the lithography mask, the geometry for resonator 3 of group 4 is implemented in Sonnet EM. First, all materials are simulated as PEC (perfect electric conductor) which should not contain any effects of kinetic inductance to determine the resonance frequency of a hypothetical lossless normal conducting resonator. The resonance frequency is $\nu_n = 2\pi\sqrt{\frac{1}{LC}}$. In contrast, the resonance frequency of a proper superconducting resonator is supposed to be $\nu_s = 2\pi\sqrt{\frac{1}{(L+L_k)C}}$, containing a contribution from the kinetic inductance. From the quotient of the square one can calculate:

$$\frac{\nu_s^2}{\nu_n^2} = \frac{L}{L + L_k} = 1 - \frac{L_k}{L + L_k} = 1 - \alpha \quad (6.3)$$

Where α is the kinetic inductance fraction as defined in eq. 2.13. Therefore, from the simulated resonance frequency without kinetic inductance and a resonance frequency from a superconducting resonator, the kinetic inductance fraction can be calculated.

The resonance frequency of the superconducting resonator is obtained by a measurement of the resonator. This implies the premise that the fabricated resonator dimensions do not differ significantly from the CAD design dimensions. The resonance frequency of the superconducting resonator can also be determined by simulation if a surface inductance resembling the kinetic inductance is assumed. Reference [90] states an surface inductance of 2.0 pH/sq for films produced on the same machines as my samples. The simulated resonance frequencies and the model are shown in fig. 6.8. The simulated resonance frequency with kinetic inductance is 1.87 GHz varies significantly from the measured 2.02 GHz, therefore the measured resonance frequency is used for determination of the kinetic inductance fraction. It is then calculated as

$$\alpha = 1 - \frac{\nu_s^2}{\nu_n^2} \quad (6.4)$$

and yields a result of $\alpha = 0.215$, which is in a physically and experimentally sane region

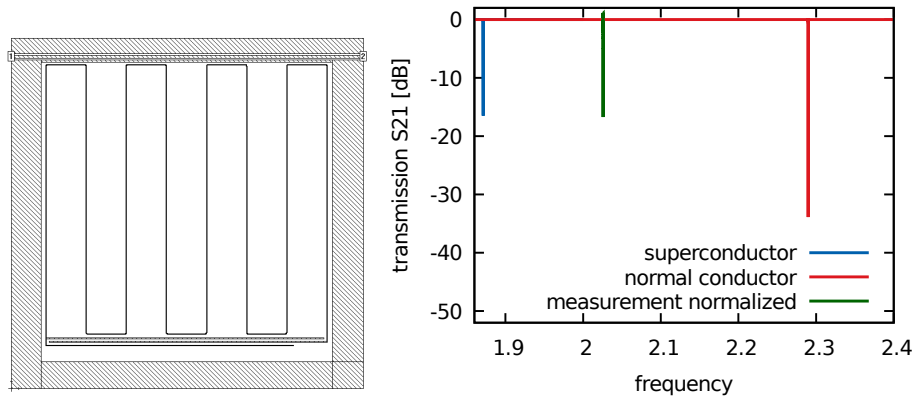


Figure 6.8: **Left:** Sonnet EM model of one resonator. **Right:** Simulated transmission of the resonator using PEC and simulated aluminum with a surface inductance 2.0 pH/sq in comparison to the actual measured resonance frequency.

and therefore treated as a constant for the next part of the analysis.

The simulation above can also be used to determine the surface inductance corresponding to the measured resonance frequency, assuming my films differ from those measured in [90]. For that the surface inductance of the metal is optimized till the resonance frequencies match. With this method, an actual surface inductance of 1.3 pH/sq is determined.

6.3.2 Correction for non-monotonical frequency shift

At low temperatures my measurements show that the resonance frequency first increases with increasing temperature before it starts to decrease as predicted by Mattis-Bardeen theory. This can be due to the presence of Two-Level Systems [8] or as newly postulated by the Kondo-effect [74]. In both cases, the imaginary part of the complex conductivity is proportional to the logarithm of the temperature. An example of this effect is shown in fig. 6.9. Since this effect is distinct from the complex conductivity created by the quasiparticle distribution analyzed in the next section, it is removed before the analysis. For that, a linear function

$$\frac{\delta f}{f_0} = \frac{\beta}{2} \log(T/T_0) = \frac{\beta}{2} \log(T) - \frac{\beta}{2} \log(T_0) \quad (6.5)$$

is fitted to the fractional frequency shift plotted against the logarithm of the temperature to determine the influence of the non-monotonic behavior. This contribution is then subtracted from the data before further analysis. The overall influence on the analysis is rather small if the temperature sweep is done up to temperatures above 300 mK. At higher temperatures, the resonance shift by the quasiparticle is dominant. The TLS contribution and the correction for G4R3 are shown in fig. 6.9. The reference temperature T_0 would be

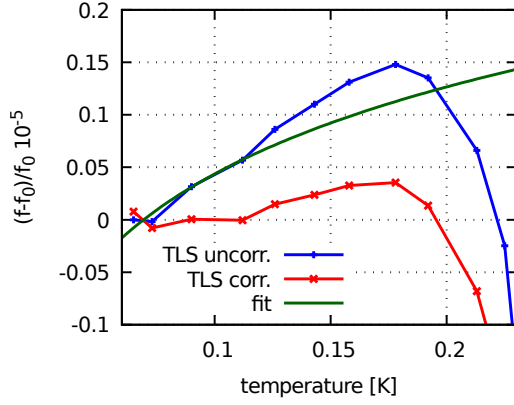


Figure 6.9: Correction of the TLS contribution to the resonance frequency shift at the example of resonator G4R3 measured with optimized external magnetic field. The fit is of the form $y = \beta/2\log(T) + K$ with $\beta = 2.39 \times 10^{-6}$. The offset is $K = 3.19 \times 10^{-6}$. The correction is not perfect but considerably reduces the non-monotonic slope.

in this case 0.07 K as can be calculated from K and β .

6.3.3 Fitting resonator parameters

Parameter	opt.mag. field	Nb shielding
$\Delta_1(\frac{f-f_0}{f_0})$	$(2.121 \pm 0.003) \times 10^{-4}$ eV	$(1.920 \pm 0.002) \times 10^{-4}$ eV
$\Delta_1(Q_i)$	$(2.390 \pm 0.016) \times 10^{-4}$ eV	$(2.290 \pm 0.003) \times 10^{-4}$ eV
Δ_2	$(0.61 \pm 0.03) \times 10^{-8}$ eV	$(1.66 \pm 0.15) \times 10^{-8}$ eV
α	0.215	0.215

Table 6.1: Averaged results of extended Mattis-Bardeen fits to the fractional frequency shift and the internal quality factor of the 10 resonances in G4 and G5, measured with two setup configurations. The measurements are done with with external magnetic field or with Niobium shielding. For comparison, the BCS value for the gap parameter calculated from T_c would be $\Delta_1 = 2.09 \times 10^{-4}$ eV.

With the kinetic inductance fraction $\alpha = 0.215$ as a fixed parameter, the complex gap parameter $\Delta = \Delta_1 + i\Delta_2$ remains to be determined (see 2.2.5). Because the gap can not be treated as constant given by the simple relation $2\Delta_1 = 3.52 k_B T_c$, the BCS value is just used as a starting value for the fit. From the examination of the complex conductivity at low temperatures another constraint can be determined. Since the internal quality factor Q_i saturates at low temperature, it can be determined fairly well by averaging the measured Q_i below the saturation temperature. This sets a constraint to the remaining parameters as shown in eq. (2.31). The consequence of determining Q_i at low temperatures directly from the measurement result and α from the simulation is that only Δ_1 remains to be fitted for both, the frequency shift and the quality factor data.

Optimally, the fit of Δ_1 should yield the same results for the temperature dependence of the fractional frequency shift and the internal quality factor. Because no agreement

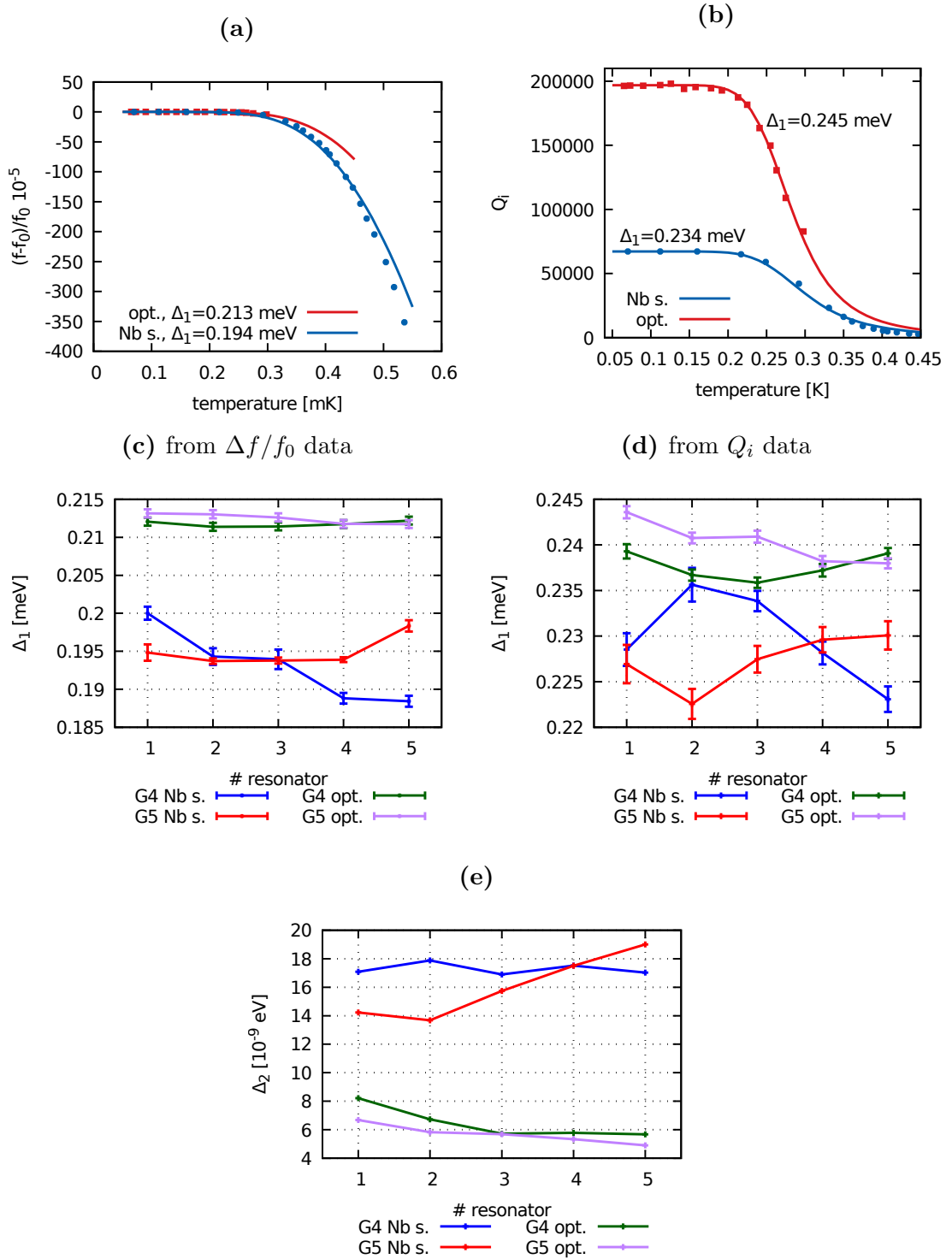


Figure 6.10: Fit of the fractional frequency shift data (a) and the internal quality factor (b) to the model for measurements of resonator 1 of group 5 with optimized external field (opt.) and with Niobium shield (Nb.s.). The discrepancy in gap parameters between both datasets and both setups becomes apparent. (c) Results of the fit of Δ_1 to the temperature sweep of the fractional frequency shift $(f - f_0)/f_0$ plotted for each resonator. The error is determined from the variance of the fit. (d) Results for Δ_1 from the fit to the internal quality factor data. (e) Δ_2 for each resonator resulting from the fits to Δ_1 and relation (2.31).

between both data sets is obtained, Δ_1 is fitted separately to the frequency shift and internal quality factor measurements. Representative results for one resonator are shown in fig. 6.10. The transition temperature of the film could only be observed from the RF transmission of the line and is determined as 1.38 K. From that, the BCS value of the gap parameter would be $\Delta_1 = 2.09 \times 10^{-4}$ eV. The temperature vs. internal quality factor data is then fitted to eq. (2.25) and the temperature vs. resonance frequency data is fitted to eq. (2.24) using a Levenberg Marquard non-linear regression fit as implemented in GNU Octave [34]. The averaged results for the complex gap separated by measurement setup and method of determination are summarized in table 6.1. The values of Δ_1 determined from quality factors and from frequency shift for all measurements are compared in fig. 6.10.

The fitted gap parameters with optimized magnetic field is 0.212 meV determined from the frequency shift and 0.293 meV determined from the quality factor. With Niobium shielding, these values are 0.192 meV and 0.229 meV respectively. The parameter Δ_2 with Niobium shielding is about 2.5 times larger than with the external field.

6.4 Measurement of the quasiparticle lifetime using excitation pulses

One of the tasks on the NIKA 2 devices we got from IRAM is to measure the quasiparticle lifetime of the aluminum film. The measurement setup for the NIKA 2 devices at IRAM is currently not equipped to do these measurements. I attempt to measure the quasiparticle lifetime with three different methods. The first two methods presented below use the excitation from either an LED pulse or from cosmic rays and observe the decay. The third method described later determines the lifetime from the roll-off in the noise spectra of the chip.

6.4.1 Measurement of LED pulse response

The measurements are done with optimized external magnetic field in western direction on chip CPWO2 using the setup described in sec. 3.4.4. Since the optical pulse from the fiber passes two small holes and emerges directly at the center of the chip, resonator G3R3 is measured despite the fact, that its resonance frequency is slightly out of the IQ mixer band starting at 2 GHz. This resonator sees the strongest pulse power. For this measurement, only a pulse response has to be visible and the degrading operating parameters of the IQ mixer do not matter too much, as long as it has some conversion. The resonance frequency

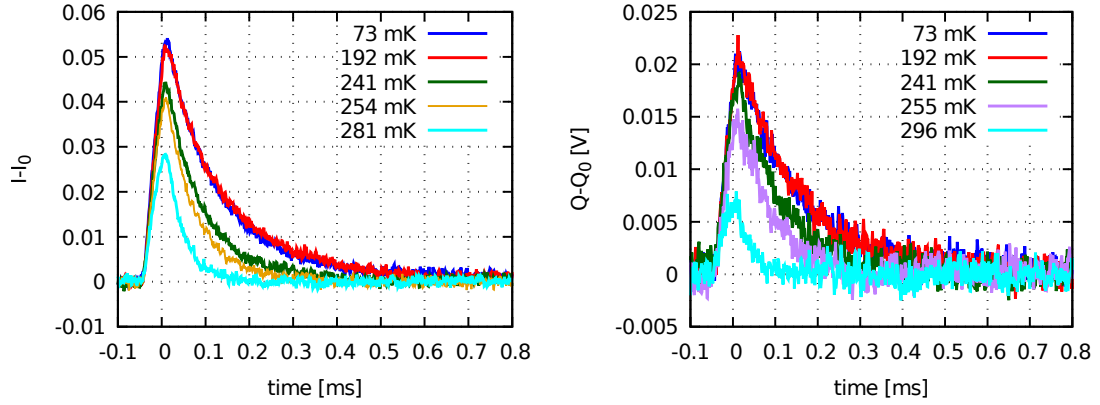


Figure 6.11: Measurement results for LED pulse measurements at 55 mA pulse current and different temperatures. **Left:** Resonator G3R3, which is in the center of the chip. **Right:** Resonator G4R3. The channel with the strongest response (I or Q) is chosen for further analysis.

of resonator G4R3 is just in the IQ mixer band, therefore this resonator is also measured. Resonators of group 5 are too far off-center of the chip to show any response to the pulse. The following measurements are made on chip CPWO2 using the IQ readout:

- At 73 mK device temperature, the pulse current is varied between 10 and 55 mA at the driver circuit. For each current, two measurements of G3R3 which each record and average the response from 50 pulses are made.
- At 73 mK, the readout signal power is attenuated in steps to a maximum of 9 dB using a variable attenuator. For each setting one measurement with 50 pulses is made. The current is set to the maximum of 55 mA.
- The ADR bath temperature is changed up to 290 mK by increasing the current in the ADR magnet. For each temperature, G3R3 and G3R4 are measured with 50 times averaging at a pulse current of 55 mA. The results are shown in fig. 6.11.

For all measurements above, the pulse duration is 50 μ s and the sampling rate is 1 MHz.

6.4.2 Processing of LED pulse measurements

To analyze the pulse measurements from 6.4.1, the time axis is shifted such that the peak is at $t = 0$. For each measurement, the I and Q response of a number of pulses determined by the averaging factor is recorded and averaged into single pulses for I and Q. The channel with the strongest response is selected and analyzed.

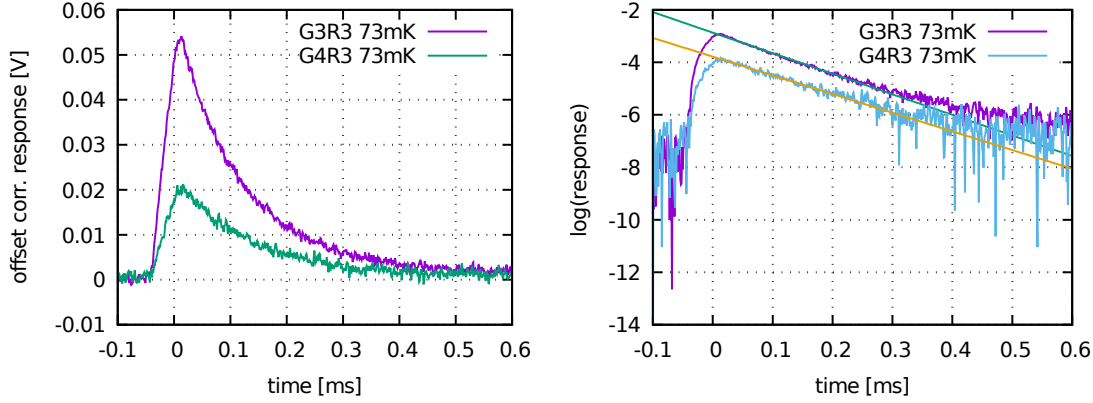


Figure 6.12: Left: 50 times averaged pulses for two different resonators. G3R3 is the center resonator of the chip which is illuminated the strongest by the LED pulse. **Right:** Logarithmic plot of the same resonances with the fitted linear functions.

The y-axis is plotted logarithmic and a linear function $f(x) = ax + v$ is fitted to the linear portion of the pulse. The slope of the linear function immediately is the inverse of the time constant $\tau = 1/a$. The fit yields an error estimation for a , from which the error $\Delta\tau = \Delta a/a^2$ can be calculated using Gaussian error propagation. Examples for the two resonators analyzed in this sections are shown in fig. 6.12. This fitting method is applied to all pulse measurements in the following. Because the quasiparticle lifetime is assumed to be the dominant time scale, τ will be in the following already called the quasiparticle lifetime.

6.4.3 Dependence on LED power and readout system power

To exclude external effects on the measurement, the influence of the LED pulse current and the readout power are investigated first. The measurements analyzed here are described in sec. 6.4.2. The result is shown in fig 6.13 on the left. The result shows a monotonically decreasing dependence of the fitted time constant to the LED current except for one measurement at the lowest current. The lifetime decreases from 132 μs at the lowest current of 10 mA down to 118 μs at 55 mA. To check if the readout signal has an influence on the measured time constant, the readout power is reduced by increasing the value of an adjustable attenuator in front of the cryostat input port from 0 to 9 dB. These measurements are done at the maximum LED current of 55 mA on resonator G3R3 to have the highest response. The result is shown in fig. 6.13 on the right. No dependence of the time constant to the readout power is apparent here. The measured quasiparticle lifetime fluctuates around 116 μs . The errorbars in the figure are determined from the uncertainty of the fit.

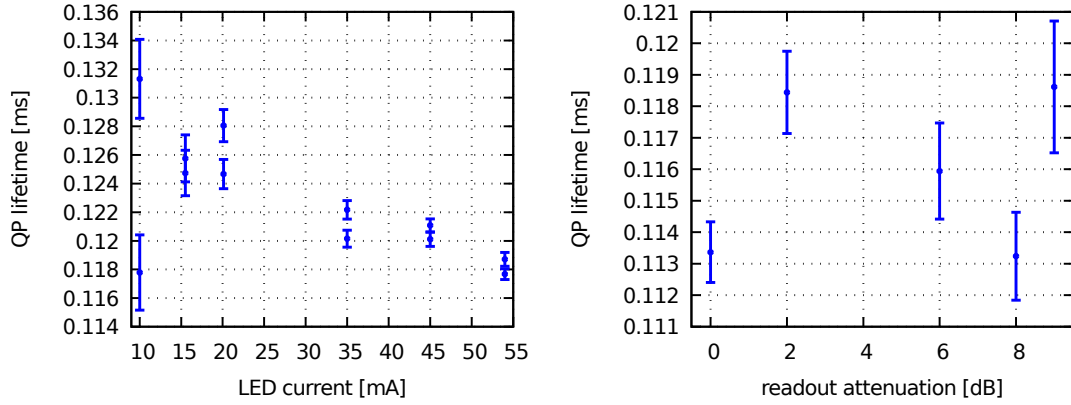
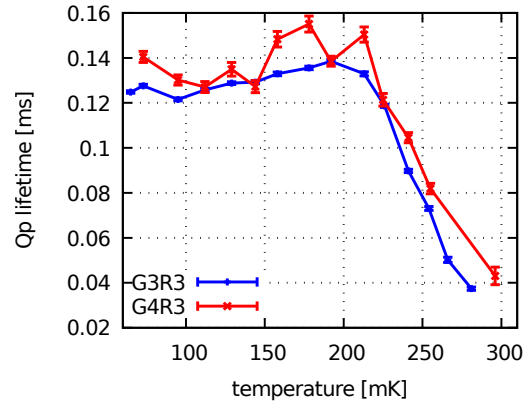


Figure 6.13: **Left:** Quasiparticle lifetime plotted against LED pulse peak current. **Right:** Quasiparticle lifetime plotted against additional attenuation in the readout line in front of the device. The error bars show the uncertainty of the fitted parameter τ .

Figure 6.14: Quasiparticle lifetimes from resonators G3R3 and G4R3, measured with the LED pulse method with optimized magnetic field at different device temperatures.



6.4.4 Temperature dependence of quasiparticle lifetime from LED pulses

The temperature dependence of the measured time constant is interesting to verify if the measured time constant is really associated to the quasiparticle system. The measurement results shown in fig. 6.11 are the average of 50 LED pulses measured at different device temperatures between 70 and 300 mK. The LED pulses are processed as described above in sec. 6.4.2. The result is shown in fig. 6.14. At low temperatures, quasiparticle lifetimes around 120 μ s to 140 μ s are measured. These stay rather constant with a small increase till 180 mK and fall down above 200 mK. Resonator G3R3 shows slightly lower quasiparticle lifetime than G4R3, which can also be an effect of the lower uncertainty.

6.4.5 Quasiparticle lifetime from cosmic ray events

Since the NIKA chip area is 400 mm^2 with a substrate thickness of $250 \mu\text{m}$, there is quite a probability that high energy particles are absorbed. Every cosmic ray particle has much more energy than the optical LED photons, therefore absorption anywhere in the substrate will cause a detector response. Since the events occur randomly at a rate of about 1 event per minute, quite long time sequences from the IQ mixer have to be recorded. For the following measurements, chunks of 10 seconds are recorded at a rate of 100 kHz to keep the amount of data manageable. Then the sequences are manually searched for cosmic ray events, the events are extracted and fitted the same way as the LED pulses mentioned above.

The cosmic ray excitations deploy considerably more energy in the chip than the LED pulse, which can be seen by the height of the measured response pulse. In contrast to the LED pulses which require a minimal pulse time of $50 \mu\text{s}$, the excitation with cosmic rays occurs quasi instantaneously, which can help diagnose eventual problems with a slow LED circuit.

The measurements are done on chip CPWO2 with the setup as used with the external magnets, but with the magnets removed. The device temperature is kept at 65 mK during the measurement. The procedure is described in sec. 3.4.5. Five strong events are measured and analyzed. One event is shown in fig. 6.15. The cosmic ray events appear as a very clear pulse shape in comparison to the rather weak LED pulses. The fitting of the lifetime is done on semilogarithmic scale with the method introduced above in sec. 6.4.2. Before that, the data set is truncated to the pulse only. An example of a cosmic ray hit and the fitted quasiparticle lifetime for five events is shown in fig. 6.15 for 63 mK sample temperature. The quasiparticle lifetime with cosmic rays is about $135 \mu\text{s}$, which is comparable to the LED results.

6.5 Noise measurements using the IQ mixer

To measure the NEP of the detectors, noise power spectra are required, which can be separated in amplitude and phase noise. The time domain data is measured using the IQ mixer and calibrated by correcting the data.

6.5.1 Measurement of time domain data for noise analysis

The time domain data for calculating noise power spectral densities is measured with chip CPWO2 with optimized external magnetic field following the procedure described in 3.4.3.

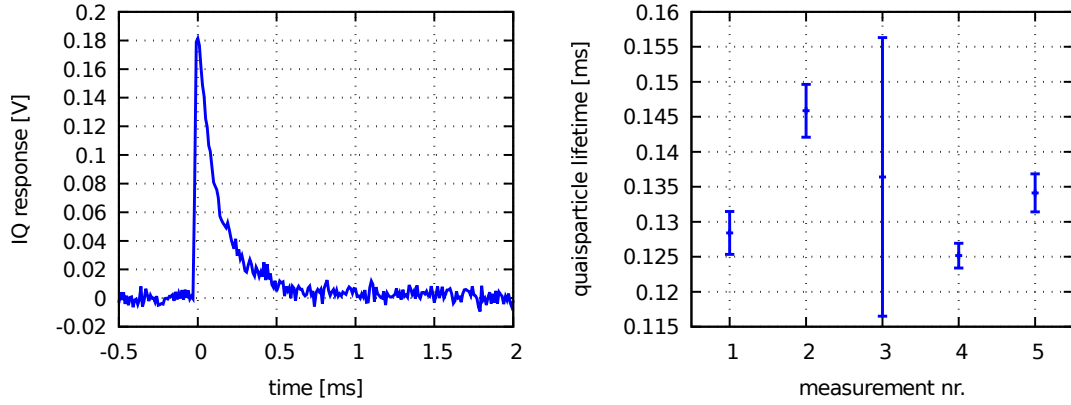


Figure 6.15: **Left:** Single cosmic ray response. **Right:** Fitted quasiparticle lifetime for different cosmic ray events. Measurement 3 is a peak with low intensity, therefore the uncertainty is larger.

The data is measured on and off the resonance, to attempt the correction for system noise. The noise measurement is performed for device bath temperatures between 73 mK and 241 mK. The temperature is set as described in sec. 3.1.5. The time domain data is visually inspected for cosmic rays which are removed before further processing. An IQ mixer frequency sweep (see sec. 3.4.2) is measured for the lowest temperature and for each two or three temperature steps, which is necessary to properly calibrate the time domain data.

6.5.2 Analysis of the measured IQ mixer frequency sweep

The IQ mixer frequency sweep data is needed to correct the time domain data for noise measurements for its gain imbalance and DC offsets, which is necessary for the separation of amplitude and phase noise later. The DC offsets mark the center of the IQ plane.

A full model for the transmission of the setup without resonances is used to correct the measured IQ sweep. The model contains gain and phase imbalance, the DC offsets and a correction of the difference in cable length between the two outputs of the directional coupler (see fig. 3.6). All these parameters are fitted anew for each resonator analysis. The model for the IQ response dependent on frequency used here is

$$I(f) = G_I \cdot \cos(\theta_\nu \cdot (f - f_{\text{ref}}) + \phi_0) + I_0 \quad (6.6a)$$

$$Q(f) = -G_Q \cdot \sin(\theta_\nu \cdot (f - f_{\text{ref}}) + \phi_0 + \Delta\phi) + Q_0 \quad (6.6b)$$

where G_I and G_Q are the respective gains, I_0 and Q_0 are the DC offsets and θ_ν is the phase change per frequency caused by the length difference of the line between the LO and signal port of the IQ mixer, measured in rad/GHz. $\Delta\phi$ is the phase imbalance between I

and Q channels and f_{ref} is an arbitrarily chosen reference frequency. The model describes two sinusoidal curves with an ideal phase difference of 90° and an period of $2\pi/\theta_\nu$. If I and Q are plotted against each other, a circle around I_0 and Q_0 is the result. The reference frequency f_{ref} just decouples the effect of a change of θ_ν to the change of absolute phase, allowing a more stable fit and less random adjustment of that parameter. It is actually just an additional phase offset dependent on the frequency as can be seen by multiplying out the expression inside the cos or sin.

This model is now fitted locally to the measured IQ frequency sweep using the following procedure, where the main difficulty is the determination of suitable starting values to ensure convergence. The process for determining starting values and for the fit is as follows:

- Starting values for I_0 and Q_0 are determined from the mean values of the measured I and Q data.
- Starting values for G_I and G_Q are determined by the peak values of the I and Q data.
- The starting value for the phase velocity θ_ν is determined manually by counting periods and set as a default value, since it only changes significantly if the cable length of the setup changes as well.
- The reference frequency is fixed to the start frequency of the measured IQ frequency sweep and the parameter is not fitted. The phase and phase imbalance are not estimated explicitly and are set to 0 because they are supposed to be small.
- With all start values set, a least square fit over all parameters is attempted. If the convergence is not achieved, the software front end offers to manually tweak the starting values while observing the result and redo the fit.

With the full parameter set, the measured IQ sweep can be corrected for offsets, the line length and the imbalance in gain and amplitude. The phase change per frequency is corrected by applying a 2D rotation matrix that rotates the I and Q data backwards. The correction is

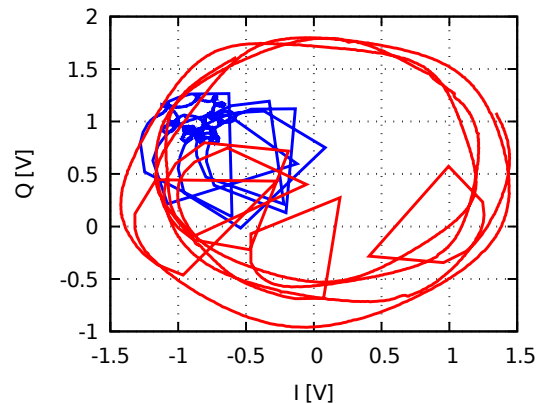
$$\begin{aligned} I_{\text{corr}} &= I \cos \theta + Q \sin \theta \\ Q_{\text{corr}} &= -I \sin \theta + Q \cos \theta \end{aligned} \tag{6.7}$$

where $\theta = -\theta_\nu \cdot (f - f_0) + \phi_0$ is the angle to correct for. In the IQ plane, this correction rotates the circle caused by the cable length backward into one single point located at a

parameter	symbol	value
DC offset I	I_0	0.099 V
DC offset Q	Q_0	0.614 V
gain I	G_I	1.277
gain imbalance	G_I/G_Q	1.012
phase imbalance	$\Delta\phi$	-0.02 rad
phase change per freq.	θ_ν	219.8 rad/GHz

Table 6.2: Resulting parameters of the IQ sweep model presented in eq. (6.6a) of resonator G5R3.

Figure 6.16: Measured IQ frequency sweep for resonator G5R3 (red) and after applying the corrections (blue). The gain is not renormalized here to keep the original scale, but the gain imbalance is corrected for. Also the phase offset is not corrected such that the origin of the resonances is not on the positive y-axis.



normalized transmission of $I = 1$ and $Q = 0$. Because the frequency dependence of gains, offsets and the phase imbalance is neglected, the IQ sweep does not collapse to a point, but to smaller circles lying on the diameter of the previous outer circle.

A measured and corrected IQ trace of G5R3 is shown in fig. 6.16. The measurement procedure is described in sec. 3.3.2 and the actual measurement in sec. 6.5.1. The fitted values for the model described above are shown for illustration in table 6.2. The edgy features pointing inward are the resonances which are badly resolved in the wide frequency range measurement. Generally, the IQ mixer is supposed to give better data, but it is operated at the lower edge of its band for G5 already, and G4 would be out of its band. It still gives signal for the lower frequencies, but all quantitative properties like gain and phase imbalance suffer at the band edges.

6.5.3 Calculation of the power spectral density

With the known DC offsets fitted in 6.5.2, the position of the time domain data measured in 6.5.1 on the IQ circle can now be determined to rotate the actual I and Q data into amplitude and phase direction. This is not yet amplitude and phase noise, but voltage

noise separated in its radial (amplitude) and circular (phase) components. The voltage noise and phase and amplitude direction can thus be compared directly. Remember that the time domain data is taken at a fixed frequency, thus it fluctuates only in I and Q directions by noise, which is very small in comparison to the radius of the resonance circle. However this noise is exactly what the measurement aims at.

The extra step of calculating the voltage noise in amplitude and phase direction is done for direct comparison of the two without having to worry about different scales. The angle to rotate the I and Q response into amplitude and phase direction is calculated by

$$\theta = \arctan\left(\frac{\bar{I} - I_0}{\bar{Q} - Q_0}\right) \quad (6.8)$$

where \bar{I} and \bar{Q} are the average of the I and Q data of the time domain measurement and give the center of the noise and I_0 and Q_0 are the DC offsets. For the calculation an implementation of the arctangent function valid in all 4 quadrants is used. The actual rotation uses the same formula as in (6.7).

We now have time domain data in units of volts in amplitude and phase direction. To calculate a power spectrum, a function from the National Instruments Enterprise Analysis library is used. In principle, the calculation follows sec. 2.3.1. This function returns a two-sided spectrum including negative frequencies, which is reduced to a single sided spectrum simply by abandoning the negative frequencies, which are symmetrical for real-valued data. The amplitude of the remaining spectrum is multiplied by 2 to compensate. Then the spectrum is rescaled to get the desired unit of V^2/Hz using Parseval's theorem which states that the integral over the power spectrum has to equal the integral over the squared time domain data to conserve energy. The function gives as output

$$S_k = \frac{|X_k|}{N^2} \quad (6.9)$$

where X_k is the k -th frequency sample of the discrete Fourier transform of the time series $x(t_i)$ and N is the number of samples. The total power is given by the sum over all S_k . The unit of S_k would be $V^2/\text{frequency channel}$. The information about the actual frequency axis has to be included separately. The width of a frequency channel limited by the Nyquist theorem is given as

$$\Delta f = \frac{f_{\text{Ny}}}{N/2} = \frac{2f_{\text{Ny}}}{N} = \frac{f_{\text{samp}}}{N} \quad (6.10)$$

where f_{Ny} is the Nyquist frequency and f_{samp} is the sample rate at which the time domain data is measured. The desired discrete power spectral density given in V^2/Hz is the total

power divided by the width of one frequency channel, which is then given by

$$S_u(f) = 2 \frac{N}{f_{\text{samp}}} S_k \quad (6.11)$$

The factor of 2 is added here since the spectrum is reduced to a single sided spectrum as the negative frequencies are identical with the positive for the DFT of a real valued time domain signal.

In summary, the measured time domain data is processed as follows:

- The DC offsets of the IQ mixer are determined from a wide IQ sweep around the resonance frequency.
- The I and Q time domain data is rotated in amplitude and phase direction.
- From the rotated data, the power spectrum is calculated and scaled to spectral density in units of V^2/Hz .
- If an averaged measurement of multiple time series is made, the steps above are executed for each time series and the resulting power spectral densities are averaged.

All time domain measurements from 6.5.1 are using the 1 kHz or the 260 kHz filter in front of the AD and the measurements on and off resonance are handled with that procedure. The resulting rotated noise power spectra for resonator G5R3 are shown in fig. 6.17. The data taken with both filters is plotted here in one color but uncut otherwise, so the roll-off of the filters is visible. This is only for illustration. For further processing, the data of the low frequency part is cut slightly below the filter cut-off and joined together with the high frequency data.

6.5.4 Calculation of amplitude and phase noise spectral density

From the voltage noise in amplitude and phase direction, the amplitude and phase noise can be calculated by using the radius of the point in the IQ plane where the measurement is made. The radius can be determined from the mean I and Q values and the IQ mixer DC offsets by the Pythagorean theorem

$$r^2 = (\bar{I} - I_0)^2 + (\bar{Q} - Q_0)^2 \quad (6.12)$$

For the calculation of a phase NEP a real phase noise power spectrum has to be calculated from the position in the IQ plane corrected by the DC-offsets and using the arctangent

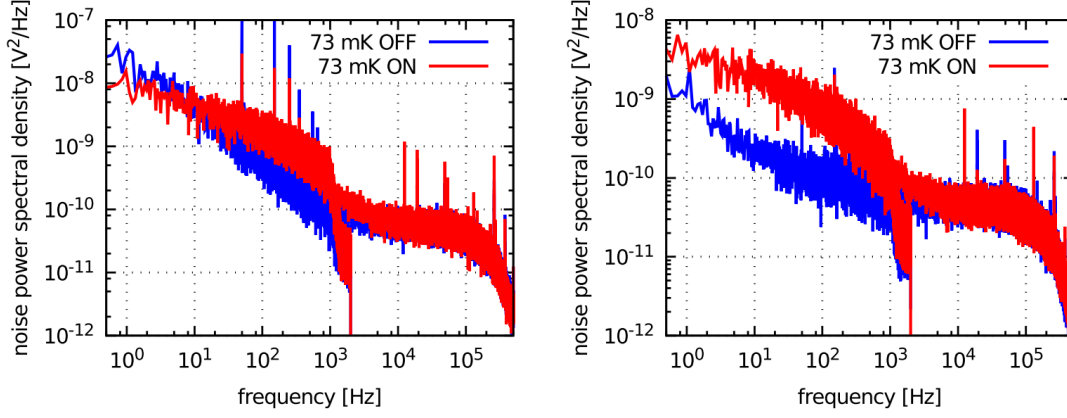


Figure 6.17: Noise power spectral density of resonator G5R3 after rotation in amplitude (**left**) and phase (**right**) direction, for the readout tone on the resonance and close to the resonance (off). The measurements are done with the 1 kHz filter at 4 kHz sampling frequency and with a 260 kHz filter at 1 MHz sampling frequency and plotted together. The cut-off frequencies of the filters are visible.

function. It is then calculated as in [67]

$$S_\phi(\omega) = \arctan\left(\frac{\sqrt{S_Q(\omega)}}{r}\right) \approx \frac{S_Q(\omega)}{r^2} \quad (6.13)$$

where S_Q is the rotated phase noise power spectrum. In contrast to my approach the radius r in [67] is measured from the center of the resonance circle, whereas I measure from the center of the IQ plane.

The voltage noise in amplitude direction is basically already usable as it is. It can be normalized to the strength of the "carrier", the undisturbed readout tone given by the off-resonance radius of the circle in the IQ plane. It can then be calculated in the dimensionless unit of dBc, decibels relative to carrier:

$$S_{\text{amp}}[\text{dBc}] = 10 \log_{10}\left(\frac{S_I}{r}\right) \quad (6.14)$$

Here S_I is the rotated amplitude noise power spectrum. The phase can also be easily converted to dBc since it is given as rad/Hz:

$$S_\phi[\text{dBc}] = 10 \log_{10} S_\phi \quad (6.15)$$

6.5.5 Logarithmic averaging

The information contained in the noise power spectra becomes best visible on a double logarithmic scale. This way, the low frequency end of the spectrum is respected as much as the high frequency end. Physically, the noise spectra calculated from the time domain spectra are linear, meaning that the high frequency end contains many more samples than the low frequency end on a logarithmic scale. To emphasize the logarithmic nature of the information, a method of averaging is used that creates an equal sample spacing on the log-scale in frequency by averaging the spectrum over a width increasing with frequency. This method might keep each single sample on the low frequency end of the spectrum while averaging massively on the high end. The result is a much less noisy spectrum on the high frequency end, which is supposed to be processed only on a log-scale. Examples for log-averaged data is shown in the further analysis sections, for instance in 6.18. I implemented this method in a gnu octave function which accepts the input frequency and amplitude and a parameter determining the number of samples desired on the output. Its output is the new frequency scale and the log-averaged amplitude data.

6.5.6 Quasiparticle lifetime from noise spectra

The noise spectra measured on the resonance frequency all show a roll-off determined by the quasiparticle lifetime. The noise spectrum limited by a single time constant is expected to have the shape of a Lorentz-curve. A full range spectrum of the stitched and log-averaged measurements for different temperatures is shown in fig. 6.18. There is a temperature dependent roll-off visible. The roll-off above 200 kHz is due to the filter cutting off the signal in front of the ADC. There is also a strong component of f^{-x} noise visible below 1 kHz which is probably TLS (see sec. 2.3.5). Both, the generation-recombination noise and the TLS noise are supposed to follow the same time-constant in the roll-off frequency. The following noise model is therefore used to fit the measurement.

$$S(f) = (S_{GR} + S_{TLS} \cdot f^{-x}) (1 + (2\pi f\tau)^2)^{-1} + S_0 \quad (6.16)$$

Here S_{GR} is the constant generation recombination noise level, S_{TLS} the TLS noise level, x is the temperature dependent TLS slope and S_0 the system noise. The usual procedure for MKID noise measurements is to record noise data on the resonance and at a frequency off the resonance, but close. Then the system noise can be removed by subtracting the off-spectrum from the on-spectrum. This is done for the amplitude noise spectra and the parameter S_0 in the noise model is consequently set to 0.

For the phase noise data which exhibits a much more pronounced roll-off, the off reso-

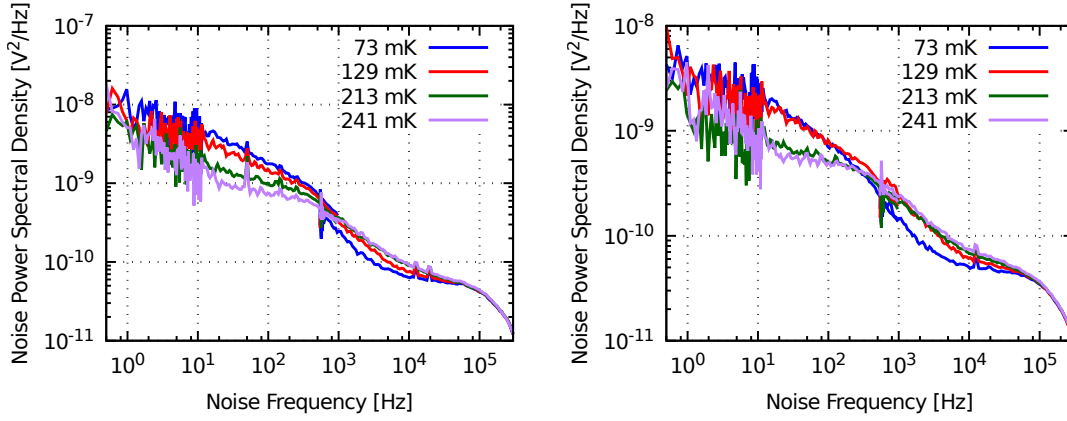


Figure 6.18: Left: Stitched amplitude noise spectra for resonator G5R3, measured with two different filters. The part of the spectra above the 1 kHz filter cutoff is removed. The raw data is rotated in amplitude direction, but still on a voltage scale. Sometimes the two data sets do not fit together smoothly, which is usually a sign of disturbances in the low frequency part causing excess noise. **Right:** Stitched phase noise spectra for G5R3, processed the same way as the amplitude spectra. Both spectra show an earlier roll-off for lower temperature.

nance data is not subtracted because the resulting slope at the high frequency side does not match the expected $1/f^2$ dependence predicted by the Lorentz-curve. In addition, the phase noise exhibits an unexpected excess noise at low frequencies for the off-resonance data. A fit of a Lorentz time constant like the quasiparticle lifetime is not possible. Therefore, the system noise is fitted with the parameter S_0 to the data just before the filter cut off and the full noise model (6.16) is used.

This noise model is fitted to the stitched and log-averaged data on a double-logarithmic scale to focus on the roll-off part of the spectrum. A representative fit of the amplitude and phase noise spectra is shown in 6.19. The resulting temperature dependence of the quasiparticle lifetime for both amplitude and phase data is shown in fig. 6.20. For the noise spectra, at the lowest temperature a quasiparticle lifetime around 250 μs is measured, which quickly drops down to 140 μs .

6.6 Calculation of dark NEP

The measurements in the previous sections deliver the necessary parameters to calculate a dark noise equivalent power (NEP, sec. 2.3.2), for the NIKA detectors. The remaining optical loading is only coming from the ADR mK stage. The dark NEP gives a lower limit for the detectors sensitivity to the extent that optical loading, increasing temperature or magnetic fields only increase the NEP and thus decrease the sensitivity of a real detector. In a real application, the detector is of course always under optical loading by the radiation

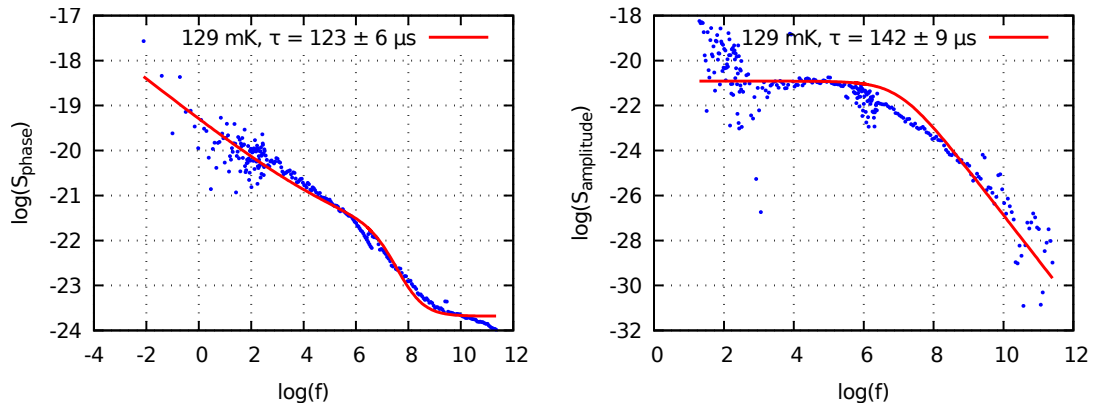


Figure 6.19: **Left:** Representative fit of the noise model in (6.16) to a phase noise measurement of resonance G5R3 at 129 mK. **Right:** Fit of the noise model with $S_0 = 0$ to corrected amplitude spectra of the same measurement. The off-resonance data is subtracted from the on-resonance data.

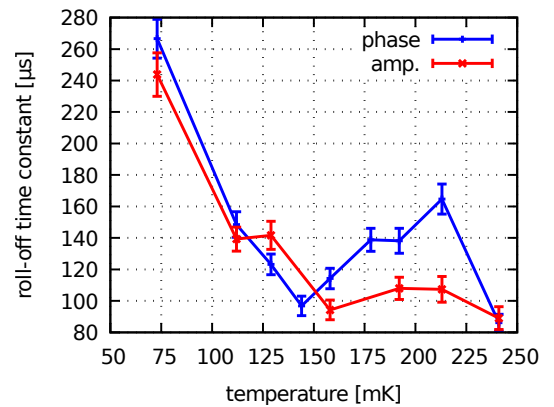


Figure 6.20: Fitted quasiparticle lifetimes of resonator G5R3 plotted against temperature. The error is the uncertainty of the fit with respect to the parameter τ .

it is supposed to detect and some thermal background. For calculating the dark NEP, some factors have to be deduced from different measurements. Because of that, the significance of that value is limited. The formula to calculate the dark NEP for a pair breaking detector using phase readout is [24]:

$$\text{NEP}_\phi^2(\omega) = S_\phi(\omega) \left(\frac{\eta\tau}{\Delta_1} \frac{d\phi}{dN_{\text{qp}}} \right)^{-2} (1 + \omega^2\tau^2) \quad (6.17)$$

Here, $S_\phi(\omega)$ is the phase noise power spectrum, $\eta \approx 0.6$ [28] is the quasiparticle generation efficiency, τ is the quasiparticle lifetime, Δ_1 is the real part of the complex gap parameter and $d\phi/dN_{\text{qp}}$ is the phase responsivity in rad/quasiparticle. The last term generates a roll-off of the detectors response at the quasiparticle lifetime which is the dominant time constant of the detector. The next sections will describe the calculation of the individual factors to calculate the NEP and present the result for resonator 3 in group 5.

6.6.1 Calculating the phase responsivity from the frequency shift data

Using the temperature sweep data for G5R3 shown in fig. 6.7, the phase responsivity can be deduced considering thermal quasiparticles instead of optically created quasiparticles. The equivalence of the effects is shown in [40]. The number of quasiparticles in dependence of the temperature is given as

$$N_{\text{qp}}(T) = 2N_0 \sqrt{2k_B T \Delta_1(0)} \cdot e^{-\frac{\Delta_1(0)}{k_B T}} \cdot V \quad (6.18)$$

where $N_0 = 1.72 \times 10^{10} \text{ eV}^{-1} \mu\text{m}^{-3}$ [26] is the single spin electron density for aluminum, k_B is the Boltzmann constant, $\Delta_1(0)$ is the gap parameter at a temperature of 0 K and V is the active volume of the detector. For the NIKA-chip, the volume of the inductor is determined from the CAD data of the lithography mask which is $1337 \mu\text{m}^3$, since only quasiparticles in the inductor can cause response. The gap parameter Δ_1 is taken from the fits in section 6.3. Since the fits for Q and the frequency shift give quite different results, the average of both values is used here. With (6.18), now temperature can be expressed as a "number of quasiparticles in the active detector volume".

When the frequency is swept across a resonance, the steepness of the phase change is given by the width of the resonance and is thus related to its Q-factor. The fractional frequency change $\delta f/f_0 = (f - f_0)/f_0$ can be calculated into a phase change by [67]

$$\delta\phi = -4Q \frac{\delta f}{f_0}. \quad (6.19)$$

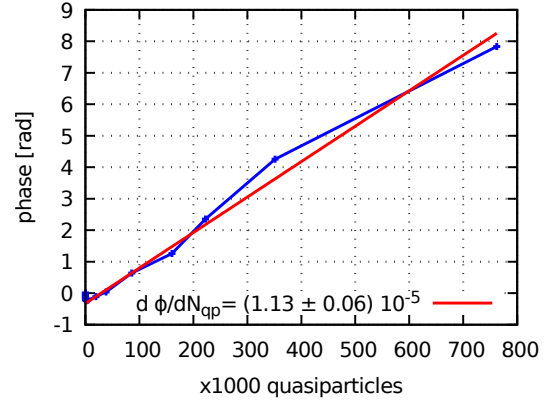


Figure 6.21: Phase response of resonator G5R3 plotted against the number of thermal quasiparticles to fit the responsivity.

parameter	value
N_0	$1.72 \times 10^{10} \text{ eV}^{-1} \mu\text{m}^{-3}$
V	$1337 \mu\text{m}^3$
Δ_1	$(2.26 \pm 0.14) \times 10^{-4} \text{ eV}$
$d\phi/dN_{\text{qp}}$	$(1.13 \pm 0.06) \times 10^{-5} \text{ rad/qp}$
η	0.57
τ_{qp}	$(150 \pm 30) \mu\text{s}$
r	0.3 V

Table 6.3: Parameters used for calculation of the phase responsivity and the dark NEP

The validity of this equation has to be limited to a phase range determined by the width of the resonance as the phase can only change till the shift is larger than half a resonance width. Now the phase response (6.19) is plotted against the quasiparticle number (6.18) using the real measurement data for resonator G5R3 and a linear function is fitted to the lower range of the plot to determine the phase change per quasiparticle, the phase responsivity. The plot and the fit is shown in fig 6.21. The determined phase change per quasiparticle is determined as $(1.13 \pm 0.06) \times 10^{-5} \text{ rad/qp}$.

6.6.2 Dark NEP

With the phase noise power spectrum, the quasiparticle lifetime, the gap parameter and the phase responsivity, now the dark NEP can be calculated using (6.17). The result is shown in fig. 6.22 on the right. This is the dark noise equivalent power using hypothetical phase readout with a readout tone positioned on the resonance. The parameters required for the calculation of the phase responsivity and the dark NEP are summarized in table 6.3. The used phase noise spectrum is shown in fig. 6.22 on the left.

At a reference frequency of 1 Hz, a dark NEP of $4 \times 10^{-18} \text{ W}/\sqrt{\text{Hz}}$ is calculated.

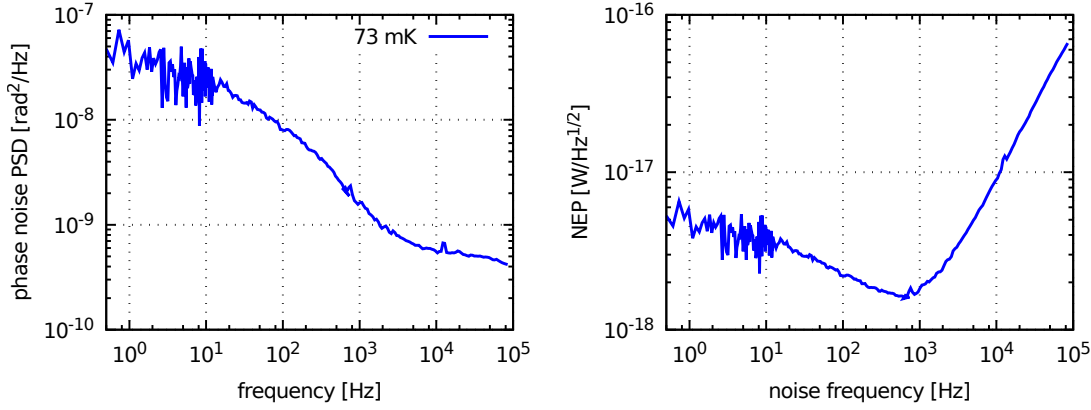


Figure 6.22: Left: Phase noise power spectrum for G5R3 calculated with (6.13) with $r = 0.3$ V using the noise spectrum from fig. 6.19. **Right:** Calculated dark NEP using (6.17) for phase readout. The parameters are summarized in table 6.3.

6.7 Determination of optical NEP

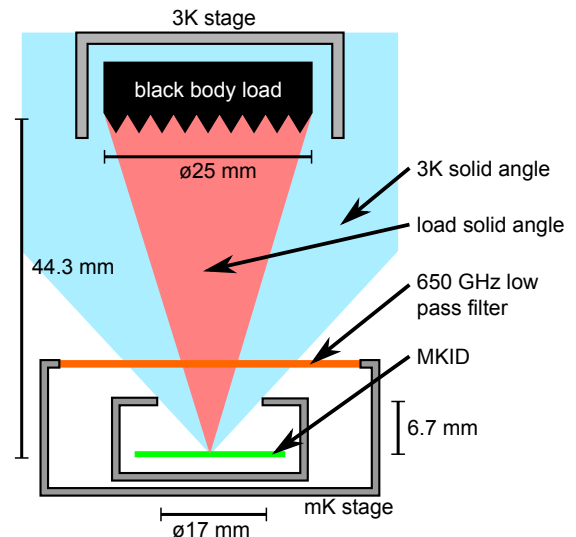
In contrast to the dark NEP, the optical NEP is always calculated with thermal radiation loading the detector. Also, the responsivity is directly measured by changing the intensity of the incident radiation on the detector. In my case this is done by changing the temperature of a blackbody radiator in front of the detector. The optical NEP is therefore expected to give a much more realistic measure for the detectors sensitivity in a real application.

6.7.1 Calculation of optical power

For the optical NEP which is measured using the internal heatable black body load it is necessary to calculate how much power in the pair-breaking frequency range reaches the chip at which load temperature. Since no exact measurement of the beam pattern and response bandwidth is available for my chip, a few assumptions and estimations have to be made:

- The substrate thickness of $250 \mu\text{m}$ suggests a response close to the 260 GHz band for NIKA 2, which uses $260 \mu\text{m}$ thick substrates. Because no 260 GHz bandpass filter is available, the band is only defined by the absorption spectrum of the chip itself and a 650 GHz low pass filter. Published FTS measurements of NIKA chips designed to absorb at 150 GHz from [86] show a fractional bandwidth of about 20%. Scaled up to a frequency of 260 GHz, this would be a bandwidth of 50 GHz. The absorption band is thus set as 235 to 285 GHz, which are the integration limits for the Planck function. The 650 GHz low pass filter has a high transmission in the determined frequency band and is neglected here.

Figure 6.23: Scheme used for calculation of the optical power at the device. The red area illustrates the solid angle seen from the MKID which is filled by the load. The blue area is the solid angle filled by the 3 K background and the remaining solid angle is filled by 100 mK.



- The sensitive area of one pixel is set to 4 mm^2 , which is the area of the inductive section of one resonator.
- The receiving solid angle is only defined by the size of the aperture of the copper package, its distance, the size of the load and the load distance. The solid angle of reception of the detector is therefore considered to be a half sphere.
- The load and the surrounding surfaces behave like perfect black body radiators. In fact the surfaces around the load are metallic and thus reflective, but as the inside of the 3 K shield of the ADR is coated with absorbing paint, it is considered that the chip effectively sees 3 K, even if through a few reflections. This argument only partly holds for the reflective inside of the 100 mK housing, but it can be justified by the argument that the device sees itself in reflection and has a temperature of 100 mK, too.
- The offset of the pixels from the center resulting in theoretically elliptic beam shapes and deviating solid angles is also neglected here. This is not entirely justified since the offset of the analyzed pixel from the center is about 4.5 mm.

Because no non-thermal radiation sources are active during the measurements using the load, the Planck formula is assumed to hold. In frequency representation it is

$$I_\nu(T) = \frac{2h\nu^3}{c^2} \frac{1}{e^{\frac{h\nu}{k_b T}} - 1} d\nu d\Omega dA \quad (6.20)$$

It describes how much radiation is emitted from a black body radiator at a temperature T from an area dA into a solid angle $d\Omega$ in a frequency interval $d\nu$. No approximation of

the Planck formula is used here because the temperatures around 3 K do not fully justify a limiting case. The determined frequency range mentioned above is integrated numerically. Integrations over the area and solid angle are replaced by multiplications since no angular dependence is assumed here. The expression derived from (6.20) and used below is then

$$P(T) = \int_{235 \text{ GHz}}^{285 \text{ GHz}} I_\nu(T) d\nu \cdot \Delta\Omega \cdot \Delta A \quad (6.21)$$

where ΔA is the area of one detector pixel and $\Delta\Omega$ is calculated in the following from the optical geometry.

The scheme used for calculation of the solid angles is illustrated in fig. 6.23. From the diameters and distances of the apertures three actual contributions to the incoming radiation can be determined. The opening angle of the load as it appears as seen from the detector ω_L is calculated from its radius r and distance d as

$$\omega_L = 2 \arctan\left(\frac{r}{d}\right) \quad (6.22)$$

Since the load and all apertures are circular, from that the approximate solid angle included by the opening angle can be calculated:

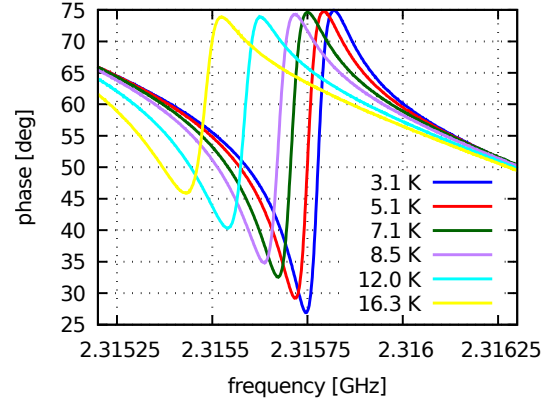
$$\Omega_L = 4\pi \sin^2\left(\frac{\omega_L}{4}\right) \quad (6.23)$$

For the the load eq. (6.23) give a solid angle of 0.23 sr from an opening angle of 31.5°. This is depicted in red in fig. 6.23. The second contribution Ω_{3K} is defined by the aperture of the mK stage and fills a solid angle of 2.15 sr which is calculated from the opening angle of 103°. The solid angle of the load is subtracted here already. The remaining solid angle Ω_{mK} necessary to fill the half sphere solid angle of 2π is 3.9 sr and is considered to see 100 mK, which is the temperature of the device. To keep a constant device temperature, the temperature is stabilized at 100 mK to give the regulation electronics room to operate. The total optical power which is received by one pixel of then NIKA 2 detector is then calculated using (6.21)

$$P_{\text{opt}} = P(T_L) \cdot \Omega_L + P(3 \text{ K}) \cdot \Omega_{3K} + P(100 \text{ mK}) \cdot \Omega_{mK} \quad (6.24)$$

A relatively small part of the actual radiation contribution is coming from the load, especially at low temperatures. Only the temperature of the load, T_L , is varied during the measurements and can be calculated into a change of optical power incident on the chip.

Figure 6.24: Phase of resonator G5R3 measured at different load temperatures. The temperature of the chip is stabilized at 100 mK.



6.7.2 Measurement of the optical phase response

With the optical setup mentioned in 3.5.2, the phase against the frequency is measured in a narrow frequency span around the resonance. The respective measurements are done with the setup also used with the optimized magnetic field, but without external magnets. The device temperature is stabilized at 100 mK as described in sec. 3.1.5. The ADR magnet current during the measurement is always lower than 200 mA. The temperature of the calibration load is varied between its minimum temperature of 3 K and 16 K for these measurements using just a power supply on a resistive heater. The resulting phase measurements for selected temperatures are shown in fig. 6.24.

6.7.3 Calculation of optical NEP

The direct measurement of the phase done in sec. 6.7.2 using the VNA replaces the calculation of the phase response from the resonance frequency as it was done for the dark NEP measurement in sec. 6.6.1. The resonance frequency at the lowest temperature (2.315 769 86 GHz) is selected as our readout frequency and the phase is interpolated at this frequency for all measurements.

The phase plotted against the received power of the MKID is plotted in fig. 6.25 which is calculated using eq. 6.24. The phase responsivity is fitted in the linear region up to 4 pW. Beyond that, the readout tone is already out of the resonance. The responsivity is determined as $\frac{d\phi}{dP} = 6.3 \times 10^{11}$ rad/W.

The phase noise is measured at 3 K load temperature and processed as mentioned in sec. 6.5.4. From the power spectrum also a quasiparticle lifetime of 135 μ s is determined. The optical NEP is then calculated as

$$\text{NEP}_{\text{opt}}(\nu) = \sqrt{S_{\phi}} \left(\frac{d\phi}{dP} \right)^{-1} \sqrt{1 + (2\pi\nu\tau)^2} \quad (6.25)$$

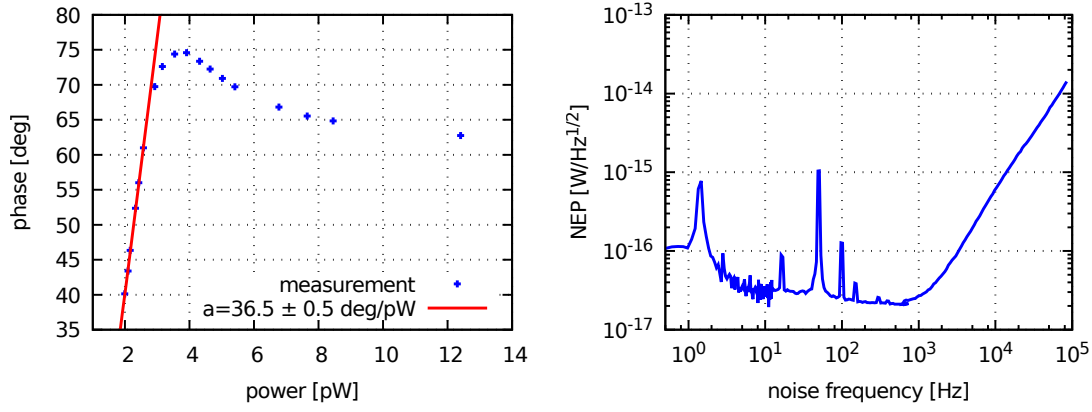


Figure 6.25: Left: Phase shift plotted against incident power in the band of 235 GHz-285 GHz. The linear fit gives the phase responsivity. **Right:** The optical NEP for the NIKA 2 chip as calculated with (6.25) for resonator G4R3 at 100 mK device temperature.

where S_ϕ is the phase noise power spectral density and τ the quasiparticle lifetime. The roll-off of the NEP is added here since the responsivity is not measured in dependence of the modulation frequency. The resulting NEP is shown in fig 6.25 on the right. At a modulation frequency of 1 Hz, a optical NEP of $1 \times 10^{-16} \text{ W}/\sqrt{\text{Hz}}$ is measured.

7 Summary and outlook

In this chapter, the results of this thesis will be summarized and evaluated.

First, the measurements of a NIKA 2 test chip supplied by IRAM will be discussed, because all measurements which are necessary to characterize a MKID are exercised with these devices. During these measurements, the full functionality of the measurement setup I developed and built within this thesis is tested. Open issues are identified and suggestions for further improvements are made in sec. 7.2.

Afterwards, the design and the measurement of the waveguide coupled detectors I designed within this thesis are discussed in sec. 7.3.

Finally, the results of this thesis are evaluated with respect to the main goals, which were the implementation and test of a measurement setup and the design of an aluminum based MKID. An outlook is given to the long term goal of contributing to the development of a camera for CCAT-prime.

7.1 Evaluation of the measurements of NIKA 2 test devices

The first big work package of my thesis is to build up a versatile and sensitive measurement setup for MKID devices. I was very fortunate that I could validate our measurement setup with measurements of test devices of the NIKA 2 MKID camera [2, 90]. This instrument is currently deployed on the IRAM 30m telescope in Spain and in scientific operation. Measurements of the noise equivalent power (NEP) for comparable devices to those I measured are available in literature. An additional task within this small collaboration is the measurement of the quasiparticle lifetime which is currently not possible in the test setup of IRAM and therefore unknown.

The NIKA 2 test devices I measured in chapter 6 are small MKID arrays with 25 lumped element resonators (pixels). To assess the capabilities of the measurement setup, a full analysis of the NIKA 2 devices is attempted. A final assessment of the measurement setup is done by demonstrating the measurement of a known MKID and achieving the expected performance.

7.1.1 Evidence for aging of the devices

A complication that was arising during the measurement of the NIKA 2 devices was, that the properties of the resonators seemed to change between individual measurement days, presumably after opening up the cryostat. This made the analysis and the optimization of the measurement setup more complicated, as it added an additional level of complexity. As described in sec. 6.2.3, VNA transmission measurements of one test chip were measured over a time span of about three months. During this time, the cryostat was opened and closed again about five times for changing the setup and for debugging purposes. From the transmission measurement, the quality factor of the resonators were determined by fitting the model described in sec. 2.2.3.

It is observed, that the quality factor decreases for one resonator from an initial value around 70000 to around 30000, and for another resonator from above 120000 to below 40000 in this time. The decrease is not uniform in time, but actually happens abruptly between two measurements. In this stage of my work, the measurement setup was still improved and step by step. Before each measurement, the cryostat was opened and changes to the measurement setup were made. These modifications targeted on improvements of the shielding, as the outer aluminum shield was added in that time. No changes were made to the readout setup with which the transmission measurements were made. The temperature of the device was always controlled using the same RuOx sensor mounted on the sample stage, therefore it was ensured that the same low device temperature was achieved. After a new sample which was stored in a desiccator is mounted, immediately higher quality factors are measured in the identical setup. Since both chips are from the same wafer, a similar initial internal quality factor is expected. In addition, it can not be well explained, why an additional shield around the device should be able to reduce the quality factors. My conclusion would therefore be, that the properties of the first chip, or rather the aluminum film changed, and not the properties of the measurement setup that have influence on the transmission measurement.

I took measures to prevent exposure of the device to ambient air and moisture. When the cryostat was warmed up after a measurement, it was always filled with dry nitrogen. This should prevent exposure of the sample and the interior of the ADR, which might still be below room temperature, from contact with ambient air. The humidity from ambient air would condense on colder parts and cause a deterioration of the device. If, and to how much moisture the device is exposed to however depends also on the Cologne air humidity on the specific day the cryostat was opened. The duration of the exposure to laboratory air was unfortunately insufficiently recorded. Therefore the exact cause for the deterioration can not be reconstructed anymore, but the results above should suggest, that

the aluminum MKID detectors have to be handled with care regarding exposure to air and humidity.

7.1.2 Influence of external magnetic field on the quality factors

As it turned out, another factor in the analysis of the measurements was the unexpectedly large influence of ambient magnetic fields. To investigate the necessity of magnetic shielding of the MKID setup, qualitative VNA transmission measurements with permanent magnets taped to the outside of the cryostat are made. These measurements are described in sec. 6.2.4. One permanent magnet is mounted on each side of the cryostat with their north poles in line. The north poles subsequently are oriented in different directions and the VNA transmission is measured. From these measurements, the internal quality factors are again determined by a fit. The measurements are once done with an aluminum magnetic shield around the sample only and once with an extra niobium thin film sputtered on the inside of the aluminum housing. The magnetic field is always applied in horizontal direction, parallel to the chip surface. Before the magnetic field configuration is changed, the whole stage containing the shield and the sample is warmed up above the critical temperature of the device, which is 1.38 K.

The fitted quality factors for the aluminum shield show a significant dependence on the direction of the external magnets. The best quality factor of about 180000 is measured with the magnets aligned in western direction. The worst quality factor is measured in eastern direction.

With the additional niobium layer, basically no influence on the direction of the external magnets can be observed. The measured quality factor is reduced to about 60000, which is close to the value measured with the aluminum shield without niobium and without external magnets. The measurements with the extra niobium shield are done about 10 months later than the measurements with aluminum shield only.

As investigated by Flanigan et al. [38], external magnetic fields can reduce the quality factors of aluminum MKID resonators, even if an aluminum magnetic shield is in place. They conclude, that because thin aluminum films have a higher transition temperature than bulk aluminum, during the cooling first the sample becomes superconducting and freezes in the magnetic field, before the aluminum shield becomes superconducting. They can improve the quality factor by applying an external field which cancels the earths magnetic field. My measurements with the aluminum shield qualitatively show the same behavior. However, it is expected that the earth magnetic field in Cologne, Germany has a strength of approximately 20 μT with a main component pointing upwards, but generally in northern direction. My experiment however shows, that best quality factors are measured

when an external field in western direction is applied. A check with a compass shows, that with all equipment surrounding the cryostat, an effective magnetic field in roughly north-western direction exists. The field in western direction would therefore not at all cancel that component. The compass could however also respond to magnetic metals in the surrounding which falsifies the result. The extra niobium indeed screens the sample from changes in the external field, but the quality factor is back to lower values comparable to those measured without additional external field.

Since the niobium film had to be sputtered on a large surface and on vertical walls, the film thickness can be too low to effectively expel the magnetic field. Maybe the niobium traps the ambient field when it becomes superconducting at around 8 K. At that stage, the ADR magnet is completely turned off and does not play a role. The sample then remains exposed to the ambient field during the whole measurement, as it is never warmed up above 8 K. This would also explain that the same quality factors are measured as with the aluminum shield only without any external magnets.

It remains unexplained why the very best quality factor was measured for the resonator with an applied field in western direction. The absolute direction of the external field relative to the chip is always in the plane of the substrate, but the direction relative to the structure was not determined. With niobium shielding, the field would then be zero and the 'enhancement effect' does not take place.

The third explanation respects the time between the measurements. The quality factor measured with niobium shield is optimal in sense of magnetic field and the best quality factors should be measured, but the chip has deteriorated. The only way to prove this hypothesis is to remove the niobium shielding again and repeat the experiment with external magnets to see if better quality factors can be still achieved. This was however not regarded as practical possibility and was therefore not done yet.

The measurement results with external magnetic field have to be interpreted with extreme caution, as the nature of these experiments is purely qualitative. The magnets are of the shelf office magnets and even different in size and strength. The alignment between the magnets is only done by eye and it can not be excluded that the sample actually does not see the small area of quasi-homogeneous field but the fringing field which has up and downward components and might even point in the opposite direction. For these reasons, the hypotheses made up above should be treated as questions to trigger careful follow-up experiments with well controlled field generated for example by large Helmholtz-coils. Ideally a measurement of the field inside the shield would give more insight into the effectivity of the shielding, but would require a cryogenic field probe.

7.1.3 Determination of complex gap parameter

The sensitivity of the MKID is measured as its noise equivalent power (NEP), which is discussed in sec. 2.3.2. The dark NEP describes the situation, where no radiation except the thermal background of the device itself reaches the MKID. For the calculation of the dark NEP, assumptions about the superconducting gap parameter Δ_1 have to be made (sec. 6.6). For BCS superconductors, this value can be approximately calculated but this is already inaccurate for the thin aluminum films. Taking the long term goal of studying more exotic superconductors like Titanium Nitride into account, it will become necessary to determine the gap parameter experimentally. Here, the gap parameter is fitted from the temperature dependence of the internal quality factor and of the resonance frequency.

With the network analyzer readout (sec. 3.4.1) the dependence of the resonance frequency and the internal quality factor on the sample temperature was measured. This was done with two setup configurations: One with external permanent magnets in western direction, resulting in high measured quality factors and one with an extra niobium magnetic shield around the samples (sec. 6.2.4). With optimized magnetic field, more than a factor of 3 higher quality factors are measured than with the niobium shield. The resonance frequencies show a slight increase with temperature, before they start decreasing as predicted from the Mattis-Bardeen theory. The quality factors saturate at a constant value below about 200 mK.

The measured temperature dependent resonance frequency and quality factor data was fitted to the extended Mattis-Bardeen theory as used in [74] (see sec. 2.2.5). Determining the complex gap parameter Δ using the extended Mattis-Bardeen theory from the measured frequency and quality factor data proved to be difficult, as the parameters describing the measurement are partly correlated (see sec. 2.2.7). To disentangle that correlation, some parameters are determined before the actual fit by other means. The kinetic inductance fraction α is determined from numerical simulations as $\alpha = 0.215$ which is in a sane region. Modeling the superconductor in the simulation, the surface inductance of the aluminum film is gained from the measured resonance frequency as 1.3 pH. The imaginary part of the complex gap parameter $\Delta = \Delta_1 + i\Delta_2$, is determined from the saturated quality factor below 200 mK.

The real part Δ_1 of the complex gap parameter is then separately fitted from both, the temperature dependence of the resonance frequency and of the internal quality factor. Unfortunately, both values for Δ_1 are not consistent. The quality factor data suggests a 11 % higher Δ_1 . To determine which result is more reliable, the transition temperature of the aluminum is taken into account.

From the RF transmission of the readout line a transition temperature of 1.38 K is

setup	$\frac{\Delta_1}{k_B T}, \delta f / f_0$	$\frac{\Delta_1}{k_B T}, Q_i$
optimized magnetic field	1.78 ± 0.03	2.01 ± 0.03
niobium magnetic shield	1.61 ± 0.02	1.92 ± 0.03

Table 7.1: The factor $k_b T_c / \Delta_1$ calculated from the results presented in table 6.1. $T_c = (1.38 \pm 0.02)$ K is used.

determined for the aluminum film. This increased T_c is expected for a thin aluminum film [79]. The measured factor $\Delta_1 / (k_b T_c)$ for my samples is shown in table 7.1 for the different configurations. A measured value for $\Delta_1 / (k_b T_c)$ for thicker films is given by [15] as 1.62, which is very close to the results obtained for the gap parameter from the fractional frequency shift data. Therefore, I would rather trust the value given by this method.

The measurements presented in [74] also fit the complex gap parameter using the same model as I do, besides they only fit the quality factor data. Their model fits the temperature dependence of the quality factor excellently, but it can be seen by inspecting Fig.1 in [74], that the fractional frequency shift data does not follow and would also suggest a lower Δ_1 . This is consistent with my analysis.

The parameter Δ_2 is directly determined from the saturated quality factors. The extended Mattis-Bardeen theory described in sec. 2.2.5 describes the temperature dependence well up to about $0.4T_c$, where however also the resonance is barely visible and the error in the fitted parameters becomes larger. The physical background of this parameter is a broadening of the quasiparticle density of states. At the gap, the density predicted by the BCS theory of states diverges. If disorder is introduced into a film as it is the case for thin aluminum, the peak becomes rounded. Dynes et al. [32] measured this effect with a tunnel junction, which can immediately probe the density of states. They modeled the broadening by introducing a complex energy $E - i\Gamma$ in the quasiparticle density of states. As argued by Mitrović et al. [70], the correct formulation is not a modified energy, but a modified gap parameter, which is the formulation also used in the model used here taken from [75].

7.1.4 Comparison and discussion of quasiparticle lifetime measurements

The quasiparticle lifetime as the limiting time constant of the detector is an important parameter for the calculation of the dark and the optical noise equivalent power (NEP). In my setup, the fast IQ mixer readout mode is used to determine the quasiparticle lifetime with three different methods. This parameter is also important for IRAM, who were

interested in a measurement of the quasiparticle lifetime, because their setup is currently not equipped for these measurements. The measurements are described in sec. 6.4. All measurements of quasiparticle lifetime are done using an aluminum magnetic shield around the sample with external magnets directed in western direction, because this configuration yielded the highest quality factors.

It is assumed throughout this thesis that the quasi particle life time is the dominating time constant of the MKID. To show that this is justified, the second participating time constant, the resonator ring time, has to be compared to the measured values. This time constant arises due to the fact that the resonator stores energy and needs a certain number of cycles to adapt to changes. This resonator ring time is calculated as [106]

$$\tau_{res} = \frac{Q}{\pi f_0} \quad (7.1)$$

where f_0 is the resonance frequency of the resonator and Q is the resonators total quality factor. For G3R5, which is one of the resonators with the highest $Q = 36000$, the resulting ring time would be $\tau_{res} = 5 \mu\text{s}$, a factor of 8 shorter than the measured time constants even around 300 mK. Therefore it is justified to assume that the measured time constant is actually dominated by the quasiparticle lifetime.

The first method used to measure the quasiparticle lifetime is to excite the device using a $50 \mu\text{s}$ long optical pulse from an light-emitting diode (LED). The setup is described in sec. 3.4.4. The response of the detectors is recorded using the IQ mixer homodyne readout setup. The pulses are then fitted on a semi-logarithmic scale to extract the decay time τ , which is dominated by the quasiparticle lifetime.

The second method waits for cosmic rays to excite the detector. This method is described in sec. 3.4.5. Since the cosmic rays are random events, the pulses have to be extracted from longer time domain measurements with the IQ mixer. The recorded pulse response is fitted the same way as with the LED excitation.

The third method uses the roll-off of the noise power spectra of the detector to fit the quasiparticle lifetime. Time domain data is recorded using the IQ mixer setup. From that data, the amplitude and phase noise spectra are calculated and a model is fitted. The measurement is described in sec. 6.5.6.

With the LED pulse method, two experiments were done to check the dependence of the measured lifetimes on the pulse intensity which is adjusted by the LED current and on the readout signal power (see sec. 6.4.3). With different pulse powers, quasiparticle lifetimes between 131 and $118 \mu\text{s}$ are measured at the lowest and highest pulse currents respectively. The quasiparticle lifetime seems to decrease linearly with pulse current. No dependence of the quasiparticle lifetime on the readout signal power was observed when

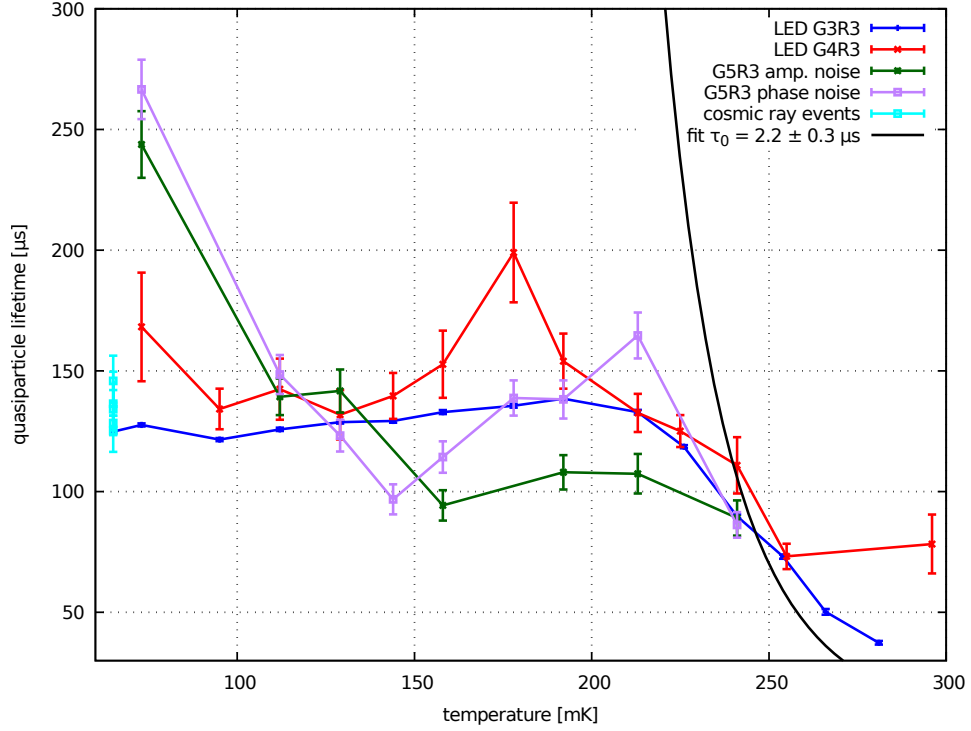


Figure 7.1: Comparison of measured quasiparticle lifetimes from LED pulses, the noise spectra and from cosmic rays.

attenuating the readout signal in steps up to 9 dB.

The quasiparticle lifetime measurement results using the LED pulse method, the cosmic rays and the noise spectra are supposed to yield consistent results. They are compared in fig. 7.1. The results of the LED pulses and the cosmic rays are kind of consistent at the low temperature where they can be compared. The noise spectra predict longer quasiparticle lifetime at low temperatures.

The theoretical temperature dependence of the quasiparticle lifetime is given by [54]

$$\frac{1}{\tau} = \frac{1}{\tau_0} \sqrt{\pi} \left(\frac{k_B T_c}{2\Delta_1} \right)^{5/2} \sqrt{\frac{T}{T_c}} e^{-\frac{\Delta_1}{k_B T}} \quad (7.2)$$

where τ_0 is a material specific time constant, T_c is the critical temperature and Δ_1 the superconducting gap parameter. Here, for the gap a value of 0.226 meV is used as an average of the values determined in sec. 6.3 and a $T_c = 1.38$ K. The black curve in fig. 7.1 is the attempt to fit τ_0 to the LED pulse data of G3R3.

My value of $\tau_0 = (2.2 \pm 0.3) \mu\text{s}$ is large compared to the results of Barends et al. who get a time constant $\tau_0 = 690$ ns for 250 nm aluminum on silicon [6]. They measure however a longer quasiparticle lifetime than I do, which seems contradictory to their shorter τ_0

looking at equation (7.2). The large uncertainty in my measurements and the spread in the values obtained by the methods makes a useful estimate of the quasiparticle lifetime more difficult.

The observed linear dependence of the quasiparticle lifetime on the pulse power could explain the somewhat shorter lifetimes measured using the resonator G3R3 which is in the center of the device and receives most optical radiation. The cosmic rays which deposit a lot of energy at once also show a reduced lifetime. The noise measurements which do not need any external excitation show the longest lifetime at low temperatures. Extrapolating the measurement of quasiparticle lifetime vs. LED current, a fictional zero current lifetime of $(129 \pm 3) \mu\text{s}$ is determined, which is still considerably below the measured value for the noise spectra and does therefore not offer a conclusive explanation for the long lifetimes measured with the noise method.

As shown in sec. 6.5.6, excess noise at low frequencies makes the analysis of the noise spectra difficult and a special model correcting for that had to be applied. At low temperatures, the roll-off due to the quasiparticle lifetime in the spectrum is close to the noise floor, therefore the quasiparticle lifetime fit is possibly affected and becomes inaccurate. If the origin of the noise would be from TLS (see sec. 2.3.5) only, it should not be visible in the amplitude spectrum. Therefore the low frequency excess noise is expected to be partly caused by the measurement setup. Possible measures against this will be discussed again in sec. 7.2.

The measured quasiparticle lifetimes are rather short in comparison to known values for aluminum. The results from Barends et al. using 100 nm aluminum films on silicon show a lifetime of 600 μs . Interestingly, their measured quasiparticle lifetimes also increase slightly with temperature with a peak around $0.15T_c$ as can also be seen for my measurements. The origin of that peak is not discussed. Higher values for the quasiparticle lifetime can be obtained on sapphire substrates. A result from the same publication shows up to 1000 μs lifetime. Values from de Visser et al. [25] range up to 4 ms from noise spectra with 40 nm aluminum on sapphire. Since there are no other published measurements of the quasiparticle lifetime of NIKA 2 devices, it can only be said that my results are low in comparison, but not unfeasible.

In my opinion, the pulse method either from LED pulses or from cosmic rays yield more accurate results for the quasiparticle lifetime, at least in my setup. The method gives a straightforward way to acquire the detector response time, while the noise methods involves many steps of calculations to obtain the noise spectra and then a final fit for the quasi-particle lifetime. Therefore I am confident, that the measured value of $(140 \pm 10) \mu\text{s}$ at a lowest temperature of 63 mK is realistic.

7.1.5 Discussion of the measured dark and optical NEP

With the quasiparticle lifetime, the gap parameter and the noise power spectra, now the dark NEP can be calculated. The dark NEP gives a lower boundary to the detectors sensitivity as it is measured with minimum optical radiation on the detector. The obtained NEP using phase readout is shown in fig. 6.22. At 1 kHz, a dark NEP around $2 \times 10^{-18} \text{ W}/\sqrt{\text{Hz}}$ is measured. Best values for the dark NEP in amplitude readout mode are given by de Visser et al. [25] of $1.5 \times 10^{-19} \text{ W}/\sqrt{\text{Hz}}$. Their quasiparticle lifetime is measured as 4 ms, which is more than a factor of 10 longer than the lifetime I measured. As shown in eq. 6.17, the NEP is inversely proportional to the quasiparticle lifetime. If such a long lifetime is assumed, measurements down to the same NEP would be possible in my setup as well. So I conclude, that the measured NEP is not limited by the setup, but by the detector itself.

For calculation of the optical NEP, the phase of the transmission through the chip is measured at different temperatures of a calibration load using the VNA. The measurement is described in sec. 6.7.2. The temperature of the device is stabilized at 100 mK during that measurement. The optical NEP obtained in my measurement setup under optical loading of 2 pW was $1 \times 10^{-16} \text{ W}/\sqrt{\text{Hz}}$ at a frequency of 1 Hz. It compares well to the range of $6.3 \times 10^{-17} \text{ W}/\sqrt{\text{Hz}}$ to $2.3 \times 10^{-16} \text{ W}/\sqrt{\text{Hz}}$ given in [86] for NIKA devices. Measurements under lower optical loading were not possible in my setup. For that, a filter with a narrow bandpass around the detectors sensitive frequency range is necessary, which was not available for the frequency range of the NIKA 2 devices. Measurements under lower optical power by Yates et al. [105] also show a NEP of $2 \times 10^{-17} \text{ W}/\sqrt{\text{Hz}}$ with 1 pW optical loading using a transmission line resonator MKID which is coupled to a planar antenna. Together with the fact that the NIKA 2 chips perform well on the telescope, these measurement results are plausible.

As a final remark, the measurements of the NIKA 2 devices are generally successful in my measurement setup. With the acquired data, a realistic sensitivity was measured and I could report an approximate quasiparticle lifetime. With the hands-on experience gathered during the measurements, the main difficulties in the measurement procedures and the general handling of the setup could be sorted out. While the NIKA measurement presented here still bear traces of the learning process, future measurements are expected to be successful much faster and yield data of higher quality.

7.2 Concluding evaluation of the measurement setup

The measurement of the NIKA 2 devices were the main test for my measurement equipment and procedures. The issues identified during those measurements will be discussed in this section, after a summary of the completed work on the setup.

Within this thesis I planned and implemented the measurement setup described in detail in chapter 3. The following tasks were fulfilled:

1. I set up the ADR cryostat for the measurement of MKID. I defined the specifications in the process of purchasing the cryostat, assisted the installation and did the initial tests. I specified and installed the necessary DC and high frequency cables down to the mK stage and ensured the cryogenic performance with cables is still sufficient for measurements.
2. I implemented the hardware necessary to measure the response of the detector to LED pulses consisting of the LED coupled to an optical fiber which transports the radiation to the sample on the mK stage. I did a conceptual design of the LED driver electronics which was then fully designed and build by our electronics workshop.
3. I designed and implemented the readout electronics consisting of the VNA and IQ mixer readout modes. The room-temperature electronics were integrated in a 19" rack casing which can be switched between the modes. Filters for the outputs of the IQ mixer were designed by me and optimized and build by out electronics workshop.
4. I developed the complete necessary measurement software for data acquisition and remote control of the VNA and the synthesizer in Visual Basic. This software also controls the ADR cryostat and monitors all temperatures and voltages. I figured out a new method to efficiently control the ADR magnet current and implemented it.
5. I did the mechanical CAD design of the cold measurement setups for two different MKID devices and for DC measurements. These parts were fabricated in our in-house mechanical workshop. Also, the optics and the mechanical parts for the heatable calibration load are designed and implemented within this thesis.

7.2.1 Remaining issues of the measurement setup

The NIKA measurements in ch. 6 show, that the measurement setup has the functionality to perform test measurements of MKID detectors. During the measurements also some issues were identified which have to be addressed in order to fully exploit the capabilities of the setup.

- The noise power spectral density measurements done in sec. 6.5.3 show a high noise in the lower frequencies close to the carrier. This noise seems to be proportional to the readout power and leads to a high noise contribution off the resonance. This noise prevents a good calibration of the noise power spectra because the correction of the spectra by subtracting the off-resonance data from the on-resonance data does not work if the off-resonance noise is larger. Therefore the readout noise can not be easily removed from the measurement. The suspected origin of this noise are instabilities in the readout system, which can come from moving cables or components. Also the LNA power supply, which is currently realized with three laboratory supplies, could contribute to instabilities.
- The magnetic field shielding can become a serious issue in future measurements. A stable solution to actively or passively compensate the external fields will become necessary. Also it has to be investigated how proper magnetic shielding can be done when optical access to the detector is necessary.
- The deterioration of the devices presumably when they are exposed to air has to be taken into account when mounting devices in the cryostat. After the cryostat has warmed up after a measurement, the vacuum was broken with dry nitrogen gas to prevent humid air from reaching the sample. Removing the device and storing it in a desiccator takes about 30 minutes. When the device is mounted, the situation is more difficult because closing the cryostat takes longer than opening it, and the sample is exposed to air till the cryostat is evacuated. Depending on how vulnerable the devices which are designed in future are, new handling procedures have to be established.

7.2.2 Suggested improvement of the measurement setup

The following suggestions should solve the issues mentioned above. In addition, there are several points which could improve the performance or make the setup more user friendly.

- The readout noise temperature calculated in sec. 3.3.7 is 89 K at 2.5 GHz, which is actually unacceptable for measuring sensitive detectors. The first measure is to remove the 3 dB attenuator between the sample and the LNA, which actually doubles the noise temperature. This increases the amplitude of a possible standing wave between the amplifier and the sample, especially as the used LNA has a high input reflection below 4 GHz (see fig 3.9). Also, the noise temperature of the LNA exceeds 15 K around 2.5 GHz, therefore the LNA should be replaced with a model covering the frequency of the IQ mixer of 2 GHz to 8 GHz. The sample could be protected

from radiation from the amplifier by a circulator mounted on 50 mK instead of an attenuator as done presently. A redesign of the LNA power supply with respect to stability should be also taken into account. A future cold readout setup could also use a superconducting parametric amplifier (see Appendix A), which would further decrease the noise contribution of the system and lower the readout power requirement.

- The readout power used in the measurement was always below the onset of non-linearity in the samples. However, depending on the devices, lower readout powers could be desirable. For that, also more gain in the amplifier chain is necessary. A convenient feature would be a set of two variable attenuators, one in front of the device and one in front of the IQ mixer, to ensure constant signal power on the IQ mixer while having the possibility to vary the readout power at the device. That way a real calibration of the IQ mixer could be attempted.
- The low-pass filters in front of the ADCs described in sec. 3.3.5 currently have to be changed manually by connecting and disconnecting BNC cables. This is cumbersome for the operator and inhibits the full automation of the noise measurement. A feature to automatically switch the filters would make an automated measurement possible, which becomes a necessity if detectors with many pixel have to be measured.
- It was shown in the measurements in sec. 6.2.4, that a magnetic field influences the resonators significantly. The attempt using a niobium film as a magnetic shield did not lead to the same high quality factors as an optimized external magnetic field. This should be investigated further. Possibly, a well designed normal conducting magnetic shield made of a low temperature shielding material like Cryoperm or A4K could help effectively shielding the sample.

The next larger changes of the measurement setup should be to create a well filtered optical access from the outside of the cryostat to enable measurements with external signal sources or with an Fourier transform spectrometer to determine the frequency dependent response of the MKID under test.

7.3 Evaluation of the waveguide coupled MKID

The second task of my thesis was to develop and measure a waveguide coupled MKID based on aluminum as the sensitive material. This detector is an experimental device which focuses on the investigation of the optical sensitivity of MKID. At high multiplexing factors,

MKID cameras do not yet achieve the promised sensitivity at the telescope, except for the NIKA 2 instrument which however still has moderate pixel number densities. Therefore, the investigation of the absorption process motivates such a device. The second aim for this kind of device would have been the test of my measurement setup. The design of the waveguide coupled MKID is described in chapter 4 in full detail.

7.3.1 Design and simulation results

The governing design idea is to couple an MKID to a waveguide, which is fed by a horn antenna. To achieve this, an established waveguide antenna design already proven with SIS mixers is adapted for an MKID [3]. Because of that, the center frequency of my detector is also chosen to be 350 GHz. A waveguide probe extracts the signal onto a 9 μm thin membrane, where it is absorbed in an aluminum absorber line which is part of the superconducting readout resonator. For the absorbing parts of the detectors, aluminum is used and for other circuit elements niobium, which is still superconducting at 350 GHz. Two different resonators are designed. A lumped-element type resonator (WGKID) and a transmission line resonator (TMKID).

Both resonator types are designed for two different resonance frequencies, which are 4 and 2.5 GHz. Also, two different coupling quality factors around 1×10^4 and 1×10^5 are designed. The resonators are simulated using Sonnet EM [35].

The high frequency side is simulated using CST microwave studio [92], which enables a full 3D simulation. The input reflection of the waveguide port for the WGKID device is better than -10 dB over a band from 280 GHz to 440 GHz. The TMKID input reflection is better than -10 dB between 280 GHz to 420 GHz. The optical measurement is going to use a bandpass filter with a width of 30 GHz around 350 GHz, which is easily covered by the simulated detector band.

7.3.2 Measurement

The fabrication and the measurement of the waveguide coupled devices are described in chapter 5. Four batches of the waveguide coupled devices were fabricated, of which the last two yielded complete devices. The devices were optically inspected and failures were found in about 30% of them. The working devices were build in a detector block and measured in the ADR cryostat. Besides the devices, also van-der-Pauw test structures and long and narrow test strips with similar geometry as the absorber lines of the MKID were fabricated. These test structures were measured at DC to determine the transition temperature and the resistance of the aluminum films.

The van-der-Pauw structures are measured in a real four-point configuration, while the test strip measurements include one contact between gold and aluminum. The transition temperature of the van-der-Pauw structures is 1.3 K and for the test strips 1.5 K. The test strips also show a residual resistance of about $50\ \Omega$ below T_c , in contrast to the not measurable residual resistance for van-der-Pauw structures.

The measurements of the waveguide coupled devices are done using an VNA in transmission measurement mode. The chip shows transmission of the readout line for both resonator designs. For the WGKID devices, no resonance feature could be measured between 1 and 12 GHz. For the TMKID devices, resonance features close to double the expected resonance frequency are visible in the VNA measurement. The resonances do not respond to increasing temperature and are still visible above the critical temperature of the aluminum. Quality factors close to 2000 could be measured for these resonances.

Because no resonance which could be attributed to the actual MKID resonator could be found, no optical measurements could be performed with the waveguide coupled devices.

7.3.3 Analysis of the failure

The measurements suggest, that the problem with the devices is related to the aluminum absorber lines. Two hypotheses are evaluated, which state that either the aluminum itself is contaminated, or that the contact between the aluminum line and the niobium parts of the resonator is faulty. As discussed in sec. 5.4, the measurement results suggest, that the contacts are the more probable candidate for the observed failure. The main argument is, that the transmission line resonator which is by design shorted at the end of the absorber line, shows a clean resonance feature at twice the designed frequency. This would be plausible, if the resonator is actually open on both ends and therefore is a half-wave resonator, whose fundamental mode has twice the resonance frequency. This can only be the case, if the contact resistance between the niobium and the aluminum is very high.

The aluminum quality of the long and narrow absorption lines can also be insufficient, which however can only be measured after the contact problems are solved. This will require a refined fabrication process for these devices.

7.3.4 Discussion of the waveguide coupled devices

Taking the difficult fabrication process into account the critical question has to be asked, whether the fabrication and measurement of this device is still a worthwhile thing to do. Since the design of this detector started, MKID research all over the world has advanced

the knowledge of these detectors significantly. It can be argued, that this device actually comes to late to investigate the fundamental questions of the optical sensitivity. Also, the devices as they are will not be useful for real detector applications, because the strength of the MKID is in the possibility of making many pixels. In that sense a single pixel MKID can only serve as an academic example. On the other hand, there are still problems with MKID, as there is currently only the NIKA 2 array deployed on the telescope. Other instruments like A-MKID [37] cross unforeseen difficulties, where maybe a step back to a device like my MKID can be a part of the diagnostic process. Also different materials like TiN [50, 60, 72] which is already discarded by most of the the community or really new materials like MgB₂ [104] or YBCO [87] might be investigated in an experimental framework like my detector. These latter two devices will however be sensitive to much higher frequency in the terahertz range, where a waveguide coupled device is probably not possible to realize.

7.4 Outlook: Towards a sub-mm MKID camera

The first goal formulated for this thesis was the implementation and test of a measurement setup for sensitive MKID. This goal could be fulfilled with the measurement of the NIKA 2 devices. The second goal of the development of an own MKID based on aluminum as a sensitive material could only be partly fulfilled. The detector is designed and the first batches ate fabricated, but the detectors do not work yet. This is going to be a matter of time because additional fabrication is required.

The long term goal of this thesis work has also become to set steps on the path towards the construction of a MKID camera for the CCAT-prime telescope, as the CCAT-prime project became reality only in the last year of my thesis. The design work within this thesis only partly contributes to this goal, as the waveguide coupled MKID is too complex to be easily multiplied. Generally, MKID arrays can be build with horn antennas [68]. The design idea could be transferred. In my opinion, a much simpler design should be attempted for many pixel cameras.

Most of the room temperature readout setup also has to be adapted, as a digital readout is necessary to measure the response of an MKID array [18, 69]. The cold readout setup can probably be used as it is with the modifications suggested in sec. 7.2.2. The existing readout setup will stay useful for measurements of the noise power spectral density or the quasiparticle lifetime for individual pixels. It can be an important advantage to have these measurement capabilities as well.

The measurement software I wrote within this thesis can serve as a basis for future array

readout software. The ADR control software is sufficient for future laboratory measurements. The analysis pipeline with the fitting scripts are useful as long as the model is not changed significantly.

Overall, this thesis should be a solid starting point for future MKID camera development in our work group. Still, the development towards an ambitious MKID array will be a challenging task, keeping in mind that a fundamental understanding of the MKID itself remains a crucial part of the process.

8 Appendix A: Non-linear effects in NbTiN resonators

Because all MKID are based on superconducting resonators, a readout signal is required which transports the information of the resonators amplitude and phase change to the outside world. The amplitude of the readout signal is limited at the low end by the signal to noise ratio of the readout circuit. With parametric amplifiers for example, this can be as low as a single photon in the resonator. At the high end, the readout power is limited by the onset of non-linear effects in the resonator. These high power effects lead to distorted resonance features when the signal used read out the transmission of the resonator itself can shift the resonance frequency by changing the kinetic inductance.

The main idea which leads to the measurements in this chapter is to separate the effect of overdriving the resonator from the readout. During the measurements I use a strong signal to distort the resonator and a second, much weaker signal to "look at" the resonators transmission. The strong signal drives the resonator out of its equilibrium state and the weak signal measures the transmission of the resonator.

Non-linear effects in superconductors is a whole topic by itself and the full analysis and theoretical explanation of the measurements here will be out of the scope of this thesis. The measurement method and the results will be presented here in an early state, the power measurements are not properly calibrated and some obvious experiments still have to be carried out. Many of the experiments below are a consequence of sheer luck and playing around with the measurement setup.

8.1 Description of the NbTiN test chip

The test chip measured here was designed, fabricated and measured already in my master thesis [16], therefore the details will not be recalled here. The chip is fabricated on 550 μm thick high resistivity silicon and contains eight NbTiN LEKID [31] resonators, which are not optimized for optical coupling (fig. 8.2). The full chip is shown in fig. 8.1. The resonance frequencies are between 5.1 and 5.55 GHz and the coupling quality factor is designed

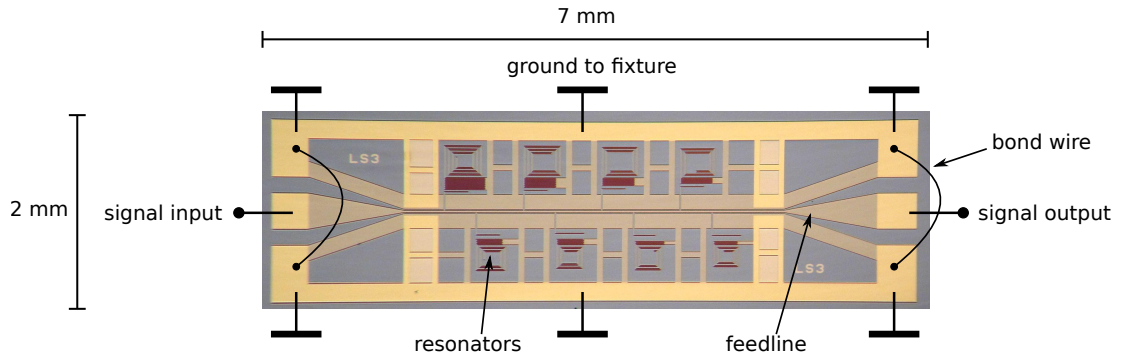


Figure 8.1: Stitched microscope image of the NbTiN test chip.

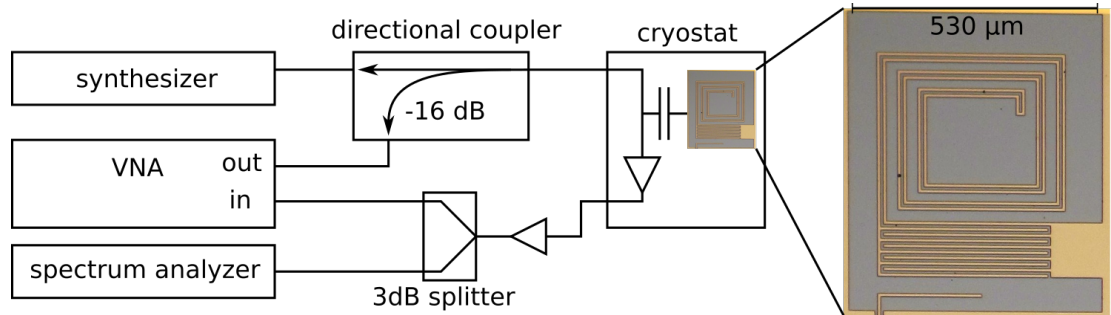


Figure 8.2: Illustration of the measurement readout used. The resonator is made of NbTiN and coupled to the feedline from the bottom.

to increase from 5000 for the first resonator to 1 million for number eight. The NbTiN thickness is 300 nm and $T_c = 14.2$ K is measured. The contact areas of the chip are additionally covered with gold for better adhesion of the bond wires. Due to crosstalk between the resonators, the maximum measured quality factor is 40000 for resonator number 6, which will be mostly used for the measurements in the following.

8.2 The two-tone readout setup

The leading idea of this setup is to use two readout tones. A rough schematic of the setup is shown in fig. 8.2 to illustrate the idea. A strong pump tone is generated by a synthesizer and the weak probe tone by the VNA. Both are combined using a directional coupler, where the VNA signal is connected to the -16 dB port. The combined signal goes to the cryostat. The cold readout setup as shown in fig. 3.8 is modified such that all attenuators in the cables going to the sample are removed or replaced by smaller attenuators, such that the total attenuation before the device is 15 dB. Directly behind the device, a 20 dB attenuator is placed to protect the low noise amplifier input from the strong signal. At

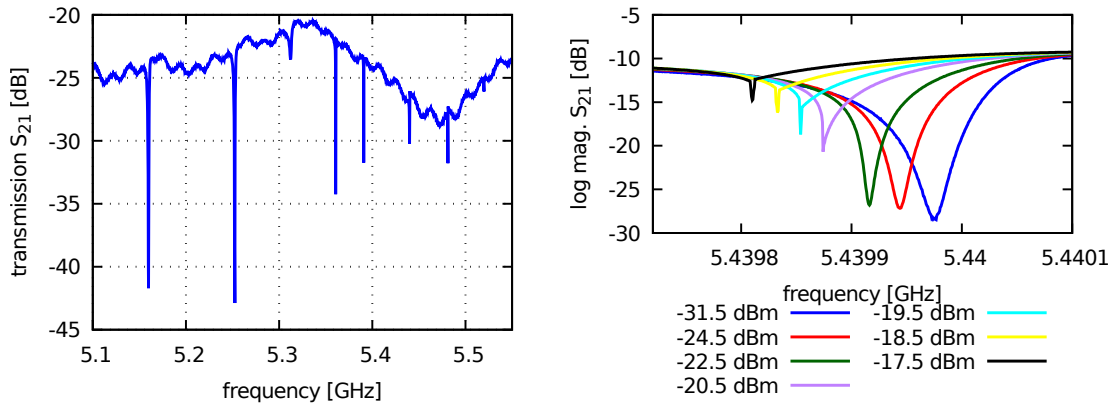


Figure 8.3: **Left:** Transmission of all eight resonators. **Right:** Shape of the resonance features at increasing VNA readout power, sweeping from left to right.

the output of the cryostat, the signal is split using a 3 dB splitter. One output goes back to the VNA and one output goes to a spectrum analyzer.

8.3 Measurement

The NbTiN test devices are mounted and cooled in the ADR cryostat described in chapter 3. The devices are stabilized on 100 mK for most of the measurements.

8.3.1 Measurement with strong VNA signal only

For this measurement, the VNA is directly connected to the cryostat. It should reproduce the measurements done with one single strong readout tone as shown in [27]. The range of the VNA is set to cover resonator 6 and the readout power of the VNA is successively increased. The result is shown in fig. 8.3. At a certain power, the resonance shows edge-like features. At lower powers, the resonance already looks asymmetric and the resonance frequency starts shifting downwards.

8.3.2 Two-tone power sweep with pump tone frequency on the resonance

During these measurements, a strong pump tone generated by a synthesizer should overdrive the resonance and a weak tone should probe the shape of the resonance. The readout setup shown in fig. 8.2 is used. Since the pump tone is also detected by the VNA but is very narrow, the IF bandwidth of the VNA is reduced to 400 Hz. By doing that, the

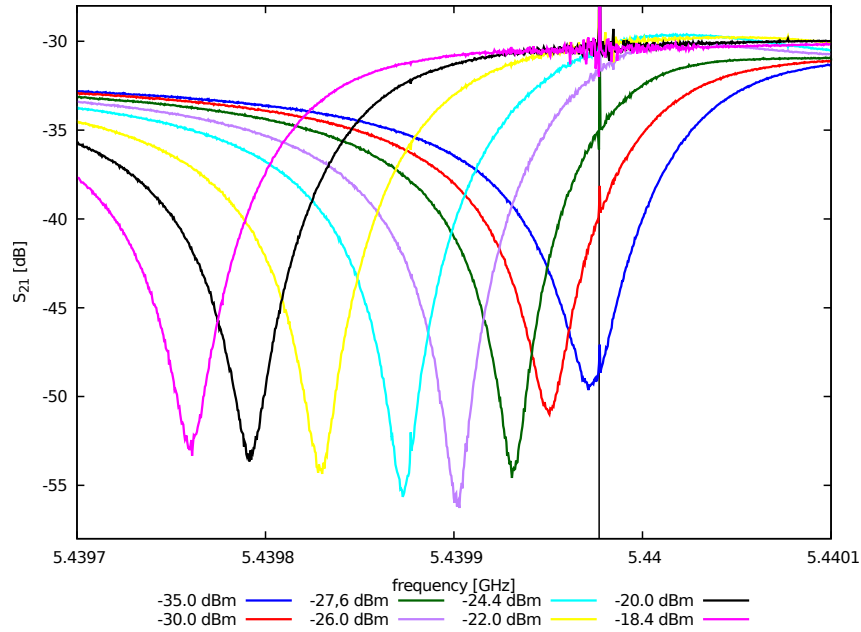


Figure 8.4: VNA measurement of resonator 6 with the fixed pump tone located on the resonance feature. The vertical line indicates the pump tone frequency.

pump tone is still visible but does not distort a large part of the spectrum. The reduced IF bandwidth however requires a long sweep time in the range of 30 s.

For the first experiment, the pump tone is set on the initial resonance frequency of resonator 6. Then the power of the pump tone is increased in steps and after each step, a VNA sweep is measured. The power is first increased and then decreased again. For each step in power, a VNA transmission measurement is done. The results of these measurements are shown in fig. 8.4. The pump tone is visible as a spike on the VNA measurement. The resonance shifts downward with increasing power. The depth of the resonance first increases and starts decreasing at higher powers. The shape of the resonance is qualitatively the same as of the resonance without pump tone. When the power is reduced again, the resonance returns to its initial resonance frequency.

8.3.3 Two-tone power sweep with pump tone frequency below the resonance

For the second experiment, the pump tone is set to the resonance frequency of resonator 6 but then decreased gradually till it is about two resonance width below the undisturbed resonance frequency. Then the pump tone power is increased. The result of this measurement is shown in fig. 8.5. The resonance frequency starts decreasing. When the resonance

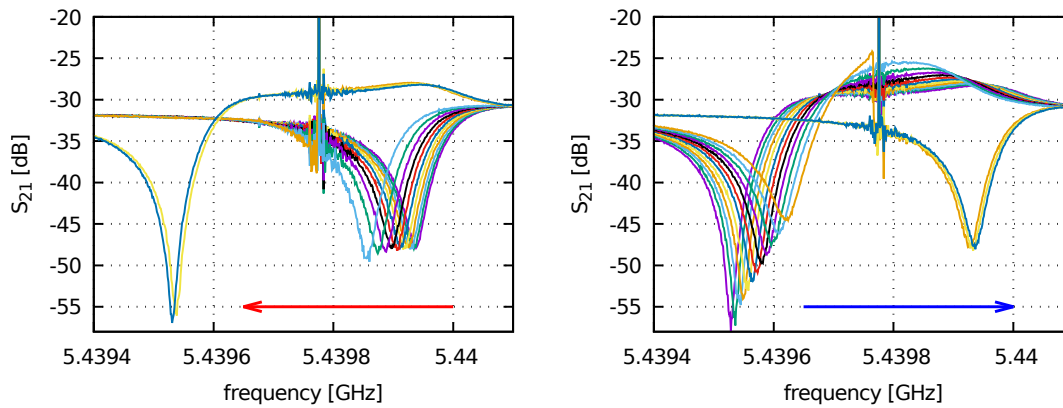


Figure 8.5: VNA measurement of resonator 6 with the fixed pump tone at a frequency below the resonance. **Left:** The power is increased between -19.5 dBm and -16.6 dBm in equal steps. The resonance first shifts monotonically downward from the highest resonance frequency and then jumps to a frequency below the pump tone. **Right:** After that, the power is decreased again in equal steps. The resonance now shifts upwards and again jumps to a resonance frequency above the pump tone.

frequency passes the pump tone, the resonance jumps to a resonance frequency below the pump tone. When power is now decreased again, the resonance frequency starts rising and approaches the pump tone frequency. In this state, the resonance starts changing the shape and higher transmission close to the pump tone is measured. At a certain power, the resonance jumps back to a resonance frequency above the pump tone.

8.3.4 Measurement with pump tone using the spectrum analyzer

The measurements above show that a hysteretic state exists. For the following measurement on resonator 6, the pump tone starts at a power above the switching threshold on the resonance frequency and is manually reduced, till the resonator switches to the hysteretic state. Then the pump tone frequency is increased again into the hysteretic regime, just before the resonator switches back to a resonance frequency above the pump tone. In this setting, the signal is measured using a spectrum analyzer. The result is shown in fig. 8.6, but only as a photograph. The strong pump tone is clearly visible. The VNA readout tone sweeps from left to right picture. Its significant sideband noise can be seen in the spectrum as well. The time per sweep of the spectrum analyzer is set at 31 ms, which enables observation of the spectrum in real time. When the VNA tone approaches the pump tone, a second tone appears above the pump tone which looks like the VNA signal as can be told by the sideband noise. The second signal is a mirrored image of the first signal, just lower in intensity. As it approaches the pump tone, it becomes stronger and

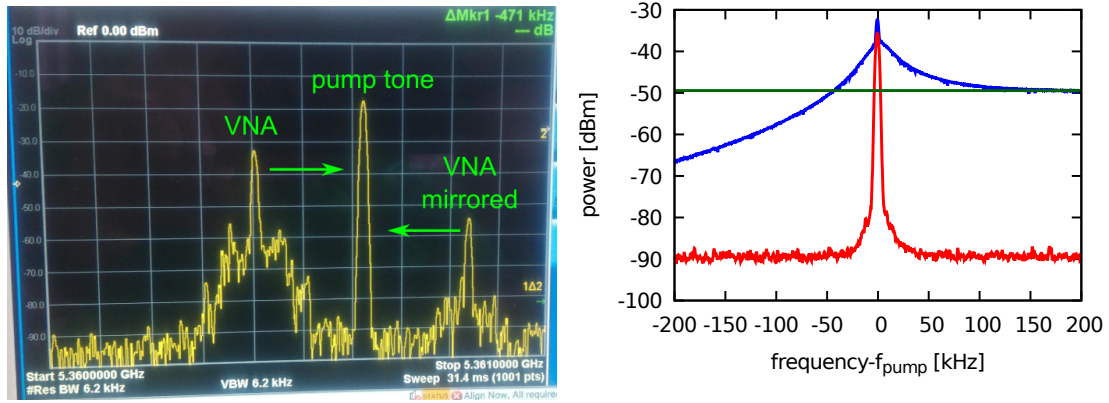


Figure 8.6: Left: Photograph of the spectrum analyzer measurement. Right: Max-hold measurement sweeping a synthesizer tone downward till the pump tone. All signal left if the pump tone is only from the mirrored tone.

stronger.

For a second experiment, the VNA is replaced by a second synthesizer. The synthesizer frequency is slowly swept downwards ending at the pump tone frequency. The spectrum analyzer is set to max-hold mode for this measurement and always tracks the peak position of the second synthesizer. The result is shown in fig. 8.6 on the right. The power at the device for this measurement is -22.7 dBm. As the second signal approaches the resonance, the intensity increases beyond its initial amplitude far from the resonance. At the same time, the second signal from the other side approaches the fixed pump tone and gains intensity as well. It is chosen to sweep downwards towards the pump tone because the resonance feature is located below the pump tone in this measurement. When sweeping upwards, the resonance shape would falsify the observed effects.

8.3.5 Measurement with very high pump tone power

The pump tone frequency is set below the resonance in the hysteretic state as prepared in 8.3.4. The pump tone power is increased up to -8 dBm and the output signal is measured using the spectrum analyzer. At a certain pump signal level which depends on the pump tone frequency relative to the resonance frequency, the result shown in fig. 8.7 is measured. This comb of frequencies appears suddenly and disappears again, as the signal power is decreased. The frequency spacing can be changed by changing the pump tone frequency and the pump tone power.

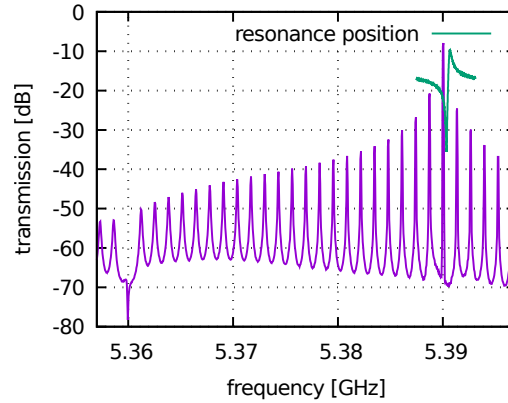


Figure 8.7: Spectrum analyzer measurement of an overdriven resonance feature. The green plot indicates the position of the resonance during that measurements as determined using the VNA (y-axis scaled).

8.4 Analysis

The measurements with high readout power show some interesting effects which are further analyzed in this section.

8.4.1 Resonance frequency and quality factor in dependence of pump tone power

The measurements with the pump tone set on the resonance frequency presented in sec. 8.3.2 can be analyzed for the quality factor and the resonance frequency. The fitting method for the resonances shown in 6.2.2 is used here. Before the fit, the resonances are filtered with a very narrow band median filter to remove the pump tone without distorting the resonance. The result is shown in fig. 8.8. The resonance frequency decreases monotonically with increasing pump tone power. The internal quality factor increases from initial 250000 up to 600000, before it decreases again.

8.4.2 The hysteretic state

The measurement with the pump tone below the resonance frequency (sec. 8.3.3) shows hysteretic switching between one 'state' where the resonance stays above the pump tone and one state where the resonance stays below the pump tone. The resonance frequency for the measurements is determined by fits using the method described in sec. 6.2.2. The resonance frequencies can be determined for these resonance features, but the quality factor results are not usable since the resonance shapes deviate from their modeled form close to

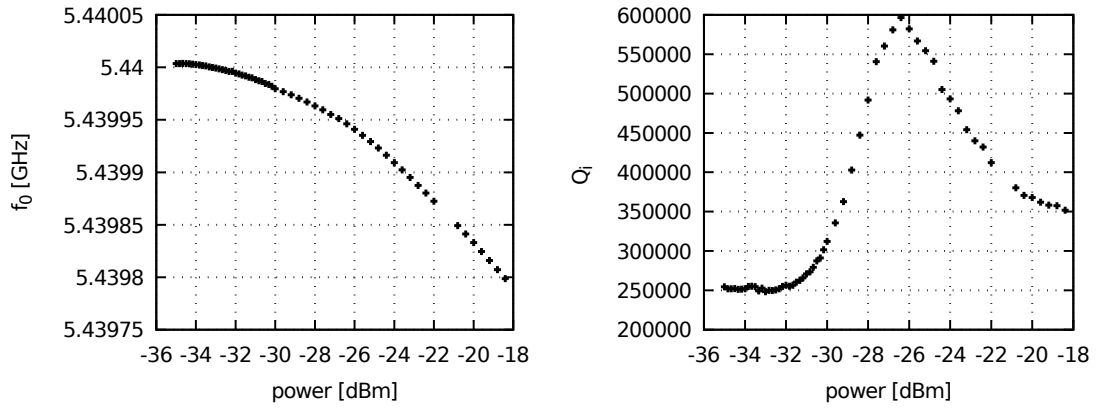


Figure 8.8: Left: Dependence of the resonance frequency on the pump tone power. Right: Dependence of the internal quality factor on the resonance pump tone power.

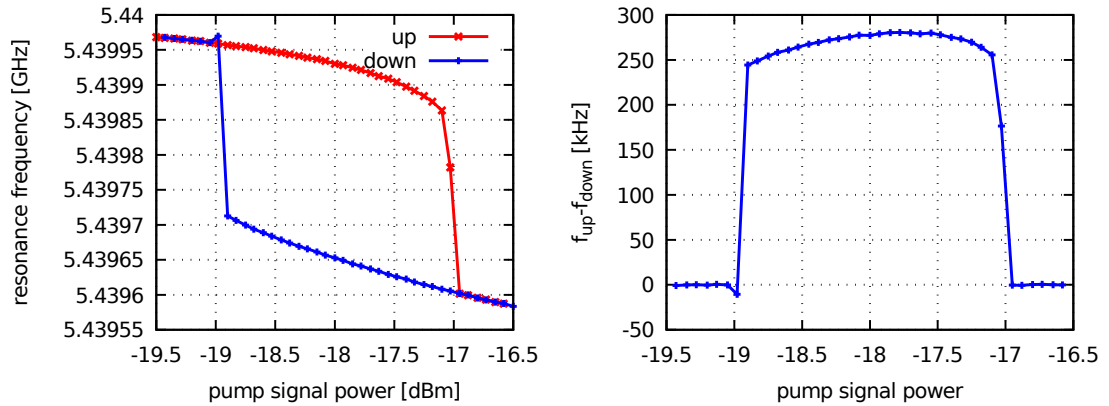


Figure 8.9: Left: Resonance frequency plotted against the readout power for increasing and decreasing power. Right: The difference between increasing and decreasing the power shows the frequency spread between the two states.

the switching point. The resonance frequency is plotted against the power for the increase and the decrease in fig. 8.9. The difference between the two states is around 250 kHz in resonance frequency.

8.4.3 Parametric amplification

The measurements in sec. 8.3.4 show two effects. First, the amplitude of the second tone increases beyond its initial amplitude as it progresses towards the pump tone. The signal is amplified. Second, the generation of the mirror image on the other side of the pump tone strongly suggests that a 4-wave mixing process like in a parametric amplifier [17] takes place. In this process, the input signal is not just amplified, but also mirrored around the

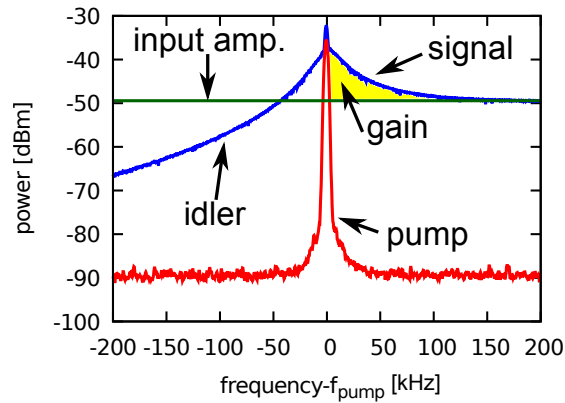


Figure 8.10: Evidence for parametric amplification illustrated in the spectrum analyzer measurement.

pump tone frequency. The mirror signal generated in the amplification process is called idler. The interpretation of the measurement is illustrated in fig. 8.10. The non-linearity would be created by the kinetic inductance of the NbTiN. The peak gain observed is around 12 dB, but with a rather poor 3 dB bandwidth of only 15 kHz.

8.4.4 Overdriven resonator

The results obtained with very high readout powers shown in fig. 8.3.5 were first attributed to saturation of the LNA, which could be excluded as this effect does only occur close to a resonance. The spacing between the peaks has been measured as 131 kHz. An interesting feature in fig. 8.7 appears at 5.36 GHz, which is the resonance frequency of a different resonator on the test chip. The frequency comb generated by the overdriven resonator therefore can interact with the other resonators. This proves, that the additional frequencies are physically present on the test chip and not just readout artifacts.

8.5 Summary and discussion

The measurements with the strong pump tone and the weak probe tone show, that the resonances do not intrinsically contain step-like discontinuities as it would be suggested by my measurement with one strong readout tone only (fig. 8.4). The resonances actually look normal and can be fitted using the common resonator model [55]. The switching behavior of the overdriven model can be explained by assuming heating and cooling processes in the resonators, which can generate an hysteretic state [43, 96]. This electro-thermal model includes an effective quasiparticle temperature [45], which shifts the resonance and decreases the quality factor. My observation, that the quality factor first increases with

increasing readout power, contradicts with the hypothesis of readout power heating, but my devices are also made of NbTiN which is not immediately taken into account in the models mentioned here. The increased quality factor could be explained by effects like microwave-enhanced superconductivity [56, 103], which is however not elaborated here.

I have been able to observe parametric amplification with a NbTiN resonator. Parametric amplification in resonators has however been observed before and the general effect is already used in kinetic inductance traveling wave amplifiers [17, 99]. These amplifiers also achieve a useful bandwidth of several GHz. The usefulness of my resonator as amplifier is however questionable, as the bandwidth of 15 kHz is indeed very limited. The gain of 12 dB is however already quite significant. For the final proof, the noise temperature of this device should be determined. I attempted this experiment, but significant additional readout hardware is necessary to yield meaningful results.

The effects on the strongly overdriven resonator, which generates a frequency-comb like spectrum can be described by parametric oscillation, which was first published as a problem in a maser amplifier [30]. The interpretation of this oscillation is pending, but a theory is that reflections from the following readout system generate some feedback which makes the amplifier into an oscillator. Other ideas could include the fact that the observed spacing between the peaks is roughly half the measured spread of the hysteretic state, which would give rise to models of a permanently switching resonator.

The measurements above are really only of phenomenological nature and barely scratch the surface of the non-linear effects. The actual amount of data for the measurements has the pump frequency, the pump power, the signal frequency and power and the history, meaning from which state the measurement started as free parameters. Future experiments should focus on the quantitative analysis of the experiments and should attempt to measure a noise temperature of the parametric amplifier. For the parametric oscillations, it would be interesting if the generated spikes can be used as a signal source for actual measurement. For that, the spectral properties of these spikes have to be investigated further.

Bibliography

- [1] B.P. Abbott et al. (LIGO Scientific Collaboration and Virgo Collaboration). Observation of gravitational waves from a binary black hole merger. *Phys. Rev. Lett.*, 116:061102, Feb 2016.
- [2] R. Adam, A. Adane, P. A. R. Ade, P. André, A. Andrianasolo, H. Aussel, A. Beelen, A. Benoît, A. Bideaud, N. Billot, O. Bourrion, A. Bracco, M. Calvo, A. Catalano, G. Coiffard, B. Comis, M. De Petris, F.-X. Désert, S. Doyle, E. F. C. Driessen, R. Evans, J. Goupy, C. Kramer, G. Lagache, S. Leclercq, J.-P. Leggeri, J.-F. Lestrade, J. F. Macías-Pérez, P. Mauskopf, F. Mayet, A. Maury, A. Monfardini, S. Navarro, E. Pascale, L. Perotto, G. Pisano, N. Ponthieu, V. Revéret, A. Rigby, A. Ritacco, C. Romero, H. Roussel, F. Ruppin, K. Schuster, A. Sievers, S. Trique-neaux, C. Tucker, and R. Zylka. The NIKA2 large-field-of-view millimetre continuum camera for the 30 m IRAM telescope. *A&A*, 609:A115, 2018.
- [3] Silke Andree-Labsch, Karl Jacobs, Jürgen Stutzki, Michael Schultz, and Cornelia E. Honingh. Near quantum limited Nb-Al-AlO_x-Nb mixers on 9 μm thick silicon substrates around 350 GHz. *Journal of Infrared, Millimeter, and Terahertz Waves*, 35(3):300–317, 2014.
- [4] J. Bardeen, L.N. Cooper, and J.R. Schrieffer. Theory of superconductivity. *Phys. Rev.*, 108(5):1175–1204, 1957.
- [5] J.C Bardin and S. Weinreb. A 0.1-5 GHz Cryogenic SiGe MMIC LNA. *IEEE Microw. Wireless Compon. Lett.*, 19:407, 2009.
- [6] R. Barends, J. J. A. Baselmans, S. J. C. Yates, J. R. Gao, J. N. Hovenier, and T. M. Klapwijk. Quasiparticle relaxation in optically excited high-Q superconducting resonators. *Phys. Rev. Lett.*, 100:257002, Jun 2008.
- [7] R. Barends, H. L. Hortensius, T. Zijlstra, J. J. A. Baselmans, S. J. C. Yates, J. R. Gao, and T. M. Klapwijk. Contribution of dielectrics to frequency and noise of NbTiN superconducting resonators. *Applied Physics Letters*, 92(22):223502, 2008.

- [8] R. Barends, N. Vercauteren, A. Endo, P.J. de Visser, T. Zijlstra, T.M. Klapwijk, and J.J.A. Baselmans. Reduced frequency noise in superconducting resonators. *Appl. Phys. Lett.*, 97(3), 2010.
- [9] R. Barends, J. Wenner, M. Lenander, Y. Chen, R. C. Bialczak, J. Kelly, E. Lucero, P. O'Malley, M. Mariantoni, D. Sank, H. Wang, T. C. White, Y. Yin, J. Zhao, A. N. Cleland, John M. Martinis, and J. J. A. Baselmans. Minimizing quasiparticle generation from stray infrared light in superconducting quantum circuits. *Applied Physics Letters*, 99(11):113507, 2011.
- [10] Rami Barends. *Photon-Detecting Superconducting Resonators*. PhD thesis, TU Delft, 2009.
- [11] J. Baselmans, S. J. C. Yates, R. Barends, Y. J. Y. Lankwarden, J. R. Gao, H. Hoovers, and T. M. Klapwijk. Noise and sensitivity of aluminum kinetic inductance detectors for sub-mm astronomy. *Journal of Low Temperature Physics*, 151(1):524–529, Apr 2008.
- [12] D. J. Benford, T. R. Hunter, and T. G. Phillips. Noise equivalent power of background limited thermal detectors at submillimeter wavelengths. *International Journal of Infrared and Millimeter Waves*, 19(7):931–938, Jul 1998.
- [13] C. L. Bennett, M. Halpern, G. Hinshaw, N. Jarosik, A. Kogut, M. Limon, S. S. Meyer, L. Page, D. N. Spergel, G. S. Tucker, E. Wollack, E. L. Wright, C. Barnes, M. R. Greason, R. S. Hill, E. Komatsu, M. R. Nolte, N. Odegard, H. V. Peiris, L. Verde, and J. L. Weiland. First-year wilkinson microwave anisotropy probe (WMAP) observations: Preliminary maps and basic results. *The Astrophysical Journal Supplement Series*, 148(1):1, 2003.
- [14] D. Bintley, M. J. Macintosh, W. S. Holland, P. Friberg, C. Walther, D. Atkinson, D. Kelly, X. Gao, P. A. R. Ade, W. Grainger, J. House, L. Moncelsi, M. I. Hollister, A. Woodcraft, C. Dunare, W. Parkes, A. J. Walton, K. D. Irwin, G. C. Hilton, M. Niemack, C. D. Reintsema, M. Amiri, B. Burger, M. Halpern, M. Hasselfield, J. Hill, J. B. Kycia, C. G. A. Mugford, and L. Persaud. Characterising the SCUBA-2 superconducting bolometer arrays. In *Society of Photo-Optical Instrumentation Engineers (SPIE) Conference Series*, volume 7741 of *Society of Photo-Optical Instrumentation Engineers (SPIE) Conference Series*, July 2010.
- [15] M. A. Biondi and M. P. Garfunkel. Millimeter wave absorption in superconducting

- aluminum. I. temperature dependence of the energy gap. *Phys. Rev.*, 116:853–861, Nov 1959.
- [16] Florian Blauth. Implementation of a first MKID test setup and measurement of a NbTiN test chip, 2009.
- [17] C. Bockstiegel, J. Gao, M. R. Vissers, M. Sandberg, S. Chaudhuri, A. Sanders, L. R. Vale, K. D. Irwin, and D. P. Pappas. Development of a broadband NbTiN traveling wave parametric amplifier for MKID readout. *Journal of Low Temperature Physics*, 176(3):476–482, Aug 2014.
- [18] O. Bourrion, C. Vescovi, J. L. Bouly, A. Benoit, M. Calvo, L. Gallin-Martel, J. F. Macias-Perez, and A. Monfardini. NIKEL: electronics and data acquisition for kilopixels kinetic inductance camera. *Journal of Instrumentation*, 7(07):P07014, 2012.
- [19] Robert W. Boyd. Photon bunching and the photon-noise-limited performance of infrared detectors. *Infrared Physics*, 22(3):157 – 162, 1982.
- [20] S. Bryan, K. Bradford, G. Che, P. Day, D. Flanigan, B. R. Johnson, G. Jones, B. Kjellstrand, M. Limon, P. Mauskopf, H. McCarrick, A. Miller, and B. Smiley. Design of Dual-Polarization Horn-Coupled Kinetic Inductance Detectors for Cosmic Microwave Background Polarimetry. *ArXiv e-prints*, March 2015.
- [21] D. Büchel, P. Pütz, K. Jacobs, M. Schultz, U. U. Graf, C. Risacher, H. Richter, O. Ricken, H. Hübers, R. Güsten, C. E. Honingh, and J. Stutzki. 4.7-THz superconducting hot electron bolometer waveguide mixer. *IEEE Transactions on Terahertz Science and Technology*, 5(2):207–214, March 2015.
- [22] CCAT consortium. Ccat pathfinder kSZ science case: Probing the transition between gravity and dark energy dominated regimes. http://www.ccatobservatory.org/docs/ccat-technical-memos/CCAT-p.kSZ_whitepaper.pdf. Accessed: Jun. 2018.
- [23] CCAT consortium. [CII] 158 μm line intensity mapping in the epoch of reionization (redshifts 6-8). http://www.ccatobservatory.org/docs/ccat-technical-memos/ccatp_im_v2.pdf. Accessed: Jun. 2018.
- [24] Peter K. Day, Henry G. LeDuc, Benjamin A. Mazin, Anastasios Vayonakis, and Jonas Zmuidzinas. A broadband superconducting detector suitable for use in large arrays. *Nature*, 425(6960):817–821, 2003. 10.1038/nature02037.

- [25] P. J. de Visser, J. J. A. Baselmans, P. Diener, S. J. C. Yates, A. Endo, and T. M. Klapwijk. Number fluctuations of sparse quasiparticles in a superconductor. *Phys. Rev. Lett.*, 106:167004, Apr 2011.
- [26] P. J. de Visser, J. J. A. Baselmans, P. Diener, S. J. C. Yates, A. Endo, and T. M. Klapwijk. Generation-recombination noise: The fundamental sensitivity limit for kinetic inductance detectors. *Journal of Low Temperature Physics*, 167(3):335–340, May 2012.
- [27] P. J. de Visser, S. Withington, and D. J. Goldie. Readout-power heating and hysteretic switching between thermal quasiparticle states in kinetic inductance detectors. *Journal of Applied Physics*, 108(11):114504, 2010.
- [28] P. J. de Visser, S. J. C. Yates, T. Guruswamy, D. J. Goldie, S. Withington, A. Neto, N. Llombart, A. M. Baryshev, T. M. Klapwijk, and J. J. A. Baselmans. The non-equilibrium response of a superconductor to pair-breaking radiation measured over a broad frequency band. *Applied Physics Letters*, 106(25), 2015.
- [29] B. Dober, J. A. Austermann, J. A. Beall, D. Becker, G. Che, H. M. Cho, M. Devlin, S. M. Duff, N. Galitzki, J. Gao, C. Groppi, G. C. Hilton, J. Hubmayr, K. D. Irwin, C. M. McKenney, D. Li, N. Lourie, P. Mauskopf, M. R. Vissers, and Y. Wang. Optical demonstration of thz, dual-polarization sensitive microwave kinetic inductance detectors. *Journal of Low Temperature Physics*, 184(1):173–179, Jul 2016.
- [30] O. Doehler and G. Dohler. Parametric oscillations in high-power injected beam crossed-field amplifiers and twt’s. *IEEE Transactions on Electron Devices*, 26(10):1602–1608, Oct 1979.
- [31] S. Doyle, P. Mauskopf, J. Naylon, A. Porch, and C. Duncombe. Lumped element kinetic inductance detectors. *Journal of Low Temperature Physics*, 151:530–536, 2008. 10.1007/s10909-007-9685-2.
- [32] R. C. Dynes, J. P. Garno, G. B. Hertel, and T. P. Orlando. Tunneling study of superconductivity near the metal-insulator transition. *Phys. Rev. Lett.*, 53:2437–2440, Dec 1984.
- [33] Warburg E. Magnetische Untersuchungen. *Annalen der Physik*, 249(5):141–164, 1881.

- [34] John W. Eaton, David Bateman, Søren Hauberg, and Rik Wehbring. *GNU Octave version 4.4.1 manual: a high-level interactive language for numerical computations*, 2017.
- [35] Sonnet em 3D Planar Simulation Software. <http://www.sonnetsoftware.com>.
- [36] A. Endo, P. van der Werf, R. Janssen, P. de Visser, T. Klapwijk, J. Baselmans, L. Ferrari, A. Baryshev, and S. Yates. Design of an integrated filterbank for DESHIMA: On-chip submillimeter imaging spectrograph based on superconducting resonators. *Journal of Low Temperature Physics*, 167:341–346, 2012. 10.1007/s10909-012-0502-1.
- [37] L. Ferrari, O. Yurduseven, N. Llombart, S. J. C. Yates, J. Bueno, V. Murugesan, D. J. Thoen, A. Endo, A. M. Baryshev, and J. J. A. Baselmans. Antenna coupled mkid performance verification at 850 ghz for large format astrophysics arrays. *IEEE Transactions on Terahertz Science and Technology*, 8(1):127–139, Jan 2018.
- [38] D. Flanigan, B. R. Johnson, M. H. Abitbol, S. Bryan, R. Cantor, P. Day, G. Jones, P. Mauskopf, H. McCarrick, A. Miller, and J. Zmuidzinas. Magnetic field dependence of the internal quality factor and noise performance of lumped-element kinetic inductance detectors. *Applied Physics Letters*, 109(14):143503, 2016.
- [39] Joseph Fraunhofer. Bestimmung des brechungs- und des farbenzerstreungsvermögens verschiedener glasarten, in bezug auf die vervollkommnung achromatischer fernröhre. *Annalen der Physik*, 56(7):264–313, 1817.
- [40] J. Gao, J. Zmuidzinas, A. Vayonakis, P. Day, B. Mazin, and H. Leduc. Equivalence of the effects on the complex conductivity of superconductor due to temperature change and external pair breaking. *Journal of Low Temperature Physics*, 151(1):557–563, Apr 2008.
- [41] Jiansong Gao, Jonas Zmuidzinas, Benjamin A. Mazin, Henry G. LeDuc, and Peter K. Day. Noise properties of superconducting coplanar waveguide microwave resonators. *Applied Physics Letters*, 90(10):102507, 2007.
- [42] W. F. Giaque. A thermodynamic treatment of certain magnetic effects. A proposed method of producing temperatures considerably below 1° absolute. *Journal of the American Chemical Society*, 49(8):1864–1870, 1927.
- [43] D J Goldie and S Withington. Non-equilibrium superconductivity in quantum-sensing superconducting resonators. *Superconductor Science and Technology*, 26(1):015004, 2013.

- [44] Christopher Groppi, Christopher Walker, Craig Kulesa, Dathon Golish, Jenna Kloosterman, Sander Weinreb, Glenn Jones, Joseph Bardin, Hamdi Mani, Tom Kuiper, Jacob Kooi, Art Lichtenberger, Thomas Cecil, Patrick Pütz, Gopal Narayanan, and Abigail Hedden. Test and integration results from SuperCam: a 64-pixel array receiver for the 350 GHz atmospheric window, 2010.
- [45] T. Guruswamy, D. J. Goldie, and S. Withington. Nonequilibrium superconducting thin films with sub-gap and pair-breaking photon illumination. *Superconductor Science and Technology*, 28(5):054002, 2015.
- [46] H. Hertz. Ueber sehr schnelle elektrische schwingungen. *Annalen der Physik*, 267(7):421–448, 1887.
- [47] High Precision Devices Inc. *HPD model 103 Rainier operation and installation manual*.
- [48] G. Hinshaw, M. R. Nolta, C. L. Bennett, R. Bean, O. Doré, M. R. Greason, M. Halpern, R. S. Hill, N. Jarosik, A. Kogut, E. Komatsu, M. Limon, N. Odegard, S. S. Meyer, L. Page, H. V. Peiris, D. N. Spergel, G. S. Tucker, L. Verde, J. L. Weiland, E. Wollack, and E. L. Wright. Three-year wilkinson microwave anisotropy probe (WMAP) observations: Temperature analysis. *The Astrophysical Journal Supplement Series*, 170(2):288, 2007.
- [49] Paul Horowitz and Winfield Hill. *The art of electronics*. Cambridge University Press, 2nd edition, 1989.
- [50] J. Hubmayr, J. Beall, D. Becker, H.-M. Cho, M. Devlin, B. Dober, C. Groppi, G. C. Hilton, K. D. Irwin, D. Li, P. Mauskopf, D. P. Pappas, J. Van Lanen, M. R. Vissers, Y. Wang, L. F. Wei, and J. Gao. Photon-noise limited sensitivity in titanium nitride kinetic inductance detectors. *Applied Physics Letters*, 106(7):073505, February 2015.
- [51] K. G. Jansky. Electrical disturbances apparently of extraterrestrial origin. *Proceedings of the Institute of Radio Engineers*, 21(10):1387–1398, Oct 1933.
- [52] R. M. J. Janssen, J. J. A. Baselmans, A. Endo, L. Ferrari, S. J. C. Yates, A. M. Baryshev, and T. M. Klapwijk. High optical efficiency and photon noise limited sensitivity of microwave kinetic inductance detectors using phase readout. *Applied Physics Letters*, 103(20):203503, 2013.
- [53] B. R. Johnson, D. Flanigan, M. H. Abitbol, P. A. R. Ade, S. Bryan, H.-M. Cho, R. Datta, P. Day, S. Doyle, K. Irwin, G. Jones, D. Li, P. Mauskopf, H. McCarrick,

- J. McMahon, A. Miller, G. Pisano, Y. Song, H. Surdi, and C. Tucker. Development of Multi-Chroic MKIDs for Next-Generation CMB Polarization Studies. *ArXiv e-prints*, November 2017.
- [54] S. B. Kaplan, C. C. Chi, D. N. Langenberg, J. J. Chang, S. Jafarey, and D. J. Scalapino. Quasiparticle and phonon lifetimes in superconductors. *Phys. Rev. B*, 14:4854–4873, Dec 1976.
- [55] M. S. Khalil, M. J. A. Stoutimore, F. C. Wellstood, and K. D. Osborn. An analysis method for asymmetric resonator transmission applied to superconducting devices. *Journal of Applied Physics*, 111(5):–, 2012.
- [56] T.M. Klapwijk and J.E. Mooij. Microwave-enhanced superconductivity in aluminium films. *Physica B+C*, 81(1):132 – 136, 1976.
- [57] Jun Kondo. Resistance minimum in dilute magnetic alloys. *Progress of Theoretical Physics*, 32(1):37–49, 1964.
- [58] J. W. Kooi, G. Chattopadhyay, S. Withington, F. Rice, J. Zmuidzinas, C. Walker, and G. Yassin. A full-height waveguide to thin-film microstrip transition with exceptional RF bandwidth and coupling efficiency. *International Journal of Infrared and Millimeter Waves*, 24(3):261–284, Mar 2003.
- [59] A. G. Kozorezov, A. F. Volkov, J. K. Wigmore, A. Peacock, A. Poelaert, and R. den Hartog. Quasiparticle-phonon downconversion in nonequilibrium superconductors. *Phys. Rev. B*, 61:11807–11819, May 2000.
- [60] Henry G. Leduc, Bruce Bumble, Peter K. Day, Byeong Ho Eom, Jiansong Gao, Sunil Golwala, Benjamin A. Mazin, Sean McHugh, Andrew Merrill, David C. Moore, Omid Noroozian, Anthony D. Turner, and Jonas Zmuidzinas. Titanium nitride films for ultrasensitive microresonator detectors. *Applied Physics Letters*, 97(10):102509, 2010.
- [61] Thomas H. Lee. *Planar Microwave Engineering*. Cambridge University Press, 2004.
- [62] F. London and H. London. The electromagnetic equations of the supraconductor. *Proceedings of the Royal Society of London A: Mathematical, Physical and Engineering Sciences*, 149(866):71–88, 1935.
- [63] N.N. Marcuvitz. *Waveguide Handbook*. Institution of Engineering & Technology, revised edition, 1985.

- [64] D. C. Mattis and J. Bardeen. Theory of the anomalous skin effect in normal and superconducting metals. *Phys. Rev.*, 111:412–417, Jul 1958.
- [65] James Clerk Maxwell. VIII. a dynamical theory of the electromagnetic field. *Philosophical Transactions of the Royal Society of London*, 155:459–512, 1865.
- [66] B. A. Mazin, S. R. Meeker, M. J. Strader, P. Szypryt, D. Marsden, J. C. van Eyken, G. E. Duggan, A. B. Walter, G. Ulbricht, M. Johnson, B. Bumble, K. O’Brien, and C. Stoughton. Arcons: A 2024 pixel optical through near-ir cryogenic imaging spectrophotometer. *Publications of the Astronomical Society of the Pacific*, 125(933):1348, 2013.
- [67] Benjamin A. Mazin. *Microwave Kinetic Inductance Detectors*. PhD thesis, California Institute of Technology, 2004.
- [68] H. McCarrick, D. Flanigan, G. Jones, B. R. Johnson, P. Ade, D. Araujo, K. Bradford, R. Cantor, G. Che, P. Day, S. Doyle, H. Leduc, M. Limon, V. Luu, P. Mauskopf, A. Miller, T. Mroczkowski, C. Tucker, and J. Zmuidzinas. Horn-coupled, commercially-fabricated aluminum lumped-element kinetic inductance detectors for millimeter wavelengths. *Review of Scientific Instruments*, 85(12):123117, 2014.
- [69] Sean McHugh, Benjamin A. Mazin, Bruno Serfass, Seth Meeker, Kieran O’Brien, Ran Duan, Rick Raffanti, and Dan Werthimer. A readout for large arrays of microwave kinetic inductance detectors. *Review of Scientific Instruments*, 83(4):044702, 2012.
- [70] Božidar Mitrović and Lee A Rozema. On the correct formula for the lifetime broadened superconducting density of states. *Journal of Physics: Condensed Matter*, 20(1):015215, 2008.
- [71] Monfardini, A., Swenson, L. J., Bideaud, A., Désert, F. X., Yates, S. J. C., Benoit, A., Baryshev, A. M., Baselmans, J. J. A., Doyle, S., Klein, B., Roesch, M., Tucker, C., Ade, P., Calvo, M., Camus, P., Giordano, C., Guesten, R., Hoffmann, C., Leclercq, S., Mauskopf, P., and Schuster, K. F. NIKA: A millimeter-wave kinetic inductance camera. *A&A*, 521:A29, 2010.
- [72] Dmitry Morozov, Simon M. Doyle, Archan Banerjee, Thomas L. R. Brien, Dilini Hemakumara, Iain G. Thayne, Ken Wood, and Robert H. Hadfield. Design and characterisation of titanium nitride subarrays of kinetic inductance detectors for passive terahertz imaging. *Journal of Low Temperature Physics*, Jul 2018.

- [73] Michael D. Niemack. Designs for a large-aperture telescope to map the CMB 10 x faster. *Appl. Opt.*, 55(7):1688–1696, Mar 2016.
- [74] T. Noguchi, A. Dominjon, and Y. Sekimoto. Analysis of characteristics of Al MKID resonators. *ArXiv e-prints*, September 2017.
- [75] T. Noguchi, M. Naruse, and Y. Sekimoto. Contribution of quasiparticles in the subgap states to the surface impedance of superconductors. *IEEE Transactions on Applied Superconductivity*, 23(3):1501404–1501404, June 2013.
- [76] Debye P. Einige Bemerkungen zur Magnetisierung bei tiefer Temperatur. *Annalen der Physik*, 386(25):1154–1160, 1926.
- [77] S. C. Parshley, J. Kronshage, J. Blair, T. Herter, M. Nolta, G. J. Stacey, A. Bazarko, F. Bertoldi, R. Bustos, D. B. Campbell, S. Chapman, N. Cothard, M. Devlin, J. Erler, M. Fich, P. A. Gallardo, R. Giovanelli, U. Graf, S. Gramke, M. P. Haynes, R. Hills, M. Limon, J. G. Mangum, J. McMahon, M. D. Niemack, T. Nikola, M. Omlor, D. A. Riechers, K. Steeger, J. Stutzki, and E. M. Vavagiakis. CCAT-prime: a novel telescope for sub-millimeter astronomy. In *Society of Photo-Optical Instrumentation Engineers (SPIE) Conference Series*, volume 10700 of *Society of Photo-Optical Instrumentation Engineers (SPIE) Conference Series*, page 107005X, July 2018.
- [78] S. C. Parshley, M. Niemack, R. Hills, S. R. Dicker, R. Dünner, J. Erler, P. A. Gallardo, J. E. Gudmundsson, T. Herter, B. J. Koopman, M. Limon, F. T. Matsuda, P. Mauskopf, D. A. Riechers, G. J. Stacey, and E. M. Vavagiakis. The optical design of the six-meter CCAT-prime and Simons Observatory telescopes. In *Society of Photo-Optical Instrumentation Engineers (SPIE) Conference Series*, volume 10700 of *Society of Photo-Optical Instrumentation Engineers (SPIE) Conference Series*, page 1070041, July 2018.
- [79] Richard B. Pettit and J. Silcox. Film structure and enhanced superconductivity in evaporated aluminum films. *Phys. Rev. B*, 13:2865–2872, Apr 1976.
- [80] Planck Collaboration et al. Planck 2013 results. I. Overview of products and scientific results. *A&A*, 571:A1, 2014.
- [81] David M. Pozar. *Microwave Engineering*. J. Wiley & Sons Inc., 1998.
- [82] R. Radebaugh and J.D. Siegwarth. Dilution refrigerator technology. *Cryogenics*, 11(5):368 – 384, 1971.

- [83] G. Reber. Cosmic static. *Proceedings of the IRE*, 28(2):68–70, Feb 1940.
- [84] G. H. Rieke. *Detection of Light from the ultraviolet to the submillimeter*. Cambridge University Press, 1994.
- [85] Wilhelm Conrad Roentgen. Ueber eine neue Art von Strahlen. *Sitzungsberichte der Würzburger physik.-med. Gesellschaft Würzburg*, 1:132–141, 1895.
- [86] M. Roesch, A. Benoit, A. Bideaud, N. Boudou, M. Calvo, A. Cruciani, S. Doyle, H. G. Leduc, A. Monfardini, L. Swenson, S. Leclercq, P. Mauskopf, K. F. Schuster, and for the NIKA collaboration. Development of Lumped Element Kinetic Inductance Detectors for NIKA. *ArXiv e-prints*, December 2012.
- [87] K. Sato, S. Ariyoshi, S. Negishi, S. Hashimoto, H. Mikami, K. Nakajima, and S. Tanaka. Evaluation of $\text{YBa}_2\text{Cu}_3\text{O}_{7-\delta}$ -based microwave kinetic inductance detectors with rewound spiral resonators. *Journal of Physics: Conference Series*, 1054(1):012053, 2018.
- [88] J.A. Schlaerth, N.G. Czakon, T.P. Downes, R. Duan, J. Glenn, S.R. Golwala, M.I. Hollister, and P.R. LeDuc, H.G. Maloney. The status of music: A multicolor sub / millimeter MKID instrument. *Journal of Low Temperature Physics*, 167(3-4):347–353, 2012.
- [89] E. Shirokoff, P. S. Barry, C. M. Bradford, G. Chattopadhyay, P. Day, S. Doyle, S. Hailey-Dunsheath, M. I. Hollister, A. Kovács, H. G. Leduc, C. M. McKenney, P. Mauskopf, H. T. Nguyen, R. O’Brien, S. Padin, T. J. Reck, L. J. Swenson, C. E. Tucker, and J. Zmuidzinas. Design and performance of SuperSpec: An on-chip, KID-based, mm-wavelength spectrometer. *Journal of Low Temperature Physics*, 176(5):657–662, Sep 2014.
- [90] Shibo Shu, Martino Calvo, Samuel Leclercq, Johannes Goupy, Alessandro Monfardini, and Eduard Driessen. Prototype high angular resolution LEKIDs for NIKA2. *ArXiv*, 10 2017.
- [91] Rainee N. Simons. *Coplanar Waveguide Circuits, Components, and Systems*. John Wiley&Sons Inc., first edition, 2001.
- [92] CST Microwave Studio 3D EM simulation software. <http://www.cst.com>.
- [93] R.A. Sunyaev and Ya. B. Zel’Dovich. Microwave background radiation as a probe of the contemporary structure and history of the universe. *Annual review of astronomy and astrophysics*, 18(1):537–560, 1980.

-
- [94] Blog: TheCuriousAstronomer. <https://thecuriousastronomer.wordpress.com/2015/07/30/what-is-the-redshift-of-the-cosmic-microwave-background-cmb/>.
- [95] C. N. Thomas, S. Withington, and D. J. Goldie. Electrothermal model of kinetic inductance detectors. *Superconductor Science and Technology*, 28(4):045012, 2015.
- [96] S. E. Thompson, S Withington, D. J. Goldie, and C. N. Thomas. Dynamical behaviour of superconducting microresonators with readout-power heating. *Superconductor Science and Technology*, 26(9):095009, 2013.
- [97] M. Tinkham. *Introduction to superconductivity*. Dover, second edition, 2004.
- [98] L. J. van der Pauw. Determination of resistivity tensor and hall tensor of anisotropic shape. *Philips Research Reports*, 16:187–195, 1961.
- [99] M. R. Vissers, R. P. Erickson, H.S. Ku, V Leila, Xian Wu, G. C. Hilton, and D. P. Pappas. Low-noise kinetic inductance traveling-wave amplifier using three-wave mixing. *Applied Physics Letters*, 108(1):012601, 2016.
- [100] M. R. Vissers, J. Hubmayr, M. Sandberg, S. Chaudhuri, C. Bockstiegel, and J. Gao. Frequency-tunable superconducting resonators via nonlinear kinetic inductance. *Applied Physics Letters*, 107(6):062601, 2015.
- [101] S. J. Weber, K. W. Murch, D. H. Slichter, R. Vijay, and I. Siddiqi. Single crystal silicon capacitors with low microwave loss in the single photon regime. *Applied Physics Letters*, 98(17):172510, April 2011.
- [102] C. M. Wilson, L. Frunzio, and D. E. Prober. Time-resolved measurements of thermodynamic fluctuations of the particle number in a nondegenerate fermi gas. *Phys. Rev. Lett.*, 87:067004, Jul 2001.
- [103] A. F. G. Wyatt, V. M. Dmitriev, W. S. Moore, and F. W. Sheard. Microwave-enhanced critical supercurrents in constricted tin films. *Phys. Rev. Lett.*, 16:1166–1169, Jun 1966.
- [104] C. Yang, R. R. Niu, Z. S. Guo, X. W. Cai, H. M. Chu, K. Yang, Y. Wang, Q. R. Feng, and Z. Z. Gan. Lumped element kinetic inductance detectors based on two-gap MgB₂ thin films. *Applied Physics Letters*, 112(2):022601, 2018.
- [105] S. J. C. Yates, J. J. A. Baselmans, A. Endo, R. M. J. Janssen, L. Ferrari, P. Diener, and A. M. Baryshev. Photon noise limited radiation detection with lens-antenna coupled microwave kinetic inductance detectors. *Applied Physics Letters*, 99(7):073505, 2011.

- [106] Jonas Zmuidzinas. Superconducting microresonators: Physics and applications. *Annual Review of Condensed Matter Physics*, 3(1):169–214, 2012.

Acknowledgements

I would like to thank Prof. Dr. Jürgen Stutzki for the opportunity of doing my PhD in his workgroup at the I. Physikalisches Institut, Universität zu Köln.

I thank Dr. Netty Honingh for the supervision of my thesis. She always showed a lot of engagement and interest in my work.

I thank Dr. Karl Jacobs for the fabrication of my MKID, which often meant pushing the available equipment and procedures to their limits.

Special thanks to Dr. Eduard Driessen and Shibo Shu from IRAM in Grenoble, who did not hesitate to send me the NIKA 2 test chips. The results of the measurements became a mayor part of this thesis.

I thank Michael Schultz for the precise mounting my devices and for support in the CAD of the measurement setup. I like to thank Stefan Wulff for unconventional clean room processing like the Niobium magnetic shield and material development. Likewise I like to thank the mechanical and electrical workshop of our institute for good collaboration.

Thanks to my (former) colleagues Sina, Sina, Matthias, Denis, Ignacio and Johanna for a pleasant working atmosphere and lively scientific (and non-scientific) discussions in the office.

Special thanks to my wife for having my back during the final phase of this thesis and to my children, Johannes and Antonia for keeping me grounded. Also thanks to my parents for supporting me on this path in life.

MKID development is carried out within the Collaborative Research Centre 956, sub-project D3, funded by the Deutsche Forschungsgemeinschaft (DFG).

I gratefully acknowledge the financial and advisory support from the Bonn-Cologne Graduate School for physics and astronomy (BCGS).



Erklärung

Ich versichere, dass ich die von mir vorgelegte Dissertation selbständig angefertigt, die benutzten Quellen und Hilfsmittel vollständig angegeben und die Stellen der Arbeit – einschließlich Tabellen, Karten und Abbildungen –, die anderen Werken im Wortlaut oder dem Sinn nach entnommen sind, in jedem Einzelfall als Entlehnung kenntlich gemacht habe; dass diese Dissertation noch keiner anderen Fakultät oder Universität zur Prüfung vorgelegen hat; dass sie – abgesehen von unten angegebenen Teilpublikationen – noch nicht veröffentlicht worden ist, sowie, dass ich eine solche Veröffentlichung vor Abschluss des Promotionsverfahrens nicht vornehmen werde. Die Bestimmungen der Promotionsordnung sind mir bekannt. Die von mir vorgelegte Dissertation ist von Prof. Dr. Jürgen Stutzki betreut worden.

Köln den